Built to Share: Modular Design Tools for Accessible Microfluidics and Decentralized Diagnostics

Cosette McLemore Craig

A dissertation submitted in partial fulfillment
of the requirements for the degree of

Doctor of Philosophy

University of Washington
2025

Reading Committee:
Ayokunle Olanrewaju, Chair
Nathan Sniadecki
Ashleigh Theberge

Program Authorized to Offer Degree:
Mechanical Engineering

© Copyright 2025
Cosette McLemore Craig

University of Washington

Abstract

Built to Share: Modular Design Tools for Accessible Microfluidics and Decentralized Diagnostics

Cosette McLemore Craig

Chair of the Supervisory Committee:
Ayokunle Olanrewaju
Department of Bioengineering

Modern microfluidics offers transformative potential for global health, but realizing that promise requires tools that are not only capable, but also accessible, adaptable, and designed for sharing. This dissertation advances a modular design philosophy for decentralized diagnostics and fluidic autonomy, focusing on approaches that eliminate reliance on expensive infrastructure.

Chapter 1 addresses a pressing global health challenge: therapeutic drug monitoring (TDM) for HIV treatment and prevention. I introduce RESTRICT and REACT, enzymatic assays that quantify pharmacologic activity of antiretroviral drugs, providing clinically validated, equipment-light alternatives to LC-MS/MS. These assays enable long-term adherence monitoring in low-resource and point-of-care settings and motivate the pursuit of self-driven microfluidic systems capable of automation without external pumps or power.

Chapter 2 develops and formalizes the microfluidic chain reaction (MCR) as a programmable capillaric architecture. By framing MCRs in a circuit-based analytical model

and producing open-source design tools, I bridge theoretical potential and practical deployment, enabling fluidic workflows to be encoded directly into chip geometry. This framework defines design rules, failure modes, and implementation strategies for autonomous fluid handling.

Chapter 3 evaluates fabrication strategies for capillaric systems outside of cleanroom environments, focusing on cost, resolution, and ease of implementation. I assess low-cost LCD 3D printers alongside conventional DLP systems, documenting achievable feature dimensions, common print failures, and post-processing techniques. Practical guidance is provided for assembly, integration of capillary pumps, interfacing components, and adapting designs for accessible manufacturing. These methods lower the barrier for fabricating functional, programmable microfluidic circuits in resource-limited settings.

Chapter 4 extends the capillarics toolkit by adapting two advanced cleanroom-fabricated geometries, phaseguides for sequential fluid routing and SCMs for reagent resuspension, into printable forms compatible with low-cost LCD 3D printers. I characterize their operation, identify design constraints imposed by printer resolution, and validate performance in fluid routing and pulse-shaped reagent delivery. A sharable STL library, failure mode atlas, and Python-based analysis scripts accompany these designs, enabling reproducibility and adaptation by other researchers.

Together, these contributions establish a shareable toolbox of assays, geometries, fabrication methods, and analytical frameworks for building autonomous, modular microfluidic devices. The work shifts high-performance microfluidics from cleanroom exclusivity toward open, distributed manufacturing, broadening who can design, build, and deploy diagnostic systems in both research and global health contexts.

To Kettle, Nimbus, Pennies, Brick,
Chip, Paddy, Wallace, Dr. Gingersnap, and Tricky

"...everything that I understand,
I understand only because I love.

Pierre Bezukhov
War and Peace, Leo Tolstoy

Acknowledgments

I extend my utmost appreciation and gratitude to all of the undergraduate students, graduate students, postdoctoral scholars, and research staff and faculty I've gotten the opportunity to collaborate with during my time at the University of Washington. I specifically want to thank the current and past members of the Ọlánrewájú Lab that I've met along the way. I couldn't have done any of this without your creativity, tenacity, and support.

Postdoctoral Scholars and Faculty: Dr. Ayokunle Olanrewaju, Dr. Megan Chang, Tim Robinson. **Graduate Students:** Dr. Cara Brainerd, Kelsey Leong, Dorothy Mims, Maya Singh, Aileen Sun, Sarina Barnes, Justus Brown, John Tatka. **Research Staff:** Carrie Lin, Noah Pham. **Undergraduate Students:** Emily Blake, Zoe Blumenkranz, Megan Castellanos, Jason Chan, Jayma Erker, Mark Fernandez, Auden Gostin, Felix Guo, Caitlyn Kwong, Hannah Nguyen, Annie Qiu, Mindy Quach, Diya Rekhi, Catherine Rodgers, Megan Vuong, Madison Walenta, Sophie Walters, Katherine Zhang, Nadir Ziane.

This work was not possible without my family and friends. **Taylor,** thank you for nearly 10 years of friendship and for building a life here in the pacific northwest with me. I cannot talk about who I am without mentioning you. **Scarlet,** thank you for the giggles only sisters (or best friends with the same last name) could share. **Colton,** thank you for sparking my curiosity about the expanse of this work in real systems and for growing our family. **Page,** thank you for joining our family and bringing your humor and sweetness in equal abundance to our life (including cooking up a new addition to it). **Margot,** thank you for bringing me a a new tier of love. You give me joy, hope, and excitement for my future. I can't wait to play with STEM toys for toddlers with you. **Dad,** thank you for silliness and seriousness. **Mom,** thank you for fire and tenderness.

Contents

Abstract and Scope of the Dissertation iii

Dedication v

Acknowledgments vi

1 Prologue: Towards improved HIV supportive care 1

1.1 Abstract . . . 1
1.2 Introduction . . . 2
1.3 Abbreviations . . . 3
1.4 HIV as a Global Pandemic . . . 4
1.5 HIV Antiretrovirals (ARVs) and Therapeutic Drug Monitoring (TDM) . . . 6
1.5.1 Tenofovir Diphosphate as a Cumulative Adherence Marker . . . 6
1.5.2 Gold-Standard Monitoring and Limitations . . . 8
1.5.3 Existing Technologies . . . 8
1.6 RESTRICT: REverSe TRanscrIptase Chain Termination Assay . . . 10
1.6.1 Clinical Validation . . . 12
1.6.1.1 Methods . . . 12
1.6.1.2 Results . . . 16
1.6.1.3 Discussion, Remaining Limitations, and Outlook . . . 18
1.7 Emergence of Long-Acting Injectable Antiretrovirals . . . 20
1.7.1 Interindividual Pharmacokinetics and the Need for TDM of Injectables 21
1.7.2 REACT: REverse transcriptase ACTivity Assay . . . 23
1.7.2.1 Materials and Methods . . . 23
1.7.2.2 Results . . . 25
1.7.2.3 Discussion . . . 28
1.8 HIV Drug Resistance . . . 29
1.8.1 Growing Prevalence and the Urgent Need for Supportive Care . . . 29

1.8.2 Motivation for New Means of Innovation 30

2 How to Build a Microfluidic Chain Reaction: A Practical Guide to Structurally Programmed Capillary Microfluidics 42

2.1 Abstract 42
2.2 Introduction 43
2.2.1 Highlighted Applications 44
2.2.1.1 Therapeutic Drug Monitoring 45
2.2.1.2 Wearables 46
2.2.1.3 Diagnostic Assays 48
2.2.2 Microfluidic Chain Reactions (MCRs) Are Powerful but Underutilized 50
2.3 Governing Equations 51
2.3.1 Capillary Pressure 51
2.3.2 Flow Rate 53
2.3.3 Resistance 55
2.4 Establishing Taxonomy of Capillaric Features 56
2.4.1 Branch 0 58
2.4.2 Capillary pump 58
2.4.3 Branches 2-4 58
2.4.4 Branch 1 59
2.4.5 Domino valves 59
2.5 Linking elements via circuitry 60
2.6 Designing Fluidic Circuit Logic 61
2.6.1 Branch 1 Draining 61
2.6.2 Branch 2 Draining 64
2.6.3 Branch 3, 4, and 0 Draining 66
2.6.4 Guidelines for Parametric Design of MCRs 70
2.6.4.1 Designing Cross-Sectional Dimensions 71
2.6.4.2 Designing Channel Lengths 71
2.6.4.3 Domino Valve Design 72
2.6.5 Transition to Fabrication 72
2.7 Conclusion 72

3 Practical Fabrication Methods for Capillarics: Tools, Techniques, and Trade-offs Beyond the Cleanroom 76

3.1 Abstract . . . 76
3.2 Introduction . . . 76
3.3 Low Cost LCD 3D-Printing . . . 77
3.4 Practical Considerations for Assembly and Integration . . . 81
3.4.1 Notes on Taping . . . 81
3.4.2 Capillary Pumps . . . 88
3.4.2.1 Paper Pumps . . . 88
3.4.2.2 Pillar Pumps . . . 89
3.4.3 Design Guidance for Interfacing Parts . . . 90
3.4.3.1 Elastic Resin . . . 90
3.4.3.2 Tolerancing . . . 91
3.5 Conclusion . . . 92

4 Expanding the Capillarics Toolbox: 3D-Printed Microfluidic Phaseguides and Self-Coalescence Modules 97
4.1 Abstract . . . 97
4.2 Introduction . . . 98
4.3 Materials and Methods . . . 99
4.3.1 Materials . . . 99
4.3.2 Proof-of-concept chip fabrication via 3D-printing . . . 99
4.3.3 Capillaric circuit fabrication via low-cost LCD 3D-printing . . . 100
4.3.4 3D-printing post-processing . . . 100
4.3.5 Flow visualization with food dye . . . 101
4.3.6 Reagent deposition . . . 101
4.3.7 Image and video capture . . . 101
4.3.8 RGB Intensity Aggregation and Plotting via Python . . . 101
4.4 Results . . . 102
4.4.1 3D-printed phaseguides . . . 102
4.4.1.1 Operating principle of phaseguides . . . 102
4.4.1.2 Sequential liquid delivery using phaseguides with distinct pressure barriers . . . 103
4.4.2 3D-printed self-coalescing modules (SCMs) . . . 105
4.4.2.1 Key features and operation of SCMs . . . 105
4.4.2.2 3D-printed SCMs scaled up 50X from cleanroom fabrication 107

4.4.2.3 Proof-of-concept reagent reconstitution using 3D-printed SCMs . . . 109
4.4.2.4 Integration of an SCM into a 3D-printed capillaric circuit . 110
4.5 Discussion . . . 112
4.5.1 Comparisons with other published work . . . 112
4.5.2 Exceptions and unaddressed aspects of 3D-printed phaseguides and SCMs . . . 114
4.6 Conclusion . . . 115

5 Conclusions, Scientific Contributions, and Future Directions 121
5.1 Summary of Scientific Contributions . . . 121
5.2 Building on Prior Work in Capillary Microfluidics . . . 122
5.2.1 Low Cost 3D-Printing: From Concept to Practice . . . 122
5.2.2 Expansion of the Capillarics Toolkit . . . 123
5.2.3 From Individual Devices to Generalizable Logic . . . 123
5.2.4 Automation with Real-World Constraints . . . 123
5.3 Perspective and Future Directions . . . 124
5.3.1 Materials and Surface Engineering . . . 124
5.3.2 Functional Limits of Low Cost Printing . . . 124
5.3.3 Broader Integration of Reagent Handling . . . 124
5.3.4 Biological and Clinical Validation . . . 125
5.3.5 Usability and Deployment . . . 125
5.3.6 Detection Modalities Beyond Fluorescence . . . 125
5.3.7 Scaling and Multiplexing . . . 126
5.4 Engineering as Translation . . . 126
5.5 Final Reflections . . . 127

A Supplementary Material For Chapter 2 128
A.1 Additional Capillaric Elements . . . 128
A.1.1 Additional capillaric elements . . . 128
A.2 Extended Design Theory . . . 129
A.2.1 Stop Valve Burst Pressure . . . 129
A.2.2 Stop valves . . . 130
A.2.3 Theoretical Effect of Perpendicularity on Bursting Pressure . . . 132
A.2.4 Serpentine Capillary Filling Behavior . . . 134

A.2.5 Derivation of Junction Pressures . . . 140
A.2.6 Note on Duplication . . . 142
A.3 Capillary Pressure Modeling for Domino Valves . . . 142
A.4 3D Printing Standard Operating Procedure . . . 154
A.5 SOP for Cutting Microfluidic Covertape with the Silhouette Cameo 4 . . . 177

A Supplementary Material For Chapter 4 **189**
A.1 SCM Technical Drawing . . . 190
A.2 Sharable STL Library of SCM Variants . . . 190
A.3 Python Scripts Used for Characterization of Reagent Reconstitution in 3D-Printed SCMs . . . 192
A.3.1 Interactive ROI Selection and Normalization from a Single SCM Video Frame . . . 192
A.3.2 Time-Stamped Frame Montage of SCM Ejection Post-Reagent Reconstitution . . . 196
A.3.3 Batch Annotation of SCM Videos Using Shared Reference ROI . . . 202
A.3.4 Aggregating and Plotting Inverted RGB Intensity from CSV Files . . . 205
A.4 Design Iterations and Lessons Learned . . . 211
A.4.1 Characterization Chip 1: Trench Depth and Width Variations . . . 211
A.4.2 Characterization Chip 2: Ramp Stops and Curl Geometry . . . 213
A.4.3 Characterization Chip 3: SCM Redesign 1 (Self-Wetting & Venting Modules) . . . 214
A.4.4 Characterization Chip 4: SCM Redesign 2 (Corrugation Configurations) . . . 214
A.4.5 Characterization Chip 5: Curl Optimization . . . 214
A.4.6 Characterization Chip 6: Ramp Stop Redesign ("Salmon Belly" Design) . . . 215
A.4.7 Characterization Chip 7: Miniaturized SCMs . . . 215
A.4.8 Beads V7/V8: Circuit-Level Testing . . . 216
A.4.9 Hydrophilic Resin Trials . . . 216
A.4.10 Conclusion . . . 216
A.5 Failure Mode Analysis . . . 217
A.5.1 Successful coalescence . . . 217
A.5.2 Instability across leading barrier . . . 217
A.5.3 Insufficient pinning on the corrugations . . . 218

A.5.4 Wide trench impedes self-coalescence 218
A.5.5 Sustained pinning between leading barrier and diversion barrier . . 218
A.5.6 Conclusion 218
A.6 Preliminary Integration of RESTRICT with SCM-Based Microfluidics 219
A.6.1 Demonstration of an Enzyme Inhibition Assay Using 3D-Printed SCMs 219

List of Figures

1.1 Global HIV Incidence and Mortality in 2021 5
1.2 Disparities in U.S. HIV Transmission by Race and Risk Group 5
1.3 Adherence Drives Effectiveness of Tenofovir-Based PrEP 7
1.4 Cumulative TFV-DP Levels Predict HIV Incidence During PrEP 7
1.5 RESTRICT Assay Uses RT Inhibition to Measure TFV-DP Activity 10
1.6 RESTRICT Accurately Detects Clinically Relevant TFV-DP Levels 11
1.7 Workflow for Measuring TFV-DP in DBS Using RESTRICT 13
1.8 RESTRICT Data Processing Pipeline for DBS Quantification 16
1.9 RESTRICT Values Strongly Correlate with Gold-Standard TFV-DP Measurements 17
1.10 RESTRICT Identifies Low, Moderate, and High Adherence with High Sensitivity and Specificity 18
1.11 Pharmacokinetic Variability of Long-Acting Cabotegravir by Sex 22
1.12 REACT Assay Measures HIV RT Inhibitors via Fluorescence Readout 24
1.13 REACT Quantifies Five NNRTIs Across Clinically Relevant Concentrations . 26
1.14 REACT Performance Is Consistent Between Portable and Benchtop Readers 27
1.15 REACT Maintains Accuracy in Human Plasma and Portable Reader Formats 28
1.16 Not All ART Failures Are Due to Drug Resistance 30
1.17 Treatment monitoring algorithm updated in 2021 31

2.1 Capillarics for Therapeutic Drug Monitoring 45
2.2 Wearable Capillary Microfluidics 47
2.3 Capillarics for Diagnostic Assays 49
2.4 Capillary pressure of common microchannel geometries 52
2.5 Storyboard of sequential flow events for a domino chip 57
2.6 MCR Branch 1 Draining 62
2.7 MCR Branch 2 Draining 65
2.8 MCR Branch 3 Draining 67

2.9 MCR Branch 4 Draining . . . 68
2.10 MCR Branch 0 Draining . . . 69
2.11 Design rules for an MCR summarized for quick reference . . . 70

3.1 Comparison between microchannels printed with identical resin on LCD and DLP printers. . . . 78
3.2 Preprogrammed sequential liquid delivery with capillaric circuits 3D-printed with low-cost, water-wash resin on an LCD printer. . . . 80
3.3 Dimensions for female Luer lock syringe fitting that can be placed on chips to easily flush closed channels. The syringe can be loaded with IPA or an appropriate resin solvent. . . . 84
3.4 Attempted print of a closed channel with an internal pillar structure using a low-cost LCD 3D printer and Leong et al print settings [1] . . . 84
3.5 Results of PLInk protocol with minor optimizations . . . 86
3.6 Two-layer domino valves constructed with patterned cover tape for selective hydrophobicity . . . 87
3.7 Example geometry for attaching a paper pump to the outlet of a chip . . . 89
3.8 Caption . . . 90
3.9 Two-layer domino valve with direct sample tube connection . . . 93

4.1 Schematic illustration of phaseguide design and operating principle. . . . 104
4.2 Sequential liquid delivery using phaseguides with distinct pressure barriers. 105
4.3 Schematic, key features, and operating principle of 3D-printed self-coalescence modules. . . . 106
4.4 3D printing enables adjustable channel heights and increased volumes in SCMs. . . . 108
4.5 Reconstitution of amaranth dye in large-volume 3D-printed SCM . . . 111
4.6 Integration of an SCM into a low-cost 3D-printed capillaric circuit. . . . 113

A.1 Burst pressure for a generalized conical stop valve . . . 130
A.2 Common stop valve geometries and their burst pressures . . . 133
A.3 Effect of printed edge perpendicularity on theoretical bursting pressure. . . . 134
A.4 Capillary filling length over time in a closed rectangular serpentine microchannel. Theoretical curve and two experimental replicates are shown, along with a metrics table summarizing flow properties and fit quality. . . . 135

A.5 Example GUI for capillary fill time simulation. Users input microchannel geometry and fluid properties, then visualize fit to experimental data. . . . 136
A.6 Example GUI for capillary fill time simulation. Users visualize fit to experimental data. . . . 136

A.1 Dimensional schematics for four SCM variants . . . 191
A.2 Annotated SCM frame with user-defined ROIs . . . 192
A.3 SCM ejection montage after reagent reconstitution . . . 197
A.4 Batch SCM frame annotation using shared ROI . . . 202
A.5 Mean RGB curves with standard deviation . . . 206
A.6 SCM Design Schematic with Annotated Features . . . 212
A.7 Annotated SCM Design with Optimization Notes . . . 213
A.8 Curl Geometry and "Salmon Belly" Variants for Enhanced Wrapping . . . 215
A.9 Failure modes in miniaturized SCMs reveal the role of Laplace barriers . . . 217
A.10 **Fluidic demonstration of RESTRICT assay integration with a 3D-printed self-coalescence module (SCM)** . . . 220

List of Tables

1.1 Abbreviations 3
1.2 Participant Demographics from Directly Observed PrEP Study 16

3.1 Print settings for Figure 3.5 86

A.1 Design parameters for sharable SCM variants 190
A.2 Fixed SCM design parameters used across all characterization chips. 211
A.3 Trench depth and width variations tested in Characterization Chip 1. 212
A.4 Step height variations between reservoir and outlet in Characterization Chip 2. 214
A.5 Curl geometry variations tested in Characterization Chip 2. 214
A.6 Trench depth and width variations tested in Characterization Chip 7. This miniaturized SCM series targeted improved performance with reduced scale. 216

1 | Prologue: Towards improved HIV supportive care

1.1 Abstract

This chapter details my foundation for the development of accessible, point-of-care technologies to support long-term HIV care and prevention. It begins by contextualizing the persistent global burden of HIV and the need for therapeutic drug monitoring (TDM) to ensure antiretroviral (ARV) efficacy. It introduces the RESTRICT assay, an enzymatic activity assay that provides a semi-quantitative measure of long-term adherence to tenofovir-based regimens, and highlights the clinical validation I conducted using dried blood spots. The chapter then extends this platform into REACT (REverse transcriptase ACTivity), a next-generation assay capable of measuring multiple non-nucleoside reverse transcriptase inhibitors (NNRTIs), including those used in long-acting injectable formulations. The chapter closes by framing HIV drug resistance as a growing challenge, motivating the need for supportive care tools. These insights catalyze a shift in focus toward automated, pump-free microfluidic systems explored in later chapters.

1.2 Introduction

This chapter includes elements adapted from three peer-reviewed journal articles:

i. **"REverSe TRanscrIptase chain termination (RESTRICT) for selective measurement of nucleotide analogs used in HIV care and prevention"**,A. O. Olanrewaju, B. Sullivan, A. Gim, Cosette A. Craig, D. Sevenler, A. Bender, P. Drain, J. Posner. *Bioengineering & Translational Medicine*, 2022. https://doi.org/10.1002/btm2.10369

ii. **"Validation of the Reverse Transcriptase Chain Termination (RESTRICT) Assay for Measuring Tenofovir Diphosphate in Dried Blood Spots from a Clinical Pharmacokinetic Trial"**, Cosette A. Craig[†], B. Sullivan[†], A. Bender, E. Blake, O. Siriprakaisil, P. Sukrakanchana, T. Cressey, P. Drain, A. O. Olanrewaju, J. Posner. [†]Authors contributed equally. *The Journal of Antimicrobial Chemotherapy*, 2025. https://doi.org/10.1093/jac/dkaf049

iii. **"REverse transcriptase ACTivity (REACT) assay for point-of-care measurement of established and emerging antiretrovirals for HIV treatment and prevention"**, C. Brainerd, M. Singh, J. Tatka, Cosette Craig, S. Gilligan-Steinberg, N. Panpradist, M. Chang, B. Lutz, A. O. Olanrewaju. *Analytical and Bioanalytical Chemistry*, 2024. https://doi.org/10.1007/s00216-024-05602-4

1.3 Abbreviations

HIV	**H**uman **I**mmunodeficiency **V**irus
PLWHIV	**P**eople **L**iving **W**ith **HIV**
ARV	**A**nti**R**etro**V**iral
PrEP	**Pr**e-**E**xposure **P**rophylaxis
TDM	**T**herapeutic **D**rug **M**onitoring
DLF	**D**rug **L**evel **F**eedback
LC-MS/MS	**L**iquid **C**hromatography tandem **M**ass **S**pectrometry
LFA	**L**ateral **F**low **A**ssay
NRTI	**N**ucleoside **R**everse **T**ranscriptase **I**nhibitor
TDF	**T**enofovir **D**isoproxil **F**umarate
TAF	**T**enofovir **A**la**F**enamide
TFV-DP	**T**eno**F**o**V**ir **D**i**P**hosphate
NNRTI	**N**on-**N**ucleoside **R**everse **T**ranscriptase **I**nhibitor
RPV	**R**il**P**i**V**irine
DPV	**D**a**P**i**V**irine
DOR	**DOR**avirine
INSTI	**IN**tegrase **S**trand **T**ransfer **I**nhibitor
CAB	**CAB**otegravir
DTG	**D**olu**T**e**G**ravir
DOT	**D**irectly-**O**bserved **T**herapy
DBS	**D**ried **B**lood **S**pot
RT	**R**everse **T**ranscriptase Enzyme
LAI	**L**ong-**A**cting **I**njectable
RESTRICT	**RE**ver**S**e **TR**anscr**I**ptase **C**hain **T**ermination
REACT	**RE**verse Transcriptase **ACT**ivity Assay

Table 1.1: Abbreviations

1.4 HIV as a Global Pandemic

HIV was first identified as a public health concern in 1981, when the U.S. Centers for Disease Control and Prevention (CDC) reported clusters of unusual illnesses among gay men in Los Angeles and New York [1]. Since that time, the World Health Organization (WHO) estimates that HIV has caused 42.3 million deaths worldwide, and transmission continues across the globe. By the end of 2023, an estimated 39.9 million people were living with HIV.

The Joint United Nations Programme on HIV/AIDS (UNAIDS) introduced the 95-95-95 targets, a global strategy aiming to end HIV/AIDS as a public health threat by 2030. These goals include: 95% of all people living with HIV (PLWH) knowing their status, 95% of those diagnosed accessing antiretroviral therapy (ART), and 95% of those on treatment achieving viral suppression. Per the most recent update at the time of writing this (end of 2023), 86% of individuals living with HIV were aware of their status. Of those who had been diagnosed, 89% were receiving antiretroviral therapy, and among those on treatment, 93% had achieved viral suppression [2].

While the global median HIV prevalence among adults aged 15 to 49 stands at 0.8%, certain populations face significantly elevated risks due to social and structural inequities (Figures 1.1 and 1.2). In regions like eastern and southern Africa, young women and girls aged 15 to 24 experience notably higher rates. Gay men and other men who have sex with men are among the most affected, with prevalence nearly 8% higher than the general adult population. Similarly, HIV prevalence is disproportionately higher among sex workers (3% higher), people who inject drugs (5% higher), transgender people (9.2% higher), and incarcerated people (1.3% higher). These disparities reflect the compounded impact of stigma, marginalization, and, in some cases, criminalization on access to prevention and care.

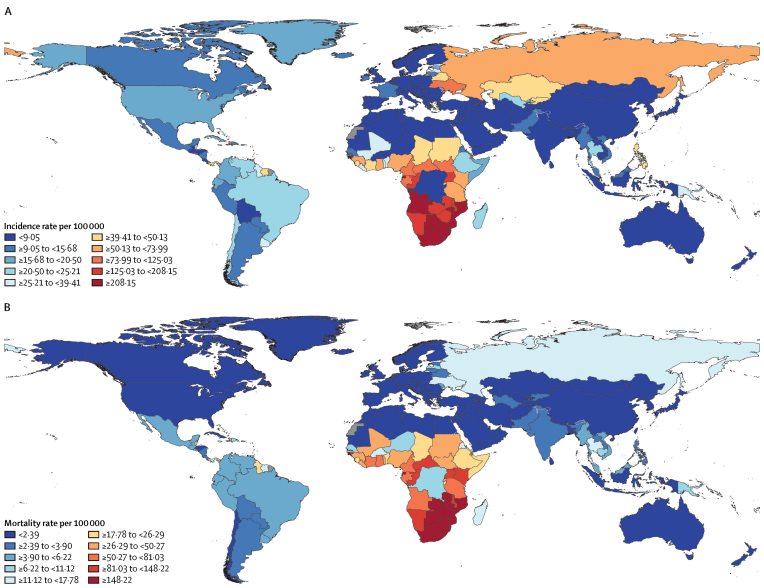

Figure 1.1: Global HIV Incidence and Mortality in 2021 Age-standardized HIV incidence **(A)** and mortality **(B)** rates by region for all sexes in 2021. Data reflect persistent global disparities in HIV burden [3].

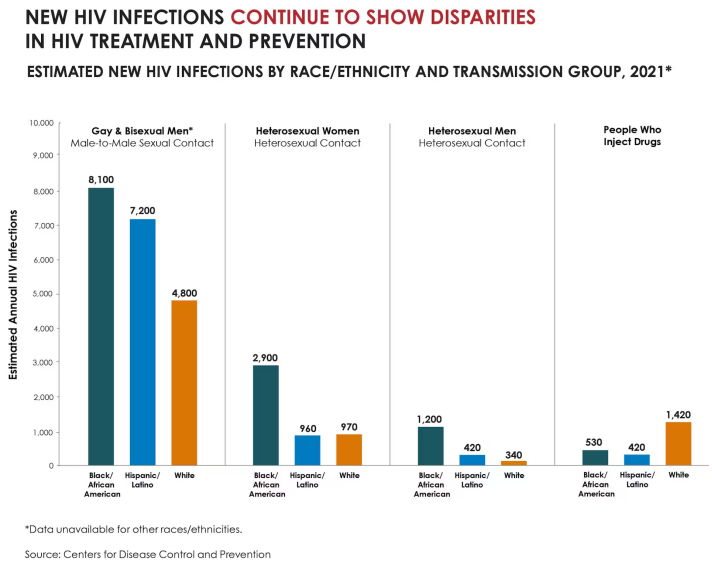

Figure 1.2: Disparities in U.S. HIV Transmission by Race and Risk Group Estimated new HIV infections in the United States in 2021, stratified by race/ethnicity and transmission group. Data highlight disproportionate burden among Black and Latino gay and bisexual men [4].

1.5 HIV Antiretrovirals (ARVs) and Therapeutic Drug Monitoring (TDM)

Antiretroviral (ARV) therapy and pre-exposure prophylaxis (PrEP) form the foundation of HIV care and prevention, offering a range of delivery methods - including daily oral tablets, monthly vaginal rings, and injections administered up to every two months - that can be customized for different population needs. Although significant progress has been made in ARV development, including combination drugs and long-acting formulations, consistently maintaining therapeutic drug concentrations remains essential for treatment effectiveness [5–7]. Suboptimal drug levels can result from factors such as irregular adherence, interruptions in treatment, and individual differences in drug metabolism and absorption [8–10]. Certain groups - such as older adults, children, pregnant individuals, and those with coexisting health conditions like tuberculosis - may face additional barriers to sustaining adequate ARV levels [11–14]. Prolonged periods of low ARV exposure increase the likelihood of drug resistance, posing serious risks to both personal health outcomes and broader public health efforts in HIV prevention and treatment [8, 15, 16].

Emerging research suggests that integrating drug-level feedback (DLF) into both clinical trials and routine HIV care can support better adherence and lead to improved health outcomes [17, 18]. For instance, a retrospective cohort study conducted in Italy showed that including therapeutic drug monitoring in standard care for people living with HIV (PLWH) was linked to shorter hospital stays and lower treatment expenses [10]. More recently, the MTN-034/REACH study—which offered DLF as one of several tailored adherence strategies for adolescent girls and young women (AGYW) on PrEP in South Africa, Uganda, and Zimbabwe—reported significantly higher adherence rates compared to earlier studies [19, 20].

1.5.1 Tenofovir Diphosphate as a Cumulative Adherence Marker

PrEP regimens based on tenofovir disoproxil fumarate (TDF) are widely recommended as a first-line option due to their strong efficacy, broad availability, and affordability through generic formulations (Figures 1.3 and 1.4) [21–24]. After oral administration, TDF is converted into tenofovir, which is then phosphorylated inside cells to its active form, tenofovir diphosphate [25, 26]. This active metabolite builds up gradually in red blood cells, where it has a relatively long half-life of 17 to 21 days [27, 28].

As a result, tenofovir diphosphate levels in red blood cells serve as a reliable indicator of cumulative adherence over the preceding one to two months [28, 29].

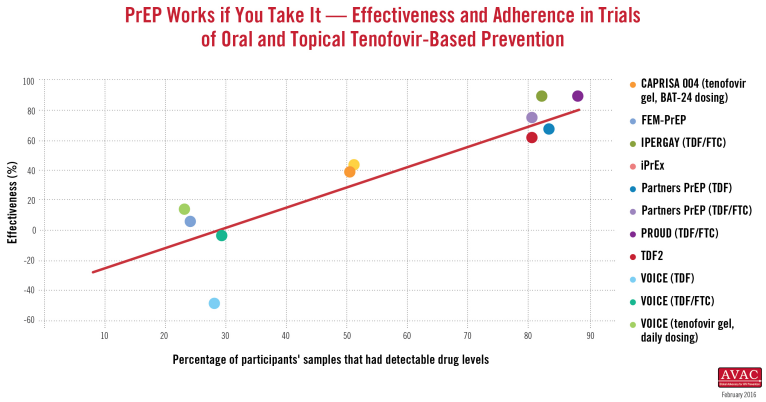

Figure 1.3: Adherence Drives Effectiveness of Tenofovir-Based PrEP Outcomes from multiple clinical trials comparing HIV prevention efficacy across oral and topical tenofovir-based regimens. Higher adherence consistently correlates with greater protective effect [23].

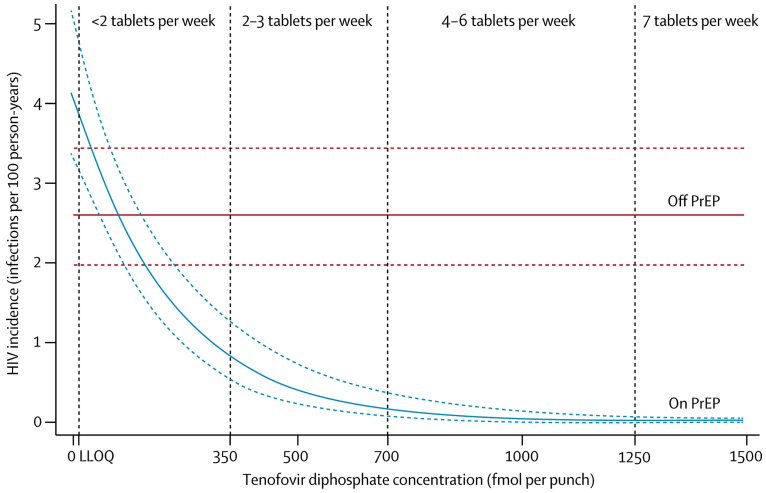

Figure 1.4: Cumulative TFV-DP Levels Predict HIV Incidence During PrEPHIV-1 incidence during PrEP use as a function of tenofovir diphosphate (TFV-DP) levels in dried blood spots. Incidence estimates were derived via exponential regression and adjusted for study site, age, receptive anal intercourse, and syphilis status. Placebo group incidence is shown for reference. Error bounds represent ± 1 standard error [24].

Other adherence biomarkers, including tenofovir and emtricitabine (both nucleotide reverse transcriptase inhibitors (NRTIs)) can also be measured in blood or urine [30]. However, these compounds have much shorter half-lives (around 15 hours), which makes them more reflective of recent dosing behavior within the past 1 to 7 days [30, 31]. Their short duration of detectability also increases the likelihood of being influenced by "white

coat" adherence, where individuals may take their medication shortly before clinical visits to appear adherent [32].

1.5.2 Gold-Standard Monitoring and Limitations

Liquid chromatography tandem mass spectrometry (LC-MS/MS) is the gold-standard method to measure tenofovir diphosphate concentrations from either dried blood spots (DBS) or hair [28, 33–35]. Both DBS and hair offer long-term insights into adherence based on the accumulation of TFV-DP [36]; DBS are a stable sample storage method [37] and hair offers granular adherence patterns based on the segment selecting for measurement [38].

Several directly observed therapy (DOT) studies have used LC-MS/MS to establish steady-state adherence thresholds for adherence, categorically as low, medium, and high adherence based on drug concentrations [28, 39].

Objective drug-level monitoring via LC-MS/MS is highly dependent on high capital cost equipment and highly trained operators [38], limiting its use to centralized laboratories with high turnaround times (>1 month) [20]. Despite its power as a gold standard drug adherence metric, these factors must be alleviated to facilitate widespread adoption [40].

1.5.3 Existing Technologies

Immunoassays, such as ELISAs, present a more accessible alternative to LC-MS/MS by offering simpler protocols and requiring less specialized equipment, which makes them well-suited for broader clinical use. However, their utility can be limited by lower specificity and the potential for cross-reactivity, which can compromise result accuracy. Recent innovations have expanded the use of antibody-based methods to detect tenofovir (TFV) in urine, enabling real-time adherence monitoring. These assays have been adapted into lateral flow formats that are inexpensive, easy to administer without extensive training, and capable of identifying recent TFV intake. For instance, a gold nanoparticle-based competitive assay developed by Pratt et al. could detect TFV at concentrations as low as 1 μg/mL in urine, though the test duration remains a drawback at 55 minutes [41].

Gandhi et al. introduced a faster lateral flow assay for urinary TFV detection that delivers results within minutes and can be used by non-specialist personnel. This rapid test achieved high diagnostic performance—100% specificity and 96% sensitivity—and showed strong correlation with LC-MS benchmarks [42]. Its implementation across 38

HIV clinics in Namibia demonstrated real-world benefits: 87% of participants who previously struggled with viral suppression achieved it after six months of using the test in combination with adherence counseling. The test was also positively received, with over 85% of patients and 90% of providers supporting its routine use [43]. In a separate randomized study in Kenya, women on PrEP who received adherence counseling informed by urine TFV test results had significantly better adherence at 12 months than those who received standard counseling. This group had higher rates of both short-term (urine) and long-term (hair) TFV detection, and most participants found the test acceptable [18].

Despite the encouraging data, current versions of the test are limited to detecting TFV alone and only provide a binary result based on a set threshold. Because urine levels reflect recent dosing, the test may also be affected by short-term behavior changes, such as taking medication just before a clinic visit. Nonetheless, the integration of urine-based TFV testing into adherence support strategies shows strong potential for improving long-term outcomes in both PrEP and HIV treatment.

1.6 RESTRICT: REverSe TRanscrIptase Chain Termination Assay

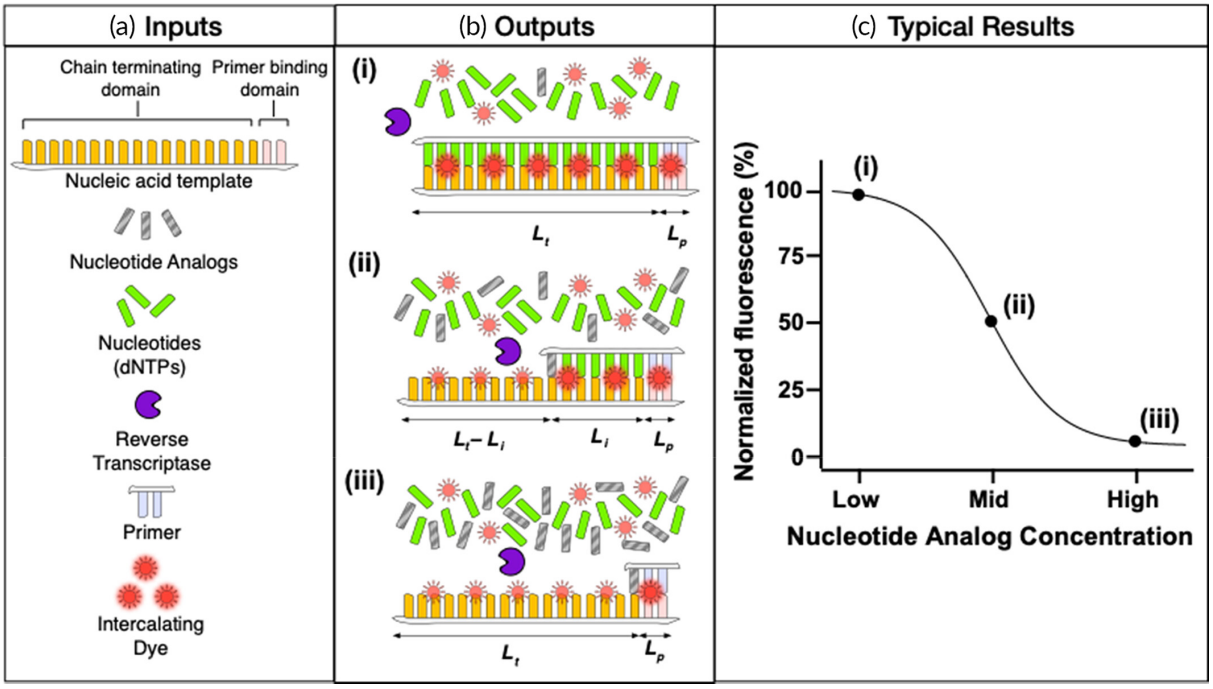

Figure 1.5: RESTRICT Assay Uses RT Inhibition to Measure TFV-DP Activity Schematic of the REverSe TRanscrIptase Chain Termination (RESTRICT) assay. High concentrations of tenofovir diphosphate (TFV-DP) inhibit reverse transcriptase, reducing DNA synthesis and fluorescence. Low TFV-DP permits greater synthesis and signal [44].

The REverSe TranscrIptase Chain Termination (RESTRICT) assay was developed in 2020 for objective detection of NRTIs based on their enzyme inhibition activity[45]. RESTRICT directly measures the pharmacologic activity of the analyte TFV-DP. RESTRICT uses DNA templates, nucleotides, recombinant HIV-1 reverse transcriptase enzyme, primers, and intercalating dyes to infer the concentration of nucleotide analogs based on the inhibition of DNA synthesis by recombinant HIV RT (Figure 1.5). DNA chain termination occurs at high drug (NRTI) concentration resulting in low DNA synthesis and low fluorescence reported by the intercalating dye. Meanwhile at low drug concentration, there is extensive DNA synthesis and high fluorescence from the intercalating dye.

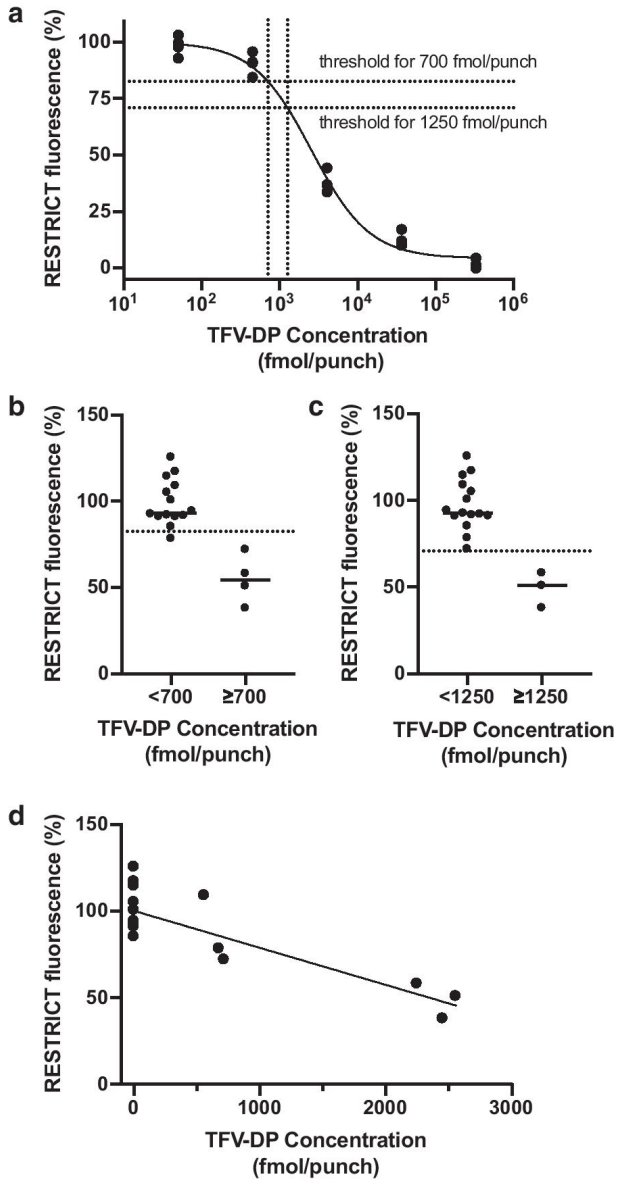

Figure 1.6: RESTRICT Accurately Detects Clinically Relevant TFV-DP Levels (A) Fluorescence thresholds for RESTRICT assay corresponding to tenofovir diphosphate (TFV-DP) concentrations indicative of adequate (700 fmol/punch) and perfect (1250 fmol/punch) adherence, interpolated from standard curves. **(B)** RESTRICT distinguished samples above 700 fmol/punch with 100% sensitivity and 92.9% specificity. **(C)** At the 1250 fmol/punch threshold, both sensitivity and specificity reached 100%. **(D)** RESTRICT fluorescence values showed strong inverse correlation with LC–MS/MS-measured TFV-DP concentrations (Pearson's $r = -0.845$, $p < 0.0001$) [46].

In a pilot clinical evaluation of n=18 samples (n=6 with detectable drug levels), RESTRICT measured clinically relevant TFV-DP concentrations in whole blood and identified participants with TFV-DP concentrations corresponding to adequate adherence ($\geq$700

fmol per 3 mm dried blood spot (DBS) punch [28])) among PrEP clients (Figure 1.6). In this early iteration of RESTRICT, dilution in water was used for sample preparation to release intracellular TFV-DP from RBCs [46]. However, heating and filtration steps were adopted for clinical validation given the improvement of %CVs of fluorescence measurements [47].

Prior to clinical validation, a probabilistic model of RESTRICT was created [44]. Assay components like nucleotide concentration, template length, and template sequence were incorporated into the model to guide design and optimization of the assay.

1.6.1 Clinical Validation

After early development and pilot validation of RESTRICT, a clinical validation was conducted with n=74 patient sample to semi-quantitatively distinguish clinically relevant ranges of TFV-DP in DBS [47]. The following section summarize the methodology, results, and conclusions from this study.

1.6.1.1 Methods

Study Population: Clinical dried blood spot samples were obtained from the DOT Tenofovir Adherence to Rapidly Guide and Evaluate PrEP and HIV Therapy (TARGET) study (ClinicalTrials.gov #NCT03012607)[39]. In TARGET, HIV and HBV negative participants between 18 and 49 years of age were randomly assigned to three 'adherence' groups of 10 participants each (n = 30). Participants received directly-observed doses of tenofovir disoproxil fumarate/emtricitabine (300/200 mg, Truvada) for 6 weeks. The dosing regimen of the groups were as follows: the first group was administered a dose 7 times/week ('high adherence'), the second group was administered a dose 4 times/week ('moderate adherence'), and the third group was administered a dose 2 times/week ('low adherence'). After the 6-week dosing schedule, participants were followed for a 4-week wash-out period. Venous blood dried blood spots were collected at Weeks 1, 3, 5, 7, 8, 9 and 10. In total, n = 74 DBS samples over the 10-week timespan from 19 participants were analyzed via RESTRICT and compared to LC-MS/MS measurements. Samples were selected to provide a wide range of tenofovir diphosphate concentrations and thus represent the initial dosing weeks (as drug was accumulating), steady-state weeks and wash-out weeks. These data are used to determine the correlation between RESTRICT and LC-MS/MS measurements over anticipated ranges and do not represent an analysis of PrEP adherence.

...

Laboratory methods: DBS were stored at -80°C until analyzed. Tenofovir diphosphate concentrations were measured in the TARGET study using a previously validated liquid chromatography mass spectrometry (LC-MS/MS) assay[28, 36, 39]. Tenofovir diphosphate concentrations are reported in fmol per 3mm diameter biopsy punch of a DBS spot.

RESTRICT reaction master mix consisted of 10 mM dithiothreitol (20–265, Sigma Aldrich, USA), 100 nM deoxynucleotide triphosphates (dNTPs) (D7295, Sigma Aldrich, USA), 10 nM primer 16S rRNA forward primer (51-1-19-06, Integrated DNA Technologies, USA) and 1 nM DNA template with 60 mM Tris (77-86-1, Sigma Aldrich, USA), 30 mM KCl (7447-40-7, Sigma Aldrich, USA), 8 mM MgCl2 (7786-30-3, Sigma Aldrich, USA) buffered to pH 8.0 using HCl (H1758, Sigma Aldrich, USA). All values represent final assay concentrations. A custom DNA template was ordered from IDT, which has a 20-nucleotide complimentary primer binding site followed by 180-nucleotide TTCA repeating region for analog-selective chain termination of tenofovir diphosphate.

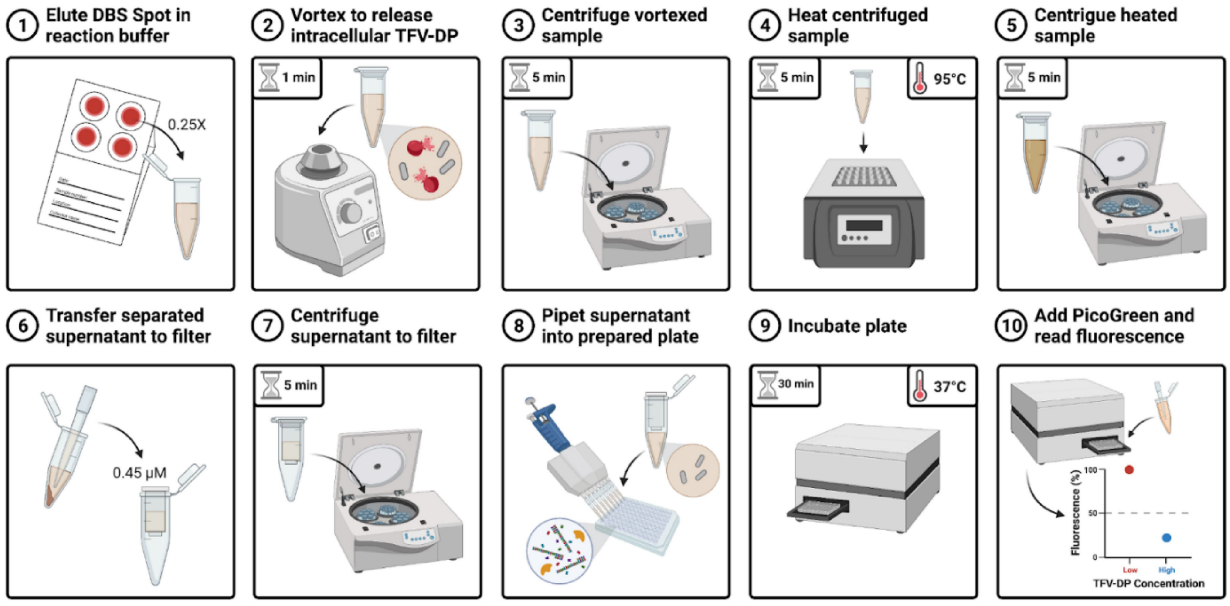

Figure 1.7: Workflow for Measuring TFV-DP in DBS Using RESTRICT Schematic of the RESTRICT assay workflow for tenofovir diphosphate (TFV-DP) measurement from dried blood spots (DBS). Red blood cells are lysed from DBS punches, and the eluate is heat-treated, filtered, and added to a reaction mix containing recombinant HIV reverse transcriptase. DNA synthesis is inhibited in the presence of TFV-DP and quantified via fluorescence.

In the RESTRICT workflow (Figure 1.7), DBS were biopsy punched (7 mm diameter) and eluted into 234 μL of nuclease-free water (AM9906, ThermoFisher Scientific, USA)

and vigorously vortexed for 1 minute to lyse red blood cells (RBCs) and release intracellular TFV-DP. Eluted DBS tubes were centrifuged at 10000 rcf for 5 min before being heated at 95°C for 5 minutes to cook proteins and hemaglobin that interfere with fluorescence. The tube was centrifuged again at 10000 rcf for 5 minutes. The supernatant was manually transferred to a 0.45 μm centrifuge filter (8170, Corning Inc., USA) and centrifuged at 10000 rcf for 5 minutes. The resulting eluate was agitated briefly before 10 μL of eluate was added to 20 μL of master mix in a flat-bottom polystyrene 96-well plate (3650, Corning Inc., USA). 10 μL of HIV-1 RT (382129-500U, Sigma Aldrich, USA) at a final concentration of 0.0212 units/μL was pipetted immediately before incubation at 37°C for 3 min in a microplate reader (SpectraMax iD3, Molecular Devices, USA). After 30 min, 40 μL of PicoGreen dye (P7581, ThermoFisher Scientific, USA) diluted 1:400 in TE buffer was added to stop the reaction, and the fluorescence of the reaction was measured.

To ensure data collected could be used to construct a normalization scheme, a negative control was included for each sample that contained no HIV-1 RT enzyme, as well as several wells in which various amounts of additional tenofovir diphosphate was spiked into the extracted DBS samples, serially diluted from 900 nM to 0.9 nM, to create a dose–response inhibition curve. Experimental conditions for each point of the inhibition curves were repeated in triplicate and averaged, with the exception of a small number of spiked-in conditions where sample volume was limited and duplicates were performed.

We also created 'blank' DBS cards from a whole blood sample from a single HIV negative, PrEP-naïve individual (BioIVT, USA). These DBS were created in quantity from the same sample and stored at -80°C before analyzing clinical samples and acted as a control for day-to-day variation in assay performance. A 'blank' DBS was included for every three clinical samples and was handled and processed identically. Three clinical samples and one 'blank' sample were processed in parallel in each 96-well plate.

...

Data analysis and statistical methods: Baseline correction of RESTRICT fluorescence intensities was performed by subtracting the average fluorescence of the negative control with no RT enzyme from the other experimental conditions. We fit a four-parameter logistic regression curve to the resulting fluorescence intensity as a function of spiked-in tenofovir diphosphate concentrations.

While simple baseline subtraction yielded a comparable correlation between RESTRICT and LC-MS/MS as a more complex normalization method, co-authors of the manuscript from which this section was adapted conducted the following additional

manipulation:

> "To extend the bounds of dose-response curves,] 'as-is' and 'no RT' trials were artificially pinned at 19 pM and 190 μM, respectively (effectively at zero and infinity, respectively)."
>
> "The baseline-subtracted fluorescence of the clinical samples was then divided by the maximum of the curve-fit of the included 'blank' DBS, and a similar four-parameter logistic regression curve-fit was applied to the resulting normalized ratio. We use the y-axis value of the IC50 point of this normalized ratio curve-fit and compared this against LC-MS/MS tenofovir diphosphate concentrations. An example of this data analysis is shown in Figure 1.8."
>
> "We calculated the Pearson correlation coefficient and the coefficient of determination between the normalized IC50 y-axis values and the log-transformed tenofovir diphosphate concentrations determined via LC-MS/MS. We performed receiver operating characteristic analysis for thresholds of established steady-state adherence benchmarks for tenofovir diphosphate concentrations in DBS. In a previous study, we established adherence benchmarks for this cohort as low adherence (2 doses/week, 466 fmol/3 mm punch), moderate adherence (4 doses/week, 779 fmol/3mm punch) and high adherence (7 doses/week, 1375 fmol/3mm punch)[48]. RESTRICT cut-off values were determined by selecting the point of the receiver operating characteristic curve that minimizes the distance to (0,1) in classifying samples as below the three respective LC-MS/MS adherence benchmark tenofovir diphosphate concentrations[49]. Data analysis was performed in Prism (GraphPad Software, USA) and MATLAB (MathWorks, USA)."

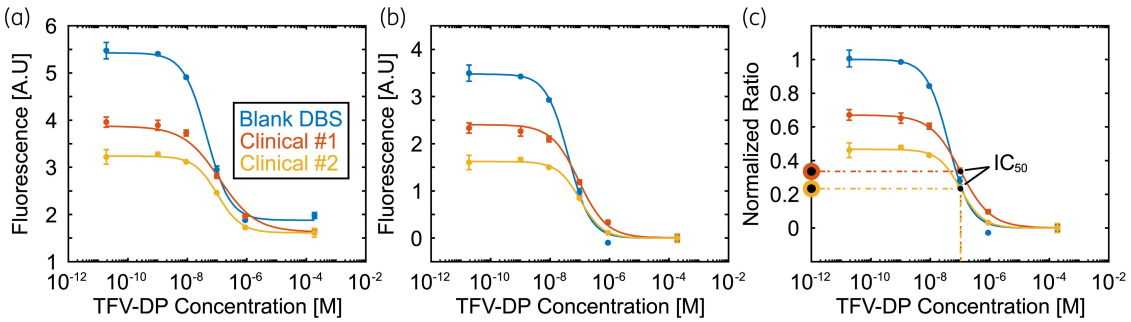

Figure 1.8: RESTRICT Data Processing Pipeline for DBS Quantification (A) Raw fluorescence curves from two clinical samples and a positive control ('blank' DBS), with TFV-DP added at various concentrations. Boundary points at 19 pM and 190 µM correspond to the 'as-is' and 'no RT' conditions, respectively. **(B)** Fluorescence values after baseline subtraction using the average signal from the 'no RT' condition. **(C)** Final normalized fluorescence curves, obtained by dividing by the maximum fluorescence of the fitted 'blank' DBS curve. Four-parameter logistic regression was applied to the normalized data to extract IC_{50} y-axis values, which were compared against LC-MS/MS results. Error bars represent standard deviation of triplicate (or duplicate) replicates.

In my opinion, the sample preparation techniques, the normalization scheme, and the representative adherence ranges selected by other authors that are represented in the final publication of these data significantly hinder the translation of this work to a point-of-care setting.

1.6.1.2 Results

n	74
Age (years)	33.5 (28-38)
Female, no. (%)	32 (43.2)

TFV-DP Concentrations			
x<466 fmol/punch	466<x<779 fmol/punch	779<x<1375 fmol/punch	x>1375 fmol/punch
27	17	19	11

Table 1.2: Participant Demographics from Directly Observed PrEP Study Demographic characteristics of participants in the directly observed PrEP study, including participant ID, age, sex assigned at birth, and PrEP regimen type.

Seventy-four DBS samples from 19 participants from the TARGET study were analyzed. TFV-DP concentrations ranged from 57 to 2580 fmol/3mm punch as measured by gold standard LC-MS/MS. Demographic data of participants and tenofovir diphosphate concentration distributions in clinical DBS samples tested are given in Table 1.2.

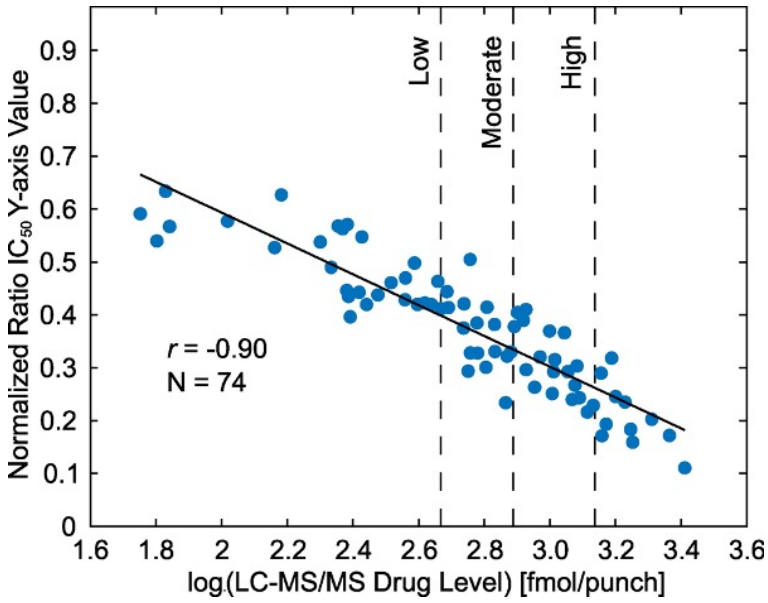

Figure 1.9: RESTRICT Values Strongly Correlate with Gold-Standard TFV-DP Measurements Normalized RESTRICT IC_{50} y-axis values plotted against $\log_{10}$-transformed TFV-DP concentrations measured by LC–MS/MS ($n = 74$). Dashed vertical lines denote established adherence thresholds for tenofovir diphosphate in DBS: low (466 fmol/3 mm punch), moderate (779 fmol/3 mm punch), and high (1375 fmol/3 mm punch) adherence. Pearson correlation coefficient: $r = -0.90$, $p < 0.0001$.

Figure 1.9 shows normalized RESTRICT fluorescence versus the log of the LC-MS/MS measurements. There is a strong correlation between LC-MS/MS tenofovir diphosphate concentrations and the RESTRICT normalized ratio IC50 y-axis value (n=74, Pearson r=-0.90; P<0.0001; 95% confidence interval (CI), -0.94 to -0.85), with a coefficient of determination ($\hat{r2}$) of 0.81. The TFV-DP concentrations for low, moderate and high levels of drug adherence reported by Niu et al. [48] are represented by dashed vertical lines.

Figure 1.10 shows the sensitivity and specificity analysis of RESTRICT as compared to gold standard LC-MS/MS. In LC-MS/MS qualified DBS samples below 466 fmol/3mm punch, the area under the receiver operating characteristic curve (AUC) is 0.974 (95% CI: 0.943-1), with a cut-off normalized ratio IC50 y-axis coordinate value of 0.426 resulting in sensitivity of 96.3% and specificity of 93.6% (1/27 false negatives, 3/47 false positives). In LC-MS/MS qualified DBS samples below 799 fmol/3mm punch, the AUC is 0.936 (95% CI: 0.885-0.988), with a cut-off normalized ratio IC50 y-axis coordinate value of 0.327 resulting in sensitivity of 93.2% and specificity of 80% (3/44 false negatives, 6/30 false positives). Finally, in LC-MS/MS qualified DBS samples below 1375 fmol/3mm punch, the AUC is 0.955 (95% CI: 0.904-1), with a cut-off normalized ratio IC50 y-axis coordinate value of 0.297 resulting in sensitivity of 87.3% and specificity of 90.9% (8/63 false negatives, 1/11

false positives).

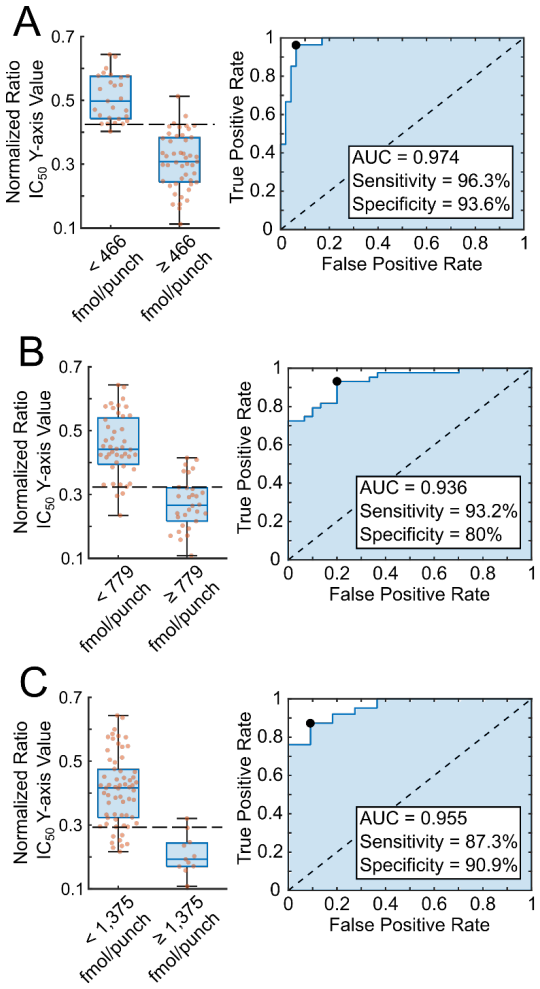

Figure 1.10: RESTRICT Identifies Low, Moderate, and High Adherence with High Sensitivity and Specificity Receiver operating characteristic (ROC) analysis of RESTRICT measurements compared to LC–MS/MS-qualified DBS samples from a directly observed therapy cohort. **(A)** Samples below 466 fmol/3 mm punch (low adherence): AUC = 0.974, sensitivity = 96.3%, specificity = 93.6%. **(B)** Samples below 779 fmol/3 mm punch (moderate adherence): AUC = 0.936, sensitivity = 93.2%, specificity = 80.0%. **(C)** Samples below 1375 fmol/3 mm punch (high adherence): AUC = 0.955, sensitivity = 87.3%, specificity = 90.9%.

1.6.1.3 Discussion, Remaining Limitations, and Outlook

This study used samples collected from the TARGET study with DOT participants on tenofovir disoproxil fumarate-based PrEP regimens to validate RESTRICT for measuring tenofovir diphosphate concentrations in DBS. RESTRICT fluorescence measurements were normalized and directly compared to LC-MS/MS measurements. A pilot

study demonstrated that RESTRICT fluorescence values correlate with LC-MS/MS measurements of TFV-DP, though this was a smaller study (n=18, with only six samples having detectable drug levels) using whole blood with no sample preparation[46]. In this work (n=74), we show that the normalized ratio IC50 y-axis value is strongly correlated with LC-MS/MS measurements of TFV-DP in DBS. We demonstrate that the RESTRICT assay is semi-quantitative, distinguishing TFV-DP concentrations in DBS as below steady-state adherence thresholds corresponding to low (466 fmol/3mm punch), moderate (779fmol/3mm punch) and high (1375fmol/3mm punch) levels of drug adherence.

Orally administered PrEP efficacy is highly dependent on medication adherence, with significantly diminished HIV-1 risk reduction observed for individuals taking 2 doses/week (low adherence) or less [50]. RESTRICT demonstrated 96.3% sensitivity and 93.6% specificity for identifying DBS samples with TFV-DP concentrations for the low adherence group.

The publication containing this work claims that this study represents "a significant step towards rapid, objective, long-term regimen adherence monitoring"..."RESTRICT may be a useful near-patient tool for identifying instances of poor PrEP or antiretroviral therapy adherence and enabling timely clinical intervention and adherence counselling".

The publication also makes the following claim:

> "RESTRICT is performed with commonly available laboratory equipment and features simple sample preparation and a runtime of less than 60 min, which may allow for decentralized testing and removal of barriers to timely linkage with appropriate interventions[38]. Other rapid methods for objective adherence monitoring include urine-based tenofovir point-of-care lateral flow assays, where undetectable tenofovir in urine has been associated with HIV viraemia[42, 51, 52]. While these tests benefit from the ease of sample collection compared to blood-based samples, urine-based tenofovir assays are limited to short-term adherence measurement due to the short half-life of tenofovir in urine (about 15 h)[27, 53]"

...

A limitation of this work (represented in the publication) is that it validates the RESTRICT assay for tenofovir disoproxil fumarate-based (TDF) PrEP monitoring but not tenofovir alafenamide-based (TAF) regimens. While TFV-DP is the active form of both TDF and TAF, TAF-based regimens accumulate less TFV-DP intracellularly as compared

to TDF-based regimens [54]. Future work cannot currently measure TAF-based PrEP regimens and preliminary data suggests the limit of detection may inhibit the use of RESTRICT for this purpose. In the Olanrewaju lab, efforts have transitioned to new test development for improved sensitivity rather than simple optimization of master mix components or sample preparation protocol.

To summarize this clinical validation, we evaluated the RESTRICT assay as an objective measure of long-term adherence to TDF via the cumulative metabolite, TFV-DP. We compared normalized RESTRICT fluorescence measurements against gold-standard LC-MS/MS for measuring TFV-DP concentrations in DBS from a DOT study. The RESTRICT assay strongly correlates with LC-MS/MS measurements and is able to distinguish TFV-DP concentrations in DBS as above or below steady-state adherence thresholds corresponding to low, moderate and high adherence. This novel assay could be used as a semi-quantitative test for objective adherence monitoring that could support interventions for improving adherence and increasing overall PrEP regimen efficacy.

1.7 Emergence of Long-Acting Injectable Antiretrovirals

Non-nucleoside reverse transcriptase inhibitors (NNRTIs) are an ARV class that has been FDA approved for use in HIV ARV regimens since 1996 [55]. In January 2021, a long-acting injectable formulation of a combinatorial NNRTI and INSTI termed Cabenuva (Cabotegravir (CAB), Rilpivirine (RPV)) was FDA-approved for use once a month for the treatment of HIV [56]. This FDA approval was extended in February of 2022 for use of injectable Cabenuva every two months, cementing it's status as a full, effective, long-acting ARV treatment regimen of HIV [57].

As reported at the Conference for Retroviruses and Opportunistic Infections in 2024 (while in attendance), the LATITUDE and MOCHA clinical trials (NCT03635788, NCT03497676) report that long-acting injectable CAB/RPV addresses barriers to daily oral pill burden in both adolescents and adults [58, 59].

Another NNRTI, Dapivirine (DPV), has been formulated into an intravaginal ring and has been shown to be an effective HIV prevention method[60–63]. Despite this and because of efficacy below FDA standards, the ring did not receive FDA approval but it is recommended by WHO as it covers key populations at risk of acquiring HIV globally [64]. Additionally, while an NNRTI component is not included in the formulation, a CAB-based injectable (Apertude) was FDA approved in December 2021 as the first long-acting HIV

prevention method [65].

As we move to effective and acceptable means of long-acting treatment and prevention of HIV, it is important to examine the role of DLF in a new drug landscape.

1.7.1 Interindividual Pharmacokinetics and the Need for TDM of Injectables

Interindividual pharmacokinetic variability plays a critical role in the effectiveness of long-acting injectable (LAI) cabotegravir (CAB) and rilpivirine (RPV) (Figure 1.11). Data from the HPTN 077 phase 2a trial, conducted across sites in Brazil, Malawi, South Africa, and the U.S., revealed wide variations in CAB plasma concentrations among participants, highlighting that some individuals may fall below therapeutic thresholds at different times. Factors such as higher body mass index (BMI), biological sex, and the injection site can influence drug absorption and clearance, with higher BMI linked to lower drug levels and sex-based differences affecting metabolism [66–69]. Additionally, inconsistencies in injection technique—even within the same person—along with clinician experience and clinic resources, can further contribute to variability in drug exposure and treatment efficacy [68].

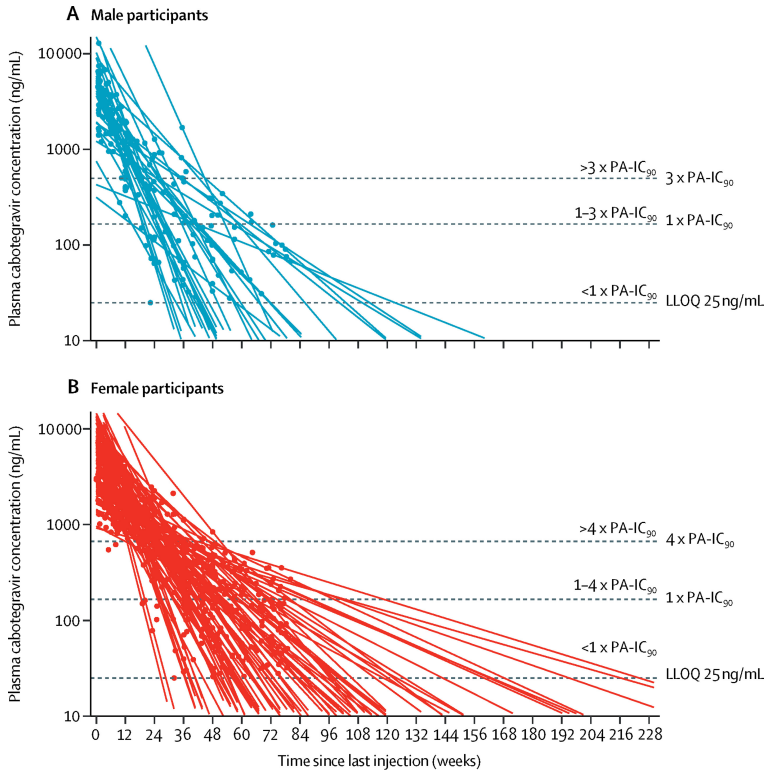

Figure 1.11: Pharmacokinetic Variability of Long-Acting Cabotegravir by Sex Individual participant log-linear regression curves of plasma cabotegravir concentrations over time, measured between peak (C_{max}) and last quantifiable drug level after final injection. Data are stratified by sex assigned at birth and highlight significant interindividual variability in drug clearance, which may impact efficacy and inform dosing strategies [66].

As the global use of long-acting injectable (LAI) HIV therapies like cabotegravir (CAB) and rilpivirine (RPV) expands, the variability observed in clinical trials is likely to be even more pronounced in everyday healthcare environments [66]. These real-world settings often involve more diverse patient populations and may lack the controlled conditions and consistent resources of clinical studies. While the longer dosing intervals of LAI regimens help overcome adherence issues associated with daily pills, staying on schedule with injections remains essential. Missing or delaying a dose can trigger the "pharmacokinetic tail"—a period when drug levels dip below therapeutic thresholds—which increases the risk of viral rebound, treatment failure, and resistance to not only the LAI drugs but other drugs in the same antiretroviral class [70]. To ensure effective use of these therapies, it's crucial to promote equitable access and support individualized approaches to dosing and care.

A key strategy in managing these risks could be the use of drug level feedback (DLF)

systems, which allow clinicians to monitor how a patient's body is processing the medication and make informed adjustments. For patients with higher BMI, a history of missed or late injections, known resistance-associated HIV subtypes (like A1/A6), or those taking medications that affect rilpivirine levels, DLF can help guide safer, more effective dosing. Personalized treatment plans informed by DLF data can help maintain adequate drug levels, prevent resistance, and improve overall outcomes—especially in populations at higher risk of treatment complications [71].

1.7.2 REACT: REverse transcriptase ACTivity Assay

In response to this emergent need, we extended the capabilities of the RESTRICT assay from NRTIs to NNRTIs. We renamed our enhanced assay the REverse transcriptase ACTivity (REACT) assay, highlighting its ability to detect both NRTIs and NNRTIs without relying on DNA chain termination. As a proof of concept, we show that REACT can successfully quantify five NNRTIs in buffer. Additionally, we demonstrate its capability to detect NNRTIs when spiked into human plasma. Lastly, we validate that REACT can be performed using a portable reader, supporting its potential for point-of-care (POC) HIV drug level feedback (DLF) in both clinical research and everyday care settings.

1.7.2.1 Materials and Methods

The following reagents were obtained through the NIH HIV Reagent Program, NIAID, NIH: etravirine [ETV] (HRP- 11609, contributed by DAIDS/NIAID), rilpivirine [RPV] (HRP-12147, contributed by the NIH HIV Reagent Pro- gram), nevirapine [NVP] (HRP-4666, contributed by the NIH HIV Reagent Program). Doravirine [DOR] (B2693- 475314, BOC Sciences), dapivirine [DPV] (Adooq Biosci- ence, A12587), etravirine, rilpivirine, and nevirapine were reconstituted in dimethyl sulfoxide (DMSO) (Fisher Sci- entific, BP231-100). NNRTI concentrations serially diluted, spanning 8 orders of magnitude (10^{-3} M to 10^{-10} M), with the exception of NVP (5×10^{-2} M to 10^{-8} M), to produce a full sigmoidal curve. We used the same DNA template and primer constructions as previous RESTRICT work, including the clinical validation[47].

REACT assays were performed in RT buffer used in the clinical validation with the exception of the the buffering agent: 60 mM Tris (Invitrogen, AM9855G), 30 mM KCl (Sigma-Aldrich, 101,553), 8 mM MgCl_2 (Sigma-Aldrich, 63,069), and 10 mM dithiothreitol (Sigma-Aldrich, 20–265) adjusted to a pH 8.0 with 1 M NaOH (Sigma- Aldrich, S8263).

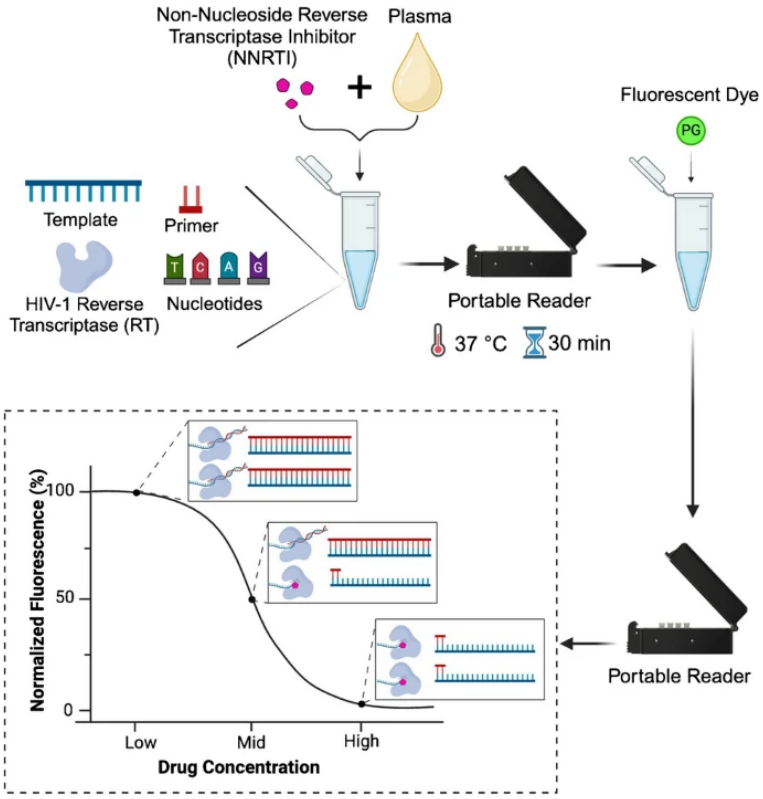

Figure 1.12: REACT Assay Measures HIV RT Inhibitors via Fluorescence Readout (A) Schematic of the REverse transcriptase ACTivity (REACT) assay, which detects HIV reverse transcriptase (RT) inhibitors by measuring DNA synthesis inhibition. A sample is incubated with nucleic acid templates, primers, nucleotides, and recombinant HIV RT enzyme. **(B)** After 30 minutes at 37°C, the reaction is quenched with PicoGreen^{TM} dye, and fluorescence readout reflects double-stranded DNA (dsDNA) synthesis as a function of drug concentration [72].

The assay is conducted in the exact same protocol as previously reported RESTRICT papers [46, 47] but final concentrations of master mix reagents in clinically-validated RESTRICT were adjusted to measure NNRTIs. The final concentrations are 1000 nM nucleotides (dNTPs), 10 nM template, and 100 nM primer. Each assay required 20 μL of master mix, 10 μL of NNRTI in DMSO, and 10 μL of HIV-1 RT (Worthington Biochemical, LS05009).

Reactions were performed in black, non-binding, flat-bottom polystyrene 96-well plates (Corning Incorporated, 3650). 10 μL of RT (0.053 units/mL) was added immediately prior to incubation at 37°C for 30 minutes in a plate reader (SpectraMax iD3, Molecular Devices). After incubation, the reaction is quenched and fluorescence is read via the addition of 40 μL of PicoGreen (Invitrogen, P7581) diluted 1:200 in 1 $\times$ TE buffer (Integrated DNA Technologies, 11–05-01–09).

Negative controls omitting the addition of RT enzyme and substituting "no enzyme" RT buffer and positive controls containing 10 μL of DMSO instead of a drug dilution were used to normalize fluorescence readings. Normalized fluorescence values were fitted to four-parameter logistic regression curves using GraphPad Prism Software (Graph- Pad Software Inc.).

REACT assays in portable reader: REACT assay fluorescence was readout using the Harmony portable reader ([73]) for DPV by pipetting 60 μL of each replicate condition measured via a plate reader into the Harmony.

REACT with spiked plasma samples: Gender-pooled, unfiltered human plasma from healthy participants collected into K2 EDTA anticoagulant from BioIVT (HUMANPLK2-0000283) was diluted 1:4 in nuclease-free water (Invitrogen, AM9937). Plasma was spiked with DOR dilutions in DMSO for final DOR concentrations matching the DOR-spiked buffer concentrations. To account for the 76% protein binding of DOR in plasma, the spiked sample concentration was multiplied by 0.24 [74].

1.7.2.2 Results

REACT measures multiple NNRTIs used in HIV treatment and prevention: Figure 1.13 shows proof-of-concept demonstration of REACT using five NNRTIs included in current HIV prevention and treatment regimens. We used maximum concentration (C_max) values in pharmacokinetic trials as benchmarks for clinically relevant concentrations of each drug.

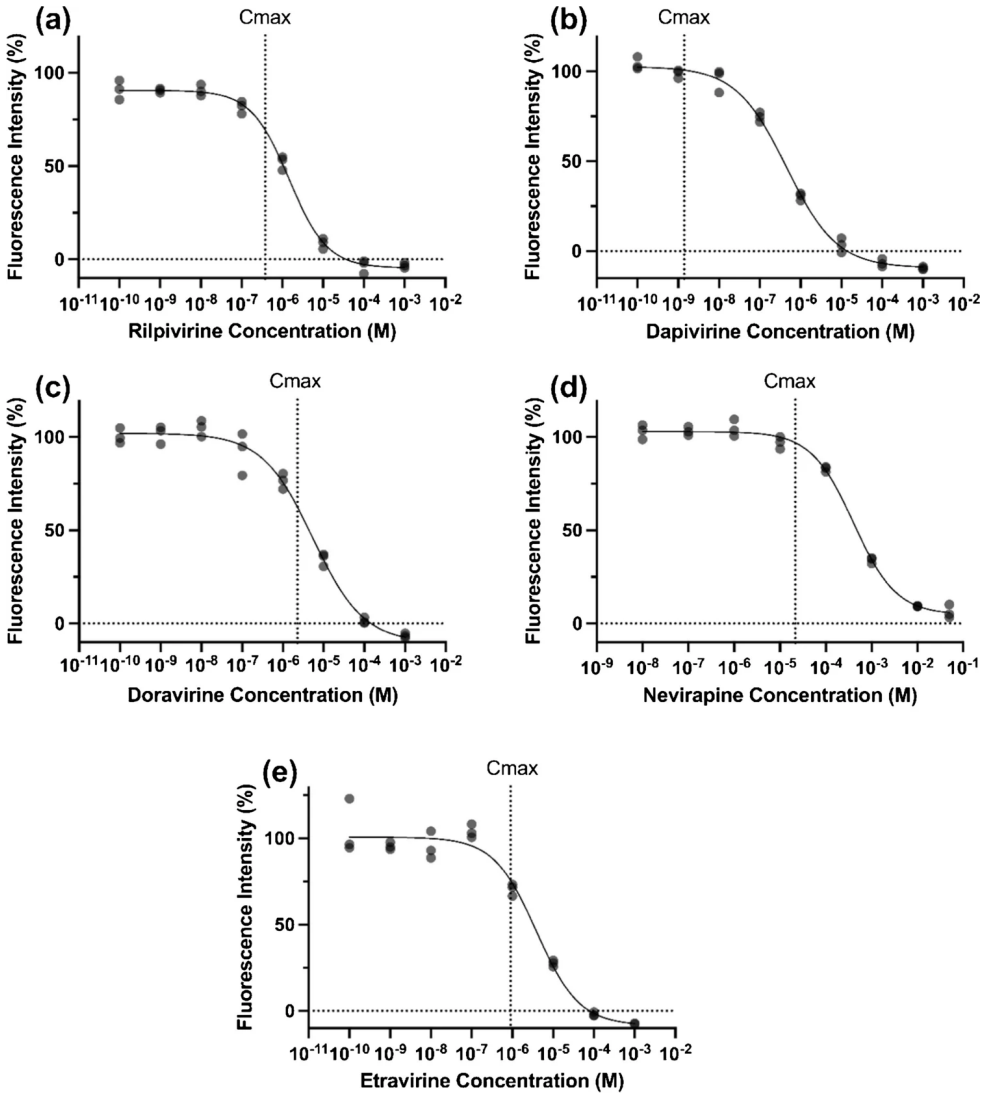

Figure 1.13: REACT Quantifies Five NNRTIs Across Clinically Relevant Concentrations Dose–response curves for five non-nucleoside reverse transcriptase inhibitors (NNRTIs) measured using the REACT assay.**(A)** Rilpivirine, **(B)** dapivirine, **(C)** doravirine, **(D)** nevirapine, **(E)** etravirine. Normalized fluorescence is plotted against drug concentration. Vertical dashed lines indicate reported C_{max} values from pharmacokinetic studies. $N = 3$ replicates per condition [72].

While C_max values are physiologically variable, they can be a useful metric for evaluating an assay for clinical relevancy[75–77]. REACT sigmoidal curves overlap C_max values, illustrating the potential utility for distinguishing clinically relevant values.

REACT with the Harmony portable reader: To further evaluate the use of REACT at the POC, used the Harmony portable heater as a portable, low-cost (<$200) [73] alternative to a benchtop plate reader. Figure 1.14 shows that measurements from the Harmony and the plate reader are highly correlated (Pearson's r = 0.9807, P < 0.0001).

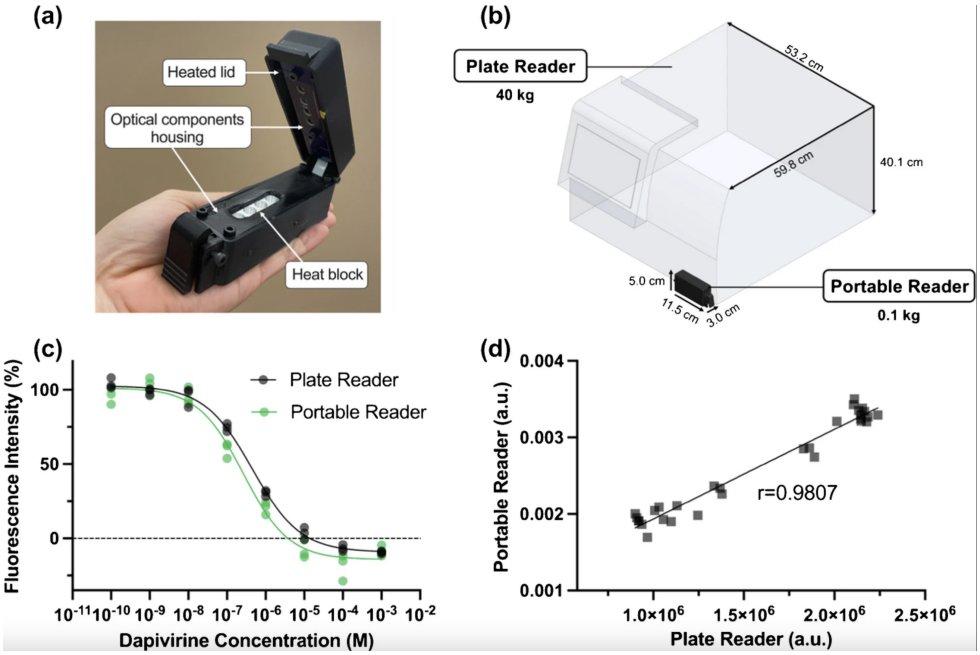

Figure 1.14: REACT Performance Is Consistent Between Portable and Benchtop Readers (A) The Harmony device integrates fluorescence detection and heating in a compact form factor with four tube wells. **(B)** Compared to a traditional benchtop plate reader, Harmony offers a substantial reduction in size and weight. **(C)** Normalized fluorescence from REACT assays measuring dapivirine (DPV) show comparable results between the two readers ($N = 3$). **(D)** Simple linear regression reveals a strong correlation between devices (Pearson's $r = 0.9807$, $p < 0.0001$, $N = 30$) [72].

REACT with spiked plasma samples: We spiked doravirine (DOR) into human plasma to evaluate REACT with a complex sample matrix (Figure 1.15). We diluted samples in water (25% v/v) as a simple sample preparation method to reduce non-specific HIV RT inhibition.

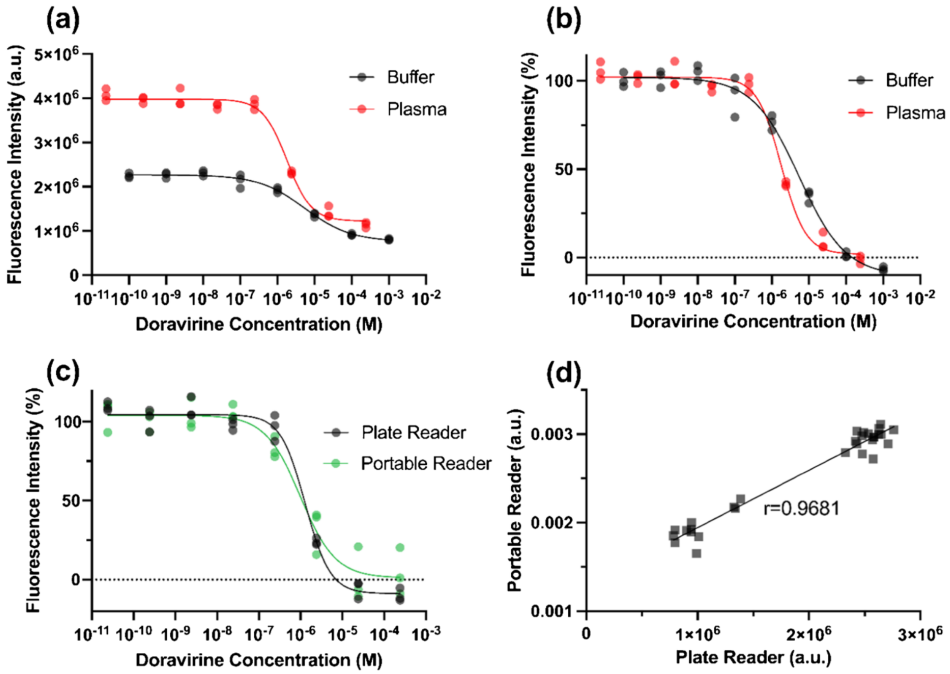

Figure 1.15: REACT Maintains Accuracy in Human Plasma and Portable Reader Formats (A) Raw REACT fluorescence from doravirine (DOR) spiked into aqueous buffer and 25% (v/v) diluted human plasma. Plasma samples exhibit higher background fluorescence. **(B)** After normalization, REACT responses in buffer and plasma are in strong agreement. **(C)** Normalized fluorescence values in plasma are comparable between the benchtop plate reader and the Harmony portable reader. **(D)** Linear regression reveals a high correlation between readers for plasma samples (Pearson's $r = 0.9681$, $p < 0.0001$, $N = 30$). DOR concentrations were adjusted to account for 76% protein binding in plasma.

1.7.2.3 Discussion

The following quote from the publication of this work ([72]) succinctly describes the advantageous optimization of the assay for NNRTIs:

> "REACT used ten-fold greater nucleotide and DNA template concentrations compared to our past work. This resulted in a fluorescence signal boost that facilitated detection with a portable and inexpensive reader like Harmony and made the assay more tolerant of matrix effects from plasma and interference from solvents used to dissolve NNRTIs that could non-specifically inhibit HIV RT."

Limitations: We have not tested clinical samples containing NNRTIs and compared REACT with gold standard LC–MS/MS to clinically validate the assay. In addition, although we have expanded from NRTIs to NNRTIs in the transition from RESTRICT to

REACT, we have not yet included other emerging RT inhibitors or tested the selectivity of the assay in presence of other drugs.

In conclusion, the REACT assay can objectively measure NNRTIs. We have demonstrated the detection of five NNRTIs – RPV, DPV, DOR, NVP, and ETV – including drugs used in long-acting injectable and extended-release HIV treatment and prevention regimens. Moreover, we verified the ability to measure REACT fluorescence in a portable reader with comparable performance to a traditional plate reader. Finally, we validated the ability of the REACT assay to detect an NNRTI in a complex biological matrix. This work makes significant steps towards objective NNRTI measurements with inexpensive equipment, increasing access to rapid drug level feedback in resource-limited settings.

1.8 HIV Drug Resistance

1.8.1 Growing Prevalence and the Urgent Need for Supportive Care

As my work on HIV ARV monitoring assays was naturally wrapping up, I attended the Conference for Retroviruses and Opportunistic Infections (CROI) 2024 in Denver, CO. The focus of my dissertation began to shift because that conference brought up two key drivers for the direction of my second act of my PhD:

1. HIV drug resistance undermines efforts to control the pandemic, fueling new infections and worsening HIV-related illness and death.

2. HIV drug resistance is on the rise, evolving quickly and diminishing the effectiveness of *all classes* of antiretroviral therapies.

Pre-treatment resistance to first-line NNRTI-based ART regimens in adults exceeds 10%, and is rapidly growing [78, 79]. Among infants, pre-treatment NNRTI resistance prevalence upwards of 50% [78, 79]. Additionally, a systematic review was conducted by the World Health Organization to determine the prevalence of drug resistance among individuals failing ARV therapy. Among the pooled data of 13,338 individuals who experienced failure on a first-line NNRTI-based regimen, nearly one-third (32%) did so without any detectable drug resistance. This indicates that their lack of viral suppression was not due to acquired drug resistance, and that many could potentially achieve suppression through improved adherence to medication—without needing to switch to costlier and more challenging second-line therapies (Figure 1.16).

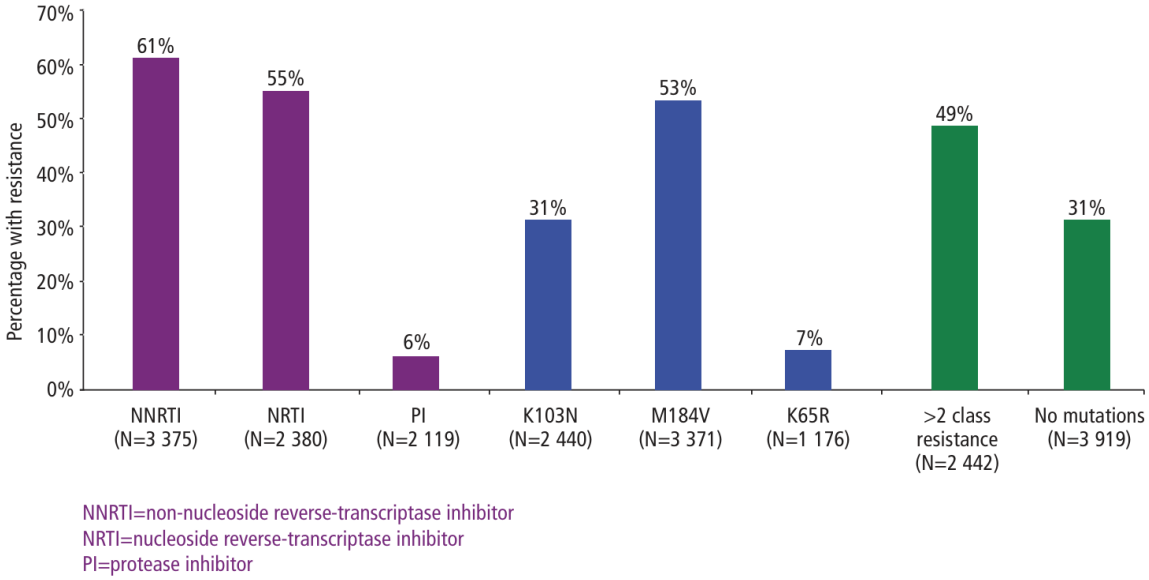

Figure 1.16: Not All ART Failures Are Due to Drug Resistance Rates of acquired HIV drug resistance among individuals experiencing first-line antiretroviral therapy (ART) failure, from a systematic review conducted between 2014 and 2017. Nearly one-third of treatment failures occurred without detectable drug resistance, underscoring the importance of adherence support in addition to resistance testing.

1.8.2 Motivation for New Means of Innovation

When examining the possible role of our lab in support of drug resistance monitoring, we turned to the HIV testing algorithm provided by WHO in 2021 (Figure 1.17) [80].

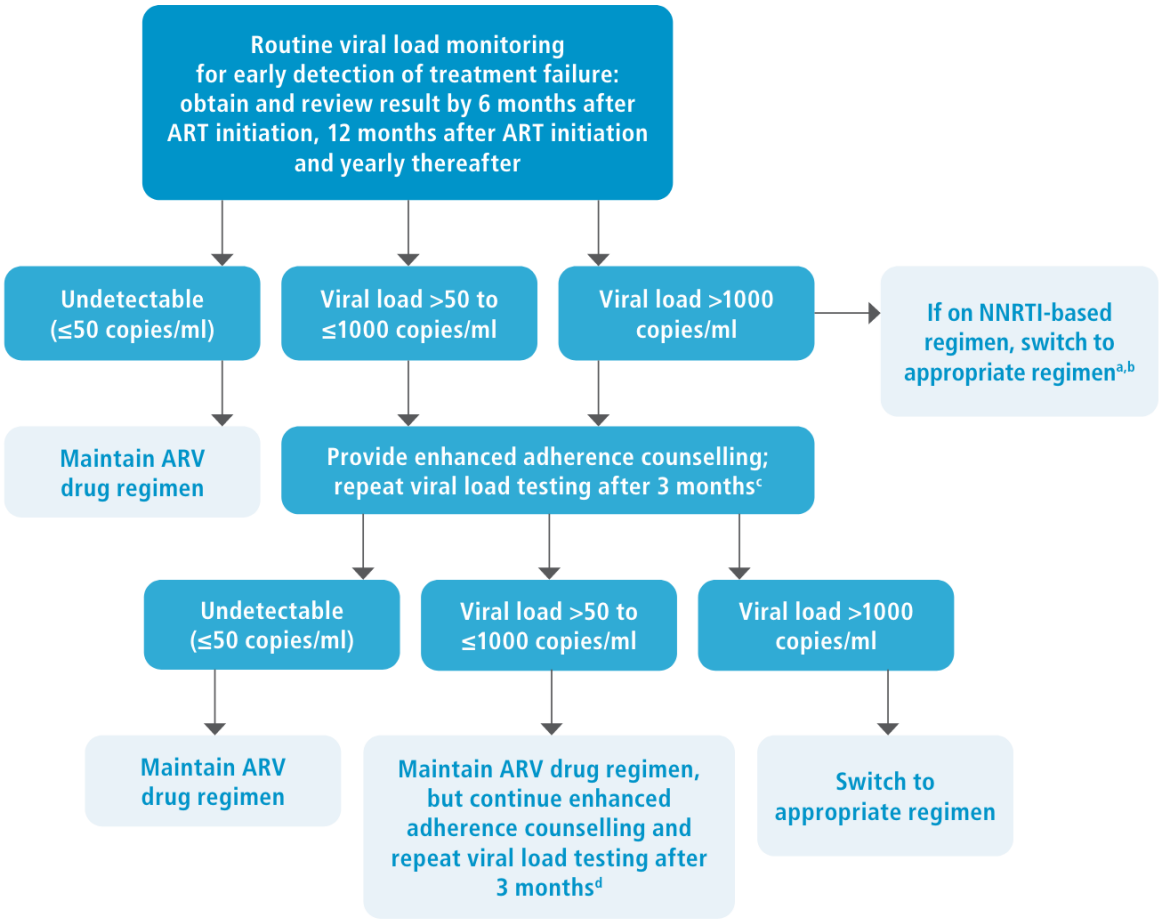

Figure 1.17: Treatment monitoring algorithm updated in 2021 The World Health Organization's 2021 updated HIV treatment monitoring algorithm guides clinical decisions based on viral load results and suspected treatment failure. The framework emphasizes timely assessment of adherence and drug resistance, presenting clear opportunities for integration of near-patient tools like RESTRICT and REACT.

Within this framework, the ARV monitoring assays previously developed and vali-

dated by our group showed promise as potential tools to support adherence. We quickly identified ways to adapt our enzymatic activity assays to detect drug-resistant enzymes—a direction that is now actively being pursued by members of the group.

Following the CROI 2024 meeting, I had the opportunity to spend several months exploring strategies to build a suite of interventions aimed at addressing HIV drug resistance. While this work ultimately did not become part of my dissertation, it sparked a critical shift in direction. The pressing need for user-friendly, automated sample preparation and assay workflows led me down a new path—one that became the foundation of the remaining chapters of this dissertation, focused on the use of rapidly fabricated, pump-free microfluidics.

References

1. Klimas, N., Koneru, A. O. & Fletcher, M. A. Overview of HIV. *Psychosomatic Medicine* **70,** 523–530. ISSN: 0033-3174 (June 2008).
2. *Global HIV & AIDS statistics — Fact sheet*
3. Carter, A. *et al.* Global, regional, and national burden of HIV/AIDS, 1990–2021, and forecasts to 2050, for 204 countries and territories: the Global Burden of Disease Study 2021. *The Lancet HIV* **11.** Publisher: Elsevier, e807–e822. ISSN: 2352-3018 (Dec. 1, 2024).
4. HIV Declines Among Young People and Drives Overall Decrease in New HIV Infections. *National Center for HIV, Viral Hepatitis, STD, and TB Prevention* (May 23, 2023).
5. Buzibye, A. *et al.* Antiretroviral concentration measurements as an additional tool to manage virologic failure in resource limited settings: a case control study. *AIDS Research and Therapy* **16,** 39. ISSN: 1742-6405 (Dec. 2019).
6. Donnell, D. *et al.* HIV Protective Efficacy and Correlates of Tenofovir Blood Concentrations in a Clinical Trial of PrEP for HIV Prevention. *JAIDS Journal of Acquired Immune Deficiency Syndromes* **66,** 340–348. ISSN: 1525-4135 (July 1, 2014).
7. Kimulwo, M. J. *et al.* Plasma nevirapine concentrations predict virological and adherence failure in Kenyan HIV-1 infected patients with extensive antiretroviral treatment exposure. *PLOS ONE* **12** (ed Abimiku, A. G.) e0172960. ISSN: 1932-6203 (Feb. 24, 2017).
8. Gardner, E. M., Burman, W. J., Steiner, J. F., Anderson, P. L. & Bangsberg, D. R. Antiretroviral medication adherence and the development of class-specific antiretroviral resistance. *AIDS* **23,** 1035–1046. ISSN: 0269-9370 (June 1, 2009).
9. Moltó, J. *et al.* Variability in non-nucleoside reverse transcriptase and protease inhibitor concentrations among HIV-infected adults in routine clinical practice. *British Journal of Clinical Pharmacology* **62,** 560–566. ISSN: 0306-5251, 1365-2125 (Nov. 2006).
10. Clementi, E. *et al.* Impact of therapeutic drug monitoring of antiretroviral drugs in routine clinical management of patients infected with human immunodeficiency virus and related health care costs: a real-life study in a large cohort of patients. *ClinicoEconomics and Outcomes Research*, 341. ISSN: 1178-6981 (July 2014).

11. *Guidelines for the Use of Antiretroviral Agents in Adults and Adolescents with HIV | Considerations for Antiretroviral Use in People With Coinfections | Tuberculosis/HIV Coinfection.* https://clinicalinfo.hiv.gov/en/guidelines/hiv-clinical-guidelines-adult-and-adolescentarv/tuberculosishiv-coinfection.

12. Cattaneo, D. *et al.* Impact of Therapeutic Drug Monitoring of Antiretroviral Drugs in Routine Clinical Management of People Living With HIV: A Narrative Review. *Therapeutic Drug Monitoring* **42,** 64–74. ISSN: 0163-4356 (Feb. 2020).

13. Gilbert, E. M., Darin, K. M., Scarsi, K. K. & McLaughlin, M. M. Antiretroviral Pharmacokinetics in Pregnant Women. *Pharmacotherapy: The Journal of Human Pharmacology and Drug Therapy* **35,** 838–855. ISSN: 0277-0008, 1875-9114 (Sept. 2015).

14. Waalewijn, H. *et al.* Optimizing Pediatric Dosing Recommendations and Treatment Management of Antiretroviral Drugs Using Therapeutic Drug Monitoring Data in Children Living With HIV. *Therapeutic Drug Monitoring* **41,** 431–443. ISSN: 0163-4356 (Aug. 2019).

15. Sethi, A. K., Celentano, D. D., Gange, S. J., Moore, R. D. & Gallant, J. E. Association between Adherence to Antiretroviral Therapy and Human Immunodeficiency Virus Drug Resistance. *Clinical Infectious Diseases* **37,** 1112–1118. ISSN: 1058-4838, 1537-6591 (Oct. 15, 2003).

16. T. Tchakoute, C., Rhee, S.-Y., Hare, C. B., Shafer, R. W. & Sainani, K. Adherence to contemporary antiretroviral treatment regimens and impact on immunological and virologic outcomes in a US healthcare system. *PLOS ONE* **17** (ed Marconi, V. C.) e0263742. ISSN: 1932-6203 (Feb. 14, 2022).

17. Hill, L. M. *et al.* Using Real-Time Adherence Feedback to Enhance Communication About Adherence to Antiretroviral Therapy: Patient and Clinician Perspectives. *Journal of the Association of Nurses in AIDS Care* **31,** 25–34. ISSN: 1055-3290, 1552-6917 (Jan. 2020).

18. Gandhi, M. *et al.* Impact of a point-of-care urine tenofovir assay on adherence to HIV pre-exposure prophylaxis among women in Kenya: a randomised pilot trial. *The Lancet HIV* **11,** e522–e530. ISSN: 23523018 (Aug. 2024).

19. Nair, G. *et al.* Adherence, safety, and choice of the monthly dapivirine vaginal ring or oral emtricitabine plus tenofovir disoproxil fumarate for HIV pre-exposure prophylaxis among African adolescent girls and young women: a randomised, open-label, crossover trial. *The Lancet HIV* **10,** e779–e789. ISSN: 23523018 (Dec. 2023).

20. Roberts, S. T. *et al.* How a menu of adherence support strategies facilitated high adherence to HIV prevention products among adolescent girls and young women in sub-Saharan Africa: a mixed methods analysis. *Journal of the International AIDS Society* **26,** e26189. ISSN: 1758-2652, 1758-2652 (Nov. 2023).

21. WHO Implementation Tool for Pre-exposure Prophylaxis (PrEP) of HIV Infection. *World Health Organization* (2017).

22. *Preexposure Prophylaxis for the Prevention of HIV Infection in the United States—2021 Update. A Clinical Practice Guideline.*

23. *Effectiveness and Adherence in Trials of Oral and Topical Tenofovir-Based Prevention* AIDS Vaccine Advocacy Coalition. https://avac.org/resource/infographic/effectiveness-and-adherence-in-trials-of-oral-and-topical-tenofovir-based-prevention/.

24. Grant, R. M. *et al.* Uptake of pre-exposure prophylaxis, sexual practices, and HIV incidence in men and transgender women who have sex with men: a cohort study. *The Lancet Infectious Diseases* **14,** 820–829. ISSN: 14733099 (Sept. 2014).

25. Kearney, B. P., Flaherty, J. F. & Shah, J. Tenofovir Disoproxil Fumarate: Clinical Pharmacology and Pharmacokinetics. *Clinical Pharmacokinetics* **43,** 595–612. ISSN: 0312-5963 (2004).

26. Markowitz, M. *et al.* Phase I/II study of the pharmacokinetics, safety and antiretroviral activity of tenofovir alafenamide, a new prodrug of the HIV reverse transcriptase inhibitor tenofovir, in HIV-infected adults. *Journal of Antimicrobial Chemotherapy* **69,** 1362–1369. ISSN: 0305-7453, 1460-2091 (May 1, 2014).

27. Yager, J. *et al.* Intracellular Tenofovir-Diphosphate and Emtricitabine-Triphosphate in Dried Blood Spots Following Tenofovir Alafenamide: The TAF-DBS Study. *JAIDS Journal of Acquired Immune Deficiency Syndromes* **84,** 323–330. ISSN: 1525-4135 (July 1, 2020).

28. Anderson, P. L. *et al.* Intracellular Tenofovir-Diphosphate and Emtricitabine-Triphosphate in Dried Blood Spots following Directly Observed Therapy. *Antimicrobial Agents and Chemotherapy* **62,** e01710–17. ISSN: 0066-4804, 1098-6596 (Jan. 2018).

29. Castillo-Mancilla, J. R. *et al.* Tenofovir, Emtricitabine, and Tenofovir Diphosphate in Dried Blood Spots for Determining Recent and Cumulative Drug Exposure. *AIDS Research and Human Retroviruses* **29,** 384–390. ISSN: 0889-2229, 1931-8405 (Feb. 2013).

30. Koenig, H. *et al.* Urine assay for tenofovir to monitor adherence in real time to tenofovir disoproxil fumarate/emtricitabine as pre-exposure prophylaxis. *HIV Medicine* **18,** 412–418. ISSN: 1464-2662, 1468-1293 (July 2017).

31. Hendrix, C. W. *et al.* Dose Frequency Ranging Pharmacokinetic Study of Tenofovir-Emtricitabine After Directly Observed Dosing in Healthy Volunteers to Establish Adherence Benchmarks (HPTN 066). *AIDS Research and Human Retroviruses* **32,** 32–43. ISSN: 0889-2229, 1931-8405 (Jan. 2016).

32. Podsadecki, T. J., Vrijens, B. C., Tousset, E. P., Rode, R. A. & Hanna, G. J. "White Coat Compliance" Limits the Reliability of Therapeutic Drug Monitoring in HIV-1—Infected Patients. *HIV Clinical Trials* **9,** 238–246. ISSN: 1528-4336, 1945-5771 (Aug. 2008).

33. Spinelli, M. A. *et al.* Approaches to Objectively Measure Antiretroviral Medication Adherence and Drive Adherence Interventions. *Current HIV/AIDS Reports* **17,** 301–314. ISSN: 1548-3568, 1548-3576 (Aug. 2020).

34. Gandhi, M. *et al.* Brief Report: Validation of a Urine Tenofovir Immunoassay for Adherence Monitoring to PrEP and ART and Establishing the Cutoff for a Point-of-Care Test. *JAIDS Journal of Acquired Immune Deficiency Syndromes* **81,** 72–77. ISSN: 1525-4135 (May 1, 2019).

35. Delahunty, T., Bushman, L., Robbins, B. & Fletcher, C. V. The simultaneous assay of tenofovir and emtricitabine in plasma using LC/MS/MS and isotopically labeled internal standards. *Journal of Chromatography B* **877,** 1907–1914. ISSN: 15700232 (July 2009).

36. Zheng, J.-H. *et al.* Application of an intracellular assay for determination of tenofovir-diphosphate and emtricitabine-triphosphate from erythrocytes using dried blood spots. *Journal of Pharmaceutical and Biomedical Analysis* **122,** 16–20. ISSN: 07317085 (Apr. 2016).

37. Edelbroek, P. M., Heijden, J. V. D. & Stolk, L. M. L. Dried Blood Spot Methods in Therapeutic Drug Monitoring: Methods, Assays, and Pitfalls. *Therapeutic Drug Monitoring* **31,** 327–336. ISSN: 0163-4356 (June 2009).

38. Drain, P. K. *et al.* Point-of-care and Near Real-time Testing for Antiretroviral Adherence Monitoring to HIV Treatment and Prevention. *Current HIV/AIDS Reports* **17,** 487–498. ISSN: 1548-3568, 1548-3576 (Oct. 2020).

39. Cressey, T. R. *et al.* A randomized clinical pharmacokinetic trial of Tenofovir in blood, plasma and urine in adults with perfect, moderate and low PrEP adherence: the TARGET study. *BMC Infectious Diseases* **17,** 496. ISSN: 1471-2334 (Dec. 2017).

40. Leung, K. S.-Y. & Fong, B. M.-W. LC–MS/MS in the routine clinical laboratory: has its time come? *Analytical and Bioanalytical Chemistry* **406,** 2289–2301. ISSN: 1618-2642, 1618-2650 (Apr. 2014).

41. Pratt, G. W., Fan, A., Melakeberhan, B. & Klapperich, C. M. A competitive lateral flow assay for the detection of tenofovir. *Analytica Chimica Acta* **1017,** 34–40. ISSN: 00032670 (Aug. 2018).

42. Gandhi, M. *et al.* Development and validation of the first point-of-care assay to objectively monitor adherence to HIV treatment and prevention in real-time in routine settings. *AIDS* **34,** 255–260. ISSN: 0269-9370, 1473-5571 (Feb. 1, 2020).

43. Spinelli, M. & Gandhi, M. Point-of-care urine tenofovir monitoring of adherence to drive interventions for HIV treatment and prevention. *Expert Review of Molecular Diagnostics* **24,** 169–175. ISSN: 1473-7159, 1744-8352 (Mar. 3, 2024).

44. Olanrewaju, A. O. *et al.* REverSe TRanscrIptase chain termination (RESTRICT) for selective measurement of nucleotide analogs used in HIV care and prevention. *Bioengineering & Translational Medicine* **8,** e10369. ISSN: 2380-6761, 2380-6761 (Jan. 2023).

45. Olanrewaju, A. O. *et al.* Enzymatic Assay for Rapid Measurement of Antiretroviral Drug Levels. *ACS Sensors* **5,** 952–959. ISSN: 2379-3694, 2379-3694 (Apr. 24, 2020).

46. Olanrewaju, A. O. *et al.* Pilot evaluation of an enzymatic assay for rapid measurement of antiretroviral drug concentrations. *Virology Journal* **18,** 77. ISSN: 1743-422X (Dec. 2021).

47. Sullivan, B. P. *et al.* Validation of the REverSe TRanscrIptase Chain Termination assay for measuring tenofovir diphosphate in dried blood spots from a clinical pharmacokinetic trial. *Journal of Antimicrobial Chemotherapy,* dkaf049. ISSN: 0305-7453, 1460-2091 (Feb. 25, 2025).

48. Niu, X. *et al.* Tenofovir-Diphosphate in Dried Blood Spots vs Tenofovir in Urine/-Plasma for Oral Preexposure Prophylaxis Adherence Monitoring. *Open Forum Infectious Diseases* **9,** ofac405. ISSN: 2328-8957 (Aug. 2, 2022).

49. Kumar, R. & Indrayan, A. Receiver operating characteristic (ROC) curve for medical researchers. *Indian Pediatrics* **48,** 277–287. ISSN: 0019-6061, 0974-7559 (Apr. 2011).

50. Anderson, P. L. *et al.* Emtricitabine-Tenofovir Concentrations and Pre-Exposure Prophylaxis Efficacy in Men Who Have Sex with Men. *Science Translational Medicine* **4.** ISSN: 1946-6234, 1946-6242 (Sept. 12, 2012).

51. Sevenler, D. *et al.* Point-of-care semi-quantitative test for adherence to tenofovir alafenamide or tenofovir disoproxil fumarate. *Journal of Antimicrobial Chemotherapy* **77,** 996–999. ISSN: 0305-7453, 1460-2091 (Mar. 31, 2022).

52. Dorward, J. *et al.* Diagnostic accuracy of a point-of-care urine tenofovir assay, and associations with HIV viraemia and drug resistance among people receiving dolutegravir and efavirenz-based antiretroviral therapy. *Journal of the International AIDS Society* **26,** e26172. ISSN: 1758-2652, 1758-2652 (Sept. 2023).

53. Drain, P. K. *et al.* Urine Tenofovir Concentrations Correlate With Plasma and Relate to Tenofovir Disoproxil Fumarate Adherence: A Randomized, Directly Observed Pharmacokinetic Trial (TARGET Study). *Clinical Infectious Diseases* **70,** 2143–2151. ISSN: 1058-4838, 1537-6591 (May 6, 2020).

54. Ray, A. S., Fordyce, M. W. & Hitchcock, M. J. Tenofovir alafenamide: A novel prodrug of tenofovir for the treatment of Human Immunodeficiency Virus. *Antiviral Research* **125,** 63–70. ISSN: 01663542 (Jan. 2016).

55. Namasivayam, V. *et al.* The Journey of HIV-1 Non-Nucleoside Reverse Transcriptase Inhibitors (NNRTIs) from Lab to Clinic. *Journal of Medicinal Chemistry* **62,** 4851–4883. ISSN: 1520-4804 (May 23, 2019).

56. Overton, E. T. *et al.* Long-acting cabotegravir and rilpivirine dosed every 2 months in adults with HIV-1 infection (ATLAS-2M), 48-week results: a randomised, multicentre, open-label, phase 3b, non-inferiority study. *The Lancet* **396,** 1994–2005. ISSN: 01406736 (Dec. 2020).

57. ViiV HEALTHCARE ANNOUNCES US FDA APPROVAL OF CABENUVA (CABOTEGRAVIR, RILPIVIRINE) FOR USE EVERY TWO MONTHS, EXPANDING THE LABEL OF THE FIRST AND ONLY COMPLETE LONG-ACTING HIV TREATMENT. *ViiV Healthcare* (Feb. 1, 2022).

58. Long-acting HIV treatment benefits adults with barriers to daily pill taking and adolescents with suppressed HIV. *NIH News Releases* (Mar. 6, 2024).

59. Moore, C. B. *et al.* Safety of combined long-acting injectable cabotegravir and long-acting injectable rilpivirine in virologically suppressed adolescents with HIV (IMPAACT 2017/MOCHA): a phase 1/2, multicentre, open-label, non-comparative, dose-finding study. *The Lancet HIV* **12,** e191–e200. ISSN: 23523018 (Mar. 2025).

60. Baeten, J. M. *et al.* Use of a Vaginal Ring Containing Dapivirine for HIV-1 Prevention in Women. *New England Journal of Medicine* **375,** 2121–2132. ISSN: 0028-4793, 1533-4406 (Dec. 2016).

61. Montgomery, E. T. *et al.* Acceptability and use of a dapivirine vaginal ring in a phase III trial. *AIDS (London, England)* **31,** 1159–1167. ISSN: 1473-5571 (May 15, 2017).

62. Nel, A. *et al.* Safety and Efficacy of a Dapivirine Vaginal Ring for HIV Prevention in Women. *New England Journal of Medicine* **375,** 2133–2143. ISSN: 0028-4793, 1533-4406 (Dec. 2016).

63. Nel, A. *et al.* Safety, adherence, and HIV-1 seroconversion among women using the dapivirine vaginal ring (DREAM): an open-label, extension study. *The Lancet HIV* **8,** e77–e86. ISSN: 23523018 (Feb. 2021).

64. WHO recommends the dapivirine vaginal ring as a new choice for HIV prevention for women at substantial risk of HIV infection. *World Health Organization* (Jan. 26, 2021).

65. FDA Approves First Injectable Treatment for HIV Pre-Exposure Prevention. *U.S. Food & Drug Administration* (Dec. 20, 2021).

66. Landovitz, R. J. *et al.* Tail-phase safety, tolerability, and pharmacokinetics of long-acting injectable cabotegravir in HIV-uninfected adults: a secondary analysis of the HPTN 077 trial. *The Lancet HIV* **7,** e472–e481. ISSN: 2352-3018 (July 2020).

67. Thoueille, P. *et al.* Guidance for the Interpretation of Long-Acting Cabotegravir and Rilpivirine Concentrations Based on Real-World Therapeutic Drug Monitoring Data and Documented Failures. *Open Forum Infectious Diseases* **11,** ofae023. ISSN: 2328-8957 (Feb. 1, 2024).

68. Swindells, S. *et al.* Long-Acting Cabotegravir and Rilpivirine for Maintenance of HIV-1 Suppression. *New England Journal of Medicine* **382,** 1112–1123. ISSN: 0028-4793, 1533-4406 (Mar. 19, 2020).

69. Orkin, C. *et al.* Long-Acting Cabotegravir and Rilpivirine after Oral Induction for HIV-1 Infection. *New England Journal of Medicine* **382,** 1124–1135. ISSN: 0028-4793, 1533-4406 (Mar. 19, 2020).

70. Margolis, D. A. *et al.* Long-acting intramuscular cabotegravir and rilpivirine in adults with HIV-1 infection (LATTE-2): 96-week results of a randomised, open-label, phase 2b, non-inferiority trial. *The Lancet* **390,** 1499–1510. ISSN: 01406736 (Sept. 2017).

71. Bangsberg, D. R. *et al.* Non-adherence to highly active antiretroviral therapy predicts progression to AIDS: *AIDS* **15,** 1181–1183. ISSN: 0269-9370 (June 2001).

72. Brainerd, C. *et al.* REverse transcriptase ACTivity (REACT) assay for point-of-care measurement of established and emerging antiretrovirals for HIV treatment and prevention. *Analytical and Bioanalytical Chemistry* **416,** 6809–6818. ISSN: 1618-2642, 1618-2650 (Dec. 2024).

73. Panpradist, N. *et al.* Harmony COVID-19: A ready-to-use kit, low-cost detector, and smartphone app for point-of-care SARS-CoV-2 RNA detection. *Science Advances* **7,** eabj1281. ISSN: 2375-2548 (Dec. 17, 2021).

74. Talwani, R. & Temesgen, Z. Doravirine: a new non-nucleoside reverse transcriptase inhibitorfor the treatment of HIV infection. *Drugs of Today* **56,** 113. ISSN: 16994019 (2020).

75. Dahri, K. & Ensom, M. H. H. Efavirenz and Nevirapine in HIV-1 Infection: Is There a Role for Clinical Pharmacokinetic Monitoring? *Clinical Pharmacokinetics* **46,** 109–132. ISSN: 0312-5963 (2007).

76. Usach, I., Melis, V. & Peris, J.-E. Non-nucleoside reverse transcriptase inhibitors: a review on pharmacokinetics, pharmacodynamics, safety and tolerability. *Journal of the International AIDS Society* **16,** 18567. ISSN: 1758-2652, 1758-2652 (Jan. 2013).

77. Turner, R. M., Park, B. K. & Pirmohamed, M. Parsing interindividual drug variability: an emerging role for systems pharmacology. *WIREs Systems Biology and Medicine* **7,** 221–241. ISSN: 1939-5094, 1939-005X (July 2015).

78. *HIV Drug Resistance Report 2021* 1st ed. 1 p. ISBN: 978-92-4-003860-8 (World Health Organization, Geneva, 2021).

79. World Health Organization. *Target product profile for HIV drug resistance tests in low- and middle-income countries: Africa* (2023).

80. World Health Organization. *Consolidated guidelines on HIV prevention, testing, treatment, service delivery and monitoring: recommendations for a public health approach* 548 pp. ISBN: ISBN 978-92-4-003159-3 (July 2021).

2 | How to Build a Microfluidic Chain Reaction: A Practical Guide to Structurally Programmed Capillary Microfluidics

2.1 Abstract

This chapter presents a practical and theoretical foundation for designing autonomous fluidic workflows using microfluidic chain reactions (MCRs), a paradigm in capillaric microfluidics that enables complex, multi-step operations through structurally programmed geometry alone. We introduce a circuit-based analytical framework to model capillary-driven flow, using pressure and resistance relationships to derive generalizable rules for the timing and direction of drainage across branching networks. These rules form the basis for encoding fluidic logic and sequencing without external pumps or electronics, allowing precise control over fluid behavior in fully passive systems. Emphasis is placed on accessibility and reproducibility, with annotated design rules and open-source tools to support rapid prototyping via widely available 3D printers. Together, these methods aim to demystify the structure–function relationships that underpin MCRs, expand the design vocabulary for capillaric circuits, and accelerate adoption of this low-cost, programmable platform for applications in decentralized diagnostics, sample preparation, and point-of-care testing.

Foreword

I wanted to introduce this chapter with insight into the lens through which I chose to view this topic while writing. My hope is that it can be a tool to demystify capillary microfluidics for my peers. I hope it offers a deconstruction of the existing literature on the topic to plain language, intuitive understanding, real-world analogies, and supportive

visuals. Hopefully, this will be useful to future microfluidicists in our lab (and our field) who would like to understand the essentials through an approachable lens and quickly progress to the design and iteration of these devices. In other words, if you ever took me out to coffee and asked me to explain everything I knew about capillary microfluidics, this is the conversation we'd have and the sketches I'd put on our napkins to show you what I mean.

2.2 Introduction

Capillary microfluidics exploit surface tension and precisely engineered microchannel geometry to autonomously manipulate small fluid volumes, encoding flow control directly into the physical structure of the device [1, 2]. By eliminating the need for external pumps, power sources, or complex instrumentation, this self-powered approach is especially well suited for point-of-care diagnostics and use in resource-limited environments, where simplicity, portability, and reliability are essential.

Traditionally, capillary microfluidic systems were limited to simple fluidic operations but advancements have led to the development of complex capillary flow circuits capable of sequentially delivering multiple liquids with distinct flow rates and even flow reversal [2–4]. Key innovations include the introduction of novel microfluidic elements such as retention burst valves and robust low aspect ratio trigger valves [3]. These components, when combined with flow resistors, capillary retention valves, capillary pumps, and reservoirs, enable the construction of capillary circuits that autonomously execute pre-programmed sequences of fluid handling steps upon sample addition.

More recently, the concept of microfluidic chain reactions (MCRs) has extended this paradigm by introducing a scalable and structurally encoded mechanism for conditionally propagating fluidic events. MCRs have demonstrated the ability to orchestrate hundreds of capillary-triggered steps using only capillary forces, enabling fully autonomous execution of complex assays such as SARS-CoV-2 antibody detection and thrombin generation from saliva and plasma samples—entirely without external instrumentation [4].

To conceptualize these advancements, the term "capillarics" has been proposed, drawing an analogy to electronic circuits. Capillaric circuits are built from a library of modular elements, allowing for the design of complex, instrument-free microfluidic systems [1]. Symbolic representations have been introduced to standardize the design process, facilitating the creation of more sophisticated circuits by expanding the repertoire of building

blocks and establishing design rules[1, 2].

2.2.1 Highlighted Applications

The evolution of capillaric design principles from simple channel geometries to highly orchestrated, structurally encoded fluidic logic has enabled a new generation of capillarics that rival the complexity and utility of traditional lab instrumentation. These innovations have been translated into diverse, high-impact applications that highlight the versatility and power of capillary microfluidics across diagnostic, therapeutic, and wearable platforms. The following sections showcase selected examples that illustrate how capillaric circuits are being deployed to automate complex biochemical workflows, enhance accessibility in resource-limited settings, and expand the frontiers of point-of-care technologies.

2.2.1.1 Therapeutic Drug Monitoring

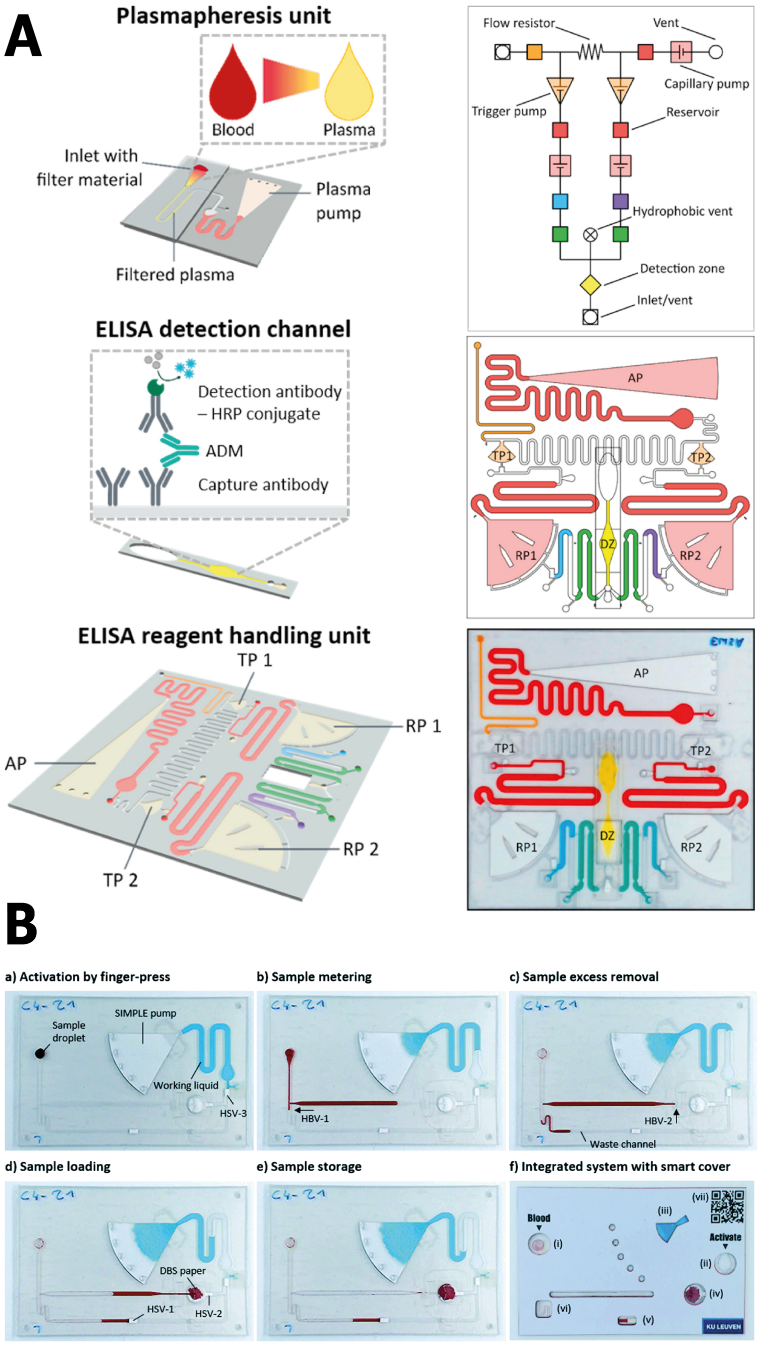

Figure 2.1: Capillarics for Therapeutic Drug Monitoring. (A) Visual abstract from Ordutowski et al., "Next generation point-of-care test for therapeutic drug monitoring of adalimumab in patients diagnosed with autoimmune diseases", Biosensors and Bioelectronics, 2022 [5], **(B)** Visual abstract from Ordutowski et al., "Next generation point-of-care test for therapeutic drug monitoring of adalimumab in patients diagnosed with autoimmune diseases", Biosensors and Bioelectronics, 2022 [5]

Vloemans et al. developed a novel microfluidic device that employs hydrophobic burst valves (HBVs) to achieve precise metering of blood samples for dried blood spot (DBS) analysis (Figure 2.1.B) [6]. These HBVs are designed to burst at specific pressures, allowing controlled splitting of a blood drop into accurately measured volumes ranging from 5–15 μl, irrespective of hematocrit variations. This precise metering is crucial for consistent and reliable DBS sampling, which is particularly beneficial in home settings or low-resource environments. The device integrates self-powered microfluidic SIMPLE technology, enabling autonomous operation without external pumps. Validation studies using adalimumab-spiked blood samples demonstrated improved recovery rates compared to traditional DBS methods, highlighting the device's potential in enhancing POC TDM applications.

Ordutowski et al. present a self-powered microfluidic chip that facilitates rapid, on-site quantification of adalimumab levels in whole blood samples Figure 2.1.A) [5]. This device integrates a fiber optic surface plasmon resonance (FO-SPR) biosensor within a disposable microfluidic cartridge based on the iSIMPLE technology. Upon a single finger press, the system autonomously separates plasma from whole blood, mixes it with reagents, and conducts a one-step FO-SPR sandwich bioassay. The entire process delivers results within 12 minutes using only 1 μl of plasma, demonstrating high sensitivity and specificity comparable to existing POC biosensors. This innovation underscores the potential of combining capillary microfluidics with advanced biosensing techniques to achieve efficient and user-friendly TDM at the POC.

2.2.1.2 Wearables

Choi et al developed a skin-mounted microfluidic device that uses capillary bursting valves (CBVs) to passively guide sweat into an array of discrete microreservoirs for chrono-sampling—capturing sweat sequentially over time (Figure 2.2.A) [7]. Designed with soft, stretchable elastomers and bonded to the skin using medical-grade adhesives, the system leverages the natural pressure generated by eccrine sweat glands to autonomously fill microchambers without external power. Each CBV opens at a different bursting pressure, enabling time-resolved sampling of sweat and preserving temporal information about biomarker fluctuations. Human studies demonstrated the device's ability to track lactate, sodium, and potassium levels across time and body positions, supporting applications in hydration monitoring, fitness tracking, and non-invasive clinical diagnostics. The devices were robust to motion and could be easily removed for

ex situ analysis via centrifugation, offering both in situ sensing and sample preservation.

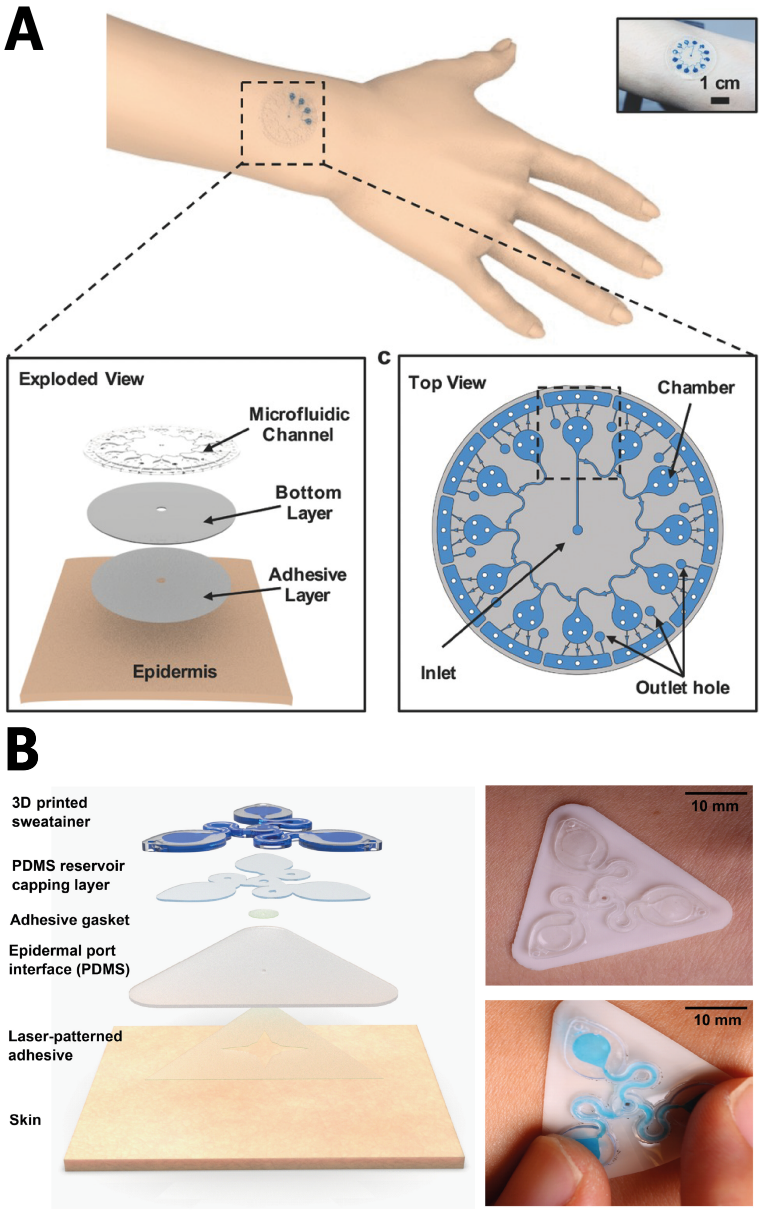

Figure 2.2: Wearable Capillary Microfluidics. (A) Visual abstract from Choi et al., "Thin, Soft, Skin-Mounted Microfluidic Networks with Capillary Bursting Valves for Chrono-Sampling of Sweat", Advanced Healthcare Materials, 2017 [7]. **(B)** Visual abstract from Wu et al., "Skin-interfaced microfluidic systems with spatially engineered 3D fluidics for sweat capture and analysis", Science Advances, 2023 [8].

Wu et al. introduced the "sweatainer," a 3D-printed, modular epidermal microfluidic system that expands the design possibilities of capillary microfluidics through true 3D architectures, including 3D capillary burst valves (CBVs) (Figure 2.2.B) [8]. Fabricated us-

ing DLP-based additive manufacturing, the sweatainer features spatially graded channels and complex geometries that support multidraw sweat sampling—the sequential collection of independent, pristine sweat samples during a single wear session. These samples are directed into microreservoirs with CBVs tuned to burst at different pressures, enabling precise temporal separation of sweat and minimizing cross-contamination. Integrated colorimetric assays allow for on-body analysis of biomarkers such as chloride, and optical transparency is optimized for smartphone-based readout. Field tests validated its performance under exercise conditions, showing robust operation during cycling with minimal leakage or motion-induced failure. The sweatainer demonstrates how 3D-printed capillarics can enable advanced diagnostic functions while remaining user-friendly, low-cost, and fully autonomous. These works collectively demonstrate how capillary microfluidics can be embedded into soft, wearable formats to achieve autonomous, temporally resolved sampling and analysis of biofluids, pushing the boundaries of non-invasive diagnostics.

2.2.1.3 Diagnostic Assays

Olanrewaju et al. demonstrated a capillaric circuit designed for the rapid and autonomous detection of bacteria in liquid samples (Figure 2.3.A) [9]. The system integrates sample preloading, reagent mixing, incubation, washing, and detection into a single microfluidic chip. The authors applied the platform to detect Escherichia coli using an enzymatic colorimetric readout, with the entire assay — from sample input to visual detection — completing in under 90 minutes. This work showcased the potential of capillaric circuits to automate multi-step pathogen detection workflows, providing a low-cost, self-contained alternative to conventional microbiological assays for use in field testing or resource-limited diagnostic settings.

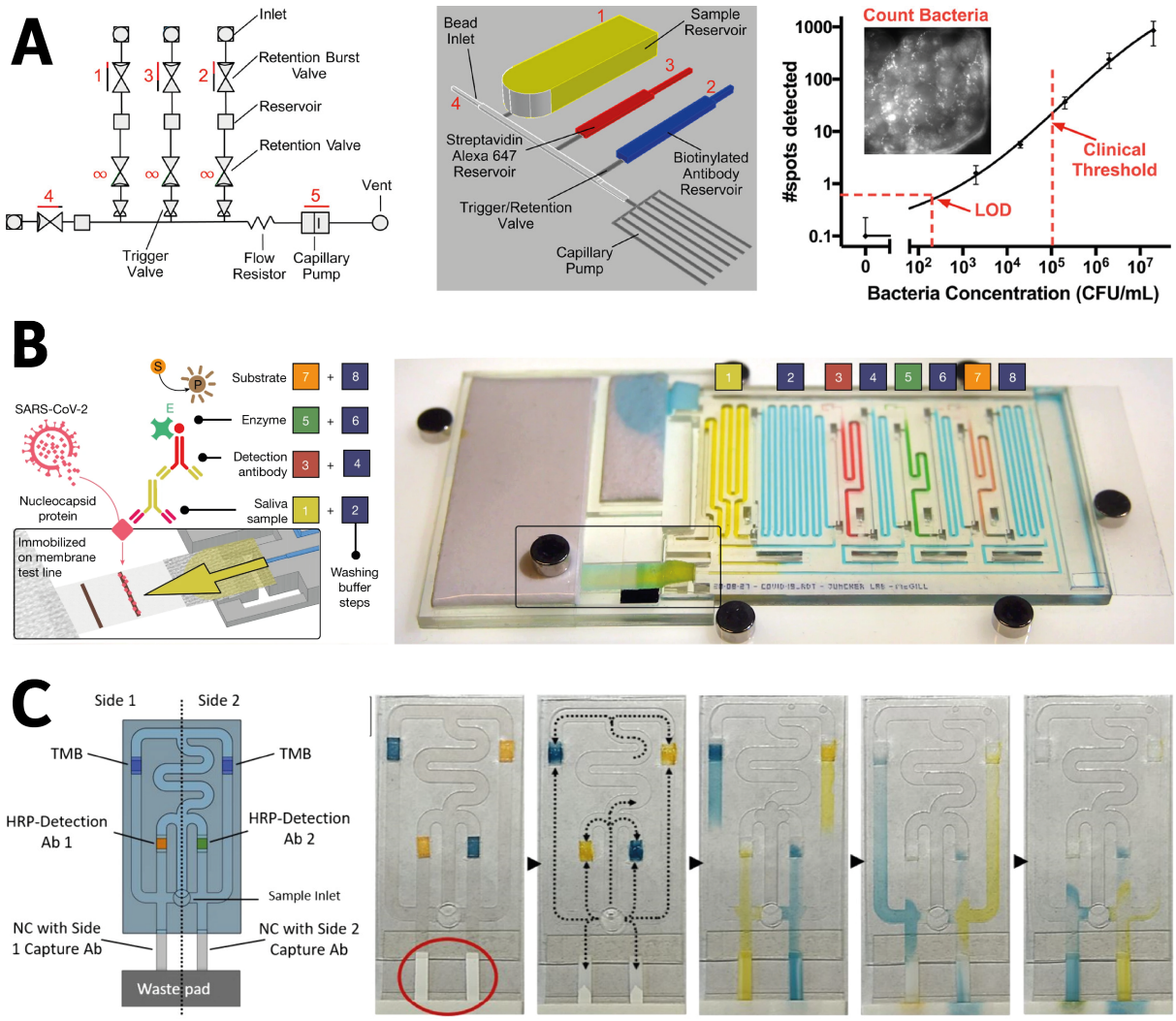

Figure 2.3: Capillarics for Diagnostic Assays. (A) Visual abstract from Olanrewaju et al., "Microfluidic Capillaric Circuit for Rapid and Facile Bacteria Detection", Analytical Chemistry, 2017 [9]. **(B)** Visual abstract from Yafia et al., "Microfluidic chain reaction of structurally programmed capillary flow events", Nature, 2022 [4]. **(C)** Visual abstract from Link et al., "Multiplexed Capillary-Flow Driven Immunoassay for Respiratory Illnesses", Analytical Chemistry, 2024 [10]

Link et al. present a novel capillary microfluidic platform designed for the simultaneous detection of multiple respiratory biomarkers (Figure (Figure 2.3.C) [10]. This device leverages capillary-driven flow to autonomously deliver reagents and washing solutions to spatially separated test zones, enabling two concurrent enzyme-linked immunosorbent assays (ELISAs) from a single sample addition. In under 15 minutes, the system can visually indicate the presence of specific antigens, with results that can be quantitatively analyzed using smartphone imaging. The platform demonstrated the ability to distin-

guish and quantify H1N1 hemagglutinin and SARS-CoV-2 nucleocapsid protein with detection limits of 840 pg/mL and 133 pg/mL, respectively, without cross-reactivity. Additionally, it successfully performed simultaneous detection of SARS-CoV-2 nucleocapsid protein and human C-reactive protein (CRP), a marker associated with inflammation and disease severity. This multiplexed approach addresses the need for rapid, sensitive, and accessible point-of-care diagnostics, particularly valuable in differentiating diseases with overlapping symptoms.

At the forefront of this field, Yafia et al. published a landmark study in Nature that introduced Microfluidic Chain Reactions (MCRs), a structurally programmed platform enabling autonomous execution of complex biomedical assays within a single capillary microfluidic device (Figure 2.3.B) [4]. They demonstrated the platform's versatility by automating the detection of SARS-CoV-2 antibodies in saliva, mimicking sequential ELISA stages, and conducting a thrombin generation assay requiring timed subsampling of coagulation-activated plasma. This seminal publication established MCRs as a transformative, electronics-free tool that programs fluidic event cascades via chip geometry, enabling scalable, autonomous biochemical workflows.

2.2.2 Microfluidic Chain Reactions (MCRs) Are Powerful but Underutilized

MCRs hit a rare sweet spot of elegance, autonomy, and accessibility. Capillary-driven flow gives the ability to program logic and sequencing into a chip's geometry, enabling timed, conditional operations without pumps, valves, or electronics. A single capillary trigger can initiate complex, pre-programmed sequences, offering maximum output from minimal input. Compatible with widely available 3D printers, MCRs break microfluidics out of the cleanroom and into desktops, making file-based sharing and local fabrication accessible. With applications ranging from diagnostics and cell culture to chemical automation and education, MCRs offer a versatile, electronics-free platform for scalable, programmable fluid handling.

Despite their intuitive, programmable, printable power, MCRs have yet to reach broad adoption beyond the labs that developed them. As highlighted above in the context of capillary microfluidics, MCRs have appeared primarily in the original landmark publication in Nature [4], subsequent iterations from the Juncker lab [11–13], and most recently, in our own Ọlánrewájú Lab [14], all within the same mentorship lineage of the initial demonstration. This limited translation is striking given that the seminal MCR article has

been cited over 150 times in just three years, reflecting substantial interest but a gap in practical dissemination.

To bridge this divide between enthusiasm and accessibility, we have prepared this tutorial review to guide readers through the design, conceptualization, and fabrication of MCR devices, empowering more researchers to adopt and build upon this transformative technology.

2.3 Governing Equations

Having established the broad utility and diverse applications of capillaric circuits, we now turn to the physical principles that underpin their operation. Despite their range of use cases, these systems are unified by a common physical foundation: passive fluid transport driven by surface tension and geometric conditions. To effectively design and optimize these capillaric devices, it is essential to understand the governing equations that dictate capillary-driven flow. The following section introduces the fundamental principles underlying capillary action in microchannels, with an emphasis on how surface tension, contact angle, and channel geometry determine fluid motion in pump-free systems.

2.3.1 Capillary Pressure

Capillary action in a microchannel, the driving force for our pump-free microfluidics, is governed by the surface tension of the working fluid, the geometry of the microchannels, and the contact angle of the working fluid with the channel walls [1].

ISOTROPIC CHANNELS

	Advancing flow	Receding flow	Pressure equation
Circular	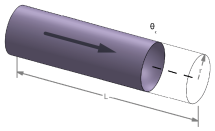	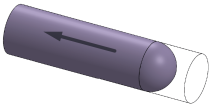	$P = \frac{-2\gamma cos\theta_c}{r}$
Rectangular	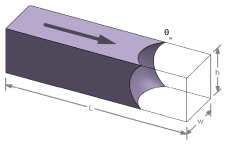	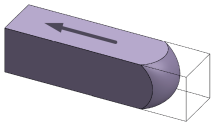	$P = -2\gamma \left[\frac{cos\theta_w}{h} + \frac{cos\theta_w}{w} \right]$

ANISOTROPIC CHANNELS

	Wide (w > h)	Tall (h > w)	Pressure equation
Rectangular	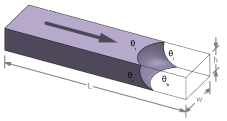	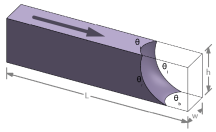	$P = -\gamma \left[\frac{cos\theta_t + cos\theta_b}{h} + \frac{cos\theta_l + cos\theta_r}{w} \right]$

Figure 2.4: Capillary pressure of common microchannel geometries

Capillary pressure of a microchannel can be derived from the Young-Laplace equation to yield the relationship between pressure, surface tension (γ), contact angle (θ), and channel geometry (r, w, h). While we typically report governing equations of capillaric microchannels with rectangular cross-sections due to the historical reliance on planar photolithography for fabrication, new advancements in 3D-printing have facilitated circular channel geometries [11, 12]. Figure 2.4 presents the capillary pressure equations for common microchannel geometries.

Calculating capillary pressure for a microchannel is imperative for designing capillaric circuits so we commonly automate the calculation (e.g. store this as a python function or build it into an excel sheet). Example code can be found in the appendix.

It is worth noting the intuitive interpretation of the pressure equations. Take the equation for a circular channel as an example: $P = \frac{-2\gamma cos\theta_c}{r}$.

Decreased surface tension results in decreased capillary pressure, but surface tension and contact angle are intrinsically linked as they're both physical properties of the working fluid and it's relationship with it's environment. Generally, as surface tension increases, contact angle also increases. The oscillatory cosine term in the capillary pressure equation zeroes out at $90°$ so advancing capillaric flow requires contact angles between $0°$ and $90°$. Within this range of $0°$ and $90°$, the cosine term decreases, meaning increased contact

angles within this range lead to decreased capillary pressure. While contact angle and surface tension can be utilized as design parameters for microchannels, it can be limiting and complex due to the entangled, conflicting relationship they have with capillary pressure and eachother. This is one of the reasons why we typically start with changing the geometry of the microchannels for fine control over capillary pressure.

It is important to understand the factors that bound channel geometry when designing these channels. Our lower end is typically dictated by fabrication limits: how small of a channel can we etch or print? Our upper end is dictated by the point at which we leave a microfluidic regime and start to feel the effects of gravity on our bulk flow. For circular channels, the capillaric regime ends around diameters of 2.71 mm [15].

2.3.2 Flow Rate

We can expand our knowledge of capillary flow in microchannels by deriving the flow rate. Flow rate in a microchannel of known geometry can be found by the following equation:

$$Q = \frac{\Delta P}{R} = \frac{\Delta P h^3 w}{12 \eta L(t)} \left[1 - 0.630 \frac{h}{w}\right] \tag{2.1}$$

This equation is derived from the Navier-Stokes equation assuming laminar, steady-state flow in a microfluidic regime ($Re << 1$, negligible gravitational effects), further simplified by approximating a summation that assumes a flat, wide, rectangular channel [1]. Channel geometry $(w, h, L(t))$ kinematic viscosity (η) are inputs, as well as the terms encompassed by ΔP (θ, γ).

With the hydraulic-electrical analogy, flow rate can also be expressed as $Q = \frac{\Delta P}{R}$, a fluidic interpretation of Ohm's law. To derive $Q = \frac{\Delta P}{R}$ from $V = IR$, current is synonymous with flow rate, voltage with pressure differential, and resistance with resistance.

Velocity of the flow is expressed as the volumetric flow rate, Q, divided by the cross-sectional area:

$$\frac{dL(t)}{dt} = \frac{Q}{wh} \tag{2.2}$$

This equation can be differentiated to solve for the fluid length traveled $(L(t))$ and filling time (t).

$$L(t) = h\sqrt{\frac{\Delta P}{6\eta L}\left[1 - 0.630\frac{h}{w}\right]t} \tag{2.3}$$

For short channels, solving this equation for t and inputting the terminal length of the microchannel yields a rough estimate of the total time it takes to fill a channel. For longer channels where resistance is accumulated over the length of a microchannel, it is more accurate to estimate the total fill time of a channel with this summation where length is a function of incremental time steps:

$$t_{total} = \sum_{n=0}^{L_{total}} \frac{6\eta L(t_n)^3 w}{\Delta P h^2 (w - 0.630h)} \tag{2.4}$$

A simple python code for using this summation to estimate fill time of a long serpentine is included in the appendix.

Fill time becomes a very important design consideration when capillaric circuits are used as analogs for timed bioassay reactions and anytime precisely timed fluid delivery is required.

As kinematic viscosity increases, fill time increases and flow rate decreases. Intuitively, we can think about it like honey moving through a straw versus water. Honey has a high kinematic viscosity and experiences much more resistance to freely flow than water, thus it would take longer for honey to travel the same distance as water in a pipe with equivalent conditions.

It's worth noting an assumption that $w \approx h$ and $L >> w, h$ for a long, rectangular channel. Increased length in the fill time equation is a dominant contributor to increased fill times (denoted by the cubic term) with h also playing a large role (denoted by the square term).

We like to characterize flow rate in our microchannels for a number of different reasons: evaluating the error between theoretical and experimental drain times, empirically determining the contact angle of our channels, and screening the fabrication fidelity of our chips. Using the governing equations established in his chapter and a simple experimental setup (Figure A.4), we can plot flow rate over time, fluid velocity over the length of a channel, and calculate the fill time of a channel. We print a simple serpentine with known cross-sectional dimensions of a microchannel as our h and w inputs, and known total length of the channel. We video the fluid as it moves through the channels and in post-analysis, we denote the entrance of fluid into the microchannel as $t = 0$ or $frame\# = 0$

and associate frame numbers with incremental lengths along the channel ($L(t)$). The discretization of measurements can be changed to review course or fine increments of the channel. By fabricating parallel serpentines on a microchip, you can evaluate replicate measurements to compare to theoretical calculations.

This tracking of flow rate, velocity, and fill time could be automated with image analysis for data collection but the scale of our work doesn't necessitate extensive automation (and this process is an ideal exercise for understanding capillary microfluidics).

2.3.3 Resistance

Solving the hydraulic-electrical analogy of Ohm's law connecting flow rate, pressure, and resistance for R yields:

$$R = \frac{\Delta P}{Q} \tag{2.5}$$

We can solve for the fluidic resistance in a microchannel using equations from previous sections. Resistances for microchannels with rectangular and circular cross-sections are:

$$R_{rect} = \frac{12\eta L}{h^3 w}\left[1 - 0.630\frac{h}{w}\right]^{-1} \tag{2.6}$$

$$R_{circ} = \frac{128\eta L}{\pi D^4} \tag{2.7}$$

As mentioned in an intuitive recap of the flow rate equation, increased viscosity leads to increased resistance. Additionally, while length (L) and width (w) of a microchannel play a role in resistance, height (h) dominates as denoted by the cubic term. Resistance increases significantly with even minor decreases to height, highlighting the importance of microchannel height as a key design factor. It is crucial to recognize that 'height' in microchannels described by the rectangular resistance equation is not directionally bound, it is an expression for the smaller dimension of a rectangular cross-section. When inputting resistance calculations into python or excel, it is thus worth noting that a check should be added to ensure that the dimension denoted by h is the minimum value between h and w.

Now that we understand the basic physics of capillary microfluidics, we shift focus to how these principles are physically implemented in MCR design.

2.4 Establishing Taxonomy of Capillaric Features

This section outlines the conceptual design process for the domino valve circuit shown in Figure 2.5.A. A conceptual sketch such as this serves as a useful starting point to delineate the key components of the circuit and organize the sequence of flow events. From this preliminary schematic, target dimensions can be defined and translated into a computer-aided design (CAD) environment for scaling and refinement.

The diagram provides a framework for identifying and analyzing the core flow control elements within the circuit. As part of the design workflow, mapping out the sequence of flow events (storyboarding) is a critical step in ensuring the system performs the intended function (Figure 2.5.C). Because this design was prototyped and tested in the laboratory, Figure 2.5.C presents selected frames from device operation to illustrate the progression of flow. These images mirror the structure and purpose of the initial schematic. Together, Figure 2.5.A and 2.5.C serve to highlight the essential components and behaviors of the circuit.

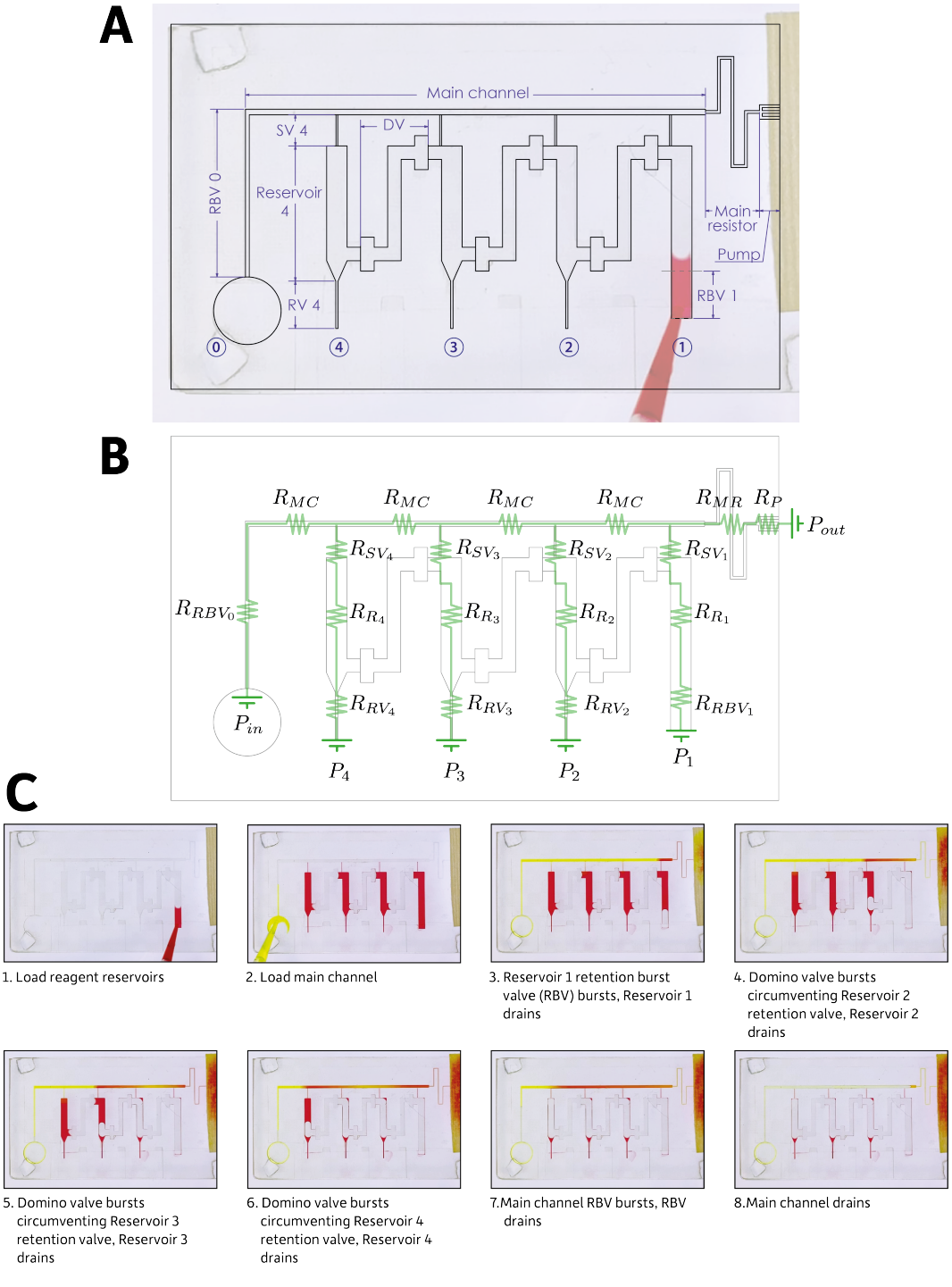

Figure 2.5: Storyboard of sequential flow events for a domino chip

2.4.1 Branch 0

Building on the conceptual layout, we next assign a taxonomy to the key structural and functional elements of the MCR. We can first look at the most direct path from the inlet to the outlet, skipping the reservoirs for now. We label the inlet as **Branch 0**, through which fluid flows sequentially from the initial retention burst valve (RBV_0), into the main channel, across the main flow resistor, and ultimately to the capillary pump.

The circular indent in the chip is meant to hold enough liquid to fill the main channel while also providing a convenient target for filling by a pipette (Figure 2.5.C.2). The circular opening is exposed to atmospheric pressure but once flow makes contact with the closed capillary channel, the designed capillary pressure kicks in at a magnitude dictated by the pressure equation and dimensions of RBV_0, a subsection of Branch 0. We will discuss later why we label this piece of the branch as a retention burst valve.

The main channel is our linkage to each reservoir. The main resistor provides enough fluidic resistance and capillary pressure to prevent back flow in the device.

2.4.2 Capillary pump

In this demonstration device, the **capillary pump** consists of two components. The first is a 3D-printed fork structure designed to generate high capillary pressure and direct fluid flow. The second is an absorbent material that is a terminal capillary sink. In this case, we used a piece of a cleanroom wipe but this can be swapped for any absorbent/high capillary pressure matrix like nitrocellulose, a 3D-printed treeline pump, etc. Together, these components serve dual functions: they must provide sufficient capillary pressure to direct all fluid toward the outlet, and offer enough absorption capacity to accommodate the full volume of waste fluid generated by the device, thereby sustaining continuous flow.

2.4.3 Branches 2-4

Now we can look at **Branches 2-4**. The top of the reservoirs is exposed to atmospheric pressure, which allows us to pre-load them with liquid prior to initiating flow through the main channel (Figure 2.5.C.1). This order of operations is important: loading the main channel first can result in air entrapment within the branches.

Although the reservoir openings are small and can be difficult to target precisely with a pipette, the device design compensates in two ways. First, wide spacing between the reservoir inlets allows easier droplet placement. Second, the strong capillary pressure in

the connected channels enables a large droplet placed near the inlet to wick efficiently into the reservoir. For added robustness, especially when working with densely packed layouts or when precise pipetting is challenging, designers can incorporate flared or enlarged inlet regions at the reservoir openings, similar to those used at the main inlet.

The tops of the reservoirs are **retention valves (RVs)** and we can label them according to their corresponding branch (e.g. RV_4). Their retention capabilities are best demonstrated by Figure 2.5.C.3. Despite being in contact with the yellow fluid in the main channel, Branches 2-4 don't leak.

After the retention valve comes the **reservoir body**, a channel that holds the bulk volume of our fluid for each branch. These are often manifested as serpentines in capillaric circuits to save space or control drain time.

Finally, we reach the **stop valve (SVs)**. The stop valve serves two main purposes: making sure fluid doesn't spill into the main channel before the main channel is filled (Figure 2.5.C.2) and offering some precise control over branch drain time. From a previous section, we saw that drain time is influenced by length, width, and height of channels. Because the stop valve is typically designed to be narrow and shallow to ensure effective fluid retention, its geometry has a particularly strong influence on the fluidic resistance. Consequently, modifying stop valve dimensions is often a more effective strategy for tuning drain time than altering reservoir geometry.

2.4.4 Branch 1

We will skip to looking at the first branch before we explore the pneumatic connections between branches that give them their characteristic chain reaction behavior. **Branch 1** is constructed with a reservoir and SV like branches 2-4 but in lieu of a RV, there is a RBV (RBV_1). We will visit the theory on the use of a RBV in detail as we move forward but intuitively, there are only two RBVs on the chip and the dimensions of RBV_1 are significantly larger than RBV_0. In a pressure-tug of war, RBV_0 is thus much stronger than RBV_1. This will be a key factor in the operation of our MCR since the bursting of RBV_1 kicks off the microfluidic chain reaction (Figure 2.5.C.3).

2.4.5 Domino valves

Now, for the domino valves. They are air links between the branches that connect from the bottom of n reservoir to the top of the $n+1$ reservoir. From Figure 2.5.C.4, we

can deduce that as soon as the air from the branch 1 reservoir drains, the air bridge snips off the RV on branch 2. In this action lies the domino power of this type of circuit. Theory will reveal more on how exactly we design these.

There is one element of these pneumatic connections that is often trivial to design but imperative to operation: a stop valve at each connection to the reservoir to prevent leakage of fluid into the connections. This necessitates a geometric expansion between the reservoirs and the domino valves that gives them their 'serifed' structures. The triviality comes because the dimensions of the pneumatic connections do not much matter, so the geometric expansion just has to be large enough to pin the fluid front from the reservoir. Often the criteria for this stop valve design is to just add $> 300\mu m$ onto the dimensions of the reservoir in all directions. We have successfully explored an alternative method of designing these valves with a multi-material hydrophobic tape patterning in the next chapter.

Now that we've intuitively walked through this circuit, we can begin the process of designing our feature dimensions to ensure all steps happen in order.

2.5 Linking elements via circuitry

The structurally designed pressures and resistances of each feature will dictate the order of the flow events. We will customize these so it is important to label the locations of pressure and resistance changes on our diagram. To do so, we take our sketch of a domino chip and label every channel stretch with a unique dimension as a new resistor and every channel with an end exposed to the atmosphere as a pressure source (anaologus to a voltage source in electrical circuit design). Figure 2.5.B shows the representative electrical circuit of our demonstrative MCR.

A few clarifying notes about this diagram: domino valves are intentionally not labeled with pressures or resistances, as properly designed stop valves should prevent any fluid from entering these paths. Thus, under ideal conditions, no flow occurs through the domino valve channels. The main channel is divided into smaller segments to reflect interruptions where it interfaces with branch structures, each of which may introduce new resistive elements or junction conditions.

2.6 Designing Fluidic Circuit Logic

With a functional taxonomy in place, we now move to the heart of MCR design: encoding conditional logic through channel geometries, pressures, and resistances.

2.6.1 Branch 1 Draining

Now we look back to our storyboard to structurally encode the first fluidic step. In Figure 2.5.C.3, we want the following conditions to be met:

- Branch 1 drains before branch 0
- Branch 1 drains before branches 2-4
- Flow from branch 1 goes into the main channel and towards the outlet, draining into the pump

We can map this out with the blue and magenta arrows denoting the flow path in Figure 2.6:

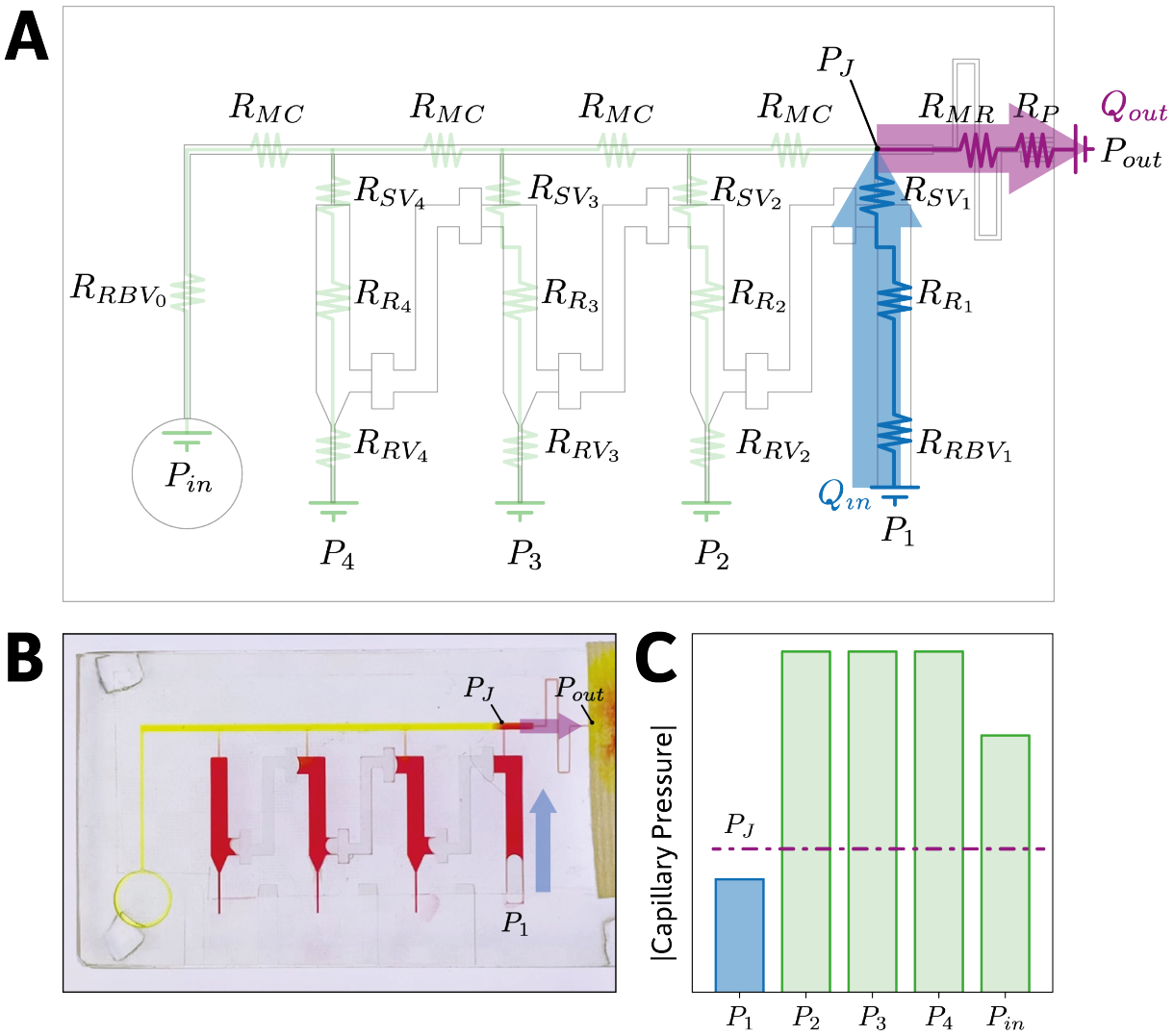

Figure 2.6: MCR Branch 1 Draining. **(A)** Circuit diagram showing the flow path in (blue) and out (magenta) of the node/junction of branch 1 and the main channel assuming no fluidic leakage. **(B)** Flow path demonstrated on chip through the junction. **(C)** Junction pressure that satisfies the conditions of branch 1 drainage.

Using our intuitive knowledge of the desired flow path, we want to create a strong pressure differential from the start of Branch 1 to the pump outlet (Figure 2.6.C). For this condition to be met, we can call upon Kirchoff's current law to ensure that the flow going into the junction at which branch 1 and the main channel meet (Q_{in}) equals the flow into the pump (Q_{out}). By setting this condition, we are going to design pressures that don't allow flow to leak in other directions in the circuit.

Kirchoff's current law:

$$Q_{in} = Q_{out} \tag{2.8}$$

Earlier, we established that the hydraulic analogy to the Ohm's law can be used to substitute flow rate with a relationship between pressure differential and resistance:

$$\frac{\Delta P_{in}}{R_{in}} = \frac{\Delta P_{out}}{R_{out}} \tag{2.9}$$

We can substitute the pressure differential terms using our circuit diagram by taking the difference of pressure from the branch to the junction and the junction to pump, establishing a new term we'll be solving for: **junction pressure,** P_{J_1}.

$$\frac{P_{J_1} - P_1}{R_{in}} = \frac{P_P - P_{J_1}}{R_{out}} \tag{2.10}$$

Given that the resistors in the Q_{in} and Q_{out} pathways are all in series, the resistances in and out are summations of the sequential resistances of the segments of channels:

$$R_{in} = R_{RBV_1} + R_{R_1} + R_{SV_1} \tag{2.11}$$

$$R_{out} = R_{MR} + R_P \tag{2.12}$$

We then solve for P_{J_1}. Work shown can be found in the appendix. This gives us an equation for the junction pressure:

$$P_{J_1} = \frac{P_P R_{out} + P_1 R_{in}}{R_{in} + R_{out}} \tag{2.13}$$

If we did this derivation for every branch, we'd see that this equation can be generalized across all branches as:

$$\boxed{P_{J_i} = \frac{P_P R_{out} + P_i R_{in}}{R_{in} + R_{out}}} \tag{2.14}$$

To solve for the junction pressure of branch 1, we can plug in the resistances:

$$P_{J_1} = \frac{P_P(R_{MR} + R_P) + P_1(R_{RBV_1} + R_{R_1} + R_{SV_1})}{(R_{RBV_1} + R_{R_1} + R_{SV_1}) + (R_{MR} + R_P)} \tag{2.15}$$

To meet the condition that $Q_{in} = Q_{out}$, $P_1 < P_J < P_P$. Jumping back to our requirements for branch 1 draining established above, we can also rank pressures for our other conditions as well:

- Branch 1 drains before branch 0 $\rightarrow \boldsymbol{P_1 < P_0}$
- Branch 1 drains before branches 2-4 $\rightarrow \boldsymbol{P_1 < P_{2-4}}$
- Flow from branch 1 goes into the main channel and towards the outlet, draining into the pump $\rightarrow \boldsymbol{P_1 < P_{J_1} < P_P}$

To combine these ensuring the right order of pressure rankings, we can add a few more conditions for our circuit:

- Pre-domino valve actuation, branches 2-4 should theoretically never drain to prevent leakage into the main channel $\rightarrow \boldsymbol{P_{2-4}} >$ all other pressures
- Branch 0 needs to eventually drain (Figure 2.5.7) so it has to be stronger than all the other branches but weaker than the capillary pump $\rightarrow \boldsymbol{P_{1-4} < P_0 < P_P}$

We can collapse these into this general rule (visualized by the plot in Figure 2.6.C):

$$\text{Condition for drainage of branch 1: } P_1 < P_{J_1} < P_0 < P_P < P_{2-4} \tag{2.16}$$

2.6.2 Branch 2 Draining

Now that we have some design bounds for branch 1, we can move to branch 2.

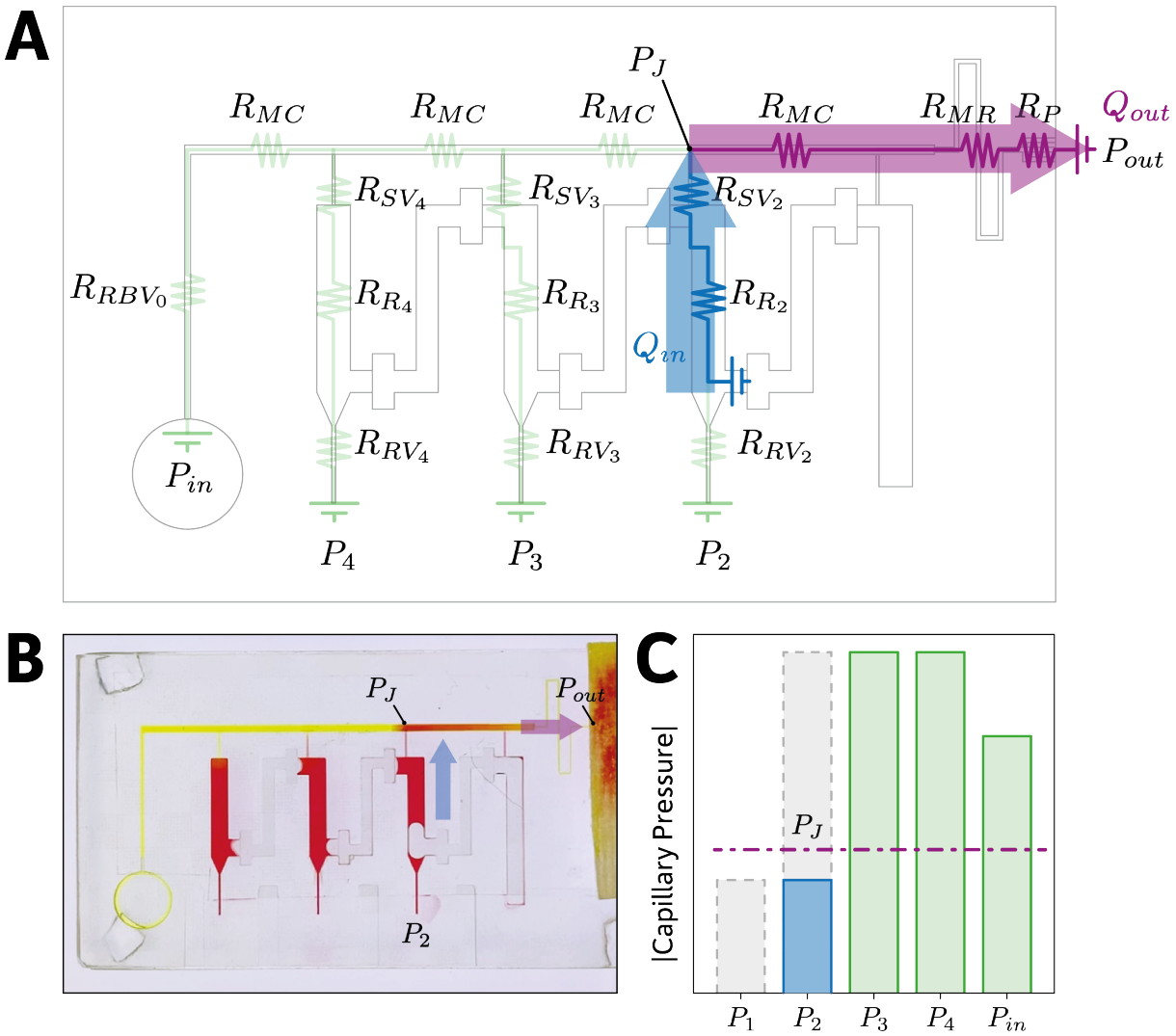

Figure 2.7: MCR Branch 2 Draining. **(A)** Circuit diagram showing the flow path in (blue) and out (magenta) of the node/junction of branch 2 and the main channel assuming no fluidic leakage. **(B)** Flow path demonstrated on chip through the junction. **(C)** Junction pressure that satisfies the conditions of branch 2 drainage.

Domino valve actuation dynamically modifies our circuitry for the draining of the next branch by allowing release of atmospheric pressure into the branch 2 reservoir, thus snipping off the extremely strong retention capability of RV_2 (Figure 2.7). This truncates branch 2, reducing cumulative resistance ($R_{in} = R_{R_2} + R_{SV_2}$) and terminal pressure (P_2, Pressure @ $RV_2 \rightarrow P_2^{'}$, Pressure @ R_2).

Now we solve for P_{J_2} at the junction of branch 2 and the main channel.

$$P_{J_2} = \frac{P_P(R_{MR} + R_P) + P_2^{'}(R_{R_2} + R_{SV_2})}{(R_{R_2} + R_{SV_2}) + (R_{MR} + R_P)} \tag{2.17}$$

Here are our conditions for the drainage of branch 2:

- Branch 2 drains after branch 1 $\rightarrow \boldsymbol{P_2^{'} < P_1 < P_2}$
- Branch 2 drains before branch 3 and 4 $\rightarrow \boldsymbol{P_2^{'} < P_{3,4}}$
- Flow from branch 2 goes into the main channel and towards the outlet, draining into the pump $\rightarrow \boldsymbol{P_2^{'} < P_{J_2} < P_P}$

All conditions can be collapsed into this rule for the draining of branch 2 (visualized by the plot in Figure 2.7):

$$\text{Condition for drainage of branch 2: } P_2^{'} < P_1 < P_{J_{1,2}} < P_0 < P_P < P_{2-4} \tag{2.18}$$

2.6.3 Branch 3, 4, and 0 Draining

The drainage of branch 2 actuates branch 3 (Figure 2.8) and the drainage of branch 3 actuates branch 4 (Figure 2.9). Branch 0 is the last thing to drain, emptying the main channel, main resistor, and pump as it goes (Figure 2.10).

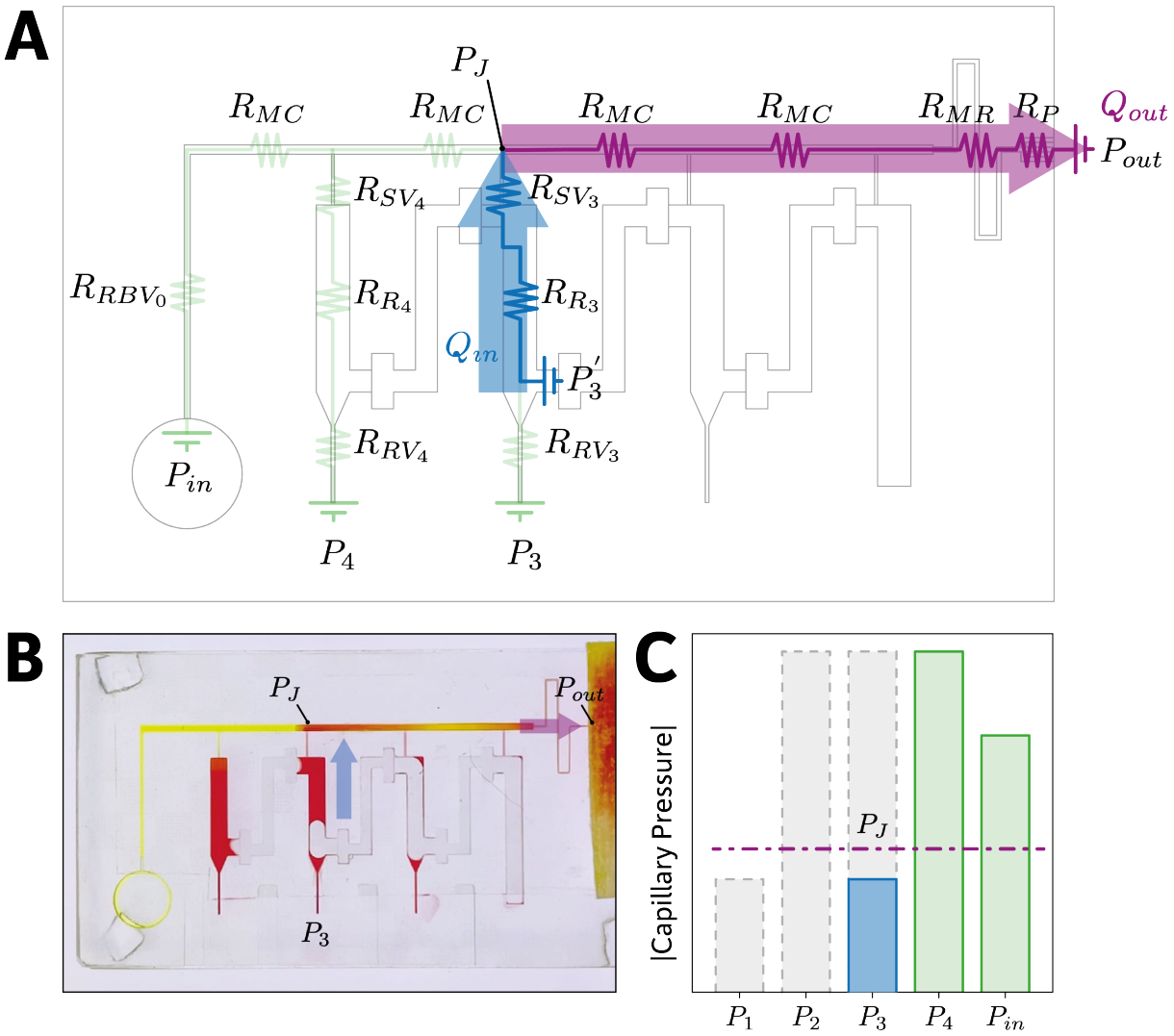

Figure 2.8: MCR Branch 3 Draining. **(A)** Circuit diagram showing the flow path in (blue) and out (magenta) of the node/junction of branch 3 and the main channel assuming no fluidic leakage. **(B)** Flow path demonstrated on chip through the junction. **(C)** Junction pressure that satisfies the conditions of branch 3 drainage.

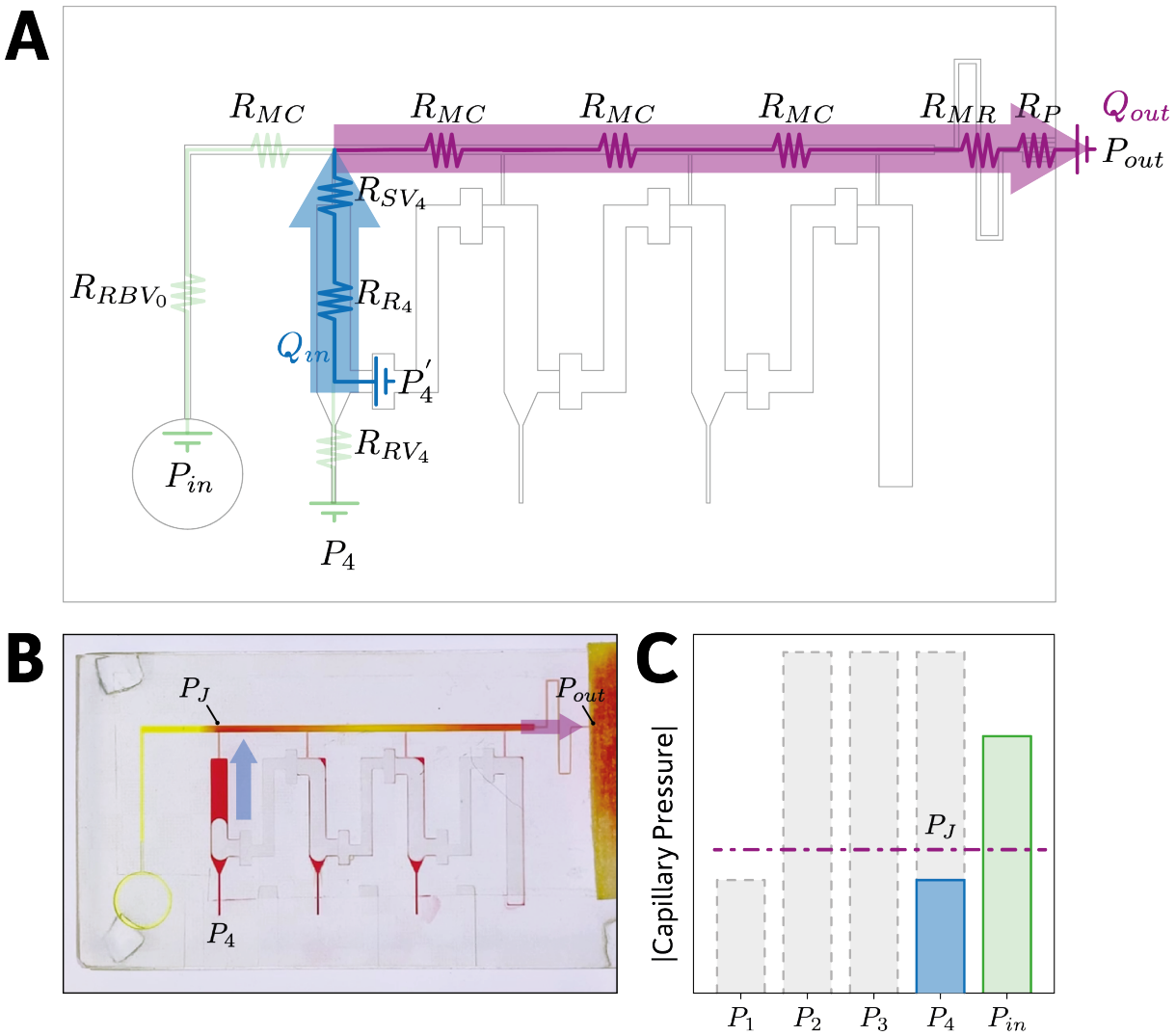

Figure 2.9: MCR Branch 4 Draining. **(A)** Circuit diagram showing the flow path in (blue) and out (magenta) of the node/junction of branch 4 and the main channel assuming no fluidic leakage. **(B)** Flow path demonstrated on chip through the junction. **(C)** Junction pressure that satisfies the conditions of branch 4 drainage.

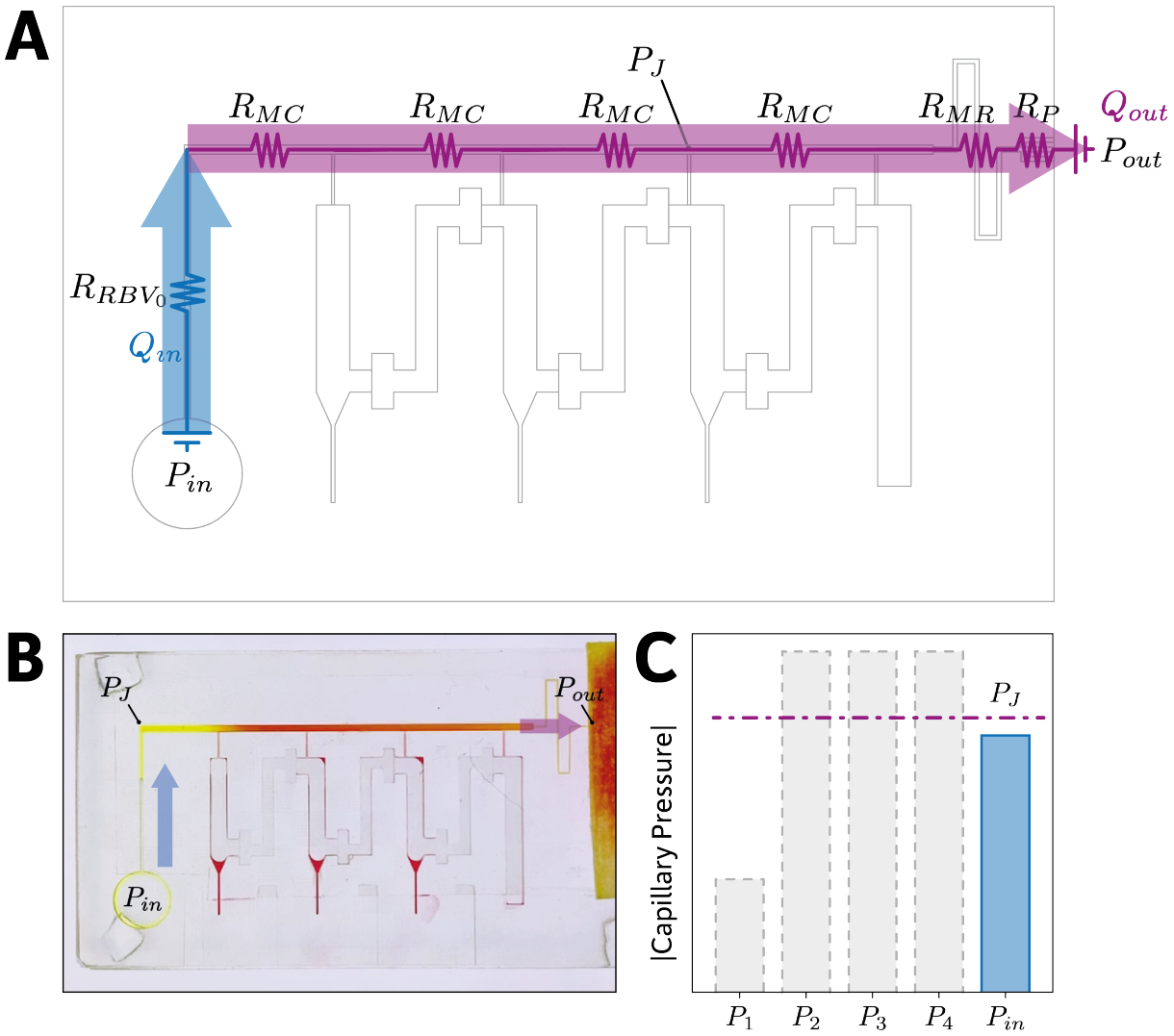

Figure 2.10: MCR Branch 0 Draining. **(A)** Circuit diagram showing the flow path in (blue) and out (magenta) of the node/junction of branch 0 and the main channel. **(B)** Flow path demonstrated on chip through the junction. **(C)** Junction pressure that satisfies the conditions of branch 0 drainage.

Figure 2.11 summarizes the design rules for an MCR.

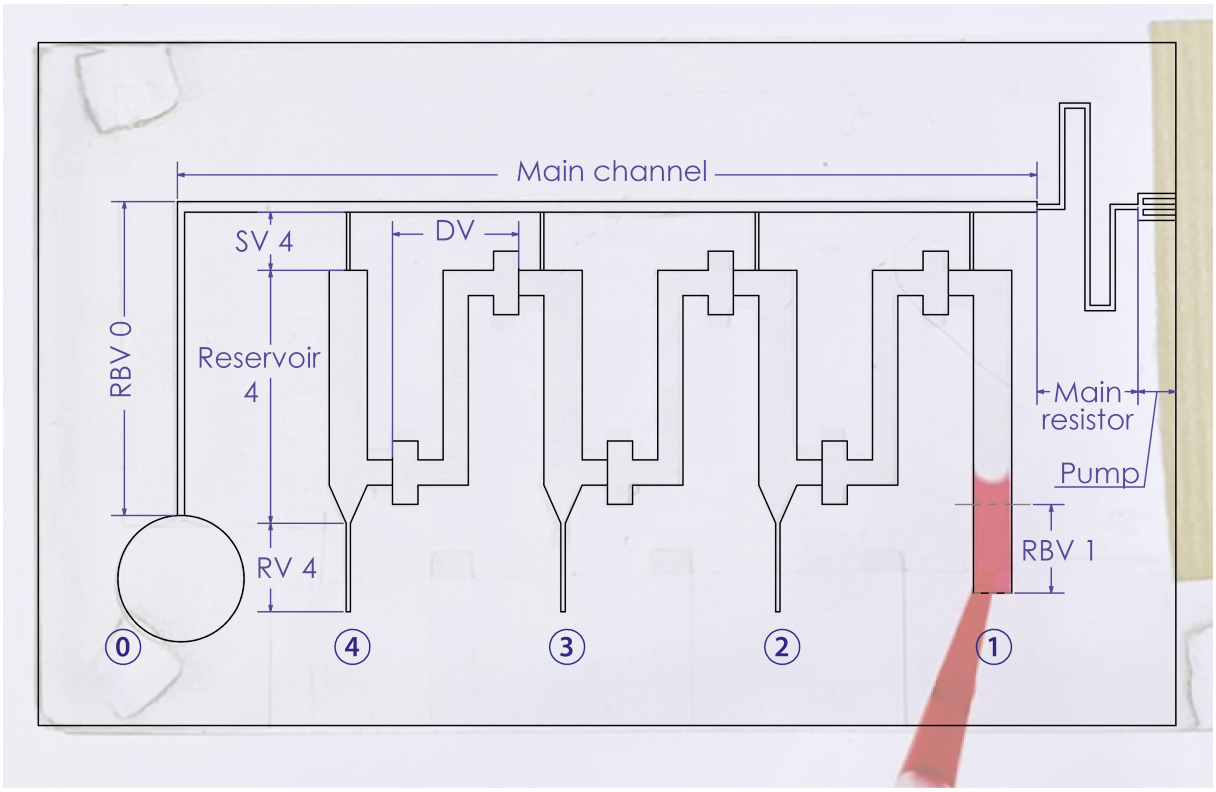

Strongest

Weakest

DESIGNED PRESSURE	DESIGNED RESISTANCE
1. RVs	1. Main resistor
2. Pump & Main resistor	2. RVs
3. SVs	3. Pump
4. RBV 0	4. RBV 0 & SVs
5. Main channel	5. RBV 1 & Main channel & Reservoirs
6. Reservoirs & RBV 1	

Figure 2.11: Design rules for an MCR summarized for quick reference

2.6.4 Guidelines for Parametric Design of MCRs

With the logic framework established, we now provide a guide for converting design rules into channel dimensions, using fabrication-aware constraints.

While the specific channel dimensions used to encode these parameters are vastly customizable, several practical considerations can simplify the design process and help identify effective starting points. One useful strategy is to use a parametric spreadsheet, where the height, width, and length of each feature can be input to compute corresponding resistances and capillary pressures. This allows rapid iteration and verification against design targets. Open-source tools have been developed to make this process more accessible [16].

2.6.4.1 Designing Cross-Sectional Dimensions

Because resistance scales strongly with cross-sectional area, a useful first step is to define the maximum and minimum channel heights and widths that will be used. These bounds are typically constrained by the fabrication method (print resolution) on the lower end, and capillarity on the upper end.

- Large features (e.g., reservoirs and the initial retention burst valve, RBV_1) generally operate at low pressures and should be set near the upper bound of the allowable cross-sectional size.
- Small features (e.g., main resistors and retention valves, RVs) often require high resistance and are typically designed near the lower bound.

Stop valves (SVs) occupy a special role: they must pin liquid in the branches until the main channel is triggered, and they can control the timing of downstream delivery. This makes them highly sensitive to both pressure and resistance, so they are ideally designed after the upper- and lower-bound features are in place. Mid-range values for cross-sectional dimensions can be selected for other intermediate components, with refinement through parametric sweeps.

2.6.4.2 Designing Channel Lengths

Although length has a weaker influence on resistance than cross-sectional area, it remains an important design lever:

- Main resistors and RVs benefit from longer lengths to ensure sufficiently high resistance, especially when their cross-sectional areas are already minimized.
- Reservoir length primarily defines fluid volume, not resistance. This can be flexibly adjusted to meet volumetric requirements, and volumes can be pre-calculated in the same parametric spreadsheet.
- Main channel and RBV_1 lengths have minimal impact on resistance and can be adjusted freely in CAD to optimize the spatial layout and user interface of the device. Because these features are already large in cross-section, extending their lengths only marginally increases resistance, allowing spatial freedom during layout design.

2.6.4.3 Domino Valve Design

Domino valves are typically the last features to be finalized and are often shaped directly within the CAD layout. Their function is enabled by SVs that prevent fluid from leaking into the pneumatic connections. To achieve this, a local expansion of greater than 300 μm in at least three directions from the reservoir is usually sufficient to form the SV. The domino valve channel itself connects the bottom of reservoir$n$ to the top of reservoir$n+1$, and its geometry can be flexibly patterned, provided it fits within the physical footprint and satisfies SV constraints.

2.6.5 Transition to Fabrication

Once pressures, resistances, and sequencing rules are translated into geometries, the final step is fabrication. In the next chapter, I outline practical methods to bring these digital designs into physical form. An open-source protocol for 3D printing these devices on low-cost hardware is available in the appendix as well. Alternatively, other manufacturing methods such as CNC milling [17], hot embossing [18], or PDMS molding [3] can be used to translate digital designs into physical microfluidic circuits.

2.7 Conclusion

Microfluidic chain reactions (MCRs) represent a transformative leap in capillary microfluidics offering a uniquely scalable, programmable, and pump-free approach to automating complex fluid handling. This tutorial has walked through the foundations of capillaric physics, introduced the design taxonomy of MCR components, and outlined how logic, resistance, and pressure can be encoded into geometry to create conditionally triggered flow sequences. By drawing analogies to electronic circuits and combining intuitive visualizations with rigorous design equations, we hope to demystify MCR design and equip researchers with the tools to build and customize their own devices.

One of the most powerful aspects of MCRs is their compatibility with accessible, low-cost fabrication methods, including desktop 3D printing. This opens the door to distributed, file-based sharing of diagnostic devices, reducing the barriers between design, prototyping, and deployment. Whether for point-of-care diagnostics, chemical automation, or educational tools, MCRs offer an elegant solution to fluidic programming requiring no pumps, electronics, or external infrastructure.

Despite the maturity of the underlying principles, MCRs remain underutilized outside a small circle of labs. We hope that by distilling their design logic and lowering the learning curve, this tutorial helps unlock broader adoption and creative applications. Microfluidics is often seen as a technically demanding field; MCRs suggest it doesn't have to be. With just capillary forces and a little structural design, it is possible to build surprisingly powerful biochemical machines.

References

1. Olanrewaju, A., Beaugrand, M., Yafia, M. & Juncker, D. Capillary microfluidics in microchannels: from microfluidic networks to capillaric circuits. *Lab on a Chip* **18,** 2323–2347. ISSN: 1473-0197, 1473-0189 (2018).
2. Safavieh, R. & Juncker, D. Capillarics: pre-programmed, self-powered microfluidic circuits built from capillary elements. *Lab on a Chip* **13,** 4180. ISSN: 1473-0197, 1473-0189 (2013).
3. Olanrewaju, A. O., Robillard, A., Dagher, M. & Juncker, D. Autonomous microfluidic capillaric circuits replicated from 3D-printed molds. *Lab on a Chip* **16,** 3804–3814. ISSN: 1473-0197, 1473-0189 (2016).
4. Yafia, M. *et al.* Microfluidic chain reaction of structurally programmed capillary flow events. *Nature* **605,** 464–469. ISSN: 0028-0836, 1476-4687 (May 19, 2022).
5. Ordutowski, H. *et al.* Next generation point-of-care test for therapeutic drug monitoring of adalimumab in patients diagnosed with autoimmune diseases. *Biosensors and Bioelectronics* **208,** 114189. ISSN: 0956-5663 (July 15, 2022).
6. Vloemans, D. *et al.* Precise sample metering method by coordinated burst action of hydrophobic burst valves applied to dried blood spot collection. *Lab on a Chip* **21,** 4445–4454. ISSN: 1473-0197, 1473-0189 (2021).
7. Choi, J., Kang, D., Han, S., Kim, S. B. & Rogers, J. A. Thin, Soft, Skin-Mounted Microfluidic Networks with Capillary Bursting Valves for Chrono-Sampling of Sweat. *Advanced Healthcare Materials* **6,** 1601355. ISSN: 2192-2640, 2192-2659 (Mar. 2017).
8. Wu, C.-H., Ma, H. J. H., Baessler, P., Balanay, R. K. & Ray, T. R. Skin-interfaced microfluidic systems with spatially engineered 3D fluidics for sweat capture and analysis. *Science Advances* **9,** eadg4272. ISSN: 2375-2548 (May 5, 2023).
9. Olanrewaju, A. O., Ng, A., DeCorwin-Martin, P., Robillard, A. & Juncker, D. Microfluidic Capillaric Circuit for Rapid and Facile Bacteria Detection. *Analytical Chemistry* **89,** 6846–6853. ISSN: 0003-2700, 1520-6882 (June 20, 2017).
10. Link, J. S. *et al.* Multiplexed capillary-flow driven immunoassay for respiratory illnesses. *Analytical Chemistry.* ISSN: 0003-2700 (Feb. 28, 2024).

11. Shafique, H. *et al.* High-resolution low-cost LCD 3D printing for microfluidics and organ-on-a-chip devices. *Lab on a Chip* **24,** 2774–2790. ISSN: 1473-0197, 1473-0189 (2024).

12. Karamzadeh, V., Sohrabi-Kashani, A., Shen, M. & Juncker, D. Digital Manufacturing of Functional Ready-to-Use Microfluidic Systems. *Advanced Materials* **35,** 2303867. ISSN: 0935-9648, 1521-4095 (Nov. 2023).

13. Parandakh, A. *et al.* 3D-printed capillaric ELISA-on-a-chip with aliquoting. *Lab on a Chip* **23.** Publisher: Royal Society of Chemistry, 1547–1560 (2023).

14. Leong, K. M. *et al.* Democratizing Access to Microfluidics: Rapid Prototyping of Open Microchannels with Low-Cost LCD 3D Printers. *ACS Omega,* acsomega.4c07776. ISSN: 2470-1343, 2470-1343 (Nov. 1, 2024).

15. *Capillary Length - an overview | ScienceDirect Topics*

16. Zhang, Y., Li, M., Tseng, T.-M. & Schlichtmann, U. Open-source interactive design platform for 3D-printed microfluidic devices. en. *Communications Engineering* **3.** Publisher: Nature Publishing Group, 1–13. ISSN: 2731-3395 (May 2024).

17. Tokihiro, J. C. *et al.* The dynamics of capillary flow in an open-channel system featuring trigger valves. *Scientific Reports* **14,** 31732. ISSN: 2045-2322 (Dec. 30, 2024).

18. Khoo, H., Allen, W. S., Arroyo-Currás, N. & Hur, S. C. Rapid prototyping of thermoplastic microfluidic devices via SLA 3D printing. *Scientific Reports* **14,** 17646. ISSN: 2045-2322 (July 31, 2024).

3 | Practical Fabrication Methods for Capillarics: Tools, Techniques, and Tradeoffs Beyond the Cleanroom

3.1 Abstract

This chapter presents a practical framework for fabricating capillaric microfluidic systems using accessible, low-cost tools and design principles. We characterize the performance of affordable LCD stereolithography (SLA) 3D printers and demonstrate their capability to produce functional open-channel microfluidics with only modest trade-offs in resolution compared to traditional DLP-SLA systems. Building on these findings, we introduce 3D-printed implementations of critical fluidic elements previously restricted to cleanroom fabrication, including phaseguides and self-coalescence modules (SCMs). We show that these elements can be scaled, integrated into circuits, and used to enable complex, pre-programmed liquid handling such as sequential valving, bubble-free reservoir filling, and reagent rehydration through self-coalescing flow. These demonstrations validate the potential of benchtop 3D printing to democratize microfluidics by expanding access to rapid, low-cost, and versatile prototyping without compromising core functionality. The chapter concludes with design considerations for interfacing printed components, optimizing material properties, and eliminating common fabrication bottlenecks, ultimately advancing the modularity and accessibility of capillaric systems for decentralized diagnostic applications.

3.2 Introduction

This chapter includes elements adapted from the peer-reviewed journal article:

i. **"Democratizing Access to Microfluidics: Rapid Prototyping of Open Microchannels with Low-Cost LCD 3D Printers"**, K. Leong, A. Sun, M. Quach, C. Lin,

Cosette A. Craig, F. Guo, T. Robinson, M. Chang, A. O. Olanrewaju. *ACS Omega*, 2024. https://pubs.acs.org/doi/10.1021/acsomega.4c07776

While Chapter 1 focused on design principles and operational logic for MCRs, this chapter addresses a key bottleneck in capillaric device deployment: fabrication. Here, I present practical methods for constructing accessible devices without a cleanroom, unlocking new possibilities for rapid iteration and global dissemination.

3.3 Low Cost LCD 3D-Printing

Compared to traditional cleanroom microfluidic fabrication techniques, 3D printing provides a faster and more affordable method for producing devices. While digital light projection (DLP) stereolithography (SLA) is commonly used for printing microfluidics, the high cost of many DLP printers ($\leq$ \$10,000 USD) remains a barrier to broader adoption. Recent improvements in liquid crystal display (LCD) SLA printing technology have introduced low-cost alternatives ($<$ \$500 USD) with sufficient resolution for microfluidic fabrication. Despite this, only a few studies have explored microfluidics using LCD printers, and comparative data on print fidelity is limited, especially direct evaluations against DLP systems.

In this work, we assessed the performance of a 40 μm pixel DLP printer ($\sim$ \$18,000 USD) alongside a 34.4 μm pixel LCD printer ($<$ \$380 USD). In alignment with earlier findings, both platforms showed a linear relationship between designed and actual channel widths for features ≤ 4 pixels wide, allowing accuracy assessments above this threshold. With a standard IPA-wash resin and printer-specific optimizations, the DLP printer achieved an average dimensional error of 2.11 $\pm$ 1.26%, while the 34.4 μm LCD printer showed a larger error of 15.4 $\pm$ 2.57%. However, when printing with a low-cost water-washable resin formulated for LCD-SLA, the 34.4 μm LCD printer's error decreased to 2.53 $\pm$ 0.94%, and a 22 μm LCD printer yielded 5.35 $\pm$ 4.49% error.

We also evaluated other key print characteristics such as surface texture, channel orthogonality, and the consistency of light exposure across the build area. As a demonstration of functional performance, we implemented LCD-printed capillaric circuits that reliably achieved multi-liquid, self-powered, and self-regulated flow. These results support the use of affordable LCD printers as viable tools for microfluidic fabrication, with only modest trade-offs in precision compared to systems that are nearly 40 times more expensive.

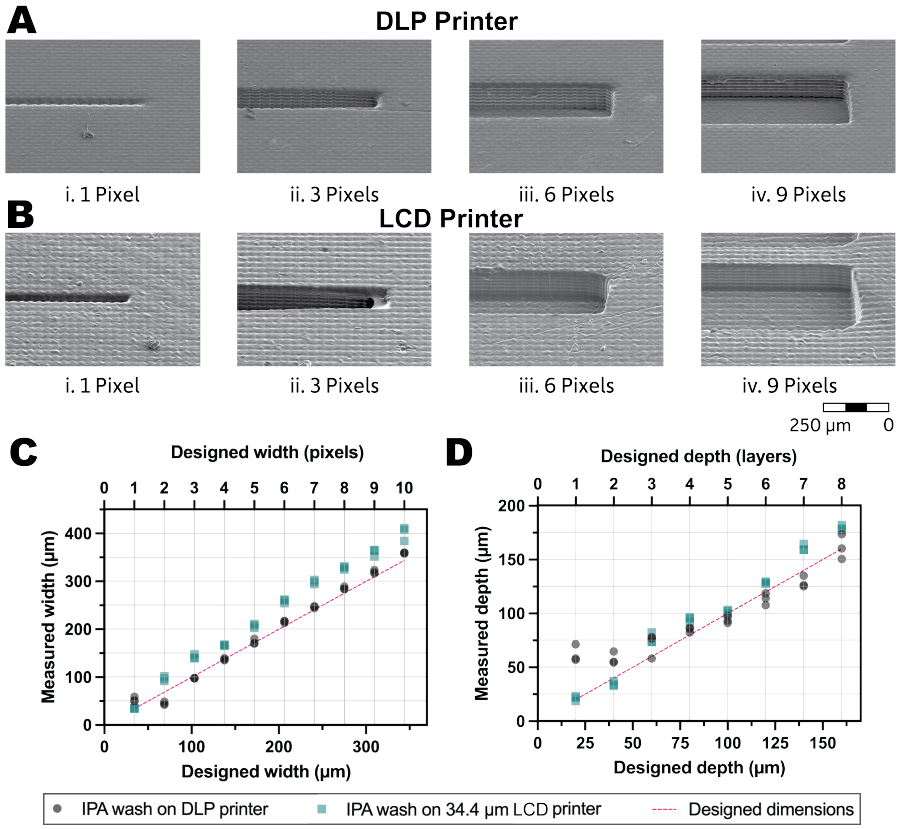

Figure 3.1: Comparison of microchannels fabricated with identical resin on LCD and DLP printers. (A) Scanning electron microscope (SEM) images show microchannels printed at a constant height, with widths ranging from 1 pixel (34.4 μm) to 9 pixels (309.6 μm). Channels printed on the DLP printer using IPA-wash resin exhibited shape distortion at widths of 3 pixels (103.2 μm) or less, while wider channels retained linear profiles. (B) On the 34.4 μm LCD printer with the same IPA-wash resin, channels narrower than 3 pixels also displayed slight edge rounding and a "cometing" artifact, though larger channels showed no significant defects. (C) Channels printed using the DLP printer closely matched their designed widths across the tested range. In contrast, LCD-printed channels were consistently oversized but followed a strong linear correlation with increasing pixel width. (D) For channel depth, the LCD printer produced measurements that scaled linearly with design dimensions at all tested layer counts, while the DLP printer maintained depth accuracy only for channels 3 layers deep (60 μm) or greater. [1]

Several of these analyses included in the original publication are not highlighted in this dissertation. Instead, I will be highlighting the **"capillaric circuits for preprogrammed instrument-free liquid delivery"**, my main contribution to this work as a coauthor.

Capillaric circuits were created to evaluate the functionality of the 3D printed components and demonstrate a range of passive fluidic features capable of self-driven, low-instrumentation liquid delivery [2, 3]. Following fabrication, the devices were washed, air dried, and post-cured. The completed chips were then treated with plasma and sealed

using a hydrophobic adhesive film (ARseal 90697, Adhesives Research, Glen Rock, PA, USA). To visualize fluid flow through the circuits, a solution of food coloring (13% v/v in water) was used. A piece of nonwoven cleanroom paper (AAWipes, Ann Arbor, MI, USA) served as the capillary pump and was secured to the device using a rubber band.

To demonstrate the functionality of microchannels produced using LCD-based 3D printing, we designed capillaric circuits incorporating multiple self-powered fluidic components (Figure 3.2A). These circuits were constructed to operate entirely through capillary action. CAD designs were aligned with the LCD printer's pixel grid and fabricated using water-washable resin on a 34.4 μm pixel LCD printer. The most dimensionally constrained features—such as the trigger valve, retention valve, and flow resistor—had widths ranging from 5 to 6 pixels and a consistent depth of 200 μm. Apart from minor narrowing observed in the flow resistor (Figure 3.2A-iv), the printed circuits exhibited no significant defects. Three devices were printed, subjected to plasma treatment, and tested using food dye solutions to illustrate their capability for sequential, automated liquid handling.

To assess the influence of illumination uniformity on print fidelity, we measured UV light intensity across the build areas of both LCD printers and characterized capillaric features printed at different locations on the build platform. In LCD printers, insufficient collimation of UV light can cause spatially variable exposure, resulting in inconsistent feature dimensions [4]. However, both printers showed uniform light intensity, and printed features retained consistent dimensions across the entire build plate.

Capillaric circuit function is shown in Figure 3.2B, and operates based on previously described capillary domino valve principles [2, 3, 5]. Initially, liquid is loaded into the reservoirs, where trigger valves retain fluid (Figure 3.2B-1) until the delivery sequence is activated by introducing liquid into the control channel that links the reservoirs to the capillary pump (Figure 3.2B-2). Unlike reservoirs 2, 3, and 4—which are held in place by retention valves—reservoir 1 drains immediately upon connection to the pump (Figure 3.2B-3). Once empty, the domino valve connecting reservoirs 1 and 2 opens, allowing reservoir 2 to drain (Figure 3.2B-4). This initiates a cascading effect where each subsequent reservoir empties only after the previous one has fully drained (Figure 3.2B-5,6). To evaluate reproducibility, we measured flow rates from each reservoir across three independently printed microchips (Figure 3.2C), and observed minimal variation, indicating high consistency between prints. These findings confirm that high-quality, fully functional capillaric circuits for autonomous liquid delivery can be reliably fabricated using a low-

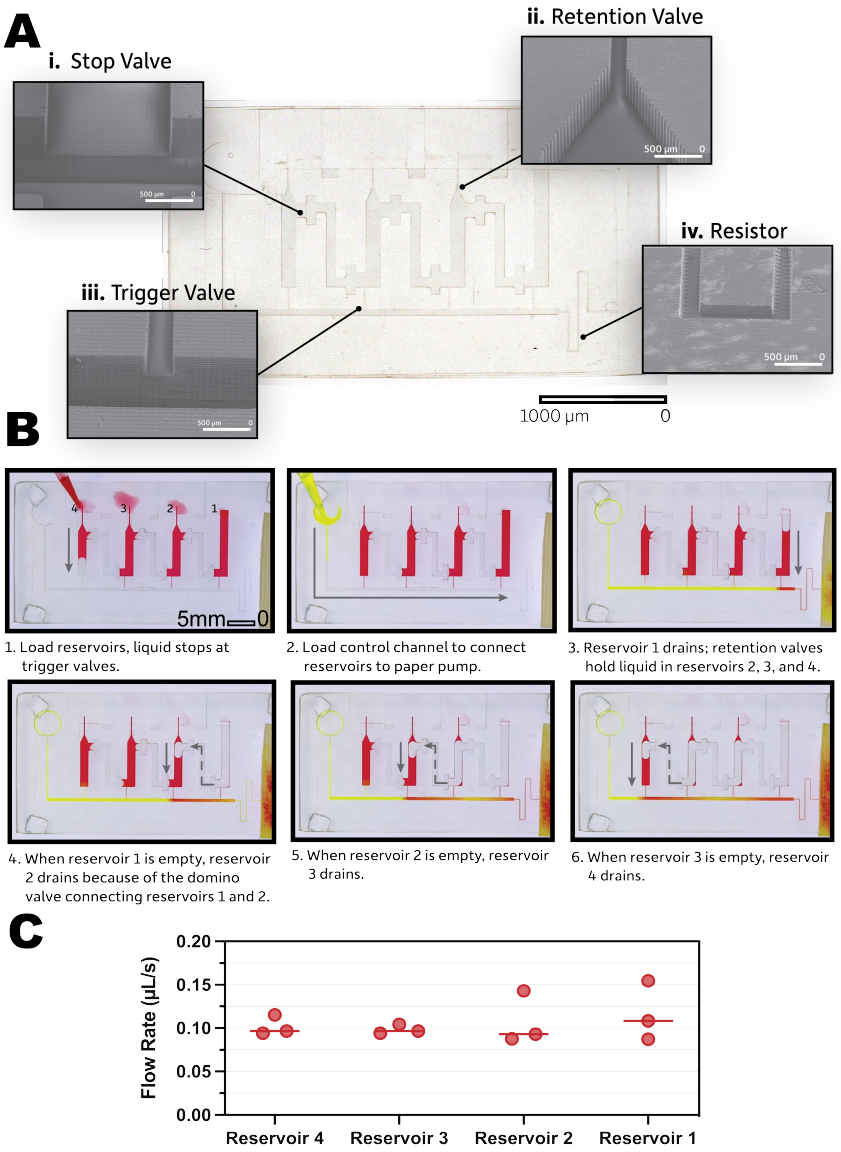

Figure 3.2: Preprogrammed sequential liquid delivery with capillaric circuits 3D-printed with low-cost, water-wash resin on an LCD printer. (A) The 3D printed circuit is shown in the center, and insets show SEM images of the fluidic components: (i) stop valve, (ii) retention valve, (iii) trigger valve, and (iv) resistor. Scale bars on SEM images are 500 μm. (B) Screenshots from Supplementary Video 1 show preprogrammed sequential liquid delivery in a capillaric circuit. The screenshots progress from filling the reservoirs and control channel (1, 2), through the sequential drainage of each reservoir (3–6). (C) Flow rates were consistent across all reservoirs and across three 3D-printed microchips. [1]

cost LCD printer.

This work provides both a practical reference and successful demonstration of low-cost LCD 3D printing for microfluidic applications. We show that it's possible to balance

printer affordability with reliable microchannel accuracy and fidelity in open microfluidic systems. A comparison between a 40 μm pixel DLP printer ($\sim$ \$18,000 USD) and a 34.4 μm pixel LCD printer ($<$ \$380 USD) revealed strong linear correlations between designed and fabricated dimensions for both platforms, with no major differences observed in surface texture or channel geometry. By systematically adjusting key LCD printing parameters—including exposure duration, light intensity, and layer height—we achieved highly accurate microfluidic features. These were evaluated for dimensional precision, surface finish, and perpendicularity, and compared across printer types. Additionally, we tested a cost-effective (\$34 USD/liter) water-washable resin with both the 34.4 μm and 22 μm LCD printers, confirming the broader applicability of our optimization strategy. This adaptable workflow could support further exploration of materials with diverse properties - such as elasticity, surface energy, optical transparency, or biocompatibility - expanding the scope of applications in biomedical research. Ultimately, this approach to low-cost microfluidic fabrication enhances accessibility and empowers a wider range of researchers to incorporate microfluidics into their work.

After publishing, we have expanded upon this work as a lab by creating an open-source protocol for printing microfluidics on a low-cost LCD 3D printer (included in the appendix).

3.4 Practical Considerations for Assembly and Integration

3.4.1 Notes on Taping

Closed capillary microfluidics are often lidded by microfluidic cover tape or PDMS [3, 5]. There are a few factors that come into play when we consider why tape has become standard practice in closed capillarics:

1. Printing channels with open faces allows them to be plasma treated for increased hydrophillicity
2. It is easy to clean open-faced channels with standard practices (solvents and compressed air)
3. Low-cost 3D printers require significant optimization to print closed features

4. Hydrophobic material/tape can encourage sustained fluid pinning

I will break down each of these factors to highlight changes I have made to capillaric fabrication to move away from tape when possible, streamlining the production process.

"Printing channels with open faces allows them to be plasma treated for increased hydrophillicity"

The contact angle of fluid with capillary channels facilitates flow [2, 6]. It is thus advantageous to adapt your chip material or working fluid to increase the driving capillaric force by decreasing the contact angle of fluid with channel walls.

Historically, plasma treating has been the primary means of increasing this contact angle [6, 7]. Plasma treating applies an unstable hydroxyl group to an open-faced chip surface. This process can change the innate contact angle of water with our 3D-printed material from $75°$ to $30 - 60°$ and is tunable by adjusting instrumentation settings like power and treatment time [8]. This process requires expensive instrumentation and specialized training, and hydrophillicity from plasma treating degrades with time (very significantly in the first 24 hours post-treatment) [7, 8]. Thus, it's not a sustainable practice for iterating capillarics with limited resources or for large-scale manufacturing and shelf-stability.

Another method of facilitating capillary flow is changing the contact angle of the fluid itself, in my case by the addition of a surfactant to water or by using fluids with innately lower contact angles (like organic solvents) [9]. This method gives you more dynamic control of contact angle since you can finely adjust liquid concentrations rather than rely on the discretized settings on a plasma treater. Additionally, surfactants are often added to enzymatic reactions, our main use case for our capillarics [3, 10, 11]. Shafique et al have demonstrated capillaric flow with PBS Tween [9] and I have adopted the use of Triton X-100 in my own devices since it is used in our typical reaction buffer for our antiretroviral medication monitoring assays [12].

Moving away from plasma treating opens up the possibility of printing closed channels directly, removing the taping/lidding process and any potential errors it may introduce. It's important to consider why it may be difficult to directly print closed channels though. That will be explored in the next subsections.

"It is easy to clean open-faced channels with standard practices (solvents and compressed air)"

Intuitively, it's easier to clean an open-faced channel that has not been lidded. You are not hindered by the lid itself and trapped resin is not susceptible to the high capillary resistance imposed by a closed channel. However, I have found an effective method to clean closed channels (Figure 3.3). A female Luer lock syringe fitting can be added to any capillaric circuit inlet to allow forced flushing on closed channels with IPA. I integrate this flushing into my fabrication process while cleaning chips, making sure to clear resin debris. Once compressed air is applied to the inlet, the low fluidic resistance of IPA allows it to easily evacuate the channels. Even though our DLP effectively prints closed channels[1], I include this feature on 3D prints for both our LCD and DLP printers to save time in the cleaning process.

"Low-cost 3D printers require significant optimization to print closed features"

Using our optimized settings for printing capillarics on low-cost 3D printers from Leong et al yielded poor quality closed features and channels that were completely blocked by unpolymerized or partially polymerized resin [1].

As a tangential effort to a project late in grad school, I attempted to recreate the work of Shafique et al to effectively print closed channels with a low-cost 3D printer rather than optimizing our current process for open-faced chips [9]. The results were enlightening, in that it was difficult to recreate the well-characterized process and subtleties of the limitations of the process were revealed when I had the work in my own hands.

The authors of this work created a custom formulation of resin that had very low viscosity, hypothetically facilitating easier evacuation of the resin from closed channels. While quite easy to produce, the resin was very expensive compared to our typical low-cost, pre-formulated resin ($\$668$ USD for raw materials, $> \$157$ USD per batch of 100 mL resin v. $\$50$ for 1L Anycubic WaterWash+ resin). It also yielded low print resolution, poor perpindicularity, and a crumbly texture that impeded its seamless integration into our manufacturing process. All procedures were followed to the letter, including the use

[1] I hypothesize that the DLP printer more effectively prints closed channels because 1) the resin used on our DLP printer is less viscous than the resin on our LCD printers, allowing it to evacuate closed channels easier, 2) the layer height of our DLP printer may be more precise with laser depth penetration v. an LCD polymerization, and 3) the build plate 'folds' into the resin by rotating about the y-axis while moving in z-on the DLP printer rather than dipping orthogonally to the z-axis on the LCD printers, facilitating better evacution of resin in between layers.

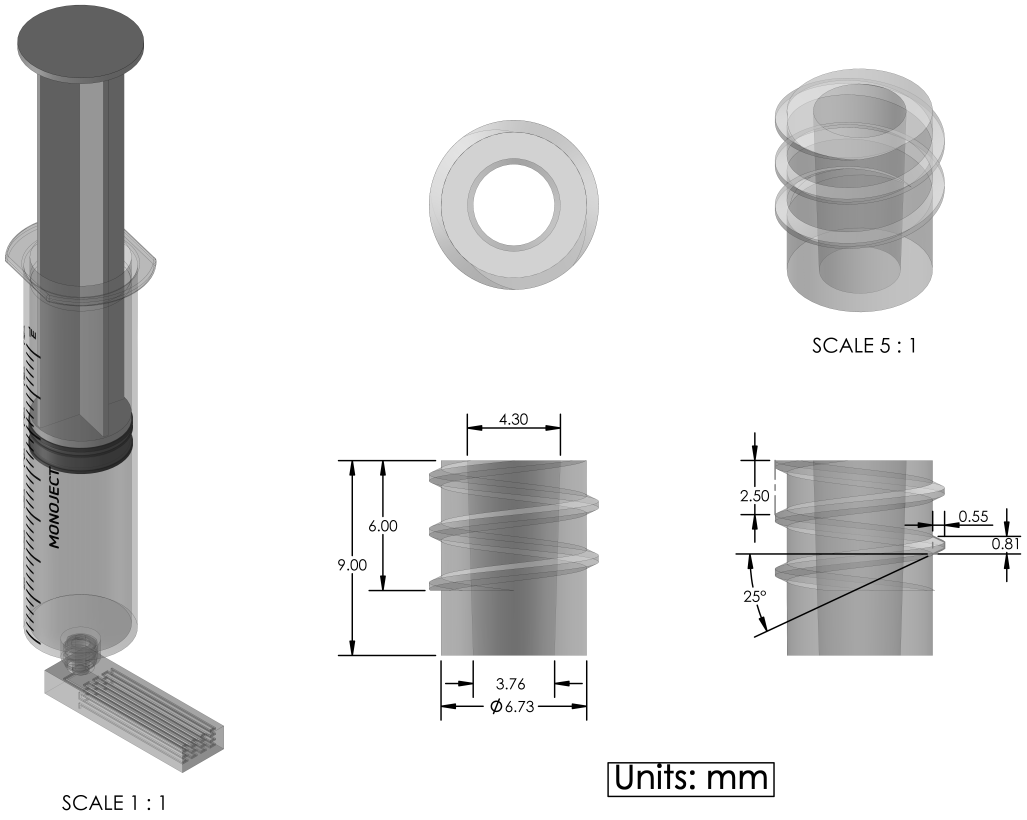

Figure 3.3: Dimensions for female Luer lock syringe fitting that can be placed on chips to easily flush closed channels. The syringe can be loaded with IPA or an appropriate resin solvent.

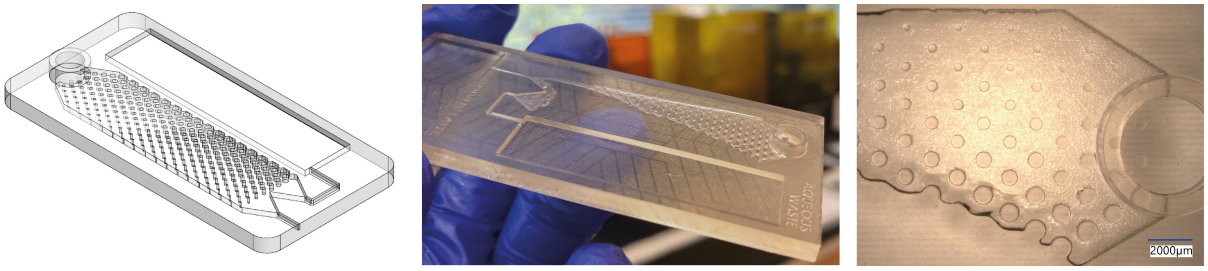

Figure 3.4: Attempted print of a closed channel with an internal pillar structure using a low-cost LCD 3D printer and Leong et al print settings [1]

of a printer purchased to specifically match the make and model of that in the original publication. The protocol is included below:

Protocol for 100 ml of PLInk [9]

Materials:

- PEGDA-250
- PETTA (pentaerythritol tetraacrylate)
- TPO (diphenyl(2,4,6-trimethylbenzoyl)phosphine oxide)
- ITX (2-isopropylthioxanthone)

Protocol:

1. Weigh out 96 g (about 90 ml) PEGDA-250 into a beaker
   - Measure PEGDA-250 by pouring in a weight boat on scale add to beaker.
   - Note that you cannot add it to the beaker directly and you must measure the weight boat on the scale or it will "error out" from too much weight eventually. This will take multiple "fills" of the weight boat and use pipette for precision as you near the amount you need. One fill of a weight boat is around 35g PEGDA-250. Carefully keep track of volume and tare scale as needed. This takes the longest to measure.
   - Density: 1.11 g/mL at 25°C

** ALL REMAINING STEPS HAPPEN IN FUME HOOD

2. Add 2 g PETTA
3. Begin stirring ingredients with a magnetic stir bar by placing one inside the beaker on top of a magnetic stir plate. (350-450 RPM)
4. Cut and prepare a sheet of light control aluminum foil to *fully cover* (except very bottom) of the beaker. It will be necessary to keep the beaker covered for the rest of the process once ITX and TPO is added.
5. Add in 0.5 g TPO
6. Add 1.5 g ITX
   - Add to the beaker, ensuring to scrape out excess, and cover with foil as soon as possible

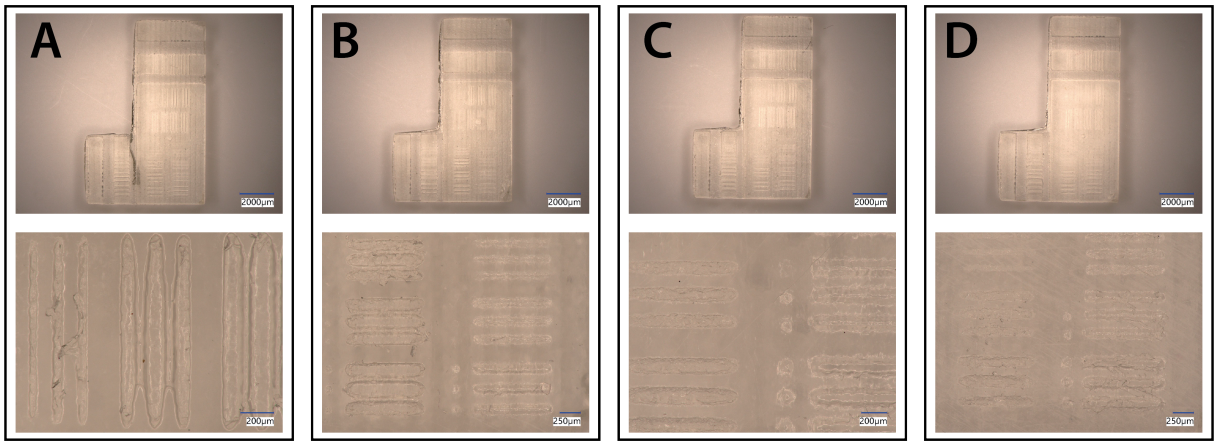

Figure 3.5: Results of PLInk protocol with minor optimizations

7. Continue to mix for 2 h then store at room temperature in an amber, opaque bottle
   - Let TPO dissolve properly first, stirring up to 500 RPM. For ITX, achieved complete dissolution with 700 RPM.

	A	**B**	**C**	**D**
Layer height (mm)	0.02	0.02	0.02	0.02
Exposure time (s)	1.5	2	1.5	1.5
Bottom exposure time (s)	10	10	10	10
Bottom lift distance (mm)	3+3.9	3+3.10	3+3.9	3+3.9
Lift distance (mm)	3+4	3+5	3+4	3+4
Bottom retract distance (mm)	5.4+1.5	5.4+1.6	5.4+1.5	5.4+1.5
Retract distance (mm)	5.5+1.5	5.5+1.6	5.5+1.5	5.5+1.5
Bottom lift speed (mm/min)	65+320	65+320	50+320	65+320
Lift speed (mm/min)	65+320	65+320	50+320	65+320
Bottom retract speed (mm/min)	210+90	210+90	210+90	80+90
Retract speed (mm/min)	210+90	210+90	210+90	80+90
Printer	Elegoo Saturn 3 Pro	Elegoo Saturn 3 Pro	Elegoo Saturn 3 Pro	Elegoo Saturn 3 Pro
Resin	PLInk	PLInk	PLInk	PLInk

Table 3.1: Print settings for Figure 3.5

A related study from the same group has have made strides to find a solution to printing closed channels on LCD printers but it was most efficient to our iteration process to

move to our more expensive 3D-printer [13]. We are still awaiting an easily translatable approach to printing closed channels on low-cost 3D printers.

"Hydrophobic material/tape can encourage sustained fluid pinning"

Pinning features are imperative to flow control in capillarics [2, 6]. Stop valves are often constructed with a two-level geometry in which the only colinear contact of the fluid with a channel wall is on the top face of the channel: hydrophobic cover tape or PDMS [6, 14]. This dependency on the hydrophobicity can be avoided by using stronger constructions of stop valves (3D geometries or large divergent angles discussed in the previous chapter) but it can also be leveraged to create selectively hydrophobic channels. By combining 3D-printed/plasma treated open-faced chips with layer-by-layer constructed hydrophobic channels made of patterning tape, I demonstrated a domino circuit that strongly discourages leakage of fluid into pneumatic channels.

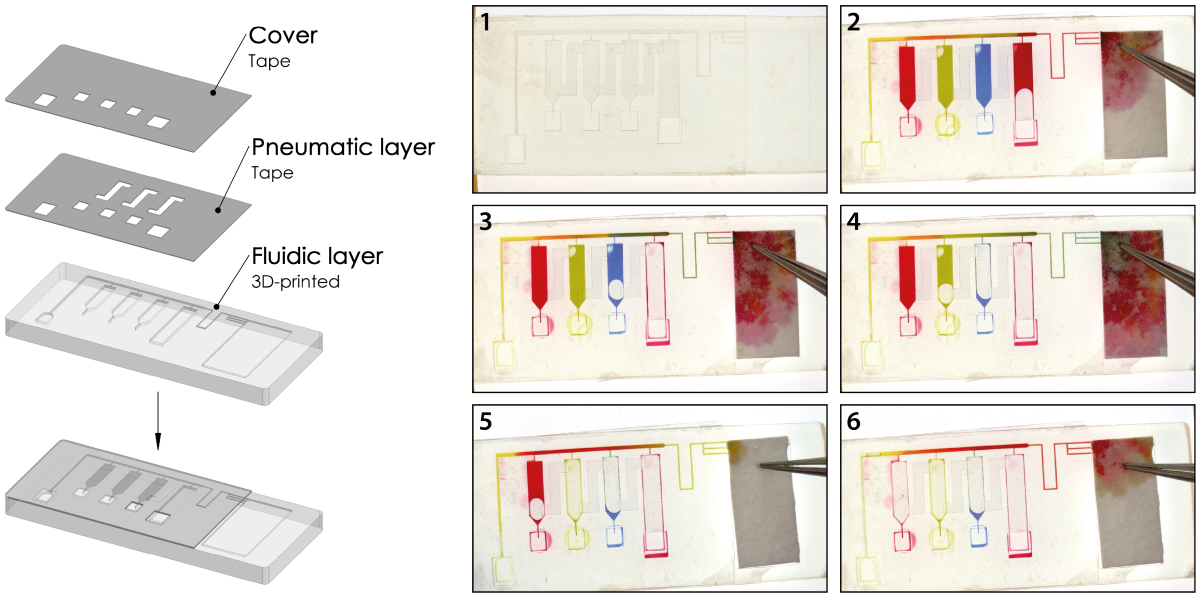

Figure 3.6: Two-layer domino valves constructed with patterned cover tape for selective hydrophobicity

The included figure shows my first iteration of domino valves created in the Ọlánrewájú Lab. The device was not optimized past minimum functionality but serves as a proof of concept of a two-level domino circuit with an alternative to PDMS [15]. To use the design for future applications, modifications to the design would be made to avoid bubble formation in initial filling of reservoirs, properly connect the paper pump to the device, and minimize diffusion of reservoirs into the main channel (among other things).

Tape patterning was introduced in our lab for this process but has become a useful tool for custom patterning of thin materials. An SOP for high resolution material patterning with a low cost craft cutter is included in an appendix. This work was inspired by the protocol included in the supplemental information from Taylor et al [16].

3.4.2 Capillary Pumps

Capillary pumps determine how far and how fast a microfluidic system can run autonomously. For accessible fabrication, they must be easy to make, scalable, and robust.

Olanrewaju et al provide the following condition regarding pumps in capillaric circuits [6]:

> "Capillary pumps need to ensure a steady flow rate in CCs. To ensure a steady flow rate, capillary pumps should provide a constant, predetermined capillary pressure regardless of filling level."

In summary, capillary pumps can help drive flow and evacuate waste from a microfluidic circuit but must not add too much fluidic resistance.

Among the most common forms are tree line pumps [6], high-surface area gyroids [8], pillar structures [17, 18], and nitrocellulose membranes [5]. In this section, I will present some design innovations to easily interface capillary pumps with 3D-printed capillaric circuits[2].

3.4.2.1 Paper Pumps

Ensuring a good connection between paper and a circuit is crucial to maintain a steady flow rate. There are many ways to achieve this including prewetting, holding the paper to the outlet with tweezers, securing the paper with a rubber band or clip, etc. but some of these methods are tedious or subject to disturbances in connection to the chip. I have included a standard attachment I create for my capillaric circuits (Figure 3.7). The nitrocellulose membrane (paper) is use-case specific (e.g. a lateral flow strip for colorimetric assays, paper with low auto-fluorescence for imaging, a cleanroom wipe for frugal flow visualization, etc.).

[2]It is important to note the specificity of the term 'capillary pump' as it's used in this section. In the previous chapter, the 'pump' was a shorthand for the penultimate small channel that's connected to a 'capillary pump' as a final destination for waste. These regions don't have to be mutually exclusive (e.g. the pump region could be entirely covered by paper).

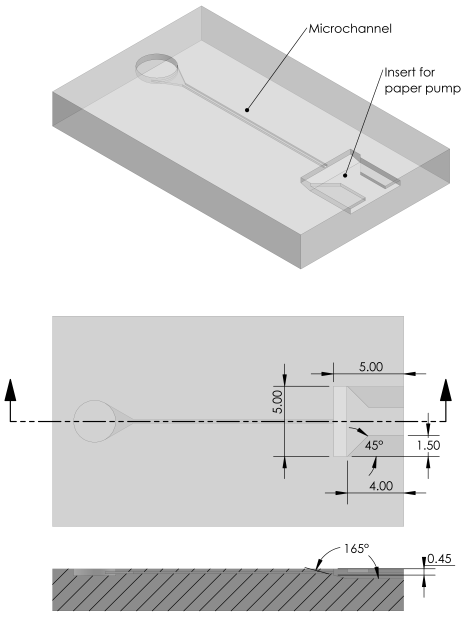

Figure 3.7: Example geometry for attaching a paper pump to the outlet of a chip

3.4.2.2 Pillar Pumps

I have also employed a micropillar array as a capillary pump, inspired by the work of Rocca et al [17]. The original device was cleanroom fabricated with pillars <50 x <50μm and a reservoir depth of 50 μm. I translated this work to a 3D-printed scale with 200 x 200 μm pillars and a 210-420 μm deep reservoir. This maximizes the waste volume that can be held in the pump and is printable by DLP and low-cost LCD 3D printers. Additionally, I find it easier to CAD model than complex 3D-gyroids so it has become my preferred printable capillary pump.

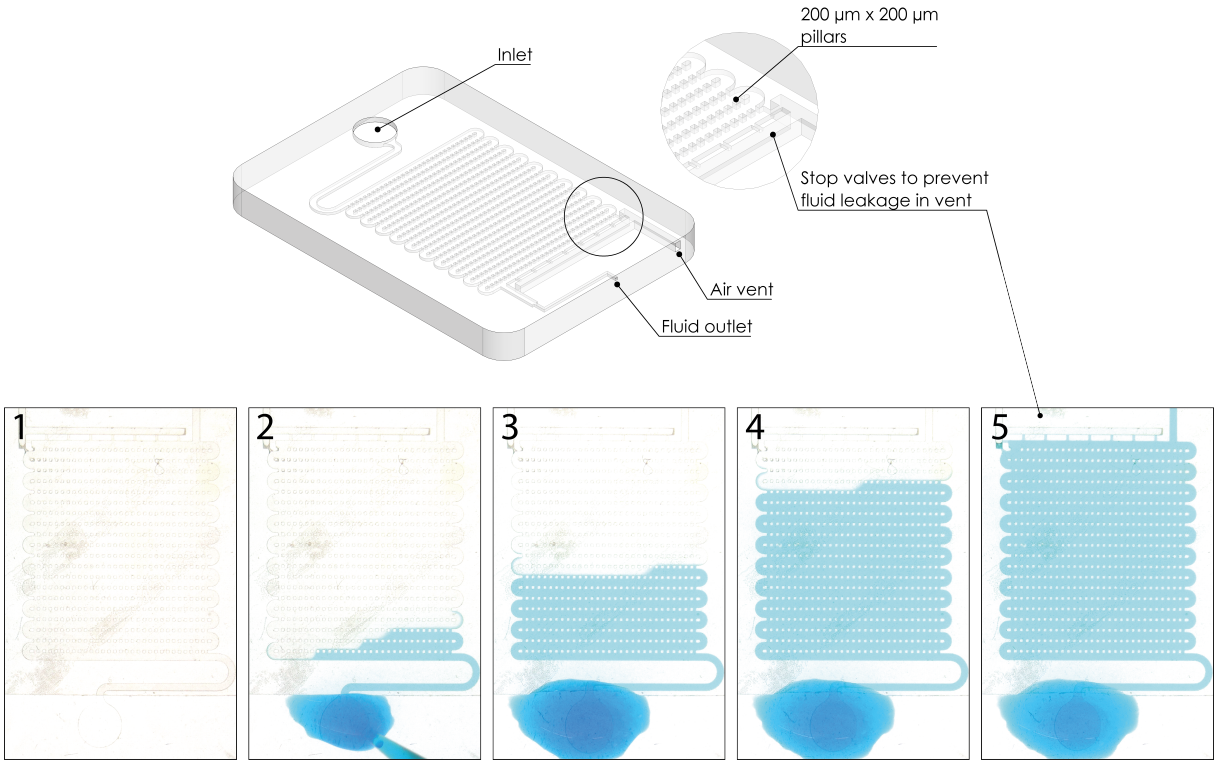

Figure 3.8: Caption

3.4.3 Design Guidance for Interfacing Parts

Because of the accessibility of LCD printing technology, hobbyists who use these machines for creative endeavors have become a huge resource for my troubleshooting. This section is a conglomeration of tips I have gathered from this community on social media that have been adapted to suit our scientific process. My design suggestions described below are empirically tested (and perhaps rough around the edges) but were imperative to prototype designs described in the chapter that follows. As a grad student, mechanical engineer, and arts and crafts enthusiasist, I could not rest easy without including this section (even though it has little chance of ever making it to the main body of a manuscript).

3.4.3.1 Elastic Resin

Our workhorse resins are Clear Microfluidics Resin V7.0a (CADworks3D, Toronto, ON, Canada) and Water-Wash Resin+ (AnyCubic, Shenzhen, Guangdong, China) for the DLP and LCD printers respectively. However, 3D-printable resin is generally very brittle.

When projects demanded interfacing of brittle resin with commercially manufactured materials (or even other 3D-printed parts), minor compression and expansion would cause part failure and cracking. Cracking can be mediated by increasing wall thicknesses of parts but we are often either 1) space-constrained where wall thicknesses have a low maximum value or 2) we are attempting to make an air tight interface that requires some material pliability.

AnyCubic, the manufacturer of a few of our in-lab printers, distributes ABS-like resin and resins with purported toughness and strength that is superior to the Water-Wash Resin+. However, we typically prefer our resins to be optically clear for flow visualization. Within the past few months of writing this, I have started to experiment with SuperElastic 3D Printer Resin (3DMaterials, Dongan-gu, Anyang-si, Gyeonggi-do, Korea). The material is reported to have similar properties to silicone with seamless integration into our low-cost LCD 3D printers. Using the companies recommended settings for printing, I was able to print microscale 3D structures with high fidelity (although I never formally characterized the performance). Per the suggestions of a Reddit thread of 3D-printing hobbyists, the resin can also be used in low concentrations to add flexibility to the Water-Wash Resin+. I currently use a 90:10 w/w mixture of Water-Wash Resin+:SuperElastic 3D Printer Resin (mixed at 700 rpm for 5 minutes) to print reusable parts that can create an airtight seal with injection molded polypropylene parts when properly toleranced.

To estimate exposure time of this hybrid resin to achieve high fidelity parts, I conducted this simple linear transformation: $(\text{Hybrid exposure}) = 0.9 \times (\text{Water-Wash exposure}) + 0.1 \times (\text{SuperElastic exposure})$

There is certainly room for proper characterization of this resin as it relates to capillary microfluidics but it has been a very effective tool for prototyping.

3.4.3.2 Tolerancing

I have collected some anecdotal rules of thumb regarding tolerancing of 3D-printed parts. They are tried and true in the sense that they work in my hands to mate parts and haven't failed me yet.

- Minimum wall thicknesses for 3D structures should be between 0.8 and 1.2 mm
- Mated features with 0.0 to -0.1 mm tolerance have a snug fit that can be subject to damage if brittle resin is used[3]

[3] All tolerances mentioned are intended to describe unilateral differences between a printed part and its

- Mated features with -0.2 mm tolerance easily fit together and come apart. Not snug enough to cause part damage but snug enough to minimize misalignment.
- Mated features with +0.2 to +0.1 mm tolerance have a snug to airtight fit (only works for hybrid or flexible resin)
- Snap fit features are very difficult to create with UV resin so I typically opt for threaded connections (e.g. luer lock syringe flushing in Figure 3.3) or press fits.
- To incorporate a gasket or O-ring for a more resilient or pliable mate (discussed in detail in a later section), I typically compress the gasket materials by subtracting 0.1 to 0.2 mm from the thickness between parts.

One example of these tolerancing principles in practice can be seen in Figure 3.9. Using Water-Wash Resin+, I created a fitting to directly connect a BD Microtainer blood collection tube to the two-layer domino circuit in Figure 3.6. I created a true-to-size model of the commercially available BD collection tubes using calipers. I then created a negative mold of the tube that was 0.2 mm larger than the true dimensions for all internal features at the entrance of one of the fluid reservoirs. The BD Microtainer could then be easily inserted into the designed fitting without any compression or expansion of the 3D-printed material. This connection did not require an airtight fit.

3.5 Conclusion

In this chapter, we demonstrated how low-cost 3D printing technologies can be leveraged to fabricate complex, functional capillaric systems, expanding access to microfluidic tools beyond traditional cleanroom environments. By systematically evaluating printer fidelity and resin compatibility, we established an optimized workflow for producing open-channel microfluidics on LCD-SLA platforms that are 40–50 times more affordable than commercial DLP printers. We extended this approach to fabricate key capillaric elements—phaseguides and self-coalescence modules (SCMs)—that have historically required high-resolution cleanroom fabrication. These 3D-printed features performed comparably to their cleanroom counterparts, enabling precise control of capillary pinning lines and unlocking functions such as sequential valving, guided reservoir filling, and pulse-shaped reagent delivery.

intended mate's true dimensions.

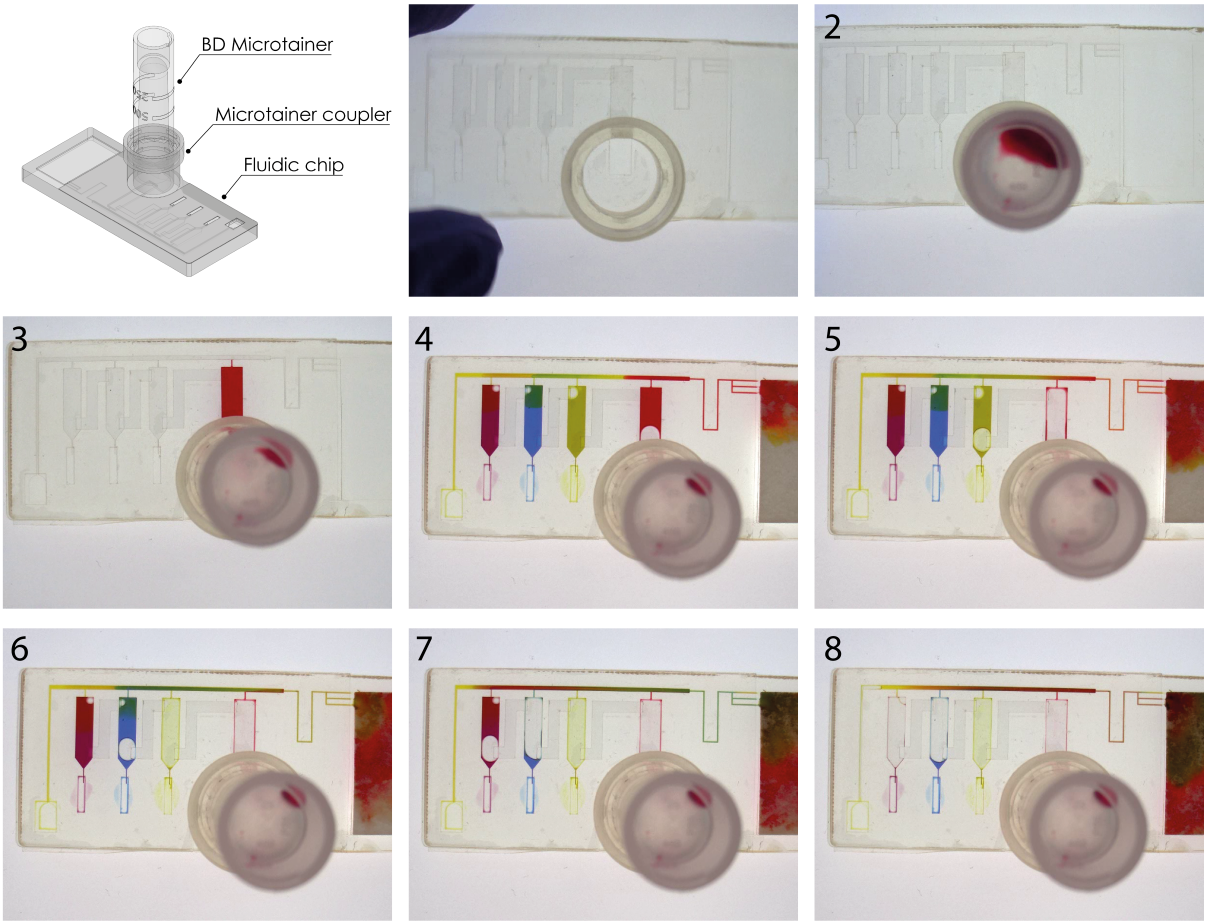

Figure 3.9: Two-layer domino valve with direct sample tube connection

Crucially, we demonstrated the scalability and adaptability of these components, showing that both geometry and volume can be tuned without compromising functionality. Integration of SCMs into complete capillaric circuits further enabled inline reagent dilution and multi-step liquid delivery without external instrumentation. The design freedom of 3D printing also allowed for alternative interfacing strategies, the use of elastic resin blends for improved sealing, and a shift away from plasma treatment and taping through clever material and design choices.

Altogether, this work provides a foundational toolkit for rapidly prototyping modular capillaric devices in resource-limited settings. By eliminating major barriers to fabrication and integration, we contribute to the broader democratization of microfluidics, fostering innovation in decentralized diagnostics, biochemical automation, and user-centered device design.

These fabrication techniques not only enable the replication of existing features,

but also open the door to entirely new classes of fluidic elements. The next chapter explores how 3D printing can extend the capillarics toolbox to include phaseguides and self-coalescing modules, once thought limited to cleanroom manufacturing.

References

1. Leong, K. M. *et al.* Democratizing Access to Microfluidics: Rapid Prototyping of Open Microchannels with Low-Cost LCD 3D Printers. *ACS Omega,* acsomega.4c07776. ISSN: 2470-1343, 2470-1343 (Nov. 1, 2024).
2. Safavieh, R. & Juncker, D. Capillarics: pre-programmed, self-powered microfluidic circuits built from capillary elements. *Lab on a Chip* **13,** 4180. ISSN: 1473-0197, 1473-0189 (2013).
3. Olanrewaju, A. O., Robillard, A., Dagher, M. & Juncker, D. Autonomous microfluidic capillaric circuits replicated from 3D-printed molds. *Lab on a Chip* **16,** 3804–3814. ISSN: 1473-0197, 1473-0189 (2016).
4. Zhu, Z. Freeform Optics for Achieving Collimated and Uniform Light Distribution in LCD-Type UV-Curable 3D Printing. *IEEE Photonics Journal* **15,** 1–7. ISSN: 1943-0655, 1943-0647 (Aug. 2023).
5. Yafia, M. *et al.* Microfluidic chain reaction of structurally programmed capillary flow events. *Nature* **605,** 464–469. ISSN: 0028-0836, 1476-4687 (May 19, 2022).
6. Olanrewaju, A., Beaugrand, M., Yafia, M. & Juncker, D. Capillary microfluidics in microchannels: from microfluidic networks to capillaric circuits. *Lab on a Chip* **18,** 2323–2347. ISSN: 1473-0197, 1473-0189 (2018).
7. Bodas, D. & Khan-Malek, C. Hydrophilization and hydrophobic recovery of PDMS by oxygen plasma and chemical treatment—An SEM investigation. *Sensors and Actuators B: Chemical* **123,** 368–373. ISSN: 09254005 (Apr. 10, 2007).
8. Karamzadeh, V., Sohrabi-Kashani, A., Shen, M. & Juncker, D. Digital Manufacturing of Functional Ready-to-Use Microfluidic Systems. *Advanced Materials* **35,** 2303867. ISSN: 0935-9648, 1521-4095 (Nov. 2023).
9. Shafique, H. *et al.* High-resolution low-cost LCD 3D printing for microfluidics and organ-on-a-chip devices. *Lab on a Chip* **24,** 2774–2790. ISSN: 1473-0197, 1473-0189 (2024).

10. Bergeron, S., Laforte, V., Lo, P.-S., Li, H. & Juncker, D. Evaluating mixtures of 14 hygroscopic additives to improve antibody microarray performance. *Analytical and Bioanalytical Chemistry* **407,** 8451–8462. ISSN: 1618-2642, 1618-2650 (Nov. 2015).

11. Cesaro-Tadic, S. *et al.* High-sensitivity miniaturized immunoassays for tumor necrosis factor ? using microfluidic systems. *Lab on a Chip* **4,** 563. ISSN: 1473-0197, 1473-0189 (2004).

12. Singh, M. A. *et al.* Rapid Enzymatic Assay for Antiretroviral Drug Monitoring Using CRISPR-Cas12a-Enabled Readout. *ACS Synthetic Biology* **14,** 510–519. ISSN: 2161-5063, 2161-5063 (Feb. 21, 2025).

13. Karamzadeh, V. *et al.* High-Resolution Additive Manufacturing of a Biodegradable Elastomer with A Low-Cost LCD 3D Printer (Adv. Healthcare Mater. 9/2024). *Advanced Healthcare Materials* **13,** 2470062. ISSN: 2192-2640, 2192-2659 (Apr. 2024).

14. Cho, H., Kim, H.-Y., Kang, J. Y. & Kim, T. S. How the capillary burst microvalve works. *Journal of Colloid and Interface Science* **306,** 379–385. ISSN: 00219797 (Feb. 2007).

15. Olanrewaju, A. *3D-printed capillaric circuits for autonomous liquid delivery* PhD thesis (McGill University, 2017).

16. Taylor, A. W. & Harris, D. M. Optimized commercial desktop cutter technique for rapid-prototyping of microfluidic devices and application to Taylor dispersion. *Review of Scientific Instruments* **90,** 116102. ISSN: 0034-6748, 1089-7623 (Nov. 1, 2019).

17. Rocca, M. *et al.* Rapid quantitative assays for glucose-6-phosphate dehydrogenase (G6PD) and hemoglobin combined on a capillary-driven microfluidic chip. *Lab on a Chip* **21,** 3573–3582. ISSN: 1473-0197, 1473-0189 (2021).

18. Safavieh, R., Tamayol, A. & Juncker, D. Serpentine and leading-edge capillary pumps for microfluidic capillary systems. *Microfluidics and Nanofluidics* **18,** 357–366. ISSN: 1613-4982, 1613-4990 (Mar. 2015).

4 | Expanding the Capillarics Toolbox: 3D-Printed Microfluidic Phaseguides and Self-Coalescence Modules

4.1 Abstract

Capillarics are microfluidic circuits that are assembled from individual fluidic elements, powered by surface tension forces encoded by microchannel geometry and surface chemistry, and enable instrument-free pre-programmed automation of multi-step liquid handling processes. 3D printing has recently transformed capillarics by enabling rapid and cost-effective prototyping, provided addition geometric degrees of freedom in multi-level fabrication, and facilitated new design paradigms with greater capabilities than traditional cleanroom fabrication. Despite widespread interest in 3D printing and development of custom high-resolution stereolithography printers for microfluidic applications, fluidic elements that require precise and tunable control over capillary pinning lines – such as fluidic phaseguides and self-coalescence modules (SCMs) – have so far only been manufactured with centralized and expensive cleanroom methods. Not only does this limit access to versatile capillaric features to only well-resourced settings, but it also slows innovation and widespread application of these fluid handling technologies. Here we expand the toolbox of 3D-printed capillarics to include phaseguides and SCMs, demonstrating their potential for precise instrument-free control over multi-step liquid handling and reagent rehydration. We employed benchtop stereolithography printers to prototype (up to 50X) scaled-up phaseguides and SCMs and integrated them into a capillaric circuit for inline reagent reconstitution, dynamic fluid control, and sequential drainage. We showcased scalable designs, customizable geometries, and robust self-coalescing flow for larger liquid volumes – up to 50 μL compared with 1.25 μL in cleanroom-fabricated SCMs. This work represents a significant advance in democratizing access to microfluidics, with

potential for broad applications in diagnostics, assay automation, and organ-on-chip systems.

4.2 Introduction

This chapter includes elements adapted from the manuscript in revision:

ii. **"Expanding the capillarics toolbox: 3D-printed microfluidic phaseguides and self-coalescence modules"**, Cosette Craig, K. Leong, C. Lin, M. Chang, A. Olanrewaju. *tbd*, 2025. https://doi.org/10.1101/2024.12.21.629531

Despite advancements in the 3D-printing of capillarics, key fluidic elements that rely on precise and tunable manipulation of capillary pinning lines (CPLs) - like phaseguides and self-coalescence modules (SCMs) - have so far been primarily prototyped with traditional cleanroom fabrication. This is because features like phaseguides and SCMs are traditionally thought to require high resolution features (down to 5 μm wide) with very smooth surfaces and perpendicular walls to prevent disruption of the capillary pinning line (CPL), which are not readily achievable using commercially available benchtop 3D-printers [1].

Phaseguides offer precise control over liquid advancement by strategically altering capillary pressure, thereby tackling the crucial challenges of priming behavior and sample retrieval in intricate channel networks [2]. Rails patterned onto substrates dictate the cross-sectional air-fluid interface to control fluid direction, overflow, and filling/emptying patterns. After their initial demonstration in 2011, phaseguide-based microfluidic systems have become widely used, with applications in 3D cell culturing for organ-on-a-chip (OoC) systems [3–15], rapid point-of-care diagnostics [16–20], RNA extraction [21, 22], electroextraction [23], and magnetic bead-based assays [24]. Outside their utility in controlling liquid priming, phaseguides have also been applied for passive valving and execution of elaborate pre-programmed liquid routing [25].

SCMs contain a patterned phaseguide-like feature in a reservoir midplane that directs flow to partially fill a space then fold in on itself, or self-coalesce [1]. When reagents are spotted and dried in an SCM, this characteristic doubling-back of flow reconstitutes dry reagents in highly tunable pulses without shear-induced accumulation of reagents at the fluid front. SCMs have been used to automate isothermal DNA amplification assays [1], bead-based immunoassays for troponin I detection in human serum [26], and enzymatic

detection of glucose-6-phosphate dehydrogenase (G6PD) [27]. These applications leverage the precision, modularity, and multiplexing made available by capillarics to integrate precise sample and reagent delivery. Recent work has sought to transfer SCMs to more rapid and accessible manufacturing with inexpensive laser-cut 'sticker' microfluidics for reagent rehydration,37 but this approach required multiple manual steps for device assembly and did not integrate the CPL with additional fluidic elements like vents and stop valves that often require high-precision fabrication, thereby precluding integration within capillaric circuits and downstream applications.

In this work, we expand the portfolio of 3D-printed capillarics to include phaseguides and SCMs. We leveraged the degrees of freedom in microchannel geometry and multi-level channel heights offered by 3D-printing to demonstrate robust and functional 3D-printed phaseguides and SCMs scaled up to 50X compared with conventional cleanroom fabrication. We demonstrated a capillaric circuit with an integrated SCM, showcasing the ability to control capillary pinning lines and automate complex tasks including dilution and pre-programmed multi-step liquid delivery, without external instrumentation.

4.3 Materials and Methods

4.3.1 Materials

Clear Microfluidics Resin V7.0a (CADworks3D, Toronto, ON, Canada) was used to optimize capillary pinning line features and Water-Wash Resin+ (Anycubic, Shenzhen, Guangdong, China) was used to demonstrate a multistep capillaric circuit utilizing a 3D-printed SCM. Isopropanol for chip post-processing and amaranth dye for dried reagent spotting was sourced from Sigma-Aldrich (Burlington, Massachusetts, USA). Colored food dyes (Watkins, Winona, Minnesota, USA) were employed for flow characterization of liquid reagents.

4.3.2 Proof-of-concept chip fabrication via 3D-printing

We 3D-printed phaseguides and SCMs using a DLP-SLA printer (CADWorks Profluidics 285D) using Clear Microfluidics Resin V7.0a (CADworks3D, Toronto, ON, Canada). Phaseguides, SCMs, and connected microfluidic channels were designed on SolidWorks (Waltham, Massachusetts, USA) and exported as Standard Tessellation Language (STL)

and sliced to 30 μm layers via the CADWorks Utility 6.44 slicer (CADworks3D, Toronto, Ontario, Canada).

The DLP-SLA 3D printer used in our demonstrations has a manufacturer-reported resolution of 20–50 μm in the x- and y-axes but empirical testing shows that consistently high-quality features that match designed dimensions must be closer to 150 μm[10]. Factors affecting this minimum resolution include light diffusion, which can inadvertently cure optically clear resin, and minimization of aliasing due to the printer's pixel grid. Although smaller features can be achieved with specialized or custom-built printers, our current setup meets the necessary specifications for pinning functionality. Thus, while printing smaller features is technically possible, the additional effort is unnecessary for our current application.

4.3.3 Capillaric circuit fabrication via low-cost LCD 3D-printing

Chips fabricated for capillaric circuit demonstrations (Fig. 6) were printed using an Anycubic Mono X 6K LCD stereolithography printer (Anycubic Mono X 6K), a commercially-available, low-cost LCD printer previously characterized by Leong et al[10]. The Chitubox Basic 1.9.5 slicer (Chitubox, Shenzhen, Guangdong, China) was utilized to prepare STL files for 20 μm-layer printing on the Anycubic Mono X 6K.

4.3.4 3D-printing post-processing

After printing, chips printed with CADWorks resin were cleaned with isopropanol (Sigma-Aldrich, Burlington, Massachusetts, USA) and chips printed with Anycubic WaterWash+ were washed with DI water. Chips were dried using a compressed nitrogen gun (Cleanroom World, Centennial, Colorado, USA). This washing and drying was repeated until remaining uncured resin was removed. After drying, the microchips were placed in a Formcure (Formlabs, Somerville, Massachusetts, USA) to post-cure for 1 minute.

Microchips were plasma treated with the Plasma Etch PE-25 (Carson City, Nevada, USA) at 56% power for 1 minute to achieve a hydrophilic surface for capillary-driven flow. Contact angle measurements were made on the Krüss DSA25S Drop Shape Analyzer (Krüss Scientific, Hamburg, Germany). Chips were sealed with ARseal™ 90697 microfluidic tape (Adhesives Research, Glen Rock, Pennsylvania, USA).

Our routine post-processing is currently dependent on use of microfluidic cover tape. Features are typically printed with open channels, plasma treated for hydrophilicity and

then sealed. Tape lacks the rigidity to bridge large negative features like the open reservoirs in phaseguide designs. To address this, we ensured the reservoirs were deep enough to prevent the tape from bowing and sticking to the guides.

4.3.5 Flow visualization with food dye

Food coloring (1.4% v/v in water, Watkins, Winona, Minnesota, USA) was used to test flow in the capillaric circuits. Nonwoven cleanroom paper (AAWipes, Ann Arbor, Michigan, USA) was used to wick excess liquid at the outlet of chips and as a capillary pump in the capillaric circuit demonstration in Fig. 6.

Figures 5 and 7 were prepared during revisions. For these figures, to alleviate the dependency on plasma treating, hydrophilic solutions with surfactant were prepared in water to visualize flow (0.06% Triton X-100 (9036-19-5, Sigma-Aldrich), Amaranth dye (3 mg/mL, 915-67-3, Sigma-Aldrich)).

4.3.6 Reagent deposition

For amaranth resuspension, 50 nL spots of amaranth dye (30 mg/mL) were spotted on SCMs using an Echo 525 Acoustic Liquid Handler (Beckman Coulter, Brea, CA, USA). Chips were printed to fit into a high skirt microfluidic handling frame (Microfluidic Chip Shop, Jena, Germany) with a footprint of a 1536 microtiter plate to align to a grid within the liquid handler. After spotting, chips were left to airdry at room temperature ($\sim$25°C) for at least 5 minutes before being sealed and tested.

4.3.7 Image and video capture

Dimensional characterization, image, and video capture were performed on a Keyence VH-S30B digital microscope (Itasca, Illinois, USA).

4.3.8 RGB Intensity Aggregation and Plotting via Python

To visualize and compare reconstitution profiles across experimental replicates, CSV files containing time-stamped RGB intensity data were batch-processed using a custom Python script (`scm_csv_plotter.py`). CSV files were exported from annotated videos and contained raw and normalized intensity values for each RGB channel, as well as the summed normalized RGB intensity.

The script prompts the user to select a working folder containing the CSV files and performs several automated steps: Each file is read and aligned to a shared timebase by rounding timestamps to six decimal places. Raw and normalized RGB channel intensities are inverted (subtracted from 255) to improve visual interpretability. Summed normalized RGB intensities were inverted from 765 for the same reason. Data are trimmed to the first 40 seconds post-reconstitution to capture early-stage ejection events. For each channel (Red, Green, Blue), the script computes the mean and standard deviation across all replicates and generates plots with shaded regions representing ± 1 SD. Three separate plots are generated: inverted normalized RGB intensity, inverted raw RGB intensity, and summed RGB intensity. All plots use consistent color mapping and axis limits for comparability across experiments.

The full Python script used for this analysis, along with additional contextual explanation and example output, is provided in the supplementary information.

4.4 Results

4.4.1 3D-printed phaseguides

4.4.1.1 Operating principle of phaseguides

Phaseguides are raised rails in microchannels that enable precise control over the liquid filling front. The abrupt height change near the edge of the rail imposes a pressure barrier that guides liquid along the rail before overflowing (Figure 4.1A.1). Phaseguides do not entirely impede flow and must be shorter than the depth of their housing-reservoir to allow flow to eventually progress. Phaseguide-mediated flow in reservoirs begins with fluid addition to the reservoir inlet, either by forced flow or capillarity. The advancing liquid front fills an area of low pressure until it interfaces with a phaseguide (Figure 4.1A.1). A strong Laplace pressure barrier is created by the decreased cross-sectional area of the liquid-air interface and the perpendicularity of the rail, allowing the remaining low-pressure area preceding the phaseguide to continue filling (Figure 4.1A.2). Once the area preceding the phaseguide is full and fluid is aligned with the rail, the pressure of the air-liquid interface increases by either forced flow via a pump or capillary pressure on transverse walls that drives flow in the microchannel (Figure 4.1A.3). The pinned fluid meniscus stretches, becomes unstable, and breaks at the weakest point along the phaseguide (Figure 4.1A.4). In the example shown in Figure 1A, the weakest point along

the phaseguide is at the smallest angle between the rail and the side wall. The breakpoint of the phaseguide is tunable and is determined by the inverse relationship between capillary pressure and the interfacing angle, analogous to the relationship between capillary pressure and cross-sectional dimensions in small channels1,6. After overflowing at the weakest point, fluid 'unzips' over the phaseguide since the Laplace pressure barrier has been overcome (Figure 4.1A.4). Overflowing fluid fills the next compartment of the reservoir and stops at the next phaseguide, repeating the cycle (Figure 4.1A.5). As a proof of concept, we designed and 3D-printed phaseguides that were 200 μm wide and 60 μm tall (Figure 4.1B). We also showed flexibility of designing and 3D-printing both curved and straight phaseguides. The reservoir was 12 mm x 14 mm x 180 μm for a filled total volume of 29.16 μl. Fluid was effectively pinned by the 3D printed phaseguides and priming behavior was maintained in ordered pinning-and-overflowing processes (Figure 4.1C). Reservoir filling proceeds via capillary pressure with no bubble formation in the reservoir because of the liquid routing provided by the phaseguides.

4.4.1.2 Sequential liquid delivery using phaseguides with distinct pressure barriers

Prior work with cleanroom-fabricated phaseguides established their capability to act as capillary burst valves to allow precise routing of liquids through channel networks [2]. We demonstrated phaseguide-mediated passive valving by designing and 3D-printing rails with different interfacing angles with the channel wall to pre-program distinct pressure barriers (Figure 4.2A). We used 3 different phaseguide designs to route liquid between 7 reservoirs in an arrangement that prevented bubble trapping while maintaining the desired flow sequence. All the phaseguides in this demonstration were 3D-printed with the same dimensions (200 μm wide and 60 μm tall), but with different interfacing angles with the side wall: $\theta_1 = 30°$ at all the reservoir inlets, $\theta_2 = 90°$ at the outlet of reservoir 1, and $\theta_3 = 150°$ at the outlets of reservoirs 2 through 7 (Figure 4.2B). Fluid first enters reservoir 1 and contacts the $30°$ (θ_1) phaseguide (Fig 2C.1) which has a pressure barrier that guides flow vertically into the reservoir but not laterally towards the remaining reservoirs. When the fluid reaches the outlet of reservoir 1, it reaches the $90°$ (θ_2) phaseguide which has a greater pressure barrier than θ_1. Liquid is pinned at θ_2 while overflow occurs at θ_1 guiding liquid towards the inlet of reservoir 2 (Figure 4.2C.2). Fluid is once again routed to fill reservoir 2 because of the positioning of phaseguide with θ_1 near the reservoir inlet. Liquid reaches the outlet of reservoir 2 and contacts a $150°$ (θ_3) phaseguide (Figure 4.2B.3) which has a greater pressure barrier than θ_1 and θ_2. Overflow occurs at the phaseguide

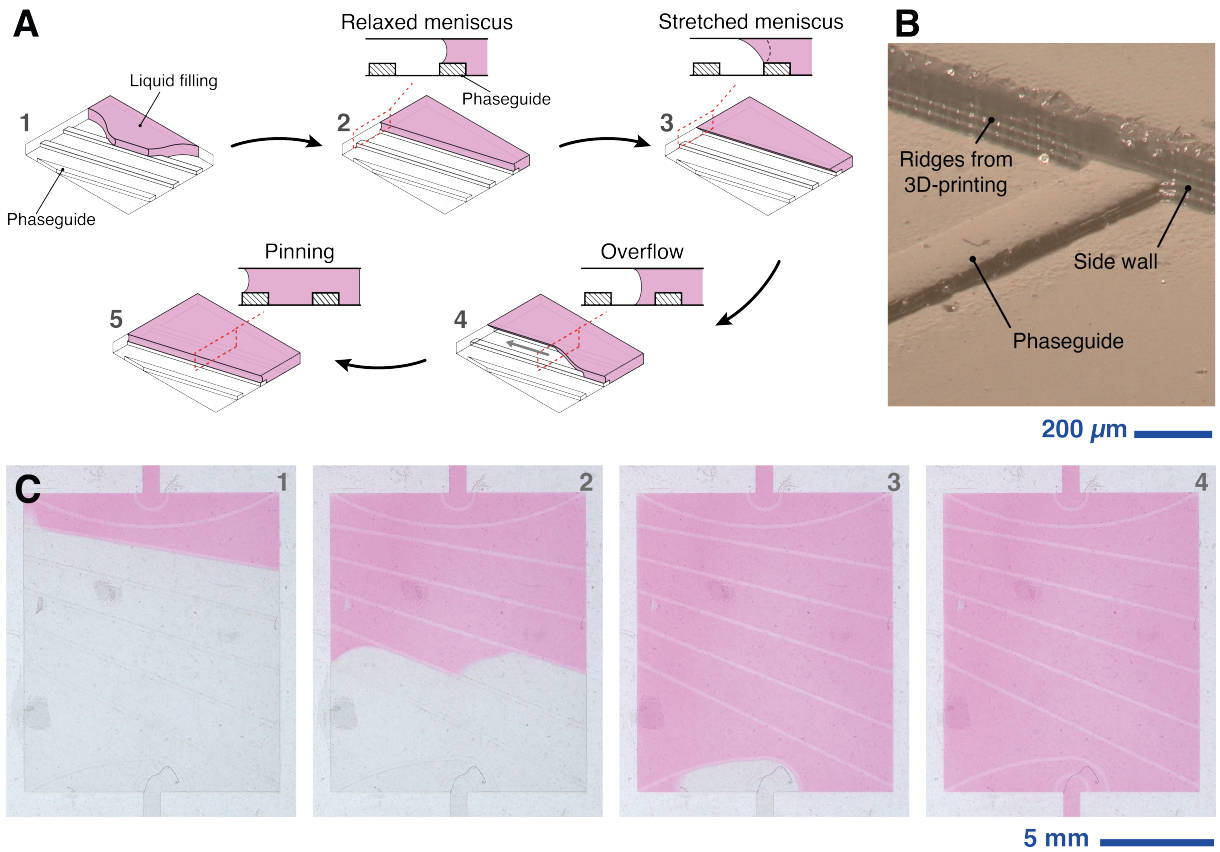

Figure 4.1: Schematic illustration of phaseguide design and operating principle. (A) Illustration of the control of a liquid filling front using phaseguides in a reservoir. 1. Fluid fills the reservoir and pins at a phaseguide, 2. The meniscus fully aligns with the phaseguide and the meniscus of the air-liquid interface remains momentarily relaxed, 3. The meniscus is stretched by capillary pressure of the fluid interfacing with the device walls, 4. The buildup of capillary pressure is significant enough to breach the phaseguide, causing overflow at the weakest point of the phaseguide, 5. Fluid fills the next segment of the reservoir and pins at the next phaseguide, repeating the cycle. (B) Image of 3D-printed phaseguide (C) Example of bubble-free filling of a reservoir using 3D-printed phaseguides (Movie S1). As laid out in the schematic, fluid pins at a phaseguide and with sufficient capillary pressure, overflows. This process cyclically repeats over all phaseguides until the reservoir is filled.

with the lowest pressure barrier (θ_1) and liquid again progresses to the next reservoir (Figure 4.2B.4). This cycle repeats for the reservoirs 3 to 7 (Figure 4.2B.5). Once all reservoirs are filled, the flow is pinned at phaseguide at θ_2 at the outlet of reservoir 1 and phaseguide θ_3 at the outlets of reservoirs 2 – 7. Again, the phaseguide with the lowest pressure barrier (θ_2) bursts first, and liquid sweeps from the outlet of reservoir 1 through the rest of the channel network to enable bubble free filling of all the reservoirs (Figure 4.2B.6).

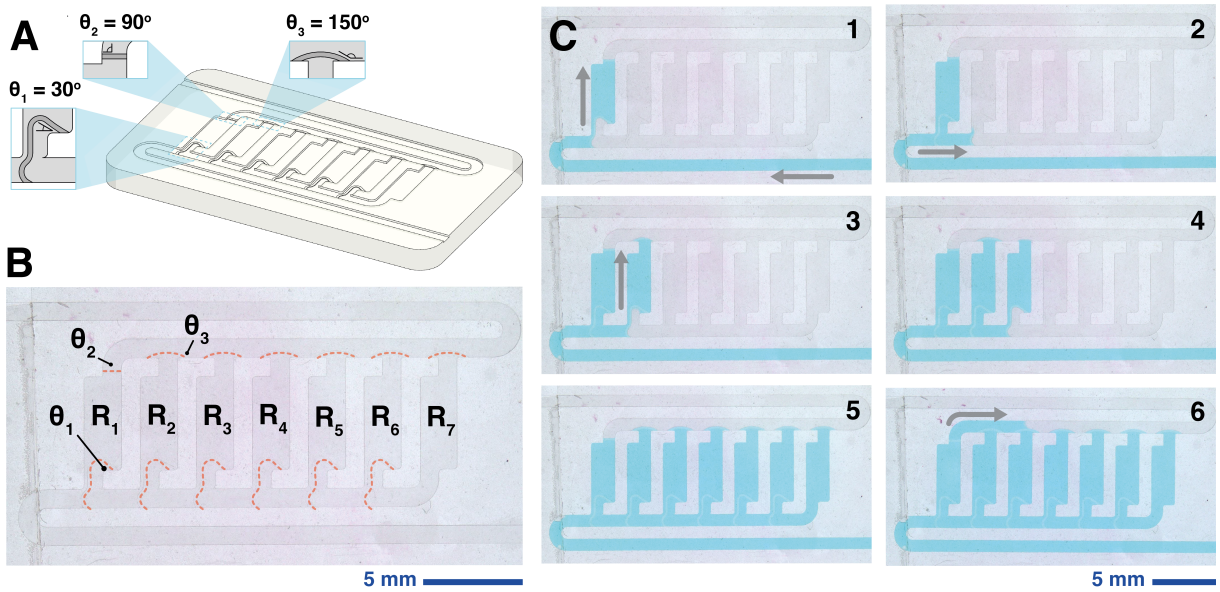

Figure 4.2: Sequential liquid delivery using phaseguides with distinct pressure barriers.(A) CAD rendering of a sequential valving network of phaseguides where the interfacing angle between the rail and the wall encodes different pressure barriers. The higher the interfacing angle the greater the pressure barrier. (B) Schematic of phaseguides, interfacing angles, and reservoirs labelled on a 3D-printed phaseguide-mediated passive valving network. Interfacing angles, θ_1 to θ_3, encode sequential filling of reservoirs from R1 to R7. (C) Demonstration of a 3D-printed valving network (Movie S2). Phaseguides can sequentially valve reservoirs in a network based on the designed stability of each inlet and outlet.

4.4.2 3D-printed self-coalescing modules (SCMs)

4.4.2.1 Key features and operation of SCMs

SCMs use phaseguides and capillary burst valves to achieve flow redirection or "self-coalescence" that enables uniform reagent rehydration and bioassay automation in microchannels[1, 26–28]. There are stopping features crucial to SCM functionality that require differentially strong pinning barriers: the leading barrier, the diversion barrier, and the vent barriers. The phaseguide (leading barrier) in SCMs creates a Laplace pressure barrier that ensures partial reservoir filling until liquid reaches a capillary burst valve (diversion barrier) at the outlet (Figure 4.3A). The diversion barrier, aided by the curled end of the leading barrier (Figure 4.3C.3), encourages flow redirection that overcomes the Laplace pressure barrier and initiates self-coalescence (Figure 4.3C.4) or "unzipping" of flow along the leading barrier. The module unzips until it reaches the end of the SCM body adjacent to the inlet (Figure 4.3C.5), where fluid is pinned by a stop valve at the vent (vent barrier), preventing leakage into the air conduit (Figure 4.3B). At this point,

the SCM body is full, and the diversion barrier becomes unstable via meniscus stretching and capillarity of the device. The diversion barrier spontaneously bursts and the flow proceeds to the outlet (Figure 4.3C.6).

3D-printed SCMs presented here rely solely on capillarity to drive flow so uncontrolled fluid migration is a crucial failure mode that must be prevented. The primary failure modes observed were short circuiting of the self-coalescence by traversing the leading barrier or obstructing reservoir filling by spreading along the back wall and plugging the air vent. Gökçe et al. added corrugations along the leading barrier to prevent short circuiting of flow to the back wall and vent [1]. We included a second set of corrugations at the interface between the back wall and the vent given the larger feature sizes (and consequently, lower pressure barrier) in our 3D-printed devices.

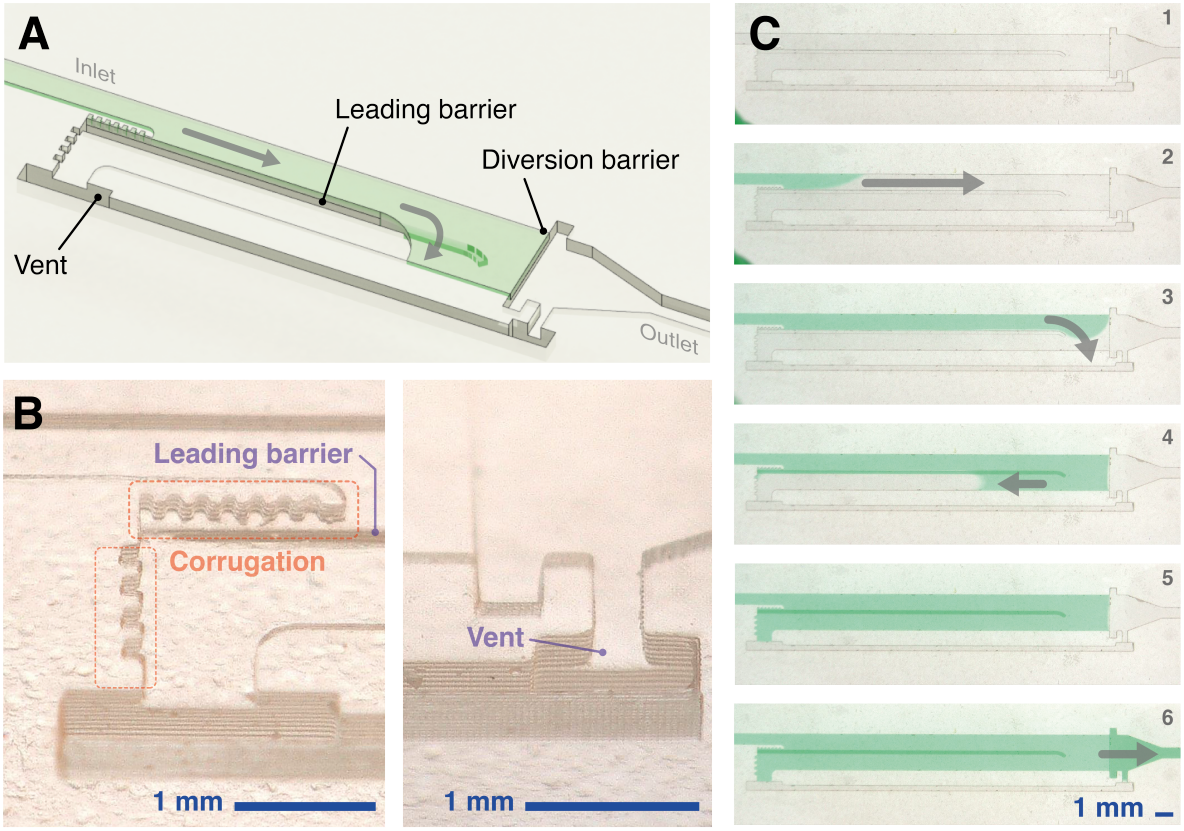

Figure 4.3: Schematic, key features, and operating principle of 3D-printed self-coalescence modules.(A) Schematic of a typical SCM that labels key features including the leading barrier, the diversion barrier, and vent and illustrates the direction of flow. Flow is guided by the leading barrier, a capillary pinning line, and redirected during filling by the diversion barrier, allowing flow to self-coalesce. (B) Zoomed images of 3D-printed SCMs highlighting additional pinning features added in 3D-printed SCMs for robust fluid pinning. (C) Demonstration of self-coalescing flow in a 3D-printed SCM.

4.4.2.2 3D-printed SCMs scaled up 50X from cleanroom fabrication

We designed SCMs according to the minimum viable dimensions using our benchtop DLP-SLA printer i.e. 30 or 50 μm minimum dimension in the z-direction and 150 μm in the x and y-directions [29]. This required scaling up of the overall device footprint and individual feature sizes, as cleanroom-fabricated SCMs have typical dimensions of 5-15 mm long, 0.5-1.5 mm wide, and 0.05 mm deep, with volumes ranging from 0.125-1.125 μl [1]. As a proof of concept, we designed 3D-printed SCMs that were 19.6 mm long, 2.0 mm wide, and 0.2 mm deep for a total volume of 8.94 μl (Fig. 4.4D). The feature that was scaled up the most in 3D-printed SCMs was the leading barrier, which was 5 μm in cleanroom manufactured devices[1] and was enlarged to 150-200 μm in our 3D-printed devices (Fig. 4.4A). The leading barrier in an SCM can be either a trench or a rail, as long as it provides a sufficient capillary pressure barrier to pin the fluid front. The key requirement is geometric interruption, not the specific shape (Fig. 4.4B).

The inlet channel and the reservoir/body of the SCM were 200 μm deep. The depths of the leading barrier, diversion barrier, and vent were 500 μm, 400 μm, and 1000 μm, respectively, to encode for different pressure barriers that control the direction of flow in the SCM. Using these dimensions, the 3D-printed SCM exhibits the unzipping or self-coalescing flow (Fig. 4.4E).

3D-printing provides additional degrees of freedom in obtaining multiple channel heights and larger volumes [30–32]. We demonstrated that SCM scaling can be applied to accommodate larger liquid volumes, either by proportionally increasing all dimensions of the reservoir (Fig. 4.4D.1-2) or by changing only the length (Fig. 4.4C). We doubled the length of SCM and kept its other dimensions constant to accommodate a 20 μl volume while maintaining self-coalescing flow (Fig. 4.4C). We also showed that we could maintain a compact footprint by adjusting the width and depth of the SCM (increased $\sim$1.5X each) to achieve the same volume doubling (Fig. 4.4D). We also scaled up the SCM volume to 50 μl, $\sim$50X the volume of cleanroom-fabricated devices, while still maintaining self-coalescing flow (Figure 4.4C). Additionally, we showed that we can arbitrarily change the shape of the capillary pinning line and the overall SCM to fit desired configurations while still maintaining precise control over the liquid filling front, as exemplified by self-coalescence in the W-shaped device (Figure 4.4E).

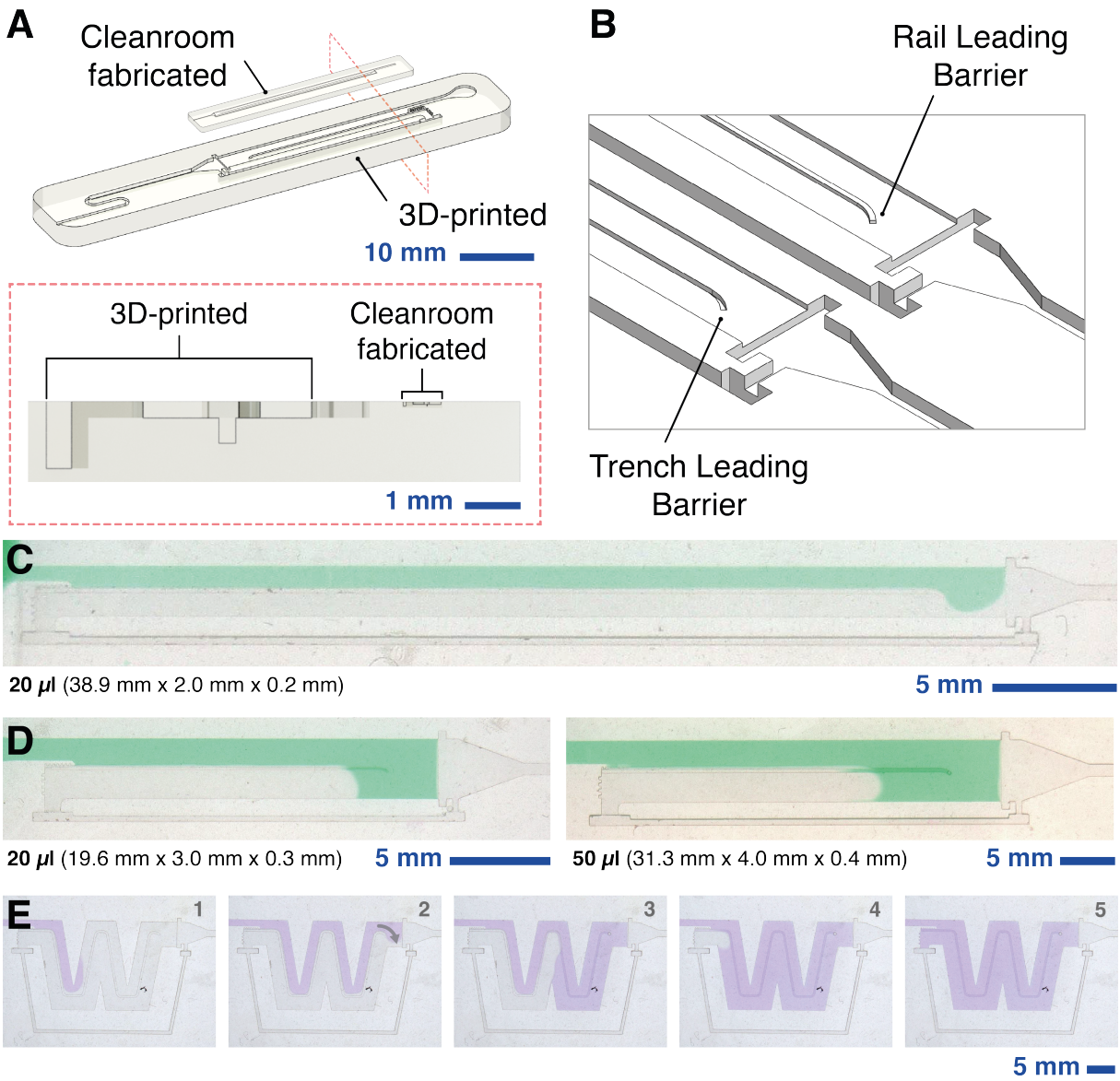

Figure 4.4: 3D printing enables adjustable channel heights and increased volumes in SCMs. Figure 4: 3D printing enables adjustable channel heights and increased volumes in SCMs. (A) Rendering depicting size comparison of traditional cleanroom-fabricated SCM and scaled up 3D-printed SCM. (B) The leading capillary barrier can be implemented as either a trench (top) or a rail (bottom), both of which effectively pin advancing fluid fronts until upstream filling is complete. (C) SCM length accommodates a 20 µL volume while preserving self-coalescing flow. (D) Width and depth of SCMs were increased with a fixed ratio to scale to 20 µl and 50 µl. (E) Arbitrarily patterned capillary pinning lines demonstrate precise control over the liquid filling front with an adaptive footprint.

4.4.2.3 Proof-of-concept reagent reconstitution using 3D-printed SCMs

Figure 4.5 shows proof-of-concept reconstitution of spotted amaranth dye in a 3D-printed SCM without shear-induced accumulation of dye occurs at the fluid front. This was achieved by precisely depositing concentrated dye droplets onto the surface of the 3D-printed SCM using an acoustic liquid handler, followed by drying at room temperature ($\sim$25°C) for ≤ 5 minutes. Fluid enters the device and is initially pinned by the leading barrier. As fluid is redirected by the diversion barrier, the leading edge becomes unstable and re-initiates flow, contacting the first dried droplet. This initiates a self-coalescing front that propagates across all spots, sequentially resuspending them (Fig. 4.5B). An experimental setup comparing self-coalescence-mediated rehydration in an SCM to uncontrolled reservoir filling is shown in Fig. 4.5A.

Unlike traditional rehydration, where reagents are swept forward and accumulate near the advancing fluid front, self-coalescence prevents shear-induced displacement. Instead, each spot is individually rehydrated and rapidly entrained into the flow. The reconstituted dye forms a characteristic "pulse" or a localized zone of high concentration that moves downstream with minimal dispersion.

Quantitative analysis of dye delivery confirms this behavior. We tracked green channel intensity across defined regions of interest (ROIs) to monitor dye movement over time (Fig. 4.5C–D). Although amaranth dye appears pink to the eye, it strongly absorbs in the green region of the visible spectrum ($\sim$500–560 nm), resulting in a measurable drop in green channel signal when present. As such, the green channel offers the greatest dynamic range for detecting dye and was used as an inverse proxy for concentration. The resulting profiles show a sharp rise and exponential decay in signal consistent with previously reported pulse-shaped delivery in cleanroom-fabricated SCMs by Gökçe et al [1].

To enhance lateral mixing and minimize dispersion effects, we incorporated short downstream serpentine channels that serve as fluidic resistors (Fig. 4.5A, right). These resistors delay flow and promote transverse diffusion across channel cross-sections, which can sharpen the trailing edge of the pulse and extend delivery time. Future work may explore how resistance magnitude, pulse width, and delivery sharpness co-vary across different SCM volumes and geometries.

In contrast, devices lacking a leading barrier (control condition) exhibited front-loaded rehydration and smeared delivery profiles (Fig. 4.5E–F). Without the SCM architecture, dried reagents were rehydrated by the advancing front and accumulated early in the channel. As a result, the green channel intensity profile was broader and less defined, with di-

minished peak amplitude and no sharp falloff (Fig. 4.5G). This side-by-side comparison highlights the functional advantage of SCM-guided reconstitution and supports its use in applications requiring controlled reagent delivery.

The preservation of self-coalescence behavior in 3D-printed SCMs, despite a 50× larger footprint than prior cleanroom-fabricated versions, demonstrates the robustness and scalability of this architecture. These results confirm that pulse-shaped reagent delivery can be maintained using accessible, low-cost fabrication methods, opening new opportunities for multiplexed reconstitution in distributed diagnostic workflows.

4.4.2.4 Integration of an SCM into a 3D-printed capillaric circuit

We demonstrate the feasibility of integrating SCMs into a capillaric circuit with additional flow control elements (Figure 4.6). This circuit was designed to combine inline reconstitution of a concentrated reagent with dynamic, multistep fluid control. The SCM acts a reservoir that can be preloaded with reagent - in this case a concentrated dye solution - that is terminated by a trigger valve on one end to keep liquid in place until a liquid control signal is provided, and a retention burst valve (RBV) on the other end to enable pre-programmed sequential drainage (Figure 4.6A).

To visualize suspension of a concentrated reagent in the SCM, we pipetted 1 μl of food dye onto the surface of the chip. In further applications, reagents could be spotted onto the chip surface using a small volume deposition spotter as in Figure 4.5. However, resuspending a concentrated liquid food dye demonstrates the flexibility to incorporate SCMs as a tool for effective dilution of liquid reagents or samples in future applications.

Self-coalescence aided dilution of a concentrated liquid happens during loading of the reagent reservoirs (Figure 4.6B.3-4). Once reservoirs are filled, fluid is pinned at trigger valves until actuation by the addition of liquid to the inlet of the main channel (Figure 4.6B.5). The weakest RBV sits atop the SCM and bursts when liquid is pinned at the RBV at the main channel inlet (Figure 4.6B.6). The "tug of war" style bursting mechanism of RBVs means that we can design the geometry of the inlet of the SCM so that it bursts first while the main channel inlet and other reservoir of the capillaric circuit hold their liquid in place. The patterning of the capillary pinning lines within the SCM do not compromise reservoir drainage. When the SCM reservoir is completely empty, the second RBV bursts (Figure 4.6B.7). Finally, the main channel drains, completing the circuit. This integrated capillaric circuit with an SCM was fabricated using a low-cost (Anycubic Mono X 6K, MSRP $\sim$ \$340 USD as of December 19, 2024) LCD-SLA printer using inexpensive

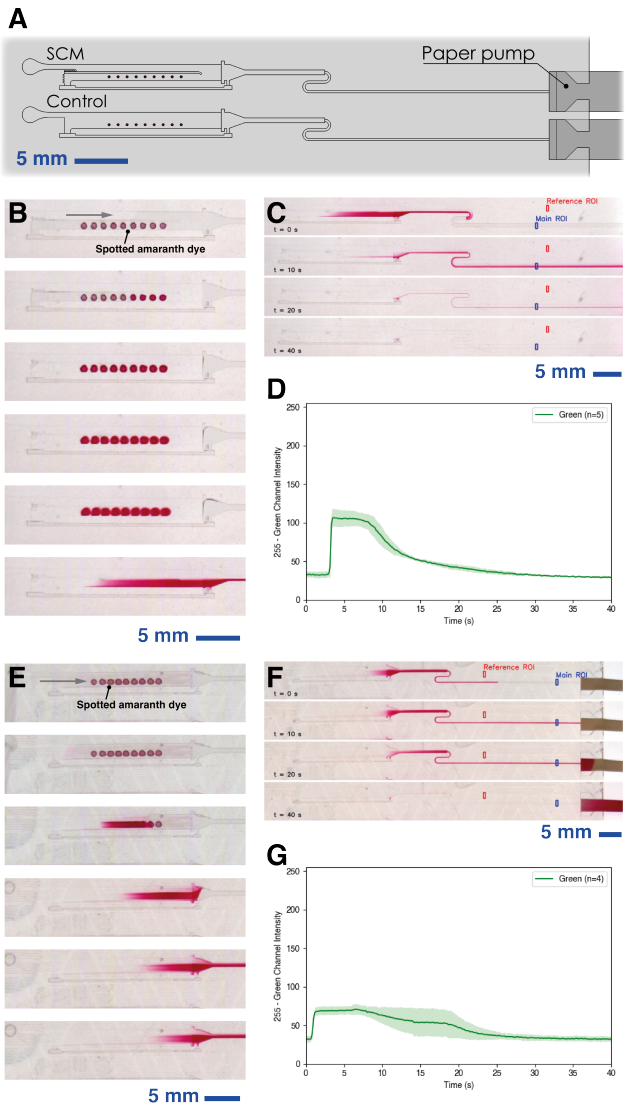

Figure 4.5: Reconstitution of amaranth dye in large-volume 3D-printed SCM. (A) Schematic of experimental setup comparing a 3D-printed SCM (top) to a control channel lacking a leading trench (bottom), both actuated by paper pumps. 50 nL spots of amaranth dye on the surface of a 3D-printed SCM undergo self-coalescence for resuspension and uniform rehydration (Movie S5). (B) Self-coalescence gently resuspends spotted dye without shear-induced accumulation at the fluid front. (C) The dye exits the SCM in a characteristic pulse-shape over a 40 second period. Regions of interest (ROI) for video analysis are noted. (D) Green channel intensity analysis confirms pulse-shaped delivery of reagents as reported in cleanroom-manufactured SCMs (n=5). (E) In contrast, the control device exhibits front-loaded rehydration, with dye accumulating near the advancing fluid front. (F) Time-lapse imaging of the control shows progressive smearing and early dye release. (G) Quantified green-channel intensity from the control confirms a broader, less defined signal with diminished peak sharpness (n=4).

WaterWash+ resin (Anycubic, MSRP $29 USD/kg). The printer is ~50X cheaper than the DLP-SLA printer used for initial characterization of SCMs and demonstrates the potential for rapid prototyping of SCMs with minimal capital and operating costs [29].

4.5 Discussion

4.5.1 Comparisons with other published work

To our knowledge, examples of 3D-printed phaseguides in the literature have so far been limited to two-photon polymerization, which is expensive and still requires cleanroom facilities[33], or scalloped channel edges in hydrogels that exhibit phase guiding behavior [32]. There was also a recent demonstration of laser cutting of capillary pinning lines in microchannels to rehydrate reagents [28]. Although that approach was inspired by SCMs and shows the capability for rapid and inexpensive prototyping of capillary pinning lines, key fluidic elements like vents and diversion barriers were not incorporated, thereby precluding the ability to showcase the full functionality and integration of SCMs within capillaric circuits. There have also been calls for vat polymerization of 3D-printed phaseguide-mediated organ-on-a-chip devices, but no demonstrations have been presented thus far in the field [31].

In comparison, our work shows functional 3D-printed phaseguides despite the greater surface roughness and layer-by-layer fabrication process of benchtop 3D printing compared with conventional cleanroom fabrication. We also 3D-printed functional SCMs and demonstrated that they can be scaled by applying a universal scaling factor to the height, width, and length of the reservoir body (Figure 4.4A.1-2) or by extending only the length while keeping height and width fixed (Figure 4.4A.3). In line with findings by Gökçe et al., shallow, wide SCMs exhibit more stable aspect ratios due to minimized liquid-air interface at the leading barrier, suggesting that maintaining an optimized aspect ratio is beneficial during scaling [1]. Lengthening the SCM provides a straightforward scaling method, but depending on the device layout, this can result in long footprints and high fluidic resistance, which may affect downstream processes/applications. In testing a 100 μl SCM, the largest volume we designed, we encountered difficulties in uniform filling upon redirection by the leading barrier, underlining the importance of asymmetrical CPL placement relative to the SCM body's centerline for large volumes. Gökçe et al.'s work shows that asymmetrical CPLs do not hinder self-coalescence and can accommodate spe-

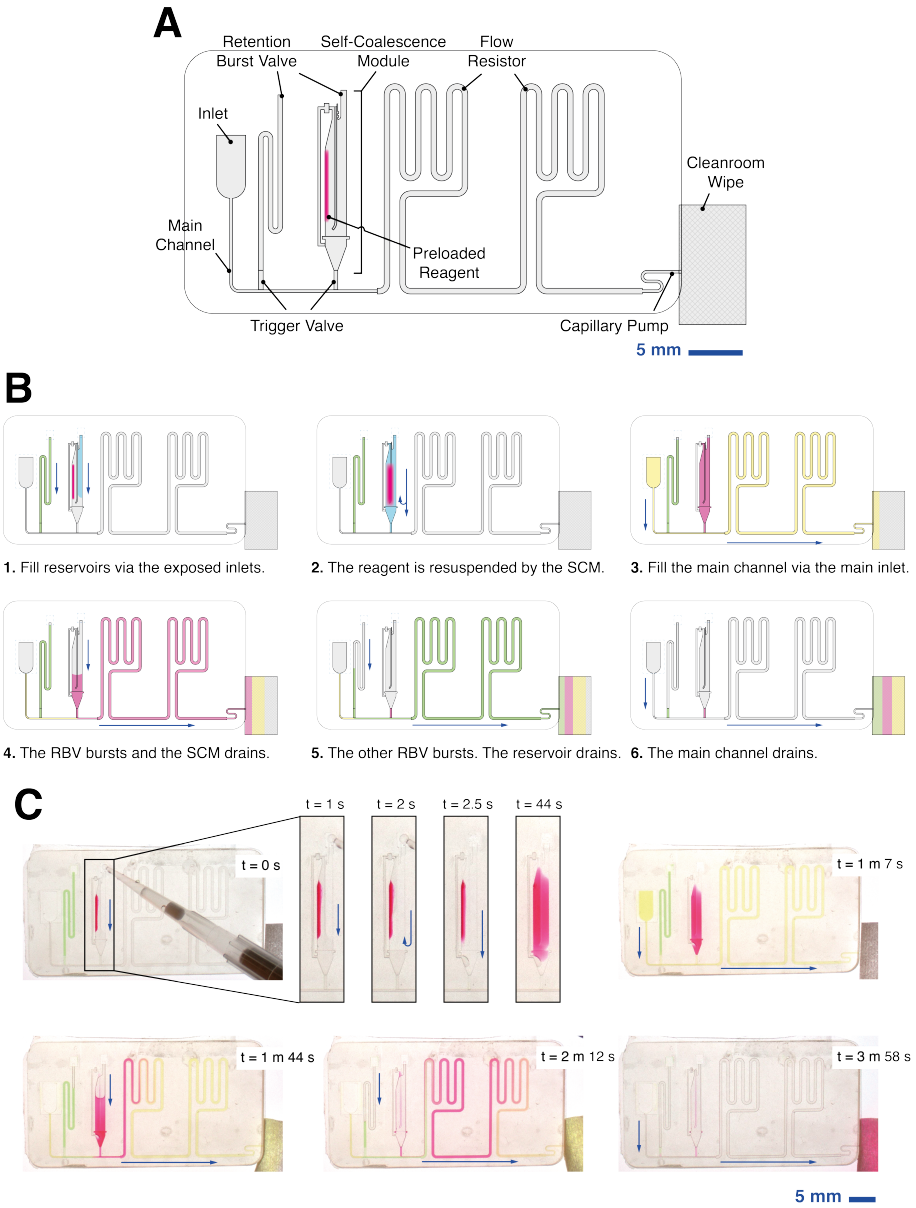

Figure 4.6: Integration of an SCM into a low-cost 3D-printed capillaric circuit. (A) Schematic of a capillaric circuit that includes an SCM, trigger valves, retention burst valves, flow resistors and a capillary pump. The SCM acts a reservoir that can be preloaded with reagent – in this case a concentrated dye solution – that is terminated by a trigger valve on one end to keep liquid in place until a liquid control signal is provided, and a retention burst valve on the other end to enable pre-programmed sequential drainage. The circuit supports inline reagent reconstitution and pre-programmed, instrument-free, multi-step fluid control. (B) Schematic illustrating expected operation of capillaric circuit with integrated SCM. (C) Timelapse images showing observed pre-programmed delivery with capillaric circuit containing SCM.

cific spotting patterns, suggesting this approach could be valuable in future work if larger SCM volumes become necessary.

4.5.2 Exceptions and unaddressed aspects of 3D-printed phaseguides and SCMs

We optimized the design of phaseguides and SCMs mainly by empirical observations given the rapid prototyping offered by 3D-printing. Further work could be done to integrate theoretical models of the air-liquid interface [1] at phaseguides and also characterize the impact of 3D-printing fabrication imperfections like feature sharpness and perpendicularity.

Although we showed sequential filling of 7 reservoirs using 3 different phaseguide strengths, we have not yet explored the limit of discretized steps that could be automated by 3D-printed phaseguides. We anticipate that, similar to past work with capillary retention burst valves, the resolution and precision of 3D-printing will limit the number of distinct pressure barriers that can be geometrically encoded4. We also expect that the imperfections in the perpendicularity of phaseguides in the z-axis introduced by the layer-by-layer nature of stereolithographic 3D printing could introduce weaknesses or nonlinearities in the pressure barriers, affecting their stability.

One major unaddressed aspect of our work is that we did not incorporate precision-deposited dried reagents into the 3D-printed SCMs. Instead, our work focused on the feasibility of fabricating functional phaseguides and SCMs using inexpensive benchtop 3D-printing. Although we observed the expected unzipping of flow and lack of accumulation of rehydrated reagents at the fluid front in Fig. 5, the imprecision of our manual spotting method limited the ability to quantitatively evaluate reagent rehydration in 3D-printed SCMs. Future work is required to validate 3D-printed SCMs with dried reagents. This could require exploring proven strategies for enhancing lateral reagent homogenization in cleanroom-fabricated SCMs such as flow mixers at the outlet of SCMs [1]. Additionally, self-coalescence across differential segments of SCMs—curved versus straight—requires validation to ensure effective reagent reconstitution and optimization of spot placement for specific assay applications.

This unaddressed aspect of validation highlights current limitations to democratization of this technology. Despite significant advances in rapid prototyping via low-cost 3D printers, reliance on expensive (and often centralized) small volume reagent deposition spotters still limits experimentation and application of this technology to highly resourced settings. Incorporation of frugal reagent deposition systems, like modified office inkjet printers [34], could help increase the adoption of SCMs without high capital costs.

Broad use of SCMs and integration with other capillaric fluidic elements and circuits could offer many advantages in the development of point-of-care diagnostics. Dried reagents that do not require cold chain storage can reduce the number of liquid loading steps, enable long-term storage and distributed deployment, and improve the user-friendliness of microfluidic devices [1].

4.6 Conclusion

We 3D-printed phaseguides and SCMs and showed comparable performance to cleanroom-fabricated features. We showed that 3D-printed phaseguides could guide the liquid filling front without bubble formation in reservoirs. Using phaseguides with different strengths, preprogrammed by the angle between the phaseguide and the channel walls, we also demonstrated sequential filling of multiple reservoirs within the same 3D-printed device. We then applied 3D-printed phaseguides as pinning features to obtain the characteristic self-coalescence or unzipping flow in SCMs. 3D-printing allows us to rapidly manufacture SCMs, easily scaling them to feature sizes up to 50X larger than those of cleanroom-fabricated devices. We also showed that we could change the shape of the 3D-printed SCMs to reconfigure device footprint and/or volume. Finally, we integrated 3D-printed SCMs with other capillaric elements – including trigger valves, retention burst valves, flow resistors, and capillary pumps – to demonstrate dilution of pre-loaded liquid and pre-programmed, instrument-free, multi-step liquid delivery. The 3D printing and integration of SCMs into capillaric circuits represents a significant advancement, combining rapid and inexpensive manufacturing with robust and scalable fluid control. While cleanroom fabrication has traditionally been essential for developing microfluidic control elements, especially features like phaseguides and SCMs that precisely manipulate capillary pinning lines, 3D printing has expanded both accessibility and versatility, enabling cost-effective prototyping without compromising functionality. This work broadens the range of fluidic elements that can be quickly produced, facilitating applications in assay automation, organ-on-chip systems, and diagnostics by addressing previous limitations in fluid control and reagent reconstitution. To further extend the utility of these systems, future designs could network phaseguides with additional capillaric elements, eliminating the need for external pumps and opening new possibilities. Altogether, the integration of 3D-printed capillaric components marks a critical step in democratizing liquid handling technology to enable broader, impactful

applications by scientists in high- and low-resource settings.

References

1. Gökçe, O., Castonguay, S., Temiz, Y., Gervais, T. & Delamarche, E. Self-coalescing flows in microfluidics for pulse-shaped delivery of reagents. *Nature* **574,** 228–232. ISSN: 0028-0836, 1476-4687 (Oct. 10, 2019).
2. Vulto, P. *et al.* Phaseguides: a paradigm shift in microfluidic priming and emptying. *Lab on a Chip* **11,** 1596. ISSN: 1473-0197, 1473-0189 (2011).
3. Streutker, E. M., Devamoglu, U., Vonk, M. C., Verdurmen, W. P. R. & Le Gac, S. Fibrosis-on-Chip: A Guide to Recapitulate the Essential Features of Fibrotic Disease. *Advanced Healthcare Materials* **13,** 2303991. ISSN: 2192-2640, 2192-2659 (Aug. 2024).
4. Ko, J., Song, J., Choi, N. & Kim, H. N. Patient-Derived Microphysiological Systems for Precision Medicine. *Advanced Healthcare Materials* **13,** 2303161. ISSN: 2192-2640, 2192-2659 (Mar. 2024).
5. Sablatura, L. K. *et al.* A 3D Perfusable Platform for In Vitro Culture of Patient Derived Xenografts. *Advanced Healthcare Materials* **12,** 2201434. ISSN: 2192-2640, 2192-2659 (June 2023).
6. Riddle, R. B., Jennbacken, K., Hansson, K. M. & Harper, M. T. Endothelial inflammation and neutrophil transmigration are modulated by extracellular matrix composition in an inflammation-on-a-chip model. *Scientific Reports* **12,** 6855. ISSN: 2045-2322 (Apr. 27, 2022).
7. Junaid, A. *et al.* A Microfluidics-Based Screening Tool to Assess the Impact of Blood Plasma Factors on Microvascular Integrity. *Advanced Biology* **5,** 2100954. ISSN: 2701-0198, 2701-0198 (Nov. 2021).
8. Park, D. *et al.* Aspiration-mediated hydrogel micropatterning using rail-based open microfluidic devices for high-throughput 3D cell culture. *Scientific Reports* **11,** 19986. ISSN: 2045-2322 (Oct. 7, 2021).
9. Spijkers, X. M. *et al.* A directional 3D neurite outgrowth model for studying motor axon biology and disease. *Scientific Reports* **11,** 2080. ISSN: 2045-2322 (Jan. 22, 2021).
10. Kane, K. I. W. *et al.* Automated microfluidic cell culture of stem cell derived dopaminergic neurons. *Scientific Reports* **9,** 1796. ISSN: 2045-2322 (Feb. 11, 2019).

11. Trietsch, S. J. *et al.* Membrane-free culture and real-time barrier integrity assessment of perfused intestinal epithelium tubes. *Nature Communications* **8,** 262. ISSN: 2041-1723 (Aug. 15, 2017).

12. Tabata, Y. & Lutolf, M. P. Multiscale microenvironmental perturbation of pluripotent stem cell fate and self-organization. *Scientific Reports* **7,** 44711. ISSN: 2045-2322 (Mar. 17, 2017).

13. Moreno, E. L. *et al.* Differentiation of neuroepithelial stem cells into functional dopaminergic neurons in 3D microfluidic cell culture. *Lab on a Chip* **15,** 2419–2428. ISSN: 1473-0197, 1473-0189 (2015).

14. Tung, C.-k. *et al.* A contact line pinning based microfluidic platform for modelling physiological flows. *Lab on a Chip* **13,** 3876. ISSN: 1473-0197, 1473-0189 (2013).

15. Trietsch, S. J., Israëls, G. D., Joore, J., Hankemeier, T. & Vulto, P. Microfluidic titer plate for stratified 3D cell culture. *Lab on a Chip* **13,** 3548. ISSN: 1473-0197, 1473-0189 (2013).

16. Xu, L. *et al.* Phaseguide-assisted blood separation microfluidic device for point-of-care applications. *Biomicrofluidics* **9,** 014106. ISSN: 1932-1058 (Jan. 1, 2015).

17. Xu, L., Lee, H., Jetta, D. & Oh, K. W. Vacuum-driven power-free microfluidics utilizing the gas solubility or permeability of polydimethylsiloxane (PDMS). *Lab on a Chip* **15,** 3962–3979. ISSN: 1473-0197, 1473-0189 (2015).

18. Gottheil, R. *et al.* Moving the solid phase: a platform technology for cartridge based sandwich immunoassays. *Biomedical Microdevices* **16,** 163–172. ISSN: 1387-2176, 1572-8781 (Feb. 2014).

19. Puchberger-Enengl, D., Krutzler, C., Keplinger, F. & Vellekoop, M. J. Single-step design of hydrogel-based microfluidic assays for rapid diagnostics. *Lab Chip* **14,** 378–383. ISSN: 1473-0197, 1473-0189 (2014).

20. Chen, C.-Y. *et al.* Sperm quality assessment via separation and sedimentation in a microfluidic device. *The Analyst* **138,** 4967. ISSN: 0003-2654, 1364-5528 (2013).

21. Vulto, P. *et al.* A microfluidic approach for high efficiency extraction of low molecular weight RNA. *Lab Chip* **10,** 610–616. ISSN: 1473-0197, 1473-0189 (2010).

22. Vulto, P., Kuhn, P. & Urban, G. A. Bubble-free electrode actuation for micro-preparative scale electrophoresis of RNA. *Lab on a Chip* **13,** 2931. ISSN: 1473-0197, 1473-0189 (2013).

23. Schoonen, J.-W. *et al.* Continuous-Flow Microelectroextraction for Enrichment of Low Abundant Compounds. *Analytical Chemistry* **86,** 8048–8056. ISSN: 0003-2700, 1520-6882 (Aug. 19, 2014).

24. Phurimsak, C. *et al.* Phaseguide assisted liquid lamination for magnetic particle-based assays. *Lab Chip* **14,** 2334–2343. ISSN: 1473-0197, 1473-0189 (2014).

25. Yildirim, E. *et al.* Phaseguides as tunable passive microvalves for liquid routing in complex microfluidic networks. *Lab on a Chip* **14,** 3334. ISSN: 1473-0197, 1473-0189 (June 17, 2014).

26. Hemmig, E., Temiz, Y., Gökçe, O., Lovchik, R. D. & Delamarche, E. Transposing Lateral Flow Immunoassays to Capillary-Driven Microfluidics Using Self-Coalescence Modules and Capillary-Assembled Receptor Carriers. *Analytical Chemistry* **92,** 940–946. ISSN: 0003-2700, 1520-6882 (Jan. 7, 2020).

27. Rocca, M. *et al.* Rapid quantitative assays for glucose-6-phosphate dehydrogenase (G6PD) and hemoglobin combined on a capillary-driven microfluidic chip. *Lab on a Chip* **21,** 3573–3582. ISSN: 1473-0197, 1473-0189 (2021).

28. Kamat, L., Delgado, P., Dissanayaka, A. & Myers, D. R. An economical self-coalescing microfluidic device with an easily observable readout. *Frontiers in Lab on a Chip Technologies* **3,** 1365774. ISSN: 2813-3862 (July 8, 2024).

29. Leong, K. M. *et al.* Democratizing Access to Microfluidics: Rapid Prototyping of Open Microchannels with Low-Cost LCD 3D Printers. *ACS Omega,* acsomega.4c07776. ISSN: 2470-1343, 2470-1343 (Nov. 1, 2024).

30. Olanrewaju, A. O., Robillard, A., Dagher, M. & Juncker, D. Autonomous microfluidic capillaric circuits replicated from 3D-printed molds. *Lab on a Chip* **16,** 3804–3814. ISSN: 1473-0197, 1473-0189 (2016).

31. Milton, L. A., Viglione, M. S., Ong, L. J. Y., Nordin, G. P. & Toh, Y.-C. Vat photopolymerization 3D printed microfluidic devices for organ-on-a-chip applications. *Lab on a Chip* **23,** 3537–3560. ISSN: 1473-0197, 1473-0189 (2023).

32. Kim, Y. T., Bohjanen, S., Bhattacharjee, N. & Folch, A. Partitioning of hydrogels in 3D-printed microchannels. *Lab on a Chip* **19,** 3086–3093. ISSN: 1473-0197, 1473-0189 (2019).

33. Blankespoor, M., Manzaneque, T. & Ghatkesar, M. K. Discrete Femtolitre Pipetting with 3D Printed Axisymmetrical Phaseguides. *Small Methods* **8,** 2300942. ISSN: 2366-9608, 2366-9608 (Mar. 2024).

34. Cho, H., Parameswaran, M. (& Yu, H.-Z. Fabrication of microsensors using unmodified office inkjet printers. *Sensors and Actuators B: Chemical* **123,** 749–756. ISSN: 09254005 (May 2007).

5 | Conclusions, Scientific Contributions, and Future Directions

5.1 Summary of Scientific Contributions

This work sets out not just to create devices, but to create design tools: modular, programmable, and accessible frameworks that lower the barriers to meaningful microfluidic innovation. From clinically validated assays for HIV drug monitoring to structurally encoded logic for fluid flow, and finally to low-cost fabrication methods that require no cleanroom, each chapter builds on the last to enable real-world diagnostic workflows that can run independently, repeatably, and affordably.

The contributions of this dissertation demonstrate that high-resolution fluidic behavior is achievable outside of traditional manufacturing environments. By modeling capillaric circuits with precision and iterating their geometry with household-scale tools, we open new doors for global deployment and local adaptation. These systems require no pumps, no electronics, and no centralized infrastructure; just geometry, gravity, and surface tension.

While the specific applications described here focus on antiretroviral monitoring and decentralized diagnostics, the broader impact lies in the methodology. The act of encoding logic into form, of replacing cost with cleverness, of turning structure into sequence are transferable insights that extend beyond any one disease or use case. As microfluidics expands into homes, field clinics, and classrooms, the tools must follow suit.

Key scientific contributions of this dissertation include:

- The clinical validation of RESTRICT and co-authored development of REACT, enzymatic assays for drug-level monitoring of nucleotide and non-nucleotide reverse transcriptase inhibitors in HIV care.
- A circuit-based analytical framework for designing microfluidic chain reactions

(MCRs), along with open-source tools that formalize and disseminate capillaric design logic.

- The introduction of 3D-printable phaseguides and self-coalescence modules (SCMs), demonstrating that complex capillaric elements can be fabricated using low-cost LCD printers with high reproducibility and functional precision.

By designing systems built to be shared (open, interpretable, and replicable), we lay the foundation for a more inclusive and distributed future in diagnostic technology.

5.2 Building on Prior Work in Capillary Microfluidics

This dissertation builds directly upon the foundational work in capillary circuits and microfluidic automation introduced in Dr. Olanrewaju's 2017 PhD thesis, "3D-Printed Capillaric Circuits for Autonomous Liquid Delivery". That work demonstrated the transformative potential of capillary microfluidics to automate complex liquid handling without pumps or electronics, and proposed 3D-printing as a rapid prototyping tool to accelerate design iteration. Over the past eight years, the capillarics landscape has evolved considerably. This dissertation contributes key technical and conceptual advances that bring many of those early visions to fruition.

5.2.1 Low Cost 3D-Printing: From Concept to Practice

Where prior work demonstrated capillaric circuits fabricated via high resolution DLP printing or replicated from cleanroom molds, this thesis establishes low-cost LCD 3D-printing as a reliable, reproducible platform for direct capillaric fabrication. By systematically characterizing dimensional accuracy, surface quality, and functional performance, we validated <$500 LCD printers as viable tools for fabricating precise microfluidic features. We also developed an open-source protocol and shared printing parameters, lowering the barrier for entry and enabling true democratization of capillaric microfluidics. This work realizes the promise of accessible, rapid prototyping that was envisioned in the early phases of the field.

5.2.2 Expansion of the Capillarics Toolkit

While the prior generation of capillary circuits relied on planar features such as stop valves and retention valves, this dissertation expands the geometric vocabulary of capillarics by introducing 3D-printed phaseguides and self-coalescence modules (SCMs). These features had previously required cleanroom fabrication due to their sub-50 μm dimensions and sensitivity to surface roughness. By scaling and re-engineering their design for 3D-printing, I enabled their integration into fully passive circuits, validating their function for controlled flow routing and reagent rehydration. These contributions extend the architectural range of capillaric circuits and open new design possibilities for autonomous fluid control.

5.2.3 From Individual Devices to Generalizable Logic

Capillary circuits have long been praised for their ability to execute specific workflows without instrumentation. However, programming such circuits typically required manual trial-and-error or empirical tuning. This dissertation introduces a circuit-based analytical framework for microfluidic chain reactions (MCRs), formalizing the relationship between geometry, resistance, and timing. I provided symbolic representations, annotated design rules, and Python-based tools to support scalable, shareable design. This shifts capillarics from a set of examples to a programmable platform and enables more researchers to not only use, but design and adapt complex fluidic logic.

5.2.4 Automation with Real-World Constraints

Dr. Olanrewaju proposed a future in which capillarics could reduce pipetting, incorporate dried reagents, and enable walk-away workflows in point-of-care settings. This dissertation attempts to deliver on those aims by demonstrating SCMs for timed reagent rehydration, surfactant-based strategies for eliminating plasma treatment, and structured design workflows for producing circuits that can be fabricated, sealed, and tested without cleanroom access. These tools bring capillarics closer to their intended users; clinicians, researchers, and diagnostic developers working in decentralized environments.

5.3 Perspective and Future Directions

5.3.1 Materials and Surface Engineering

This work experimented with surfactant-based alternatives to plasma treatment, enabling closed-channel printing and mitigation of hydrophobic aging without relying on specialized equipment. While effective for prototyping, surfactants can introduce trade-offs such as potential assay interference, lot-to-lot variability, and dependence on fluid composition. Recent work from Juncker lab explored hydrophilic, photocurable resins for capillary microfluidics, but their approach showed poor reproducibility and limited capillary performance, highlighting the need for more robust material formulations. Future work could focus on developing or identifying intrinsically hydrophilic resins with stable surface energies that retain wetting properties over time and across print batches. Additionally, post-print surface treatments could offer an alternative to plasma for creating durable, biocompatible wettability. Long-term material stability under realistic storage conditions, especially in humid or field-deployable formats, remains an important area for investigation.

5.3.2 Functional Limits of Low Cost Printing

Although I validated high-fidelity features using low-cost LCD printers, challenges remain in closed-channel fidelity, resin clearing, and z-resolution limitations—especially for SCMs and multi-layer architectures. Developing custom low-viscosity resins, integrating solvent-based clearing methods, or designing features that are tolerant to print variation (e.g., adaptive geometries for pinning lines) could improve robustness. There's also an opportunity to create printability design guidelines (analogous to PCB trace clearances) specifically for capillaric circuits on consumer-grade printers.

5.3.3 Broader Integration of Reagent Handling

SCMs were demonstrated with dried dye and food coloring as proxies for reconstitution, but real diagnostic reagents (enzymes, antibodies, or nucleic acids, etc.) additional considerations. These include drying and stabilization chemistries, storage compatibility, and repeatability of rehydration volumes. Future work should systematically test SCM performance with actual clinical reagents, benchmark against lateral flow standards, and

explore integration with blister packs, humidity barriers, or shelf-stable spotting techniques.

5.3.4 Biological and Clinical Validation

Chapter 1 describes a clinically validated enzymatic assay for HIV drug adherence monitoring using DBS samples. However, the capillaric platforms described in Chapters 2 and 3 have not yet been tested with biologically relevant fluids or complex matrices like blood, plasma, or saliva. Translating these designs into real assays will require validation for non-specific binding, flow disruption due to debris, and variability in fluid properties. Applications in therapeutic drug monitoring, infectious disease detection, or at-home testing would benefit from this next level of performance validation.

5.3.5 Usability and Deployment

While this work emphasizes modularity and shareability, there is still a gap between technical functionality and true end-user accessibility. Device operation still often requires pipetting, sealing, or reagent handling. To bridge that gap, future designs could:

- Reduce user steps by integrating pre-loaded reagents, single-inlet loading, or multi-reservoir fill paths
- Explore pre-laminated formats or snap-fit assemblies for chip sealing
- Co-develop with target users (e.g., community health workers, educators) to identify and remove usability barriers

5.3.6 Detection Modalities Beyond Fluorescence

While this work focused on flow control and reagent handling, detection remains a key enabler for translating capillaric systems into diagnostic tools. Most characterization was performed using fluorescence or visual inspection in the lab, but future implementations will require detection schemes that preserve the system's strengths: low cost, minimal instrumentation, and structural programmability. Several complementary strategies could be explored to match the capabilities of the circuits developed here:

- Electrochemical sensing, which can be integrated into printed substrates or interfaced with low-power, smartphone-based readers. Capillaric circuits could automate sample delivery to electrochemical chambers for real-time monitoring of redox-active analytes or enzyme reactions.
- Signal amplification strategies such as enzyme cascades, nanomaterial-enhanced readouts, or redox cycling could increase sensitivity while minimizing the need for bulky optics or expensive instrumentation.
- Simplified optical readers, such as LED–photodiode pairs, reflectance-based detection, or ambient-light absorbance modules, offer more compact and affordable alternatives to fluorescence microscopy. These can be readily integrated with 3D-printed housings or smartphone attachments.

Modular plug-and-play detection zones, such as swappable test strips or embedded transducers, could make circuits agnostic to readout mode—enabling reuse across different analytes or detection schemes.

These approaches align with the core goals of this work: enabling programmable, instrumentation-light assays that can scale in complexity without increasing user or equipment burden.

5.3.7 Scaling and Multiplexing

This dissertation laid the groundwork for programmable sequencing via MCRs and SCMs, but most demonstrations involved <5 liquids. As microfluidic needs grow—e.g., for protein panels, multi-step bioassays, or parallel diagnostics—the ability to handle dozens of fluids becomes critical. Future work can draw from prior DCC efforts to design 3D-printed routing layers, common inlet architectures, and overflow protection structures that support higher throughput in a compact footprint.

5.4 Engineering as Translation

The tools described in this thesis—assays, circuits, fabrication methods—are only as valuable as the problems they are built to solve. In that sense, engineering is not just invention; it is translation. To make microfluidics matter, engineers must listen closely to the constraints, needs, and lived realities of those they hope to serve: patients, clinicians,

researchers, and community health workers. Those insights must then be reflected in the design of systems that are usable, contextual, and enduring. Design should begin not with what is possible, but with what is relevant. The real questions are not only "what can we build?" but "what would be useful?" and "for whom?"

This work embraces that ethos. The assay development was shaped by real clinical workflows. The printable diagnostics were built for fabrication on standard equipment, not just in cleanrooms. The fluidic logic was embedded directly into the geometry, requiring no electronics or programming. These choices reflect a commitment to bridging technical possibility with practical application. As the field continues to evolve, engineers must take seriously their role as translators—interpreting needs, lowering barriers, and shaping tools that work in the settings where they're most needed.

5.5 Final Reflections

This thesis began with a question: how can we design microfluidic systems that are not only functional, but shareable? How do we build tools that lower the barrier to entry, respect local constraints, and actually work in the hands of those who need them? The answers took shape not just through channels and assays, but through frameworks and principles that help others build and adapt their own. What emerged is not simply a collection of devices, but a design philosophy rooted in modularity, accessibility, and thoughtful translation.

Ultimately, this work is a reminder that design choices carry meaning. Geometry can direct behavior, structure can encode logic, and the accessibility of a tool often matters as much as its performance. The future of diagnostics will be shaped not by what is technically possible in the lab, but by what is intentionally made usable, adaptable, and available to others. What we choose to make easy to share will define how far these systems can reach.

A | Supplementary Material For Chapter 2

Guide to This Appendix

This appendix provides supplementary material and extended discussion for concepts presented in Chapter 2 of the dissertation. It includes:

- Advanced Capillaric Elements not included in the main chapter.
- Extended Design Theory for Stop Valves and Junction Pressures.
- Domino Valve Capillary Pressure Calculator (Jupyter Notebook)
- 3D Printing Standard Operating Procedure

A.1 Additional Capillaric Elements

See Chapter 2 for an overview of common microfluidic components. This appendix extends that discussion to emerging design tools, including:

A.1.1 Additional capillaric elements

The three articles detailed below explore advanced applications of capillary microfluidics, particularly focusing on autonomous flow control mechanisms such as capillary field-effect transistors (cFETs) and open trigger valves (TVs), which are pivotal in enhancing the functionality of lab-on-a-chip systems.

Meffan et al. present a novel cFET design that functions as a normally closed valve, which can be opened by applying a trigger fluid to a control channel [1]. This mechanism allows for precise control over fluid flow in capillary circuits without the need for external power sources. The cFETs can be integrated into complex microfluidic networks to perform sequential operations, such as reagent addition and sample processing, autonomously. The study demonstrates the potential of cFETs in developing self-powered,

programmable microfluidic devices for various applications, including point-of-care diagnostics and chemical analysis.

Mak et al. introduce a reversible cFET that enables autonomous reopening of previously closed microchannels without external intervention [2]. This is achieved by leveraging competing capillary pressures to withdraw liquid from a connected reservoir, creating suction that removes an occluding air bubble, thereby restoring flow. The design allows for complex flow control scenarios, such as simultaneously opening one valve while closing another or parallel reopening of multiple valves. Additionally, the system can autonomously achieve transient mixing ratios between multiple liquids through a series of triggering events, enhancing the capabilities of fully automatic diagnostic capillaric devices.

Tokihiro et al. extend the application of TVs to open microfluidic channels [3]. Trigger valves in this context stop fluid at abrupt geometric expansions and release it upon flow in an orthogonal channel (discussed later in this chapter). The researchers developed a closed-form model based on average friction length to predict flow dynamics at these valves, validated through experiments. Implementing TVs in open channels enables layered capillary flow, where fluids from side channels can be sequentially introduced into a main channel, facilitating complex fluidic operations such as timed reagent addition and mixing. This has significant implications for autonomous microfluidic systems used in biosensing, at-home diagnostics, and organ-on-a-chip models.

Collectively, these studies highlight the advancements in capillary microfluidic technologies, emphasizing autonomous flow control through innovative valve designs. The integration of reversible cFETs and TVs into microfluidic systems paves the way for more sophisticated, self-regulating lab-on-a-chip devices, enhancing their applicability in diagnostics, biosensing, and biomedical research.

A.2 Extended Design Theory

A.2.1 Stop Valve Burst Pressure

A detailed derivation of the burst pressure for conical stop valves is provided here. This material expands upon the brief introduction in Chapter 2.

If you've already read the main chapter, you may wish to skip to the geometric design guidelines below.

A.2.2 Stop valves

With a rapid change in microchannel geometry comes a rapid change in capillary pressure that can be harnessed to control flow behavior. Rapid contraction of channels simulates a pumping effect by augmenting a pressure differential that can drive flow. Rapid expansion, however, can be used to temporarily halt flow. These expansions are known as stop valves.

Stop valves can take many different geometries so long as rapid expansion of geometry in at least one direction is created. Since stop valves introduce an abrupt decrease in capillary pressure, it is not desirable for flow to continue. The 'bursting' of a stop valve relies on spontaneous progression of the flow over the geometric impediment or intersection with another stream of flow to wet the pinned fluid front. In the case of spontaneous progression, we can explore the relationship between the nature of geometric expansion of a stop valve and its propensity to burst.

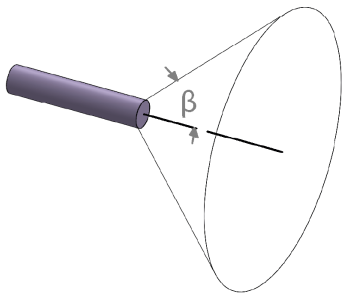

Figure A.1: Burst pressure for a generalized conical stop valve

Let us first look at a simple version of a stop valve in Figure A.1. A small conduit with a circular cross-section meets a geometric expansion in all directions with an angle of β. The derivation of the burst pressure is detailed in Cho et al but we will take an intuitive approach to understanding how the minimum burst pressure of this valve can be calculated [4]. The equation for the burst pressure of a simple conical stop valve with a divergent angle β, a surface tension γ, and a contact angle of the fluid with the channel walls θ is:

$$BP = \frac{-4\gamma cos\theta_I^*}{D}, \quad \theta_I^* = min[\theta + \beta, 180^\circ] \tag{A.1}$$

To understand this equation, Cho et al suggest we imagine a drop of liquid on a tilting

horizontal surface. At a plane parallel with the ground, we imagine the drop to have a contact angle with the surface. As you continually tilt the surface, moving the plane from parallel to the ground to approach perpendicular, the drop deforms until it starts to slide down the surface. The edge of the drop positioned in the direction of it's eventual slide deforms in a way that it's contact angle with the surface changes, thus we have an equilibrium contact angle on a parallel plane and a critical advancing contact angle that is the maximum deformation of the drop before it slide. Conceptually, we can think of our 'droplet' as having an equilibrium contact angle in the lead-up channel to a stop valve that then abruptly interfaces with a tilted plane at an angle of β (this is perhaps easier to picture in a 2-dimensional picture. To overcome the rapid change in geometry, the flow must bulge from the equilibrium contact angle in the lead-up channel to the critical advancing contact angle needed to slide down the tilted plane. The increase in the contact angle that a stop valve presents can be represented as the contact angle in the lead-up channel plus the geometric expansion, $\theta + \beta$. A bound is placed on this term since the maximum contact angle a fluid can have with a surface is $180°$.

Let's break this down with some more intuition regarding each term. If we tilted a slick surface with a drop of water and a drop of honey on it, we'd expect the honey to have a larger critical advancing contact angle. This is captured in the equation; When surface tension of a fluid increases, so does the burst pressure of a stop valve. The interface of a higher surface tension fluid requires more back pressure to create the bulge needed to overcome the expansion.

As we increase the diameter of the lead-up channel, we'd see the burst pressure decrease. Giving the significance of contact forces in this phenomena, it makes sense that increasing the proportion of bulk volume to fluid in contact with the surface would weaken a stop valve.

To understand the influence of the contact angle, we can look at two distinct regimes, hydrophilic ($< 90°$) and hydrophobic ($> 90°$) contact angles and assume a divergent angle of $\beta = 90°$. As we move to more hydrophilic contact angles approaching $0°$ from $90°$, the cosine term approaches 1 from 0. Thus, the burst pressure decreases with increasing hydrophilicity. As we move to more hydrophobic contact angles, the minimum term in θ_I^* takes the argument $180°$. Thus, the burst pressure is maximized, intuitively tracking that a hydrophobic fluid would need to have applied back pressure from a pump to overcome the geometric expansion.

Now let's assume a hydrophilic contact angle of $\theta = 45°$ with a changing value of

β. Burst pressure increases as β increases, meaning that intuitively the fluid front needs to bulge more to reach a critical advancing contact angle with a surface that's tilted at a greater angle.

With this intuition established, we can revisit the Young-Laplace equation and make a table of the burst pressure for common stop valve geometries (Figure A.2).

A.2.3 Theoretical Effect of Perpendicularity on Bursting Pressure

Figure A.3 illustrates how the perpendicularity of a printed edge governs the Laplace pressure barrier it can sustain and why real-world 3D printing often falls short of theoretical predictions. In principle, a perfectly vertical drop-off forces the advancing meniscus into steep curvature, maximizing capillary pressure and enabling strong pinning. This is the basis for a stop valve geometry that, in theory, could hold indefinitely: the pressure required to spontaneously overcome the abrupt geometric expansion cannot be generated by capillarity alone.

However, two manufacturing quirks undermine this ideal. First, theory assumes an infinitely sharp change in geometry, which is impossible to achieve in practice. On consumer-grade DLP printers, the orthogonal pixel grid and light diffusion through the resin produce filleted or "scalloped" edges instead of true verticals. Second, perpendicularity depends strongly on feature height. Steps shorter than 200–300 μm, even if designed as vertical drop-offs, often print as shallow ramps. This inadvertent divergent angle weakens the Laplace barrier, lowering the bursting pressure and allowing premature valve failure.

In the context of self-coalescence modules (SCMs) presented in Chapter 4, this geometric softening emerged as a leading cause of trench failure. Trenches with sub-threshold phaseguide heights often showed stable initial pinning but could not sustain the pressure differential needed to initiate coalescence or pinned so weakly that flow bypassed the intended sequence entirely.

This effect likely explains prior reports of stop valves with designed perpendicular edges but sub-300 µm height differences failing to pin indefinitely, as described by Olanrewaju et al. [6]. By mapping how bursting pressure varies with printed edge perpendicularity, we identified a threshold feature height necessary for reliable pinning in self-coalescence modules. This transforms perpendicularity from a subtle geometric detail into a critical design parameter for 3D-printed capillarics.

Trimetric View	Top view	Side view	Burst pressure equation
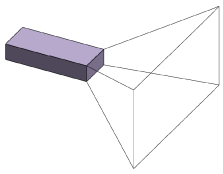	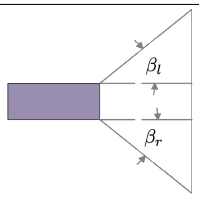	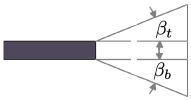	$BP = -\gamma \left[\frac{cos\theta^*_{I,l} + cos\theta^*_{I,r}}{w} + \frac{cos\theta^*_{I,t} + cos\theta^*_{I,b}}{h} \right]$
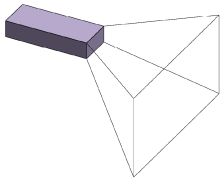	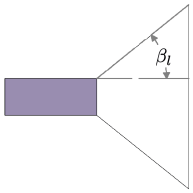	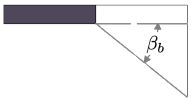	$BP = -\gamma \left[\frac{cos\theta^*_{I,l} + cos\theta^*_{I,r}}{w} + \frac{cos\theta_t + cos\theta^*_{I,b}}{h} \right]$
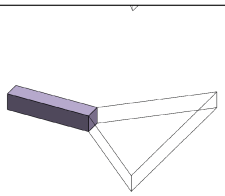	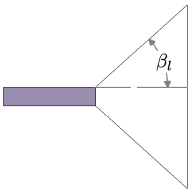		$BP = -\gamma \left[\frac{2cos\theta^*_I}{w} + \frac{cos\theta_t + cos\theta_b}{h} \right]$
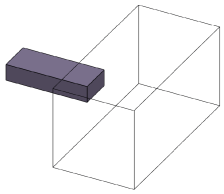	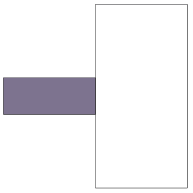		$BP = -\gamma \left[\frac{cos\theta^*_{I,l} + cos\theta^*_{I,r}}{w} + \frac{cos\theta^*_{I,t} + cos\theta^*_{I,b}}{h} \right]$ $\beta_{t,b,l,r} = 90^\circ$
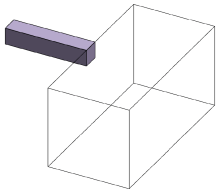	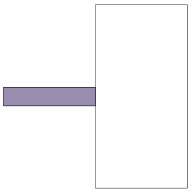		$BP = -\gamma \left[\frac{cos\theta^*_{I,l} + cos\theta^*_{I,r}}{w} + \frac{cos\theta_t + cos\theta^*_{I,b}}{h} \right]$ $\beta_{b,l,r} = 90^\circ$
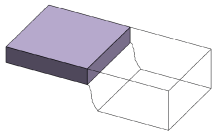			$BP = -\gamma \left[\frac{cos\theta_l + cos\theta_r}{w} + \frac{cos\theta_t + cos\theta^*_{I,b}}{h} \right]$

$\theta^*_{I,t} = min\left[\theta_t + \beta_t, 180^\circ\right]$ $\theta^*_{I,b} = min\left[\theta_b + \beta_b, 180^\circ\right]$ $\theta^*_{I,l} = min\left[\theta_l + \beta_l, 180^\circ\right]$ $\theta^*_{I,r} = min\left[\theta_r + \beta_r, 180^\circ\right]$

Figure A.2: Common stop valve geometries and their burst pressures

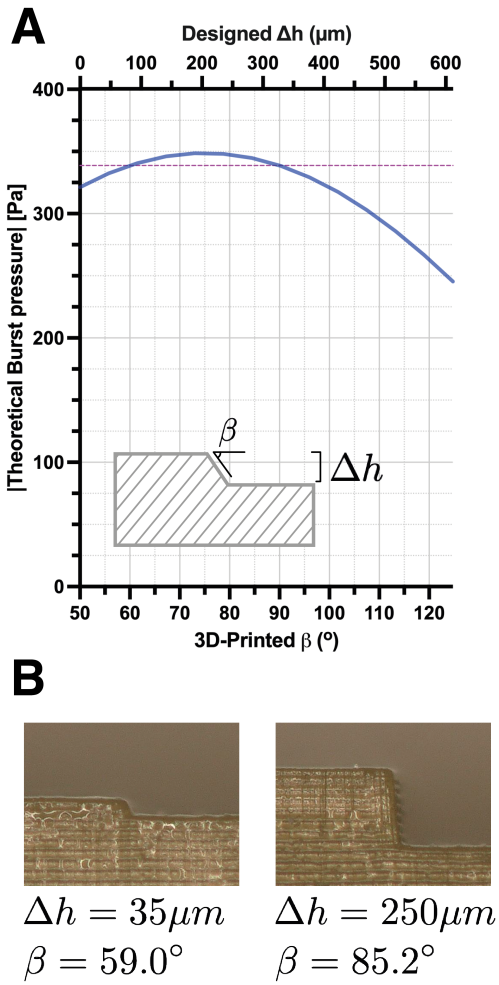

Figure A.3: Effect of printed edge perpendicularity on theoretical bursting pressure. **(A)** Modeled relationship between printed wall angle (β) and theoretical Laplace bursting pressure, showing that maximum barrier strength occurs near perpendicular edges. Blue line represents burst pressure according to divergent angle theory [5], Fuschia line represents burst pressure assuming perpendicularity. Designed feature height (Δh) influences achievable perpendicularity, with sub-200–300 μm steps often printing as shallow ramps due to voxel geometry and light diffusion. **(B)** Cross-sectional micrographs of 3D-printed steps illustrate this effect: a short step ($\Delta h = 35\mu m$, $\beta = 59.0°$) prints with a pronounced slope, while a taller step ($\Delta h = 250\mu m$, $\beta = 85.2°$) maintains near-vertical geometry. In self-coalescence modules, insufficient perpendicularity weakens the Laplace barrier, contributing to trench failures and preventing reliable coalescence initiation.

A.2.4 Serpentine Capillary Filling Behavior

Serpentine microchannels are commonly used in capillary microfluidics to conserve space while maintaining a long fluid path for flow regulation, timed reactions, or controlled mixing. In this example, we examine a rectangular serpentine channel fabricated

for fill time measurements. The design is 696 mm long and 600 × 250 µm in cross-section. The channel was closed with a glass slide and filled with aqueous solution containing 0.05% Tween 20.

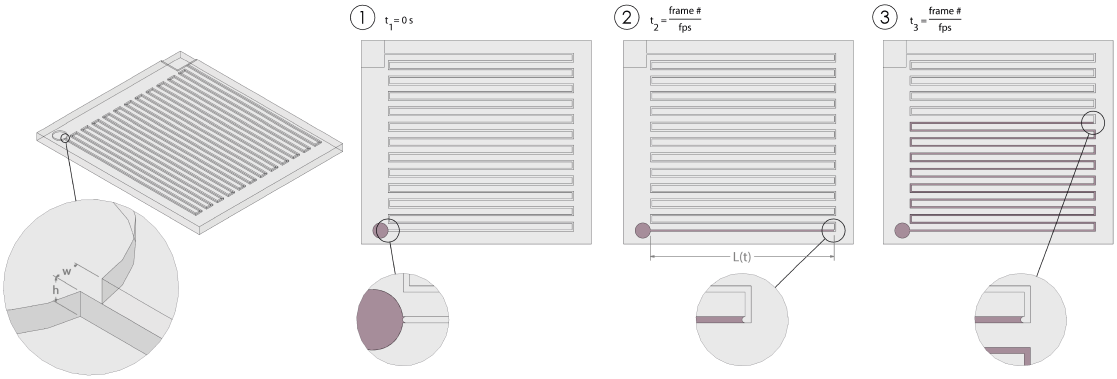

Figure A.4: Capillary filling length over time in a closed rectangular serpentine microchannel. Theoretical curve and two experimental replicates are shown, along with a metrics table summarizing flow properties and fit quality.

Python Code for Serpentine Fill Time

The script used to generate Figure A.6 models capillary flow and compares it to experimental data. It calculates capillary pressure, flow resistance, and theoretical fill time using microchannel geometry, contact angles, and fluid properties. The GUI overlays experimental replicates and outputs both error metrics and a summary table.

Python Code Explanation

The following code calculates theoretical capillary fill time and compares it to experimental data collected from a closed rectangular serpentine channel. A GUI allows users to input channel geometry, contact angles, and fluid properties, and view plots and error metrics.

GUI Layout Example

Full Python Script for Capillary Fill Time Analysis

```
import numpy as np
import matplotlib.pyplot as plt
import tkinter as tk
```

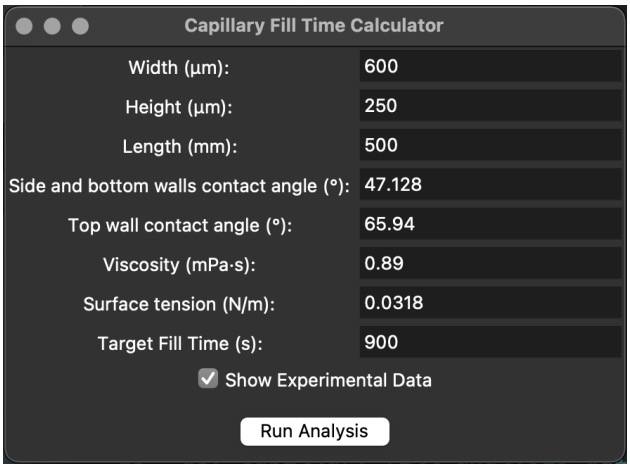

Figure A.5: Example GUI for capillary fill time simulation. Users input microchannel geometry and fluid properties, then visualize fit to experimental data.

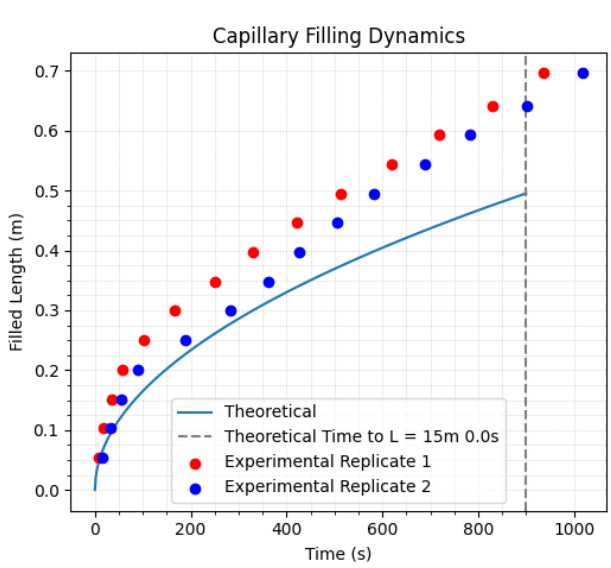

Width (µm)	600
Height (µm)	250
Length (mm)	500.0
Viscosity (mPa·s)	0.89
Surface tension (N/m)	0.032
Side and bottom contact angles (°)	47.1
Top contact angle (°)	1.2
Capillary pressure (Pa)	210.52
Resistance per unit length (Pa·s/m³)	1.54e+12
Fill time by approximation	4m 35.2s
Fill time by summation	15m 0.0s
Time_{approx} / Time_{sum}	0.31
Replicate 1 Mean Percentage Error (%)	38.58
Replicate 2 Mean Percentage Error (%)	20.94

Figure A.6: Example GUI for capillary fill time simulation. Users visualize fit to experimental data.

```
from tkinter import messagebox

# Experimental data from 4-30-2025, 0.05% tween in closed 0.6x0.3
   x696 mm serpentine
x_exp = np.array([54, 103, 152, 201, 250, 299, 348, 397, 446, 495,
   544, 593, 642, 696]) * 1e-6
x_exp2 = np.array([54, 103, 152, 201, 250, 299, 348, 397, 446, 495,
   544, 593, 642, 696]) * 1e-6
```

```
t_exp = np.array([8.37, 17.67, 34.27, 58.00, 103.20, 165.17, 251.30,
    329.73, 421.30, 512.63, 618.80, 718.93, 829.83, 935.17])
t_exp2 = np.array([15.37, 31.47, 55.07, 90.80, 188.77, 282.13,
   362.23, 427.23, 506.57, 581.27, 688.37, 783.10, 900.53, 1017.03])

def capillary_fill_analysis_gui(w, h, L, mu, gamma, theta_deg,
   theta_top_deg, t_exp, x_exp, t_exp2, x_exp2, show_experimental,
   target_fill_time):
    theta = np.deg2rad(theta_deg)
    theta_top = np.deg2rad(theta_top_deg)

    Pc = gamma * ((np.cos(theta) + np.cos(theta_top)) / h + 2 * np.
       cos(theta) / w)
    R0 = 12 * mu / (w * h**3 * (1 - 0.63 * h/w))

    R_full = R0 * L
    A = w * h
    t_steady = (R_full * A * L) / Pc

    t_vals = np.linspace(1e-9, target_fill_time, 500)
    x_vals = np.sqrt((2 * Pc / R0) * t_vals)
    R_vals = R0 * x_vals
    Q_vals = Pc / R_vals

    x_target = L
    t_at_max_x = np.interp(x_target, (x_vals * 1e3), t_vals)
    ratio_steady_to_max = t_steady / t_at_max_x

    mins_theoretical, secs_theoretical = divmod(t_at_max_x, 60)

    fig, axs = plt.subplots(1, 2, figsize=(10, 5))
    axs = axs.flatten()

    axs[0].plot(t_vals, x_vals * 1e3, label="Theoretical")
    axs[0].axvline(x=t_at_max_x, color='gray', linestyle='--',
       linewidth=1.5,
```

```
                label=f"Theoretical Time to L = {int(
                    mins_theoretical)}m {secs_theoretical:.1f}s")

    if show_experimental:
        axs[0].scatter(t_exp, x_exp * 1e3, color='red', label="
            Experimental Replicate 1")
        axs[0].scatter(t_exp2, x_exp2 * 1e3, color='blue', label="
            Experimental Replicate 2")

    axs[0].set_ylabel("Filled Length (m)")
    axs[0].set_xlabel("Time (s)")
    axs[0].set_title("Capillary Filling Dynamics")
    axs[0].minorticks_on()
    axs[0].grid(True, which='both', linestyle=':', linewidth=0.5,
        alpha=0.5)
    axs[0].legend()

    # Calculate error
    x_theoretical_at_exp = np.interp(t_exp, t_vals, x_vals)
    x_theoretical_at_exp2 = np.interp(t_exp2, t_vals, x_vals)
    percentage_error_1 = np.mean(np.abs(x_exp - x_theoretical_at_exp
        ) / x_theoretical_at_exp * 100)
    percentage_error_2 = np.mean(np.abs(x_exp2 -
        x_theoretical_at_exp2) / x_theoretical_at_exp2 * 100)

    results = [
        ["Width ( m )", f"{w*1e6:.0f}"], ["Height ( m )", f"{h*1e6
            :.0f}"], ["Length (mm)", f"{L*1e3:.1f}"],
        ["Viscosity (mPa s)", f"{mu*1e3:.2f}"], ["Surface tension (
            N/m)", f"{gamma:.3f}"],
        ["Capillary pressure (Pa)", f"{Pc:.2f}"], ["Resistance (
            Pa s/m )", f"{R0:.2e}"],
        ["Approx fill time", f"{int(*divmod(t_steady, 60))}"], ["
            Summed fill time", f"{int(*divmod(t_at_max_x, 60))}"],
        ["Time ratio", f"{ratio_steady_to_max:.2f}"],
        ["Mean % Error (Rep 1)", f"{percentage_error_1:.2f}"], ["
            Mean % Error (Rep 2)", f"{percentage_error_2:.2f}"]
```

```
    ]

    axs[1].axis("off")
    axs[1].table(cellText=results, loc="center", cellLoc="center",
       colWidths=[0.8, 0.2]).scale(1,2)

    plt.tight_layout()
    plt.show()

def run_analysis():
    try:
        w = float(entry_w.get()) * 1e-6
        h = float(entry_h.get()) * 1e-6
        L = float(entry_L.get()) * 1e-3
        mu = float(entry_mu.get()) * 1e-3
        gamma = float(entry_gamma.get())
        theta_deg = float(entry_theta.get())
        theta_top_deg = float(entry_theta_top.get())
        target_fill_time = float(entry_target_fill_time.get())
        show_exp = plot_exp_data.get()

        capillary_fill_analysis_gui(w, h, L, mu, gamma, theta_deg,
           theta_top_deg, t_exp, x_exp, t_exp2, x_exp2, show_exp,
           target_fill_time)
    except Exception as e:
        messagebox.showerror("Error", str(e))

# GUI
root = tk.Tk()
root.title("Capillary Fill Time Calculator")

# GUI input layout
labels = ["Width ( m ):", "Height ( m ):", "Length (mm):",
          "Side/Bottom Contact Angle (  ):", "Top Contact Angle (  )
             :",
          "Viscosity (mPa s):", "Surface Tension (N/m):", "Target
             Fill Time (s):"]
```

```
defaults = ["600", "250", "500", "47.128", "65.94", "0.89", "0.0318"
    , "900"]
entries = []

for i, (label, default) in enumerate(zip(labels, defaults)):
    tk.Label(root, text=label).grid(row=i, column=0)
    e = tk.Entry(root)
    e.insert(0, default)
    e.grid(row=i, column=1)
    entries.append(e)

entry_w, entry_h, entry_L, entry_theta, entry_theta_top, entry_mu,
    entry_gamma, entry_target_fill_time = entries

plot_exp_data = tk.BooleanVar(value=True)
tk.Checkbutton(root, text="Show Experimental Data", variable=
    plot_exp_data).grid(row=8, column=0, columnspan=2)
tk.Button(root, text="Run Analysis", command=run_analysis).grid(row
    =9, column=0, columnspan=2, pady=10)

root.mainloop()
```

Listing A.1: Capillary fill time simulation and GUI overlay for experimental data

A.2.5 Derivation of Junction Pressures

Full derivations for junction pressures under MCR operation are included here for completeness. The final result is also presented in Chapter 2:

$$P_{J_i} = \frac{P_P R_{out} + P_i R_{in}}{R_{in} + R_{out}} \tag{A.2}$$

This derivation relies on:

- Kirchhoff's current law
- Ohm's law fluidic analog
- Assumption of series resistances

For a full step-by-step walkthrough, see the following pages.

Kirchoff's current law:

$$Q_{in} = Q_{out} \tag{A.3}$$

Earlier, we established that the hydraulic analogy to the Ohm's law can be used to substitute flow rate with a relationship between pressure differential and resistance:

$$\frac{\Delta P_{in}}{R_{in}} = \frac{\Delta P_{out}}{R_{out}} \tag{A.4}$$

We can substitute the pressure differential terms using our circuit diagram by taking the difference of pressure from the branch to the junction and the junction to pump, establishing a new term we'll be solving for: **junction pressure,** P_{J_1}.

$$\frac{P_{J_1} - P_1}{R_{in}} = \frac{P_P - P_{J_1}}{R_{out}} \tag{A.5}$$

Given that the resistors in the Q_{in} and Q_{out} pathways are all in series, the resistances in and out are summations of the sequential resistances of the segments of channels:

$$R_{in} = R_{RBV_1} + R_{R_1} + R_{SV_1} \tag{A.6}$$

$$R_{out} = R_{MR} + R_P \tag{A.7}$$

We then solve for P_{J_1}. For simplification, the resistances will be kept symbolic.

$$\frac{P_{J_1}}{R_{in}} - \frac{P_1}{R_{in}} = \frac{P_P}{R_{out}} - \frac{P_{J_1}}{R_{out}}$$

$$\frac{P_{J_1}}{R_{in}} + \frac{P_{J_1}}{R_{out}} = \frac{P_P}{R_{out}} + \frac{P_1}{R_{in}}$$

$$P_{J_1}\left(\frac{R_{out} + R_{in}}{R_{in}R_{out}}\right) = \frac{P_P R_{out} + P_1 R_{in}}{R_{in}R_{out}}$$

$$P_{J_1} = \left(\frac{\cancel{R_{in} R_{out}}}{R_{in} + R_{out}} \right) \frac{P_P R_{out} + P_1 R_{in}}{\cancel{R_{in} R_{out}}}$$

This gives us an equation for the junction pressure:

$$P_{J_1} = \frac{P_P R_{out} + P_1 R_{in}}{R_{in} + R_{out}} \tag{A.8}$$

If we did this derivation for every branch, we'd see that this equation can be generalized across all branches as:

$$\boxed{P_{J_i} = \frac{P_P R_{out} + P_i R_{in}}{R_{in} + R_{out}}} \tag{A.9}$$

Visuals to aid in this completed derivation can be found in Chapter 2

A.2.6 Note on Duplication

Governing equations for capillary pressure, resistance, and flow rate are presented in full in Chapter 2. To avoid redundancy, they are not included here.

A.3 Capillary Pressure Modeling for Domino Valves

This appendix includes the full Jupyter Notebook export for simulating capillary pressures in a domino valve chain. It has been converted to PDF for readability and reproducibility. The simulation models burst thresholds across plugs and visualizes whether junction pressures are sufficient to trigger failure.

Document: *DVCalc_jupyter.pdf*

DominoValveCalculator_dissertation

July 17, 2025

1 Authors

- Created on Wed Jun 15 2016 by Ayokunle Olanrewaju
- Edited on Tue May 17 2022 by Kelsey Leong
- Edited on Thu Mar 23 2023 by Cosette Craig
- Finalized for dissertation on Wed Apr 2 2025 by Cosette Craig

1.0.1 Import libraries for math and plotting

[1]:
```
import numpy as np
import matplotlib.pyplot as plt
```

1.0.2 Constants in SI units (water properties used as example)

[2]:
```
viscosity = 8.9e-4
surfTension = 0.073
```

1.0.3 Contact angles (from contact angle measurement on 4/8/22)

[3]:
```
thetaTopAdvancing = np.pi * 114/180
thetaTopReceding = np.pi * 89/180
thetaBottomAdvancing = np.pi * 36.6/180
thetaBottomReceding = np.pi * 36.6/180
```

1.0.4 3D printing parameters

These pixel sizes can be used as a factor of dimensions to make designs with discrete, pixel-calibrated designed dimensions.

[4]:
```
xPixelSize = 40e-6 # for width calculations
yPixelSize = 40e-6 # for length calculations
zPixelSize = 50e-6 # for depth calcuations
```

1.0.5 Functions for governing equations

[5]:
```
def flowResistance(w,h,l):
    a = min(w,h)
    b = max(w,h)
    flowRes = ((12*viscosity*l)/(1-0.63*(a/b)))*(1/(b*a**3))
    return flowRes

def capPressure(w, h, thetaTopWall, thetaSideWalls):
    capPressure = surfTension*(2*np.cos(thetaSideWalls)/w + np.
 ↪cos(thetaSideWalls)/h + np.cos(thetaTopWall)/h)
    return capPressure

def junctionpress(Qin_res, Qout_res, Qin_press, Qout_press):
    Pj = (Qin_res*Qout_press + (Qout_res*Qin_press)) / (Qin_res + Qout_res)
    return Pj

def Volume(w,h,l):
    V = w*h*l
    return V

def drainTime(flowRate,w,h,l):
    time=(w*h*l)/flowRate
    hours = time/3600
    return hours
```

1.0.6 Import library for reading in a table of dimensions

[6]:
```
import pandas as pd
dims = pd.read_csv("~/Desktop/DimensionsUI.csv")
print(dims)
```

```
                             Unnamed: 0     Unnamed: 1  Width (µm)  \
0  Retention Valve upstream of stop valve            NaN         200
1     Retention Valve at top of reservoir            NaN         200
2                          Capillary Pump  Flow Resistor         150
3                                     NaN     Pump lines         150
4                                     NaN      Feed rows         150
5                          RBV @ branch 0            NaN         200
6                          RBV @ branch 1            NaN        3000
7                            Main Channel            NaN         400
8                               Reservoir       Branch 1        1000
9                                     NaN   Branches 2-7         700

   Height (µm)  Length (µm)
0          100         1500
1          500          200
```

2	200	20000
3	100	4000
4	100	850
5	500	16000
6	500	15000
7	500	26750
8	500	4500
9	500	4500

2 Pressure, volume, and resistance calculations

2.0.1 Stop valves

Dimensions

[7]:
```
r = 0
RVstopw = dims.values[r,2]*10**-6 # m
RVstoph = dims.values[r,3]*10**-6 # m
RVstopl = dims.values[r,4]*10**-6 # m
```

Capillary pressure, volume, and resistance

[8]:
```
pressRVstop = capPressure(RVstopw, RVstoph, thetaTopReceding,␣
↪thetaBottomReceding)
volRVstop = Volume(RVstopw, RVstoph, RVstopl)
resRVstop = flowResistance(RVstopw, RVstoph, RVstopl)
```

2.0.2 Retention valves

Dimensions

[9]:
```
r = 1
RVresw = dims.values[r,2]*10**-6 # m
RVresh = dims.values[r,3]*10**-6 # m
RVresl = dims.values[r,4]*10**-6 # m
```

Capillary pressure, volume, and resistance

[10]:
```
pressRVres = capPressure(RVresw, RVresh, thetaTopReceding, thetaBottomReceding)
volRVres = Volume(RVresw, RVresh, RVresl)
resRVres = flowResistance(RVresw, RVresh, RVresl)
```

2.0.3 Main resistor and capillary pump

[11]:
```
r = 2
widthFR= dims.values[r,2]*10**-6 # m
heightFR = dims.values[r,3]*10**-6 # m
lengthFR = dims.values[r,4]*10**-6 # m
```

Pump lines are the vertical/parallel segments of the capillary pump

[12]:
```
r = 3
widthPumpLine = dims.values[r,2]*10**-6 # m
heightPumpLine = dims.values[r,3]*10**-6 # m
lengthPumpLine = dims.values[r,4]*10**-6 # m
```

Feed rows are the horizontal, series segments of the capillary pump.

[13]:
```
r = 4
widthPumpFeedRow = dims.values[r,2]*10**-6 # m
heightPumpFeedRow = dims.values[r,3]*10**-6 # m
lengthPumpFeedRow = dims.values[r,4]*10**-6 # m
```

Equivalent resistance was found by solving for the parallel and series connections of feed rows and pump lines from the main feed Work shown here: https://miro.com/app/board/uXjVMdZSLvk=/

[14]:
```
R0 = flowResistance(widthFR,heightFR,lengthFR)

Rp1 = flowResistance(widthPumpLine, heightPumpLine, lengthPumpLine)
Rp2 = Rp1 # all pump lines are identical in dimensions
Rp3 = Rp1 # all pump lines are identical in dimensions

Rf1 = flowResistance(widthPumpFeedRow, heightPumpFeedRow, lengthPumpFeedRow)
Rf2 = Rf1 # all feed rows are identical in dimensions
```

Total length of pump assuming that cross-sectional area of channels is constant across the main feed, pump lines, and feed rows

[15]:
```
n = 3 # branches of the capillary pump
lengthTotalPump = (n*lengthPumpLine) + ((n-1)*lengthPumpFeedRow) # m
```

!!!! when calculating capillary pressure of pump, use "Advancing contact angle of the Top cover

[16]:
```
pressPump =␣
  ↪capPressure(widthPumpLine,heightPumpLine,thetaTopAdvancing,thetaBottomAdvancing)
volPump = Volume(widthPumpLine,heightPumpLine,lengthTotalPump)
resPump = ((1/Rp1) + (1/(Rf1 + Rp2)) + (1/(Rf2 + Rp3)))**-1
```

2.0.4 RBV_0

Dimensions

[17]:
```
r = 5
RBV0w = dims.values[r,2]*10**-6 # m
RBV0h = dims.values[r,3]*10**-6 # m
RBV0l = dims.values[r,4]*10**-6 # m
```

Capillary pressure, volume, and resistance

[18]:
```
pressRBV0 = capPressure(RBV0w, RBV0h, thetaTopReceding, thetaBottomReceding)
volRBV0 = Volume(RBV0w, RBV0h, RBV0l)
resRBV0 = flowResistance(RBV0w, RBV0h, RBV0l)
```

2.0.5 RBV_1

Dimensions

[19]:
```
r = 6
RBV1w = dims.values[r,2]*10**-6 # m
RBV1h = dims.values[r,3]*10**-6 # m
RBV1l = dims.values[r,4]*10**-6 # m
```

Capillary pressure, volume, and resistance

[20]:
```
pressRBV1 = capPressure(RBV1w, RBV1h, thetaTopReceding, thetaBottomReceding)
volRBV1 = Volume(RBV1w, RBV1h, RBV1l)
resRBV1 = flowResistance(RBV1w, RBV1h, RBV1l)
```

2.0.6 RBV_1

Dimensions

[21]:
```
r = 7
RBV1w = dims.values[r,2]*10**-6 # m
RBV1h = dims.values[r,3]*10**-6 # m
RBV1l = dims.values[r,4]*10**-6 # m
```

Capillary pressure, volume, and resistance

[22]:
```
pressMain = capPressure(RBV1w, RBV1h, thetaTopReceding, thetaBottomReceding)
volMain = Volume(RBV1w, RBV1h, RBV1l)
resMain = flowResistance(RBV1w, RBV1h, RBV1l)
```

2.1 Reservoirs

2.1.1 Branch 1

Dimensions

[23]:
```
r = 8
R1w = dims.values[r,2]*10**-6 # m
R1h = dims.values[r,3]*10**-6 # m
R1l = dims.values[r,4]*10**-6 # m
```

Capillary pressure, volume, and resistance

[24]:
```
P1 = capPressure(R1w, R1h, thetaTopReceding, thetaBottomReceding)
V1 = Volume(R1w, R1h, R1l)
R1 = flowResistance(R1w, R1h, R1l)
```

2.1.2 Branches 2-4

Dimensions

[25]:
```
r = 9
R2w = dims.values[r,2]*10**-6 # m
R2h = dims.values[r,3]*10**-6 # m
R2l = dims.values[r,4]*10**-6 # m
```

Capillary pressure, volume, and resistance

[26]:
```
P2 = capPressure(R2w, R2h, thetaTopReceding, thetaBottomReceding)
V2 = Volume(R2w, R2h, R2l)
R2 = flowResistance(R2w, R2h, R2l)

P3 = P4 = P2
V3 = V4 = V2
R3 = R4 = R2
```

2.2 Calculated pressures and resistances:

[27]:
```
print('\nCapillary Pressures (Pa) \n')
print('Stop valves: ', "{:.2f}".format(pressRVstop))
print('Retention Valves: ', "{:.2f}".format(pressRVres))
print('Capillary Pump: ', "{:.2f}".format(pressPump))
print('Retention Burst Valve @ branch 0: ', "{:.2f}".format(pressRBV0))
print('Retention Burst Valve @ branch 1: ', "{:.2f}".format(pressRBV1))

print('\nResistances, (Pa*s/m^3)\n')
print('Main Resistor: ', "{:.2e}".format(R0))
print('Stop Valves: ', "{:.2e}".format(resRVstop))
print('Retention Valves: ', "{:.2e}".format(resRVres))
print('Equivalent Resistance of pump: ', "{:.2e}".format(resPump))
print('Main Channel: ', "{:.2e}".format(resMain))
print('Retention Burst Valve @ branch 0: ', "{:.2e}".format(resRBV0))
print('Retention Burst Valve @ branch 1: ', "{:.2e}".format(resRBV1))
```

```
Capillary Pressures (Pa)

Stop valves:  1184.85
Retention Valves:  705.82
Capillary Pump:  1070.55
Retention Burst Valve @ branch 0:  705.82
Retention Burst Valve @ branch 1:  158.83

Resistances, (Pa*s/m^3)
```

```
Main Resistor:  6.00e+11
Stop Valves:  1.17e+11
Retention Valves:  7.14e+08
Equivalent Resistance of pump:  1.85e+11
Main Channel:  1.80e+10
Retention Burst Valve @ branch 0:  5.71e+10
Retention Burst Valve @ branch 1:  4.77e+08
```

3 Junction pressures

3.0.1 Calculations

[29]:
```
def getjunctionpressures():
    # split the main channel into sections
    R_m = resMain/4

    # Junction Pressures
    Qin_res = [(resRVstop+R1+resRBV1),(resRVstop+R2+R_m),(resRVstop+R3+2*R_m),
               (resRVstop+R4+3*R_m),(resRVstop+resRBV0+4*R_m)]
    Qout_res = [(R0+resPump),(R0+resPump+R_m),(R0+resPump+2*R_m),
                (R0+resPump+3*R_m),(R0+resPump+4*R_m)]

    Qin_press = [pressRBV1, P2, P3, P4, pressRBV0]
    Qout_press = [pressPump] * 5

    Pj = []

    for i in range(0,5):
        Pj.append(junctionpress(Qin_res[i], Qout_res[i], Qin_press[i],␣
 ↪Qout_press[i]))

    # Resting branch pressures
    # Qout_res and Q_out press stay the same

    restingQin_res = [(resRVstop+R1+resRBV1),(resRVstop+R2+R_m+resRVres),
                      ␣
 ↪(resRVstop+R3+2*R_m+resRVres),(resRVstop+R4+3*R_m+resRVres),
                       (resRVstop+resRBV0+4*R_m)]
    restingpressures = [pressRBV1,pressRVres,pressRVres,pressRVres,pressRBV0]
    return restingpressures, Qin_press, Pj

def createjunctionpressureplot():
    restingpressures, Qin_press, Pj = getjunctionpressures()

    fig,ax = plt.subplots(2,3,figsize = (10,6))
    ax[1][2].set_visible(False)
    fig.tight_layout(pad=3.0)
```

```
    labels = ['P1','P2','P3','P4','P0']
    burstcolors = ['r','g','g','g','g']

    a = ax.flatten()

    a[0].bar(labels, restingpressures, color = burstcolors,width = 0.4)
    a[0].axhline(y = Pj[0], color = 'k', linestyle = '--')
    a[0].set_xticks(range(0,5))
    a[0].set_xticklabels(('$P_{1}$', '$P_{2}$', '$P_{3}$','$P_{4}$','$P_{0}$'))
    a[0].set_ylabel('|Capillary Pressure|, [Pa]')
    a[0].annotate('$|P_{J}|$=%d' % Pj[0],xy=(0,Pj[0]),xytext=(-0.
↪7,Pj[0]+40),color='k')
    a[0].set_ylim(0,900)
    a[0].set_xlim(-0.75,4.75)

    plotpressures = restingpressures

    for i in range(1,5):
        plotpressures[i] = Qin_press[i]
        burstcolors[i-1], burstcolors[(i)] = '0.95', 'r'
        a[i].bar(labels, plotpressures, color =burstcolors, width = 0.4)
        a[i].axhline(y = Pj[i], color = 'k', linestyle = '--')
        a[i].set_xticks(range(0,5))
        a[i].set_xticklabels(('$P_{1}$', '$P_{2}$',␣
↪'$P_{3}$','$P_{4}$','$P_{0}$'))
        a[i].set_ylabel('|Capillary Pressure|, [Pa]')
        a[i].annotate('$|P_{J}|$=%d' % Pj[i],xy=(0,Pj[i]),xytext=((-0.
↪7+i),Pj[i]+40),color='k')
        a[i].set_ylim(0,900)
        a[i].set_xlim(-0.75,4.75)

def showjunctionpressureplot():
    createjunctionpressureplot()
    plt.show()

####################################

export_dict = {
    'Element': ['Flow Resistor',
                'Retention Valve upstream of stop valve',
                'Retention Valve at top of reservoir',
                'Capillary Pump',
                'Main Channel',
                'Retention Burst Valve @ branch 0',
                'Retention Burst Valve @ branch 1'],
    'Pressure (Pa)':␣
↪['na',pressRVstop,pressRVres,pressPump,'na',pressRBV0,pressRBV1],
```

```
    'Resistance (Pa*s/m^3)':␣
 ↪[R0,resRVstop,resRVres,resPump,resMain,resRBV0,resRBV1]
}

calc = pd.DataFrame(export_dict)

df = pd.concat([dims,calc], axis = 1)
```

4 User Interface for saving file version

[30]:
```
import tkinter as tk

root = tk.Tk()
root.title("Filename")
h = 300
w = 350
root.geometry(("%dx%d" % (w,h)))

buttonframe = tk.Frame(root)
buttonframe.pack()

pad = w/10

def savefile():
    # Import the current date and time
    from datetime import datetime
    str_current_datetime = str(datetime.now().date())

    # Make an empty string variable to hold the filename
    filename_var = tk.StringVar()
    filename_label = tk.Label(root, text = 'Filename')
    filename_entry = tk.Entry(root, textvariable = filename_var)

    def submit(e):
        suffix = filename_var.get()
        filename_var.set("")
        print(suffix)

        filename = str_current_datetime + '_' + suffix + '.xlsx'
        plotfilename = str_current_datetime + '_' + suffix + '.png'
        saved_label = tk.Label(root, text = filename + ' and ' + plotfilename +␣
 ↪' Saved!')
        saved_label.pack()
```

```
        df.to_excel(filename, index=False)

        createjunctionpressureplot()
        plt.savefig(plotfilename)

        done = tk.Button(root, text = "Done", command = root.destroy)
        done.pack()

    filename_label.pack()
    filename_entry.pack()

    root.bind('<Return>', submit)

save = tk.Button(buttonframe, text="Save As", command=savefile)
save.pack( side = 'left', padx = pad, pady = pad)

dontsave = tk.Button(buttonframe, text="Don't Save", command = root.destroy)
dontsave.pack(side = 'left', padx =pad, pady=pad)

junctionplot = tk.Button(root,command=showjunctionpressureplot,text = 'Show␣
 ↪Junction Pressure Plot')
junctionplot.pack()

root.mainloop()
```

```
2025-04-02 15:25:19.820 Python[57002:2720940] WARNING: Secure coding is not
enabled for restorable state! Enable secure coding by implementing
NSApplicationDelegate.applicationSupportsSecureRestorableState: and returning
YES.
```

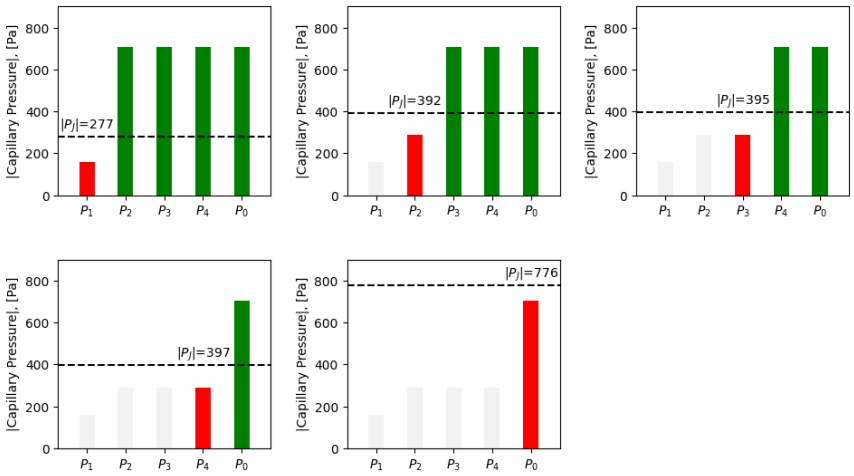

A.4 3D Printing Standard Operating Procedure

This section contains the full standard operating procedure (SOP) for preparing and executing prints of capillaric devices using our LCD 3D printer. It complements the fabrication techniques discussed in Chapter 2 and serves as a practical reference for users replicating designs or developing new geometries.

Document: *printSOP.pdf*

A Guide to Fabrication of Capillary-Driven Microfluidic Devices with Liquid Crystal Display 3D Printers

This article is intended for anyone who is exploring low-cost microfluidic device fabrication with liquid crystal display (LCD) 3D printers. Microfluidic devices enable the manipulation of fluids at the microscale (1-1000 µm), potentially miniaturizing and automating liquid handling across a wide range of applications[1]. These applications include diagnostics, bioreactors, and microphysiological systems[2–4]. Recent advances in low-cost LCD 3D printers have the potential to broaden access to high-resolution 3D printing[5].

This article provides a guided walkthrough of fabricating microfluidic devices using LCD 3D printers, from design to the final printed part. The following topics will be addressed:

Table of Contents

1 BACKGROUND ON LCD 3D PRINTER TECHNOLOGY 2

2 IMPLEMENTATION 3

2.1 CAD DESIGN 3
2.2 SLICING 3
2.2.1 Slice Settings 4
2.2.2 Slicing Walkthrough 4
2.3 PRINTING 9
2.3.1 Preparation 9
2.3.2 Post Processing 13
2.4 CHARACTERIZATION 14
2.5 PLASMA TREATING/SEALING 19

3 REFERENCES 20

1 Background on LCD 3D Printer Technology

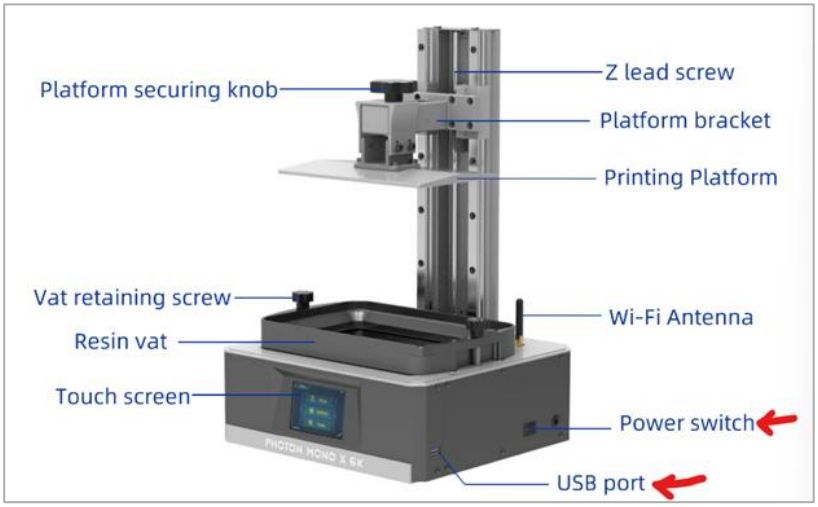

- **How LCD 3D Printers Work:** LCD 3D printers use an LCD screen to selectively mask ultraviolet (UV) light, which cures a photosensitive resin, layer by layer, to create a 3D object. This process is known as masked stereolithography (mSLA). LCD printers are a cost-effective alternative to digital light processing (DLP) printers, which use a projector to selectively polymerize photosensitive resin. The Olanrewaju lab uses primarily LCD printers due to their lower price point with relatively insignificant loss in print resolution[5].
- **Resolution and Pixel Size:** The resolution of a 3D printer is determined by its pixel size. The Anycubic Photon Mono X 6K has a specified XY resolution of 34.4 µm and a Z axis accuracy of 10 µm. The pixel size affects the level of detail that the printer can achieve, with smaller pixel sizes correlating to higher detail.
- **Key Components**
  - Build Plate: Where the 3D printed object is formed.
  - Resin Vat: Holds the liquid resin that is cured by the UV light.
  - LCD Screen: Modulates the UV light to cure the resin in a specific pattern.
  - Light Source: Provides the UV light needed for curing.
- **Software for 3D Printing:** A slicing software is used to convert a 3D model into layers that the printer can read. Examples of slicing software include Photon Workshop, which is compatible with Anycubic printers, and Chitubox, which is compatible with many printers.

2 Implementation

2.1 CAD Design

We use SolidWorks to design our microfluidic chips in the Olanrewaju Lab, but a free 3D CAD platform like Onshape will work. The key thing to keep in mind is that your model needs to align with the pixel grid of your printer, otherwise the parts will not print correctly. In our designs, we use global variables based on the pixel dimensions of the 3D printer to make the designs easily adapted to different printers.

- Example microfluidic chip: Pixel Test Chip (courtesy of Carrie Lin)

2.2 Slicing

A slicing software is used to convert 3D models into layers that a 3D printer can read. Slicers allow a user to configure how the part will print. This article goes into depth about slicing.

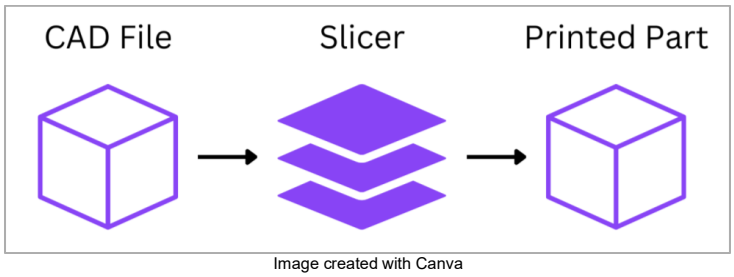

Image created with Canva

A slicing software cuts the input 3D model into horizontal slices. Each slice forms a single layer of the print. Slicers provide control over how each layer prints via “Slice Settings.” These slicing settings are different based on your slicer software, version of that software, and printer type. Some settings can only be altered directly on the printer itself, such as **Exposure Intensity**.

These settings generally present a tradeoff between the amount of time the part will take to print and print quality. When changing these settings, you also need to consider the chemical behavior of the polymerization process that resin printers use. This comes into play when considering how higher light intensities and longer exposure times can create off-target polymerization, occluding microfluidic features.

Below is a list of Slice Settings and their general effects that roughly follows the options available for the Anycubic Photon Mono X 6K in Chitubox V2.3. If you are using a different Slicer, or a different version of Chitubox, these settings may appear different, but you will most likely be able to find close analogs to those listed below.

2.2.1 Slice Settings

Layer thickness: Height of each cured layer of the print. Thinner layers increase overall print time but can improve print fidelity.

Normal exposure time: Amount of time the light source is turned on to cure each layer. Different resins take different times to cure. Due to light scattering through the resin, longer exposure times can cause resin to harden in off-target locations. This can occlude small features like microfluidic channels.

Bottom Exposure Time and **Bottom Layers:** Control the first few layers of the print. These first layers of the print are responsible for adhering the base of the print to the build plate. A larger number of bottom layers with increased exposure times will attach the print more securely without much effect on any microfluidic features in the upper layers but will increase print time.

Transition Settings: Controls the transition between the base layers and the top layers. If your print breaks or has an abrupt change between the bottom and top layers, more transition layers, or a smoother transition may be needed.

Z Lift Settings: Controls the distance and speed at which the build plate moves up and down from the resin. This changes how resin flows back (reflows) into the space between the print and the Teflon screen of the vat to prepare for printing the next layer. Larger, slower Z Lifts take longer, but improve resin reflow and can lower the intensity of the forces experienced by the print, potentially improving print quality.

Off time: Amount of time the light source is powered off when the build plate is settled at the next layer height. Increasing this increases print time but allows the resin flow back and settle.

Anti-alias: Creates a gray-scale in between black and white pixels. Anti-aliasing smooths out edges between print layers, making surfaces more rounded. For our application, sharp, predictable edges are preferred, so anti-aliasing should be turned off.

Exposure Intensity: Controls the light source intensity. For the Anycubic Photon Mono X 6K, this can only be changed from the printer itself, not from the slicer settings.

Note: Generally, slicers accept only certain file types (e.g. .STL) and only output files of certain other types (e.g. .PWS).

2.2.2 Slicing Walkthrough

In the Olanrewaju Lab, we use Chitubox as one of our slicers. Chitubox is an open-source slicer compatible with multiple printer types. In this slicing walkthrough, we use Chitubox V2.3. If you are using a different software platform or version, your user interface may look different, and you may have different setting options. It may take some experimentation to understand how these settings can be manipulated to optimize your prints.

We design and 3D print calibration chips to confirm that the 3D printing parameters we used are optimal for printing high resolution microfluidic features. We characterize the

quality of the printed microfluidic features by comparing their widths and depths to our designed dimensions. Through the process of characterizing the chip, we make informed alterations to the printer and slice settings to lower the error between the designed and printed parts. Note that our calibration chip was designed specifically for the Anycubic Photon Mono X 6K. This required aligning the chip features to the printer model's pixel grid. You will need to adapt your chip to the pixel size of the printer you are using.

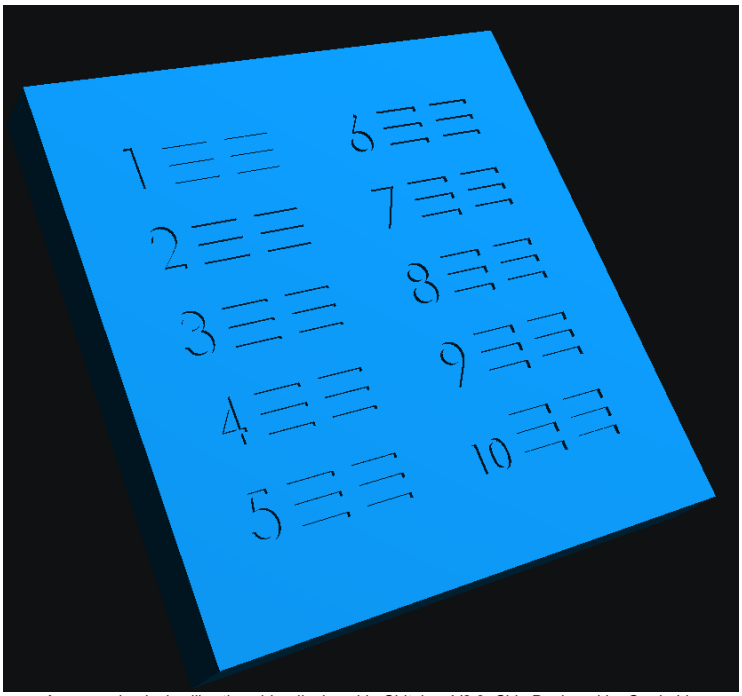

An example pixel calibration chip, displayed in Chitubox V2.3. Chip Designed by Carrie Lin

1. Begin by uploading a 3D model of a calibration chip to the slicing software.

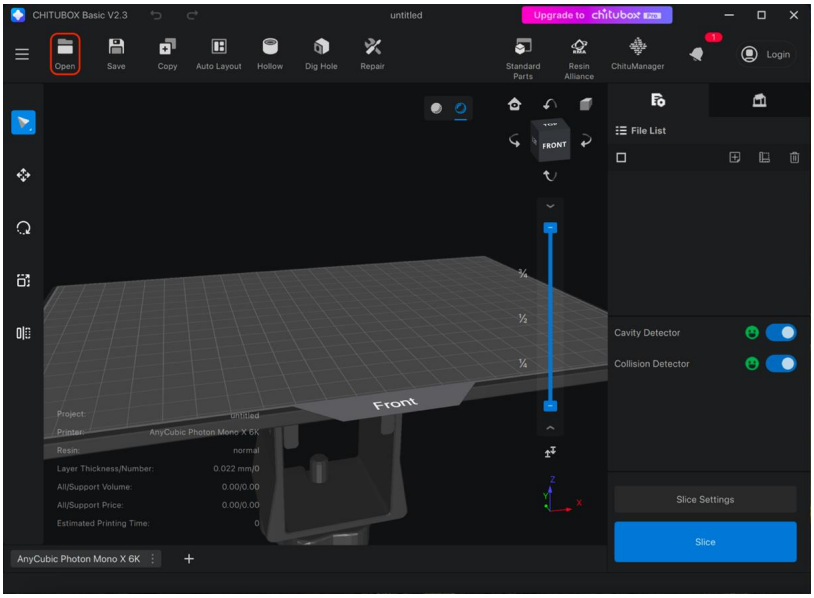

2. Center the part by clicking the four-arrow symbol on the left and clicking centered.

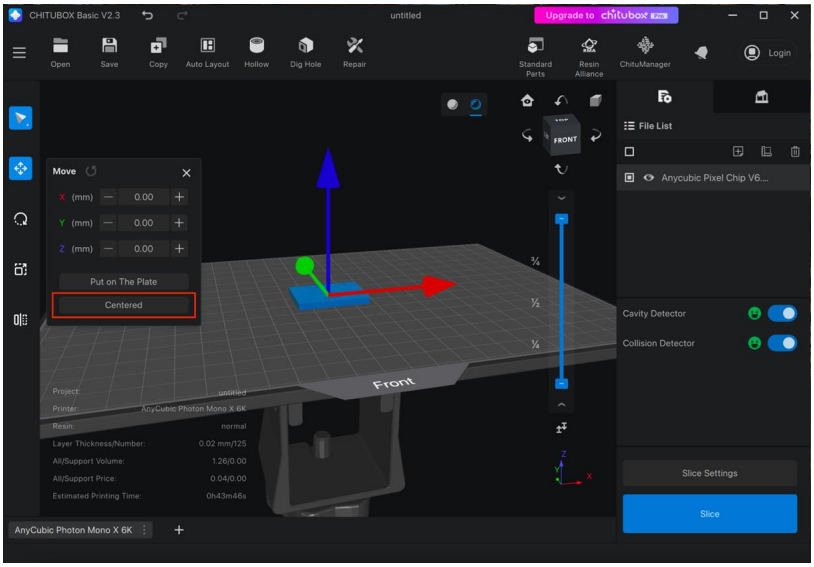

3. Orient the part by clicking on the gimbal beneath the four-arrow symbol. This will allow you to rotate the part. Make sure to rotate the part so that your microfluidic features are on the top surface.

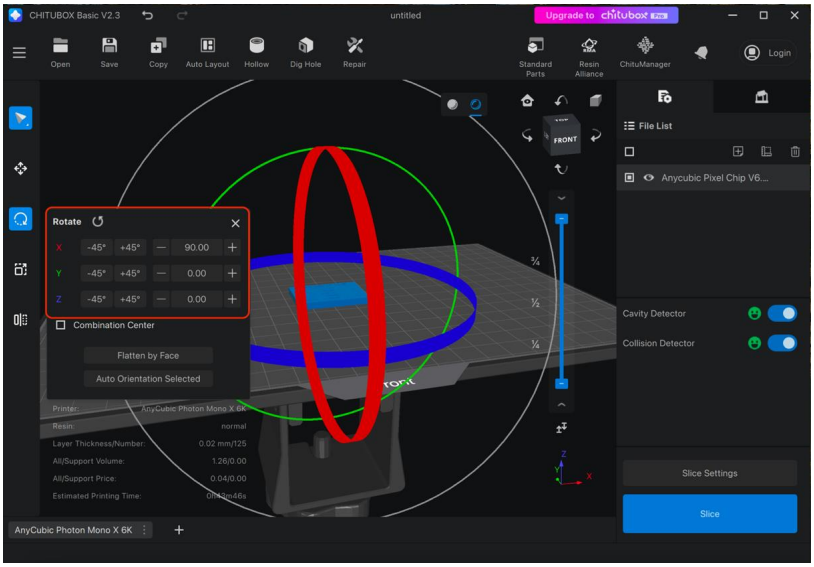
CHITUBOX Basic V2.3
untitled
Upgrade to chitubox pro
Open
Save
Copy
Auto Layout
Hollow
Dig Hole
Repair
Standard Parts
Resin Alliance
ChituManager
Login
File List
Anycubic Pixel Chip V6...
Rotate
X -45° +45° 90.00
Y -45° +45° 0.00
Z -45° +45° 0.00
Combination Center
Flatten by Face
Auto Orientation Selected
Printer: AnyCubic Photon Mono X 6K
Resin: normal
Layer Thickness/Number: 0.02 mm/125
All/Support Volume: 1.26/0.00
All/Support Price: 0.04/0.00
Estimated Printing Time: 0h43m46s
Cavity Detector
Collision Detector
Slice Settings
Slice
AnyCubic Photon Mono X 6K

4. Click the **[Slice Settings]** button on the right side.

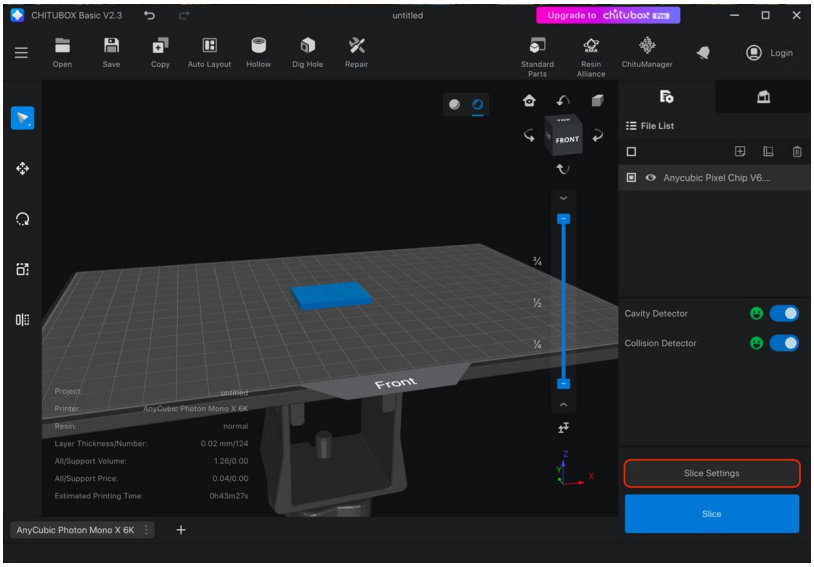

5. Adjust the Slice Settings to optimize printing for your printer and resin. Below are the optimal settings for the Anycubic Photon Mono X 6K with the AnyCubic Water-Wash+ resin (adapted from *Table S1* from *Leong et al., ACS Omega, 2024, 9, 45, 45537-45544*).

Normal Exposure Time (sec)	**Off Time (sec)**	**Bottom Time Exposure (sec)**	**Bottom Layers**
1.8	1	23	6
Layer Thickness (mm)	**Normal Layer Z Lift Speed (mm/s)**	**Normal Layer Z Retract Speed (mm/s)**	**Anti-alias**
0.020	1	1.5	1

6. After adjusting the printer settings, slice and save the part with the **Slice** button on the bottom right. Save the .PWMB file in the root folder of a USB drive.

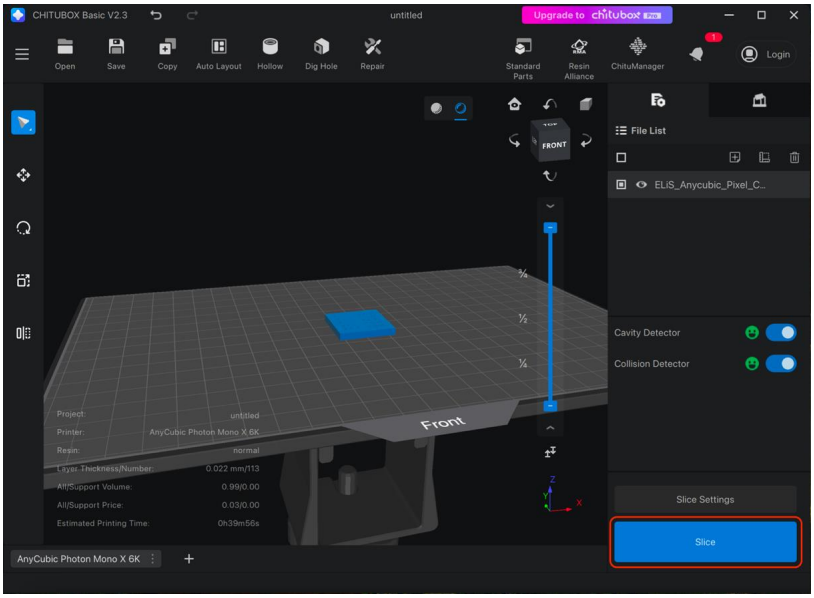

2.3 Printing

We use the Anycubic Photon Mono X 6K 3D printer with the Anycubic Water-Wash+ resin as an example in this document. If you are using a different printer or resin, the overall protocol should be similar. However, it may take some experimentation to find optimal printing parameters and procedures.

2.3.1 Preparation

1. **Personal Protective Equipment (PPE):** Wear a lab coat, safety glasses, gloves, and any other PPE required by your environment. Ensure proper ventilation as 3D printing resins may contain irritants.

2. **Printer Setup:** Power on the printer and insert the USB containing the print file.

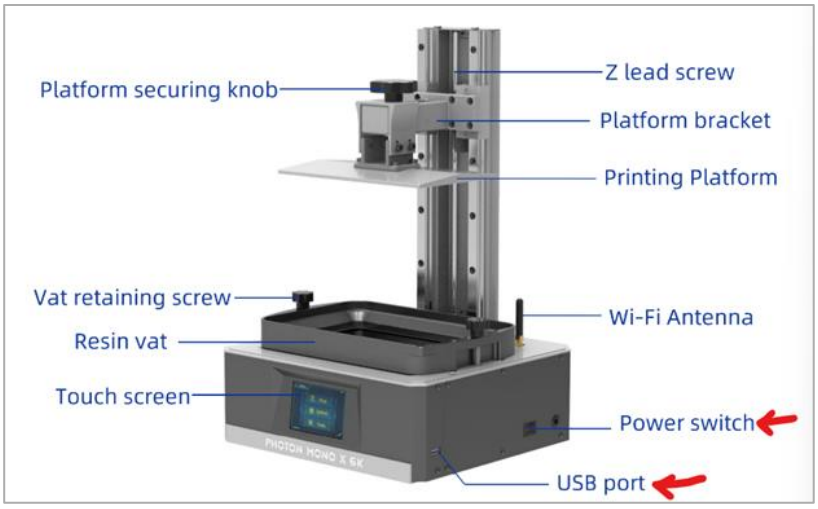

3. **Cleaning**: Inspect the printing platform and resin vat for damage or leftover debris from previous prints.
    a. **Dirty printer components**: Remove the component, clean it with 70% isopropyl alcohol (IPA) and cleanroom wipes, and securely reattach it.
    b. **All components are visually clean:** Use compressed air, if available, to blow any accumulated dust off the components before securely attaching all components to the printer.

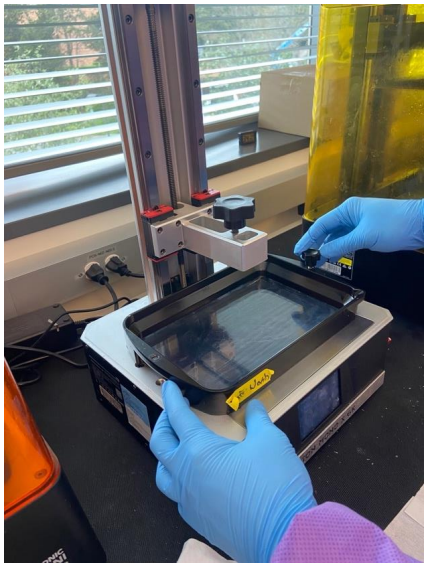

4. **Resin Preparation**: Pour your resin into the vat, ensuring it does not exceed the max fill line. Remove any air bubbles using a thin card.

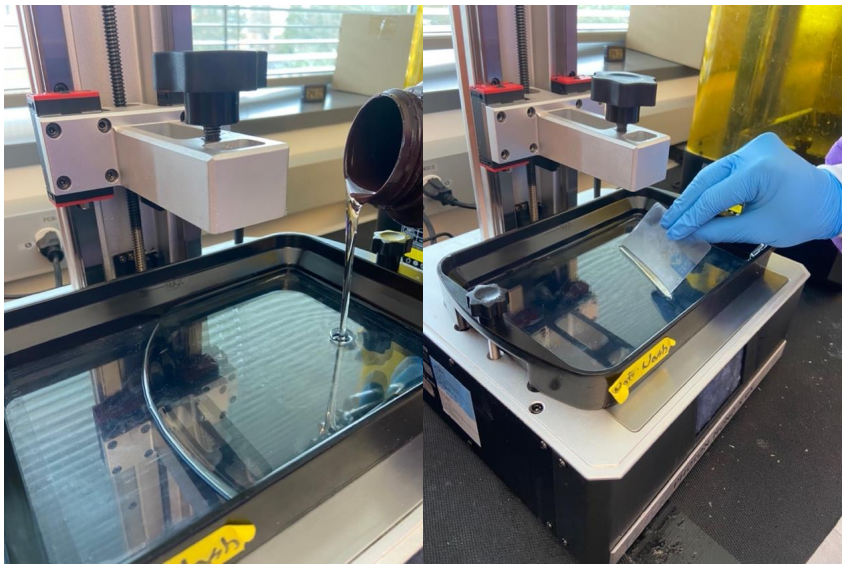

5. **Start Printing**: Replace the cover.

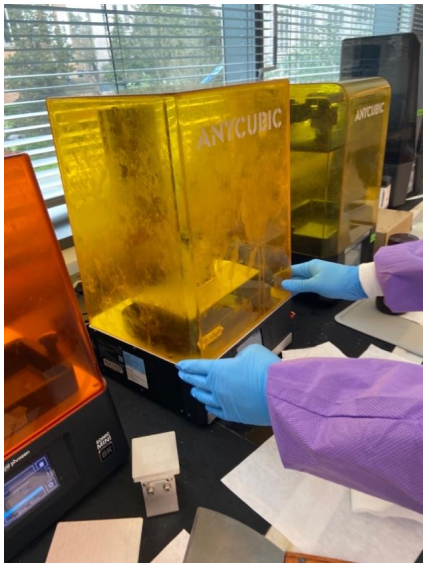

6. Navigate to **[Print]** on the home menu, select the file, and initiate the print.

2.3.2 Post Processing

1. **Part Removal**:
    a. Once printing is complete, remove the cover and detach the build platform.
    b. Allow excess resin to drain into the vat before using a scraper to carefully remove the print.
        - If part removal is difficult, apply 70% IPA to loosen the part.
        - DO NOT use sharp implements like razor blades to loosen the part.

c. To minimize bending or chipping of the chip and build plate, gently scrape under the printed part, keeping the scraping tool as parallel to the platform as possible.

2. **Print Wash**: Our lab uses the Wash and Cure 2.0 from Anycubic. Alternatively, you could use a magnetic stirrer, as long as you have a method for protecting the chip from physical damage from the stir bar.
    a. Holding the part with tweezers, place the part in the basket of the washing machine. Ensure full submersion in 70% IPA.
    b. Secure the lid and start a 2-5 minute wash cycle.
    c. Once the timer ends, lift the basket back up and use tweezers to pick up the part.
    d. Rinse the part with a spray bottle of 70% IPA or DI water. The Anycubic Water-Wash+ is washable with water but 70% IPA washes slightly better.
    e. Spray the part with pressurized air to dry the part and remove any excess resin.
3. **Post Curing**: Our lab uses the Form Cure from Formlabs. For a more affordable alternative, a UV nail lamp could be used to cure chips.
    a. Place the chip in a UV chamber for 30 seconds on each side.
4. **Cleanup**:
    a. Save any excess resin by pouring it into a bottle through a filter. Thoroughly clean all printer parts with 70% IPA and cleanroom wipes before drying and safely storing the printer parts.
    b. Any excess uncured resin will be cured by ambient light. Once it has cured, it will be very difficult to remove. It is important to clean all parts thoroughly to prevent buildup.
    c. This also provides the method for disposing of resin-contaminated waste – towels, filters, etc. The resin should be cured by ambient UV from sunlight or in a curing station before being disposed.

2.4 Characterization

For our characterization process, we use the Keyence VHX-970F Digital Microscope with the 5x-50x and 20-200x zoom lenses. Your process may vary based on the microscope you have access to, and the software it comes with.

1. Place the fully processed chip on the stage of the microscope.

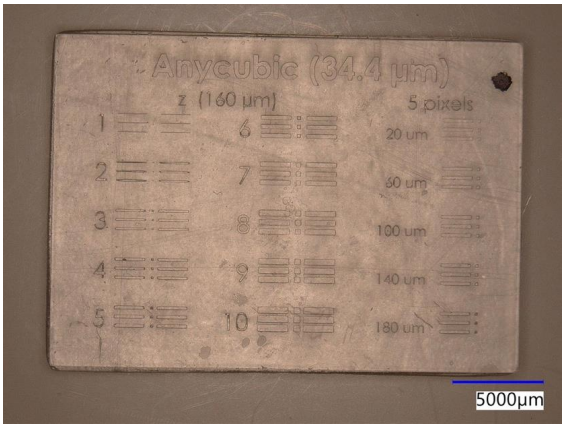

1. Focus the image and save it as a photo using the built-in Keyence utility.
    a. The Keyence VHX-970F offers a lighting profile setting that enables a sure to take images with consistent lighting. This is useful when trying to compare images from trials done on different days with different ambient lighting conditions.
    b. The image above shows some glare, this can indicate incomplete cleaning.
2. Save the image as a .jpg with a descriptive name.
3. Center your view port on the 10-pixel wide channels.
4. Save an image of the channels.

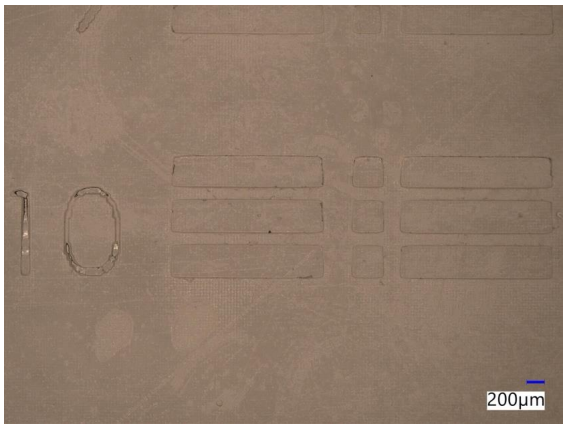

5. Zoom in on 3 of the 6 channels and focus the image.
6. Make sure that the microscope focus clicks into place on one of the discrete focal lengths, or the output dimensions in the images will be incorrect.
7. Use a line measuring tool to select the upper and lower longitudinal edges of the channels. This will output the channel widths.

8. Save an image of the channels with their labeled widths.

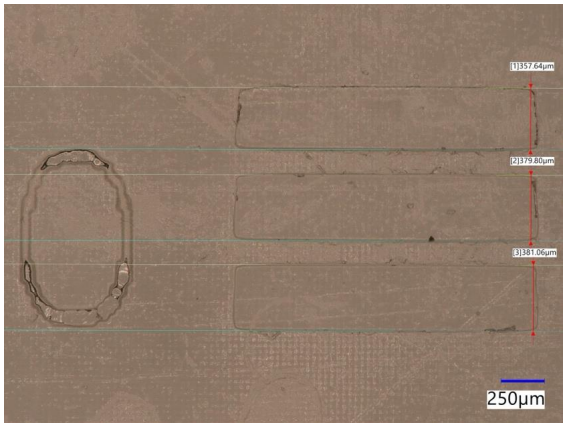

9. Then, we use the Keyence VHX-970F to construct a 3D representation of the portion of the pixel chip in our view port. The following steps may be different for you if you do not have access to the Depth Composition tool or something similar.
    a. Note: If you do not have access to a depth composition tool, an alternative method for measuring depths is to design channels that extend all the way to the edge of the chip. This chip design can be turned onto its side to allow a measurement of the channel profile and depth. An example of this is shown below.

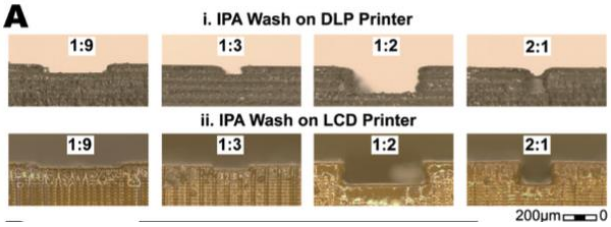

Figure 2A from *Leong et al.*, ACS Omega, *2024, 9, 45, 45537-45544.*

10. Select the Depth Composition tool, and de-focus the microscope by moving the focus below the plane. The tool will run the rest automatically, generating a 3D model of the chip.
11. You can view cross sections of the chip in profile to qualitatively analyze the chip quality. The tool also allows you to compare profiles of the chip to observe consistency along a single channel.

12. Save an image of the 3D representation of the chip and its cross sections.

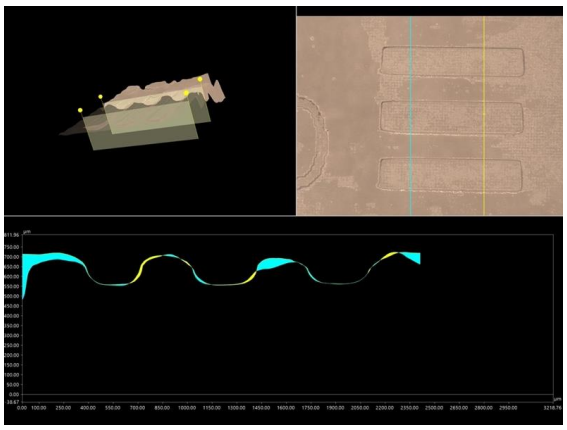

13. Repeat steps 3-12 for all remaining channels widths.
14. Once you have taken all the images, extract the measured widths and depths for each channel type.

15. Compare the designed and measured dimensions of the printed channels by plotting them. A good example of this is Figure 1 parts C and D from *Leong et al.*, ACS Omega, *2024, 9, 45, 45537-45544.*

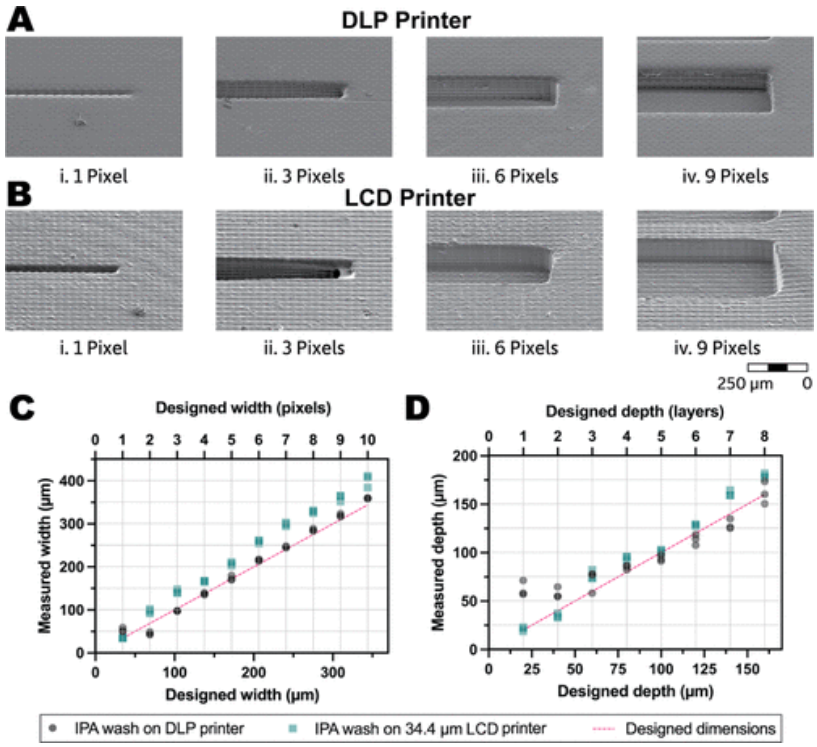

If your percent error is too high (>10%), you can alter the slicing settings to rectify this. We optimize our print parameters to ensure the Percent Error (PE) between the design and measured dimensions falls within 10%, with a Coefficient of Variation (CV) less than 20%.

2.5 Plasma Treating/Sealing

Most resins create hydrophobic parts. Capillary microfluidic applications require hydrophilic surfaces to drive capillary flow. Hydrophilic surfaces form a contact angle of

78* or less with water. In the Olanrewaju Lab, we use a plasma etch to convert the hydrophobic parts to hydrophilic ones.

We use the PlasmaEtch 50 with the following settings to achieve hydrophilicity.

	Plasma Time (mins)	Vacuum set point (mTorr)	Atmospheric vent (min):	Purge vent (sec)	Gas stabilization (sec)	Vacuum Alarm (min)	Auto-cycle off	RF Power
Initial Pump-Down	5	201.1	5	50	50	6	on	56
Plasma Treating Resin	5	201.1	5	50	**20**	6	on	56

Once the printed part has been treated with oxygen plasma, we seal the chip with a hydrophobic tape to create enclosed channels for microfluidic flow.

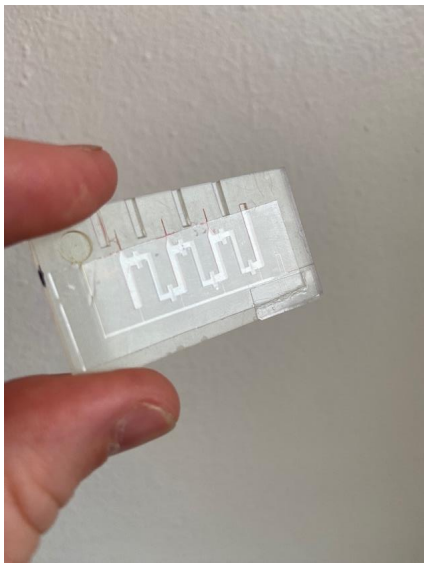

An alternative to using a plasma etch is to use surfactants like Tween or Triton as an additive in the fluid passed through the chip. These surfactants improve the ability of the water to bind to hydrophobic surfaces.[6,7]

3 References

(1) Duncombe, T. A.; Tentori, A. M.; Herr, A. E. Microfluidics: Reframing Biological Enquiry. *Nat. Rev. Mol. Cell Biol.* **2015**, *16* (9), 554–567. https://doi.org/10.1038/nrm4041.

(2) Aydin, O.; Passaro, A. P.; Raman, R.; Spellicy, S. E.; Weinberg, R. P.; Kamm, R. D.; Sample, M.; Truskey, G. A.; Zartman, J.; Dar, R. D.; Palacios, S.; Wang, J.; Tordoff, J.; Montserrat, N.; Bashir, R.; Saif, M. T. A.; Weiss, R. Principles for the Design of Multicellular Engineered Living Systems. *APL Bioeng.* **2022**, *6* (1), 010903. https://doi.org/10.1063/5.0076635.

(3) Chin, C. D.; Laksanasopin, T.; Cheung, Y. K.; Steinmiller, D.; Linder, V.; Parsa, H.; Wang, J.; Moore, H.; Rouse, R.; Umviligihozo, G.; Karita, E.; Mwambarangwe, L.; Braunstein, S. L.; Van De Wijgert, J.; Sahabo, R.; Justman, J. E.; El-Sadr, W.; Sia, S. K. Microfluidics-Based Diagnostics of Infectious Diseases in the Developing World. *Nat. Med.* **2011**, *17* (8), 1015–1019. https://doi.org/10.1038/nm.2408.

(4) Imaoka, T.; Huang, W.; Shum, S.; Hailey, D. W.; Chang, S.-Y.; Chapron, A.; Yeung, C. K.; Himmelfarb, J.; Isoherranen, N.; Kelly, E. J. Bridging the Gap between in Silico and in Vivo by Modeling Opioid Disposition in a Kidney Proximal Tubule Microphysiological System. *Sci. Rep.* **2021**, *11* (1), 21356. https://doi.org/10.1038/s41598-021-00338-y.

(5) Leong, K. M.; Quach, M. L.; Lin, C. H.; Craig, C. A.; Sun, A. Y.; Guo, F.; Robinson, T. R.; Olanrewaju, A. O. Democratizing Access to Microfluidics: Rapid Prototyping of Capillary Microfluidics with a Low-Cost Masked Stereolithography 3D Printer. *bioRxiv* **2023**, 2023.09.26.558021. https://doi.org/10.1101/2023.09.26.558021.

(6) Parandakh, A.; Ymbern, O.; Jogia, W.; Renault, J.; Ng, A.; Juncker, D. 3D-Printed Capillaric ELISA-on-a-Chip with Aliquoting. *Lab. Chip* **2023**, *23* (6), 1547–1560. https://doi.org/10.1039/D2LC00878E.

(7) Shafique, H.; Karamzadeh, V.; Kim, G.; Shen, M. L.; Morocz, Y.; Sohrabi-Kashani, A.; Juncker, D. High-Resolution Low-Cost LCD 3D Printing for Microfluidics and Organ-on-a-Chip Devices. *Lab. Chip* **2024**, *24* (10), 2774–2790. https://doi.org/10.1039/D3LC01125A.

A.5 SOP for Cutting Microfluidic Covertape with the Silhouette Cameo 4

This section includes the full standard operating procedure (SOP) for cutting layered microfluidic covertape materials using the Silhouette Cameo 4 cutter. It supports the device fabrication methods discussed in Chapter 5 and is intended for use by lab members preparing elastomeric, adhesive, or paper layers for diagnostic devices.

Document: *Silhouette Cameo 4 SOP.pdf*

UNIVERSITY of WASHINGTON
COLLEGE OF ENGINEERING

Silhouette Cameo 4 SOP

Olanrewaju Lab

Section 1 – Lab-Specific Information

Building/Room(s) covered by this SOP:	Nano ES 205A
Department:	Mechanical Engineering
SOP Prepared by:	Cosette Craig
Super-User Name:	Cosette Craig
Super-User Contact:	cosettec@uw.edu
Principal Investigator Name:	Ayokunle Olanrewaju
Principal Investigator Signature:	Click here to enter text.

Section 2 – Biological Hazard Information

n/a

Section 3 – Other Hazards

n/a

Section 4 – Personal Protective Equipment (PPE)

n/a, you may wear gloves and a lab coat when using the machine to avoid debris from clothing getting onto cover tape or the cutting mat

Section 5 – Protocol

Materials:

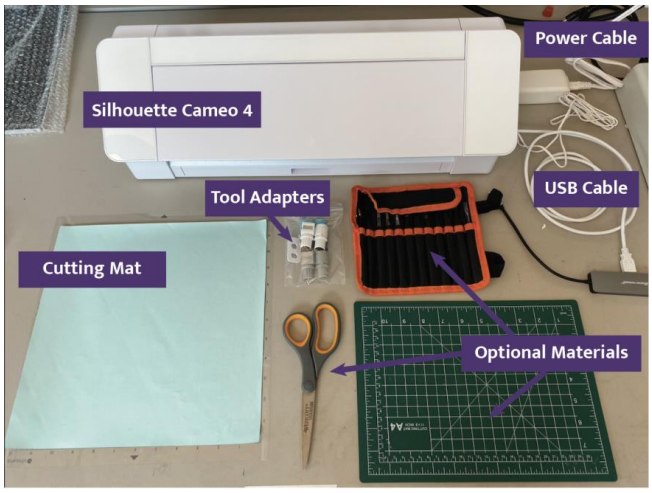

Software:

https://www.silhouetteamerica.com/software

Operating Procedure:

1. *Prepare your SolidWorks file for print by saving it as a .dxf file with 1:1 scale*
2. *Turn on the machine and open the cover*

3. *Make sure the AutoBlade is loaded into the machine. If it is not loaded, locate the blade and insert (https://www.youtube.com/watch?v=KEg0C1SzA30)*

4. *Launch the Silhouette Studio software*

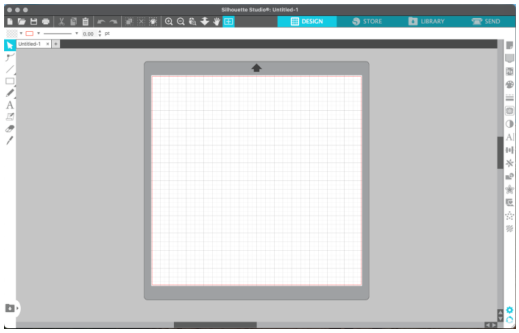

5. *Navigate to Edit>Preferences>Import>Open="Centered" to ensure your .dxf file will be imported to scale*

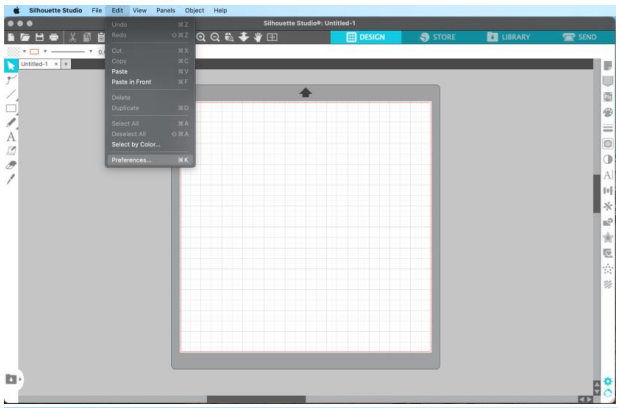

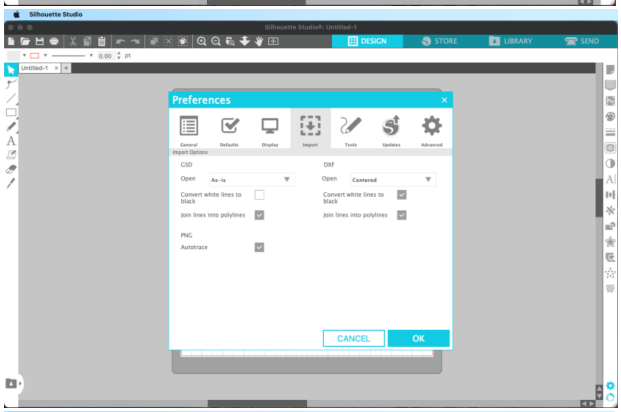

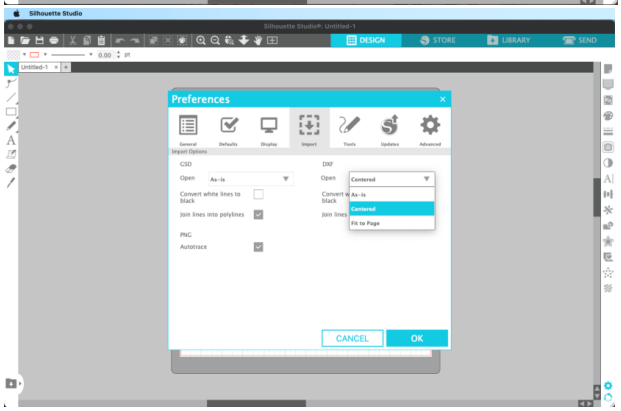

6. *Open your .dxf file. Ensure that the "Design Area Setup" settings on the right side of the screen for numbers 1 - 4 match the photo below.*

7. *You should see a thin outline of your design in the center of the cutting mat. The location of this outline will be the location of the cut material when you send it to print so click and drag the outline to move it to another part of the cutting mat. You can also copy and paste your design to make replicates.*

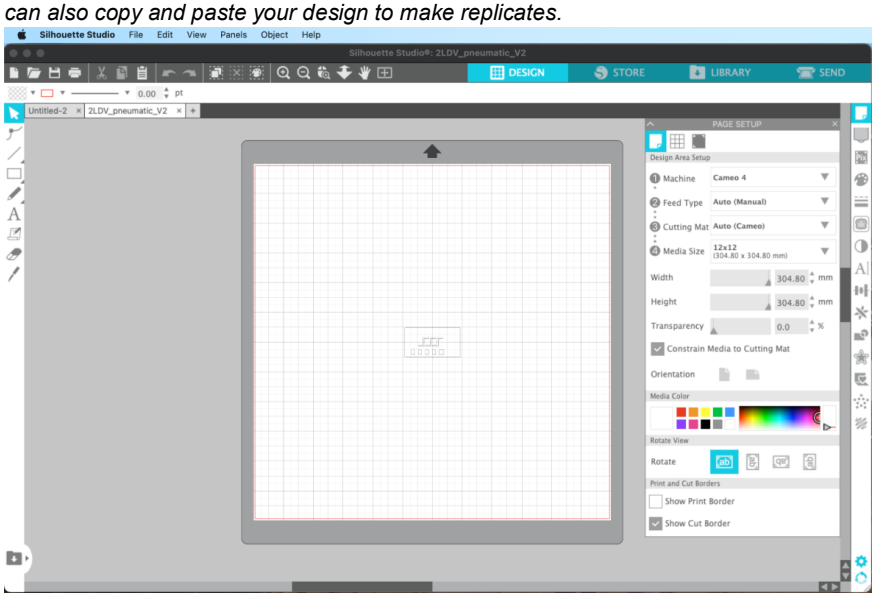

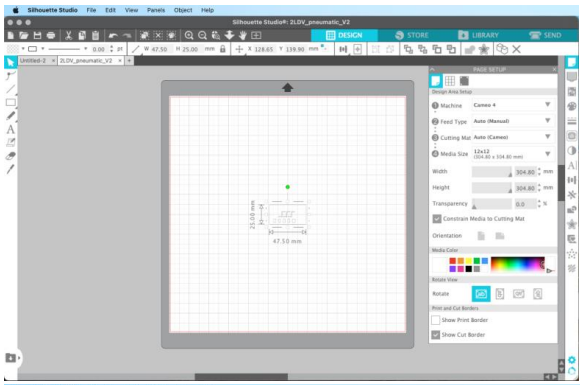

8. *When you're ready to print, navigate to the "Send" tab at the top right corner of the screen.*

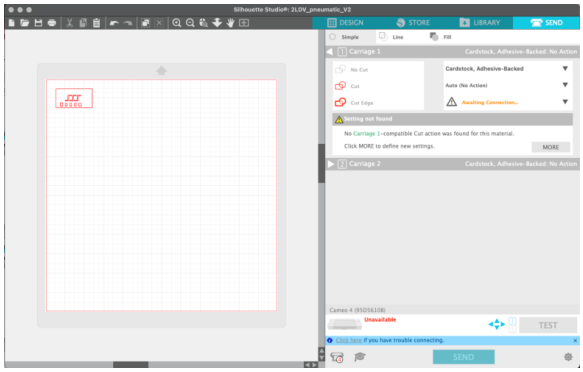

9. *You can connect the printer by the USB cable or by Bluetooth. The cutter may auto connect when you plug in the USB cable but to ensure you've connected the*

device, click on the Cameo Icon at the bottom left corner of the "Send" tab and select the Cameo machine to connect.

10. *The autoblade will cut along the paths highlighted in red on your drawing. Depending on your drawing, the software may automatically recognize the lines you'd like to cut but if it doesn't, select your objects on the cutting mat and then select "Cut" at the top left of the "Send" window.*

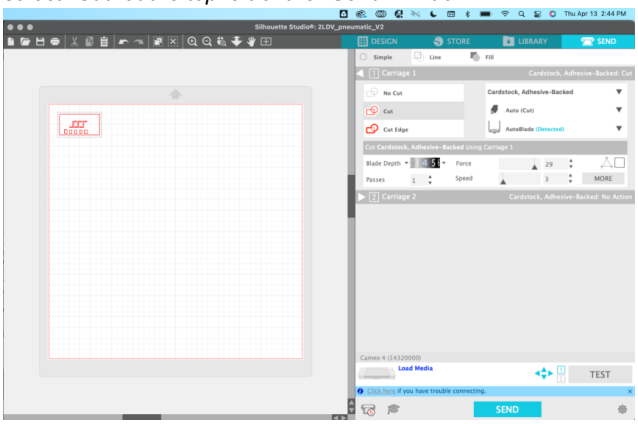

11. *Select your cut settings:*

Material to cut	*Material in Silhouette Studio*	*Force*	*Speed*	*Passes*	*Blade Depth*
Adhesives Research ARseal 90697 Hydrophobic Tape (1 layer)	*Cardstock, Adhesive Backed*	*1*	*1*	*1*	*9*
Adhesives Research ARseal 90697 Hydrophobic Tape (2 layers)	*Cardstock, Adhesive Backed*	*1*	*1*	*2 (or 3 for easy removal)*	*9*
Whatman Fusion 5 Paper (must be scotch taped to a business card to ensure it doesn't stick to cutting mat)	*Cardstock, Adhesive Backed*	*1*	*1*	*2 (or 3 for easy removal)*	*9*
Silicone Gasket Material with one-side of backing removed	*Cardstock, Adhesive Backed*	*1*	*1*	*3*	*9*
ARseal 7815 (3 layers)	*Cardstock, Adhesive Backed*	*15*	*3*	*4*	*10*

If you cut a new material, please add it to the table. We based our initial cut settings on this paper for the optimization of this cutter for microfluidics: https://doi.org/10.1063/1.5123130

12. *Prepare your cutting mat by applying materials to the light adhesive in your cutting area*

13. *Load your cutting mat into the machine by lining up the edge of the mat with the gray guidelines on the left side of the Silhouette. You should aim well but it's not imperative to be extremely precise; the machine will calibrate the blade to cut accurately.*

14. *Once you have the cutting mat aligned with the gray guidelines, press the up arrow that is lit up on the right side of the Silhouette. The Silhouette will roll the cutting mat into alignment. You may need to support the backside of the cutting mat while pressing the arrow to ensure the cutting mat feeds into the machine.*

15. *Navigate back to the software and press "Send" to begin cutting your material. During the cutting process, the autoblade will click about 10 times on the left side of the machine before navigating to its starting position. This is part of the calibration process so do not be concerned. Cutting is relatively quick so expect the machine to cut for just a few minutes (depending on the complexity of your design). In the "Send" window, you will be provided with an estimated time the completion when the cut begins.*

16. *When the cut is finished, press the down arrow lit up on the right side of the machine to release the cutting mat.*

17. *To finish using the Silhouette, remove your cuts from the mat, throw away any trash, tidy up the work station, and re-cover the cutting mat with the blue cover sheet. Turn off the Silhouette and roll the cover down to conceal the gantry and carriages. All done!*

Section 6 – Waste Disposal Procedures

Section 7 – Versions

Version Number	Posted Date	Implementation Date	Summary of Changes

1.0	04/23/2023	04/13/2023	New document

References

1. Meffan, C. *et al.* Capillaric field effect transistors. *Microsystems & Nanoengineering* **8,** 33. ISSN: 2055-7434 (Mar. 21, 2022).
2. Mak, D. *et al.* The reversible capillary field effect transistor: a capillaric element for autonomous flow switching. *Lab on a Chip* **25,** 1993–2003. ISSN: 1473-0197, 1473-0189 (2025).
3. Tokihiro, J. C. *et al.* The dynamics of capillary flow in an open-channel system featuring trigger valves. *Scientific Reports* **14,** 31732. ISSN: 2045-2322 (Dec. 30, 2024).
4. Cho, H., Kim, H.-Y., Kang, J. Y. & Kim, T. S. How the capillary burst microvalve works. *Journal of Colloid and Interface Science* **306,** 379–385. ISSN: 00219797 (Feb. 2007).
5. Cho, H., Parameswaran, M. (& Yu, H.-Z. Fabrication of microsensors using unmodified office inkjet printers. *Sensors and Actuators B: Chemical* **123,** 749–756. ISSN: 09254005 (May 2007).
6. Olanrewaju, A. O., Robillard, A., Dagher, M. & Juncker, D. Autonomous microfluidic capillaric circuits replicated from 3D-printed molds. *Lab on a Chip* **16,** 3804–3814. ISSN: 1473-0197, 1473-0189 (2016).

A | Supplementary Material For Chapter 4

Guide to This Appendix

This appendix provides supplementary material, technical documentation, and characterization data related to the development and implementation of self-coalescence modules (SCMs). It supports and extends the results presented in Chapter 4 of the dissertation.

This appendix includes:

- **SCM Technical Drawing** – Overview of SCM geometry with labeled dimensions.
- **Sharable STL Library of SCM Variants** – STL files for SCMs with different volume capacities and integration notes.
- **Python Scripts Used for SCM Characterization** – Scripts for ROI selection, montage creation, video annotation, and RGB plotting.
- **Design Iterations and Lessons Learned** – Overview of seven generations of SCM characterization chips.
- **Failure Mode Analysis** – Taxonomy of failure types and the emergence of optimal trench geometry.
- **Preliminary Integration of RESTRICT with SCM-Based Microfluidics** – Prototype results for integrating the RESTRICT assay onto 3D-printed SCMs.

A.1 SCM Technical Drawing

To support reproducibility and adaptation of this design, a detailed technical drawing of the self-coalescence module (SCM) is included in the supplemental archive. This drawing annotates all relevant dimensions and feature labels, including inlet geometry, trench depth and width, wrap radius, and vent alignment. It is intended to serve as a reference for CAD-based design and modification, enabling other researchers to replicate or adapt SCMs to their own circuit layouts.

A.2 Sharable STL Library of SCM Variants

To support reproducible and modular microfluidic design, we provide a set of four 3D-printable SCMs as sharable STL files. Each variant corresponds to a commonly used reagent volume (10, 20, or 50 µL), with form factors optimized for capillary-driven flow and compatibility with downstream circuit features. These modules are intended for plug-and-play use in custom CAD assemblies, reducing the design burden for new users and facilitating integration into more complex diagnostic workflows.

The table below summarizes key physical dimensions for each module.

Table A.1: Design parameters for sharable SCM variants

Target Volume	Length (mm)	Height (mm)	Notes
10 µL	27.87	4.05	Compact format for limited sample volume
20 µL (long)	47.17	4.05	Same height as 10 µL; longer channel for added volume
20 µL (tall)	29.75	5.30	Shortened footprint with increased height
50 µL	37.21	6.42	Highest capacity SCM with flared inlet for easy priming

Integration Instructions:

- Import the desired STL file into your CAD software.
- Align the inlet and outlet planes with neighboring features.

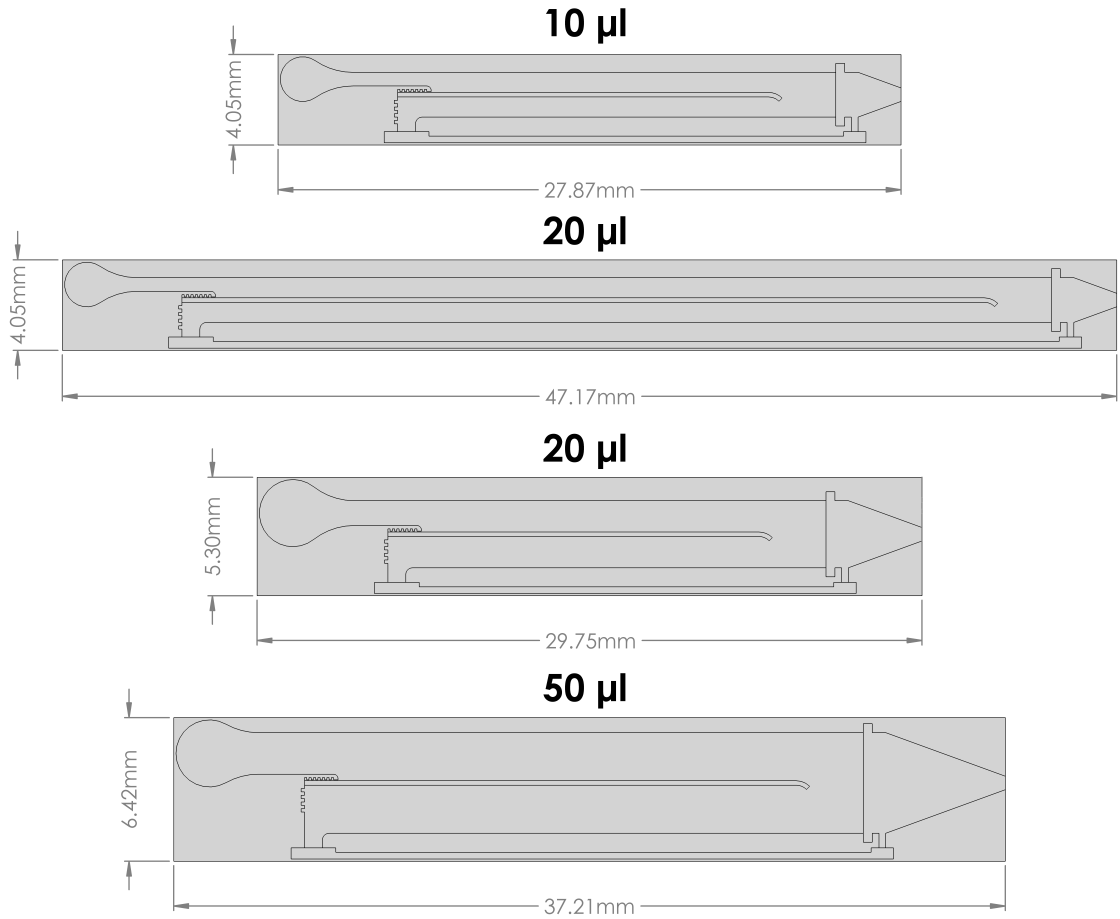

Figure A.1: Dimensional schematics for four self-coalescence module (SCM) variants designed for 10, 20, and 50 µL of fluid. These modules are provided as STL files for seamless insertion into CAD assemblies and can be used as modular building blocks in larger microfluidic circuits.

- Ensure floor height matches surrounding channel depth to preserve capillary continuity.
- Print the module as part of a complete circuit or as a standalone insert.

These modules are shared to promote accessible, reusable hardware design for microfluidics. STL files and example assemblies are available in the supplemental archive.

A.3 Python Scripts Used for Characterization of Reagent Reconstitution in 3D-Printed SCMs

A.3.1 Interactive ROI Selection and Normalization from a Single SCM Video Frame

Figure A.2: Annotated frame captured from a reagent reconstitution video of an SCM at 57 seconds. The main ROI (blue) and reference ROI (red) were selected interactively by the user. The frame was brightness-normalized to the reference region to account for lighting variation.

This Python script extracts a single video frame of fluid reconstitution from a self-coalescence module (SCM) and allows the user to define two fixed-size regions of interest (ROIs): one for reference normalization and one for monitoring the main fluidic region. ROIs are selected via interactive mouse clicks on the frame. Once defined, the frame is brightness-normalized using the mean color of the reference ROI, and both ROIs are outlined and labeled. The script outputs a normalized, annotated frame to support consistent ROI placement and brightness correction across analyses.

Listing A.1: Python script `scm_single_frame_roi_selector.py` used to extract, normalize, and annotate a single frame from an SCM reconstitution video based on user-defined ROIs.

```
import cv2
import numpy as np
import matplotlib.pyplot as plt
import os
import matplotlib as mpl
from tkinter import Tk, filedialog

# --- Prompt user to select input files and save paths ---
Tk().withdraw()

video_path = filedialog.askopenfilename(title="Select input video
    file", filetypes=[("MP4 files", "*.mp4")])
```

```
main_roi_file = filedialog.asksaveasfilename(title="Save MAIN ROI .
    npy file", defaultextension=".npy", filetypes=[("NumPy files", "
    *.npy")])
ref_roi_file = filedialog.asksaveasfilename(title="Save REFERENCE
    ROI .npy file", defaultextension=".npy", filetypes=[("NumPy files
    ", "*.npy")])

# --- Fixed ROI dimensions (in pixels) ---
ROI_WIDTH = 10
ROI_HEIGHT = 30

# --- Interactive ROI selection centered on mouse click ---
def fixed_size_roi_selector(window_name, image, label):
    roi_position = {"x": 0, "y": 0}
    clone = image.copy()

    def draw_fixed_box(event, x, y, flags, param):
        if event == cv2.EVENT_LBUTTONDOWN:
            clone[:] = image[:]
            top_left_x = max(0, x - ROI_WIDTH // 2)
            top_left_y = max(0, y - ROI_HEIGHT // 2)
            bottom_right_x = min(image.shape[1], top_left_x +
                ROI_WIDTH)
            bottom_right_y = min(image.shape[0], top_left_y +
                ROI_HEIGHT)
            roi_position["x"], roi_position["y"] = top_left_x,
                top_left_y
            cv2.rectangle(clone, (top_left_x, top_left_y), (
                bottom_right_x, bottom_right_y), (0, 255, 0), 2)
            cv2.imshow(window_name, clone)

    cv2.namedWindow(window_name)
    cv2.setMouseCallback(window_name, draw_fixed_box)
    print(f"Click to place {label} ROI of size {ROI_WIDTH}x{
        ROI_HEIGHT}. Press ENTER or SPACE to confirm.")

    while True:
```

```
        cv2.imshow(window_name, clone)
        key = cv2.waitKey(1) & 0xFF
        if key in [13, 32]:  # ENTER or SPACE
            break

    cv2.destroyWindow(window_name)
    x, y = roi_position["x"], roi_position["y"]
    print(f"{label} ROI selected at x={x}, y={y}, width={ROI_WIDTH},
        height={ROI_HEIGHT}")
    return (x, y, ROI_WIDTH, ROI_HEIGHT)

# --- Load ROI from file or prompt for new selection ---
def get_roi(frame, roi_file, label):
    if os.path.exists(roi_file):
        roi = np.load(roi_file)
        print(f"Loaded {label} ROI from file: {roi}")
    else:
        roi = fixed_size_roi_selector(f"Select {label} ROI", frame,
            label)
        np.save(roi_file, roi)
    return roi

# --- Load and verify video ---
vid = cv2.VideoCapture(video_path)
if not vid.isOpened():
    raise IOError(f"Could not open video file: {video_path}")

fps = vid.get(cv2.CAP_PROP_FPS)
frame_count = int(vid.get(cv2.CAP_PROP_FRAME_COUNT))
frame_time_sec = 57
frame_index = int(frame_time_sec * fps)

if frame_index >= frame_count:
    raise ValueError(f"Frame index {frame_index} exceeds total frame
        count {frame_count}.")

vid.set(cv2.CAP_PROP_POS_FRAMES, frame_index)
```

```
ret, frame = vid.read()
if not ret:
    raise ValueError(f"Couldn't read frame at {frame_time_sec}s.")

# --- Crop frame to remove 50px from top, bottom, and right edge ---
frame = frame[50:-50, :frame.shape[1]-50]
frame_h, frame_w = frame.shape[:2]

# --- Load or select ROIs and adjust for cropping ---
ref_x, ref_y, ref_w, ref_h = get_roi(frame, ref_roi_file, "Reference
    ")
x, y, w, h = get_roi(frame, main_roi_file, "Main")

ref_x -= 50
ref_y -= 50
x -= 50
y -= 50

ref_x = max(0, min(ref_x, frame_w - ref_w))
ref_y = max(0, min(ref_y, frame_h - ref_h))
x = max(0, min(x, frame_w - w))
y = max(0, min(y, frame_h - h))

# --- Normalize brightness of entire frame to the reference ROI ---
ref_region = frame[ref_y:ref_y+ref_h, ref_x:ref_x+ref_w]
ref_mean_color = np.mean(ref_region, axis=(0, 1))

frame_normalized = frame.copy().astype(np.float32)
for c in range(3):
    mean_val = np.mean(ref_region[:, :, c])
    if mean_val > 0:
        frame_normalized[:, :, c] *= ref_mean_color[c] / mean_val
frame_normalized = np.clip(frame_normalized, 0, 255).astype(np.uint8
    )

# --- Draw labeled ROIs on frame ---
frame_with_box = frame.copy()
```

```
cv2.rectangle(frame_with_box, (x, y), (x + w, y + h), (255, 0, 0),
    3)
cv2.rectangle(frame_with_box, (ref_x, ref_y), (ref_x + ref_w, ref_y
    + ref_h), (0, 0, 255), 3)

font = cv2.FONT_HERSHEY_SIMPLEX
font_scale = 1.2
thickness = 2

ref_label_pos = (ref_x, max(0, ref_y - 10))
main_label_pos = (x, max(0, y - 10))
cv2.putText(frame_with_box, "Reference ROI", ref_label_pos, font,
    font_scale, (0, 0, 255), thickness, cv2.LINE_AA)
cv2.putText(frame_with_box, "Main ROI", main_label_pos, font,
    font_scale, (255, 0, 0), thickness, cv2.LINE_AA)

# --- Display frame with ROIs using matplotlib ---
mpl.rcParams['font.family'] = 'Helvetica'
fig, ax = plt.subplots(figsize=(8, 6))
ax.imshow(cv2.cvtColor(frame_with_box, cv2.COLOR_BGR2RGB))
ax.axis('off')
ax.text(20, 180, f"t = {frame_time_sec - 47} s", color='black',
    fontsize=12, fontweight='bold', fontname='Helvetica')
plt.show()
```

A.3.2 Time-Stamped Frame Montage of SCM Ejection Post-Reagent Reconstitution

This Python script generates a visual summary of fluid ejection from a self-coalescence module (SCM) following reagent reconstitution. It prompts the user to select a video file and two region-of-interest (ROI) files—one for the main observation area and one for a reference region used for brightness normalization. The code extracts video frames at 5-second intervals during the ejection event, normalizes each frame to the reference ROI to correct for lighting variations, and overlays labeled boxes around both ROIs. These annotated frames are stacked vertically with white padding between them to form a

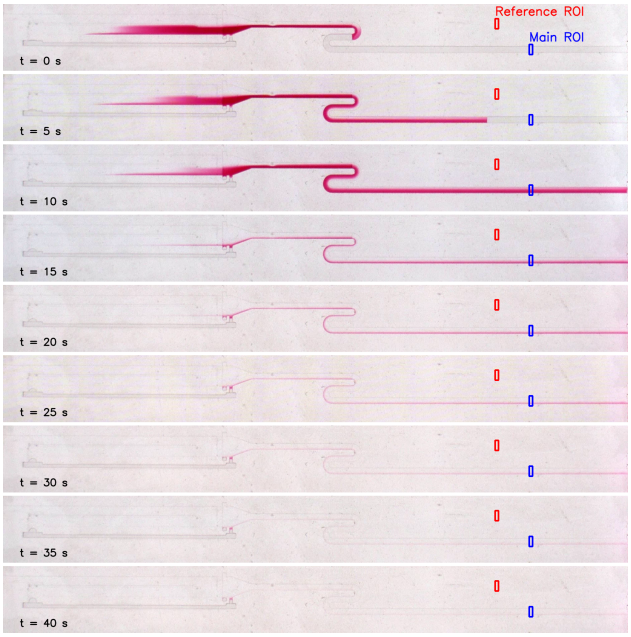

Figure A.3: Montage of annotated video frames showing fluid ejection from a self-coalescence module (SCM) following reagent reconstitution. Frames were sampled every 5 seconds and normalized to a reference region to account for lighting variation. Main and reference ROIs are boxed in blue and red, respectively. Time stamps indicate elapsed time since reconstitution.

single montage image, which is saved at high resolution. This figure allows for easy comparison of fluid motion across time, capturing the shape and timing of each pulse-like ejection event.

Listing A.2: Python script `scm_reconstitution_montage_generator.py` used to generate a time-stamped image montage of SCM ejection dynamics following reagent reconstitution. The script samples video frames, normalizes them to a reference ROI, and overlays labeled ROIs for visualization.

```
import cv2
import numpy as np
import matplotlib.pyplot as plt
import os
import matplotlib as mpl
from tkinter import Tk, filedialog

# --- Prompt user to select files interactively ---

# Suppress root window from showing up
Tk().withdraw()
```

```
# Prompt for video file
video_path = filedialog.askopenfilename(title="Select input video
    file", filetypes=[("MP4 files", "*.mp4")])

# Prompt for main ROI .npy file
main_roi_file = filedialog.askopenfilename(title="Select MAIN ROI .
    npy file", filetypes=[("NumPy files", "*.npy")])

# Prompt for reference ROI .npy file
ref_roi_file = filedialog.askopenfilename(title="Select REFERENCE
    ROI .npy file", filetypes=[("NumPy files", "*.npy")])

# Prompt for output file path
output_path = filedialog.asksaveasfilename(title="Save output image
    as", defaultextension=".png",
                                           filetypes=[("PNG files",
                                              "*.png")])

# --- Constants ---
ROI_WIDTH = 10
ROI_HEIGHT = 30

# --- Load ROI from file ---
def get_roi(frame, roi_file, label):
    if os.path.exists(roi_file):
        roi = np.load(roi_file)
        print(f"Loaded {label} ROI from file: {roi}")
    else:
        raise FileNotFoundError(f"{label} ROI file not found.")
    return roi

# --- Load and verify video ---
vid = cv2.VideoCapture(video_path)
if not vid.isOpened():
    raise IOError(f"Could not open video file: {video_path}")
```

```
fps = vid.get(cv2.CAP_PROP_FPS)
frame_count = int(vid.get(cv2.CAP_PROP_FRAME_COUNT))

# --- Read initial frame to determine cropped frame size ---
ret, temp_frame = vid.read()
if not ret:
    raise ValueError("Failed to read initial frame.")
temp_frame = temp_frame[50:-50, :temp_frame.shape[1]-50]
frame_h, frame_w = temp_frame.shape[:2]

# --- Load ROIs from reference frame at start_time ---
start_time = 26  # in seconds
vid.set(cv2.CAP_PROP_POS_MSEC, start_time * 1000)
_, ref_frame = vid.read()
ref_frame = ref_frame[50:-50, :ref_frame.shape[1]-50]
ref_x, ref_y, ref_w, ref_h = get_roi(ref_frame, ref_roi_file, "
   Reference")
x, y, w, h = get_roi(ref_frame, main_roi_file, "Main")

# Adjust ROI coordinates due to cropping
ref_x -= 50
ref_y -= 50
x -= 50
y -= 50

# Clip ROIs to stay within frame bounds
ref_x = max(0, min(ref_x, frame_w - ref_w))
ref_y = max(0, min(ref_y, frame_h - ref_h))
x = max(0, min(x, frame_w - w))
y = max(0, min(y, frame_h - h))

# --- Sample every 5 seconds from t=26s to t=71s ---
sample_times = np.arange(start_time, start_time + 45, 5)
processed_frames = []

for i, t in enumerate(sample_times):
    frame_index = int(t * fps)
```

```
    if frame_index >= frame_count:
        continue

    vid.set(cv2.CAP_PROP_POS_FRAMES, frame_index)
    ret, frame = vid.read()
    if not ret:
        continue

    # Crop frame (remove borders)
    frame = frame[50:-50, :frame.shape[1]-50]

    # Normalize intensity to reference region
    ref_region = frame[ref_y:ref_y+ref_h, ref_x:ref_x+ref_w]
    ref_mean_color = np.mean(ref_region, axis=(0, 1))
    frame_normalized = frame.astype(np.float32)

    for c in range(3):  # For each color channel
        mean_val = np.mean(ref_region[:, :, c])
        if mean_val > 0:
            frame_normalized[:, :, c] *= ref_mean_color[c] /
               mean_val

    frame_normalized = np.clip(frame_normalized, 0, 255).astype(np.
       uint8)

    # Draw ROI boxes
    frame_with_box = frame_normalized.copy()
    cv2.rectangle(frame_with_box, (x, y), (x + w, y + h), (255, 0,
       0), 3)
    cv2.rectangle(frame_with_box, (ref_x, ref_y), (ref_x + ref_w,
       ref_y + ref_h), (0, 0, 255), 3)

    # Add labels to first frame
    if i == 0:
        font = cv2.FONT_HERSHEY_SIMPLEX
        font_scale = 1.2
        thickness = 2
```

```
        cv2.putText(frame_with_box, "Main ROI", (x, max(0, y - 10)),
            font, font_scale, (255, 0, 0), thickness, cv2.LINE_AA)
        cv2.putText(frame_with_box, "Reference ROI", (ref_x, max(0,
           ref_y - 10)), font, font_scale, (0, 0, 255), thickness,
           cv2.LINE_AA)

    # Add time label
    display_time = int(t - start_time)
    timestamp_text = f"t = {display_time} s"
    cv2.putText(frame_with_box, timestamp_text, (50, 180), font, 1,
       (0, 0, 0), 2, cv2.LINE_AA)

    processed_frames.append(frame_with_box)

# --- Stack processed frames vertically with 10px padding ---
padded_frames = []
for i, frame in enumerate(processed_frames):
    padded_frames.append(frame)
    if i < len(processed_frames) - 1:
        spacer = 255 * np.ones((10, frame.shape[1], 3), dtype=np.
           uint8)
        padded_frames.append(spacer)

stacked = np.vstack(padded_frames)

# --- Display and save result using matplotlib ---
mpl.rcParams['font.family'] = 'Helvetica'
fig_height = stacked.shape[0] / 100  # ~100 px per inch

fig = plt.figure(figsize=(8, fig_height))
plt.imshow(cv2.cvtColor(stacked, cv2.COLOR_BGR2RGB))
plt.axis('off')
plt.savefig(output_path, dpi=600, bbox_inches='tight', pad_inches=0)
plt.show()
```

A.3.3 Batch Annotation of SCM Videos Using Shared Reference ROI

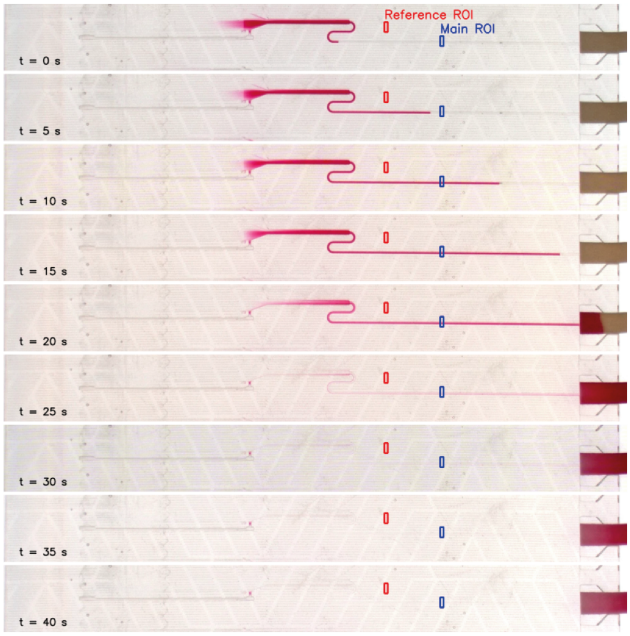

Figure A.4: Example frame annotated using the batch processing script. Videos were processed using a shared reference ROI (red box), while individual main ROIs (blue boxes) were loaded from pre-generated files. This enabled consistent labeling and normalization across multiple SCM reconstitution trials.

This script enables batch processing and annotation of multiple SCM reconstitution videos using a shared reference region of interest (ROI). The user selects three locations: a folder containing input '.mp4' videos, a folder containing '.npy' files for each main ROI, and a single '.npy' file containing the shared reference ROI. For each video, the script extracts a frame at 57 seconds, adjusts the ROI positions to match a predefined crop, and overlays labeled bounding boxes on the image. The output provides a standardized way to verify ROI placement and ensure consistency in downstream normalization and analysis.

Listing A.3: Python script `scm_batch_roi_annotator.py` used to annotate frames from multiple SCM reconstitution videos using a shared reference ROI and individually saved main ROI files.

```
import cv2
import numpy as np
import os
from tkinter import Tk, filedialog

# --- Initialize file dialog ---
Tk().withdraw()
```

```
# --- Prompt user to select input folder containing .mp4 videos ---
video_folder = filedialog.askdirectory(title="Select folder
    containing input MP4 videos")

# --- Prompt user to select folder where main ROI .npy files are
    saved ---
roi_folder = filedialog.askdirectory(title="Select folder containing
    main ROI .npy files")

# --- Prompt user to select the shared reference ROI .npy file ---
ref_roi_file = filedialog.askopenfilename(title="Select shared
    REFERENCE ROI .npy file", filetypes=[("NumPy files", "*.npy")])

# --- Constants ---
ROI_WIDTH = 10
ROI_HEIGHT = 30

# --- Load shared reference ROI ---
if os.path.exists(ref_roi_file):
    ref_roi = np.load(ref_roi_file)
    print(f"Loaded shared reference ROI from file: {ref_roi}")
else:
    raise FileNotFoundError("Reference ROI file not found.")

# --- Loop through video files in selected folder ---
for filename in os.listdir(video_folder):
    if not filename.endswith(".mp4"):
        continue

    video_path = os.path.join(video_folder, filename)
    roi_path = os.path.join(roi_folder, f"main_roi_{filename.replace
        ('.mp4', '')}.npy")

    print(f"\nProcessing: {filename}")
    print(f"Video path: {video_path}")
    print(f"Main ROI path: {roi_path}")
```

```
    # --- Load video ---
    vid = cv2.VideoCapture(video_path)
    if not vid.isOpened():
        print(f"Could not open video file: {video_path}")
        continue

    fps = vid.get(cv2.CAP_PROP_FPS)
    frame_time_sec = 57
    frame_index = int(frame_time_sec * fps)
    vid.set(cv2.CAP_PROP_POS_FRAMES, frame_index)
    ret, frame = vid.read()

    if not ret:
        print(f"Could not read frame at {frame_time_sec}s in {
            filename}")
        continue

    # --- Crop 50px from top, bottom, and right edge ---
    frame = frame[50:-50, :frame.shape[1]-50]
    frame_h, frame_w = frame.shape[:2]

    # --- Load main ROI ---
    if os.path.exists(roi_path):
        main_roi = np.load(roi_path)
        print(f"Loaded main ROI from file: {main_roi}")
    else:
        print(f"Main ROI file not found: {roi_path}")
        continue

    # --- Adjust ROI coordinates to account for cropping ---
    ref_x, ref_y, ref_w, ref_h = ref_roi
    x, y, w, h = main_roi
    ref_x -= 50
    ref_y -= 50
    x -= 50
    y -= 50
```

```
# --- Clamp ROIs to frame bounds ---
ref_x = max(0, min(ref_x, frame_w - ref_w))
ref_y = max(0, min(ref_y, frame_h - ref_h))
x = max(0, min(x, frame_w - w))
y = max(0, min(y, frame_h - h))

# --- Draw bounding boxes ---
frame_annotated = frame.copy()
cv2.rectangle(frame_annotated, (x, y), (x + w, y + h), (255, 0,
    0), 3)
cv2.rectangle(frame_annotated, (ref_x, ref_y), (ref_x + ref_w,
    ref_y + ref_h), (0, 0, 255), 3)

font = cv2.FONT_HERSHEY_SIMPLEX
font_scale = 1.2
thickness = 2
cv2.putText(frame_annotated, "Main ROI", (x, max(0, y - 10)),
    font, font_scale, (255, 0, 0), thickness, cv2.LINE_AA)
cv2.putText(frame_annotated, "Reference ROI", (ref_x, max(0,
    ref_y - 10)), font, font_scale, (0, 0, 255), thickness, cv2.
    LINE_AA)

# --- Show result ---
cv2.imshow("Annotated Frame", frame_annotated)
print("Press any key to continue...")
cv2.waitKey(0)
cv2.destroyAllWindows()
```

A.3.4 Aggregating and Plotting Inverted RGB Intensity from CSV Files

This Python script reads a folder of CSV files containing RGB intensity values extracted from videos of self-coalescence modules (SCMs). For each file, it inverts the raw and normalized channel values to improve contrast and aggregates data by timepoint. It then trims each curve to the first 40 seconds of the trial and computes the mean and standard deviation across replicates for each color channel. Three plots are generated: normalized

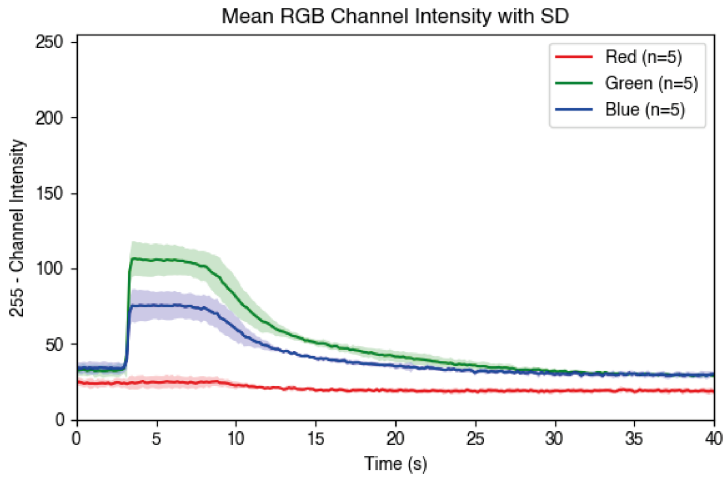

Figure A.5: Plots showing mean inverted RGB channel intensity across time for multiple SCM videos. Shaded areas represent ± 1 standard deviation across replicates. Each CSV file contributes one curve per channel, and the results are aggregated and aligned by timestamp.

RGB channels, raw RGB channels, and summed RGB intensity. This script is useful for comparing dye signal strength and stability across conditions.

Listing A.4: Python script `scm_csv_plotter.py` used to aggregate inverted RGB intensity curves from multiple CSV files and visualize the mean $\pm$ SD over time.

```
import matplotlib.pyplot as plt
import pandas as pd
import os
import glob
import numpy as np
from tkinter import Tk, filedialog

# --- Prompt user to select working directory containing CSV files
    ---
Tk().withdraw()
data_folder = filedialog.askdirectory(title="Select folder
    containing CSV intensity data")
file_pattern = '*.csv'

# --- Set global font to Helvetica for all plots ---
plt.rcParams['font.family'] = 'Helvetica'
```

```
# --- Find all CSV files in the selected folder ---
csv_files = glob.glob(os.path.join(data_folder, file_pattern))
if not csv_files:
    raise FileNotFoundError(f"No CSV files found in folder: {
       data_folder}")

# Initialize combined dataframes
combined_norm = pd.DataFrame()  # normalized R, G, B
combined_raw = pd.DataFrame()   # raw R, G, B
combined_sum = pd.DataFrame()   # summed normalized RGB

# --- Loop through each CSV and process channels ---
for i, file_path in enumerate(sorted(csv_files)):
    df = pd.read_csv(file_path)
    if 'Time (s)' not in df.columns:
        print(f"Skipping {file_path} due to missing 'Time (s)'
           column.")
        continue

    df['Time (s)'] = df['Time (s)'].round(6)
    time = df['Time (s)']

    # Invert normalized channel values
    channels_norm = {c: 255 - df[c] if c in df.columns else pd.
       Series([np.nan]*len(df))
                     for c in ['Red Normalized Intensity', 'Green
                        Normalized Intensity', 'Blue Normalized
                        Intensity']}

    # Invert raw channel values
    channels_raw = {c: 255 - df[c] if c in df.columns else pd.Series
       ([np.nan]*len(df))
                    for c in ['Red Raw Intensity', 'Green Raw
                       Intensity', 'Blue Raw Intensity']}

    # Invert summed normalized RGB intensity (if present)
    summed_inv = 765 - df['Summed Normalized RGB Intensity'] if '
```

```
        Summed Normalized RGB Intensity' in df.columns else pd.Series
        ([np.nan]*len(df))

    # Build and merge normalized RGB dataframe
    norm_df = pd.DataFrame({'Time (s)': time})
    for c in channels_norm:
        norm_df[c] = channels_norm[c]
    norm_df.rename(columns={
        'Red Normalized Intensity': f'Red_norm_{i}',
        'Green Normalized Intensity': f'Green_norm_{i}',
        'Blue Normalized Intensity': f'Blue_norm_{i}'
    }, inplace=True)
    combined_norm = norm_df if combined_norm.empty else pd.merge(
        combined_norm, norm_df, on='Time (s)', how='inner')

    # Build and merge raw RGB dataframe
    raw_df = pd.DataFrame({'Time (s)': time})
    for c in channels_raw:
        raw_df[c] = channels_raw[c]
    raw_df.rename(columns={
        'Red Raw Intensity': f'Red_raw_{i}',
        'Green Raw Intensity': f'Green_raw_{i}',
        'Blue Raw Intensity': f'Blue_raw_{i}'
    }, inplace=True)
    combined_raw = raw_df if combined_raw.empty else pd.merge(
        combined_raw, raw_df, on='Time (s)', how='inner')

    # Build and merge summed RGB dataframe
    sum_df = pd.DataFrame({'Time (s)': time, f'Summed_{i}':
        summed_inv})
    combined_sum = sum_df if combined_sum.empty else pd.merge(
        combined_sum, sum_df, on='Time (s)', how='inner')

# --- Trim all datasets to the first 40 seconds ---
def trim_to_40(df):
    return df[df['Time (s)'] <= 40].copy() if not df.empty else df
```

```
combined_norm = trim_to_40(combined_norm)
combined_raw = trim_to_40(combined_raw)
combined_sum = trim_to_40(combined_sum)

# --- Helper to plot mean    SD for RGB channels ---
def plot_multi_channel(df, title, channels_prefixes, ylabel="255 -
   Channel Intensity"):
    plt.figure(figsize=(6, 4))
    time = df['Time (s)'].values
    colors = {'Red': 'red', 'Green': 'green', 'Blue': 'blue'}

    for color in colors:
        cols = [c for c in df.columns if c.startswith(
           channels_prefixes[color])]
        if not cols:
            continue
        data = df[cols].values
        mean, std = np.nanmean(data, axis=1), np.nanstd(data, axis
           =1)
        plt.plot(time, mean, color=colors[color], label=f"{color} (n
           ={len(cols)})")
        plt.fill_between(time, mean - std, mean + std, color=colors[
           color], alpha=0.2, edgecolor='none')

    plt.title(title)
    plt.xlabel("Time (s)")
    plt.ylabel(ylabel)
    plt.xlim(0, 40)
    plt.ylim(0, 255)
    plt.legend()
    plt.tight_layout()
    plt.show()

# --- Plot normalized and raw RGB intensities ---
if not combined_norm.empty:
    plot_multi_channel(combined_norm, "Mean Normalized RGB Intensity
           SD", {'Red': 'Red_norm_', 'Green': 'Green_norm_', 'Blue':
```

```
        'Blue_norm_'})
if not combined_raw.empty:
    plot_multi_channel(combined_raw, "Mean Raw RGB Intensity    SD",
        {'Red': 'Red_raw_', 'Green': 'Green_raw_', 'Blue': '
       Blue_raw_'})

# --- Plot summed RGB intensity (inverted) ---
def plot_summed(df, title):
    plt.figure(figsize=(6, 4))
    time = df['Time (s)'].values
    cols = [c for c in df.columns if c != 'Time (s)']
    data = df[cols].values
    mean, std = np.nanmean(data, axis=1), np.nanstd(data, axis=1)
    plt.plot(time, mean, color='blue', label=f"Mean Summed Intensity
        (n={len(cols)})")
    plt.fill_between(time, mean - std, mean + std, color='blue',
       alpha=0.2, edgecolor='none', label=' 1  SD')
    plt.title(title)
    plt.xlabel("Time (s)")
    plt.ylabel("765 - Summed RGB Channel Intensity")
    plt.xlim(0, 40)
    plt.ylim(0, 765)
    plt.tight_layout()
    plt.show()

if not combined_sum.empty:
    plot_summed(combined_sum, "Mean Summed RGB Intensity    SD")
```

References

1. Sullivan, B. P. *et al.* Validation of the REverSe TRanscrIptase Chain Termination assay for measuring tenofovir diphosphate in dried blood spots from a clinical pharmacokinetic trial. *Journal of Antimicrobial Chemotherapy,* dkaf049. ISSN: 0305-7453, 1460-2091 (Feb. 25, 2025).
2. Lin, C., Craig, C., Leong, K., Chang, M. & Olanrewaju, A. *TOWARDS AUTONOMOUS MEASUREMENT OF ANTIRETROVIRAL DRUGS WITH 3D-PRINTED MICROFLUIDICS* en. in *2024 MicroTAS Book of Abstracts* (Chemical and Biological Microsystems Society, Montréal, QC, CANADA, Oct. 2024).

A.4 Design Iterations and Lessons Learned

To optimize SCM performance for integration with full circuits, we systematically varied geometric features using a series of characterization chips.

Fixed Design Variables

Variable Name	**Dimension [μm]**
Inlet Width	2000
Reservoir Depth	1000
Total Reservoir Width	4000
Reservoir Length	15000 (V = 60 μl)
Wrap Width	2000
Wrap Radius/Angle	2000/45
CPL Trench Length	

Table A.2: Fixed SCM design parameters used across all characterization chips.

A.4.1 Characterization Chip 1: Trench Depth and Width Variations

We tested trench depths from 1200–1500 μm and widths from 200–500 μm. Shallower trenches often failed to coalesce, while excessively deep or wide trenches led to unwanted

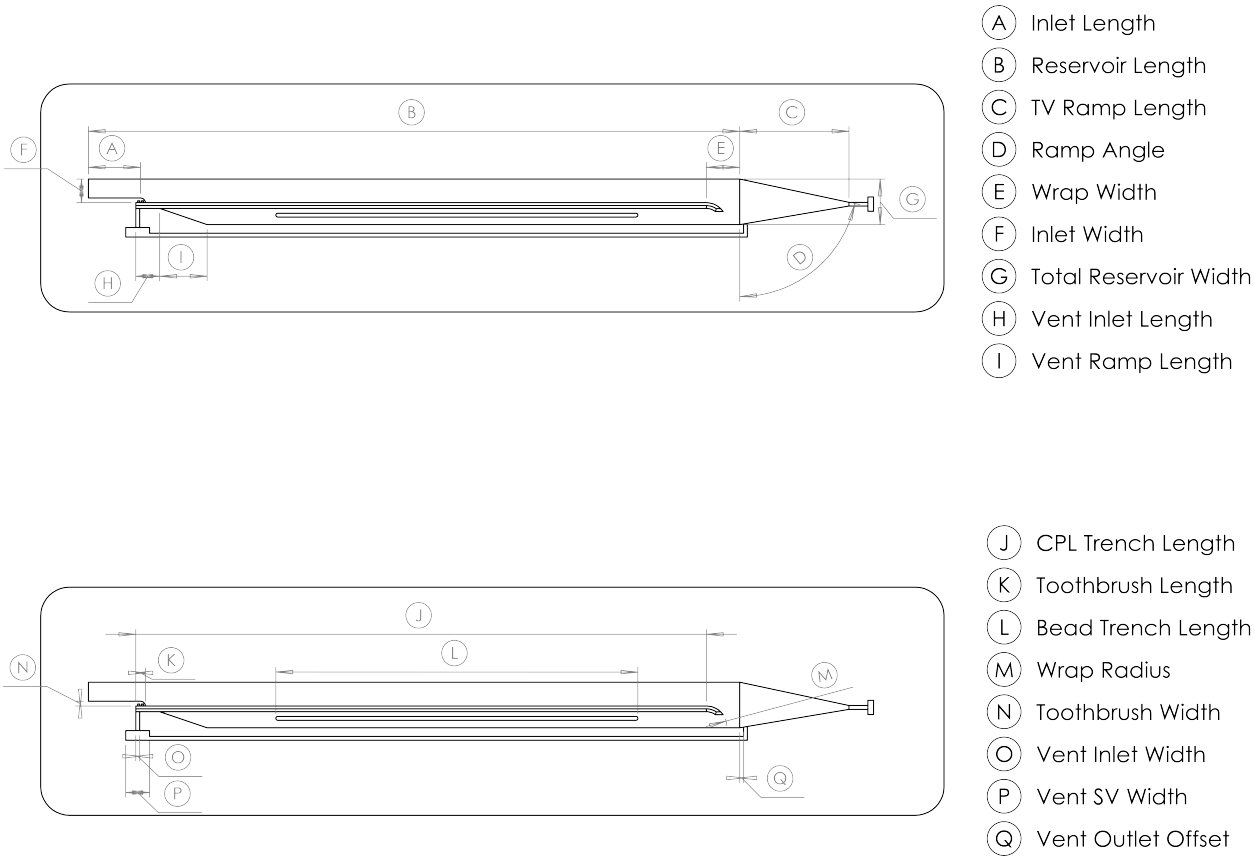

Figure A.6: SolidWorks schematic of the self-coalescence module (SCM) geometry used to guide chip characterization.

pre-wetting. These tests informed the dimensional constraints used in later chips.

	CPL Trench Depth	**CPL Trench Width**	**CPL Trench Chamfer**
Characterization Chip 1: Varying CPL Trench Depth	1200 μm	500 μm	0 μm
	1300 μm	500 μm	0 μm
	1400 μm	500 μm	0 μm
	1500 μm	500 μm	0 μm
Characterization Chip 1: Varying CPL Trench Width	1500 μm	200 μm	0 μm
	1500 μm	300 μm	0 μm
	1500 μm	400 μm	0 μm
	1500 μm	500 μm	0 μm

Table A.3: Trench depth and width variations tested in Characterization Chip 1.

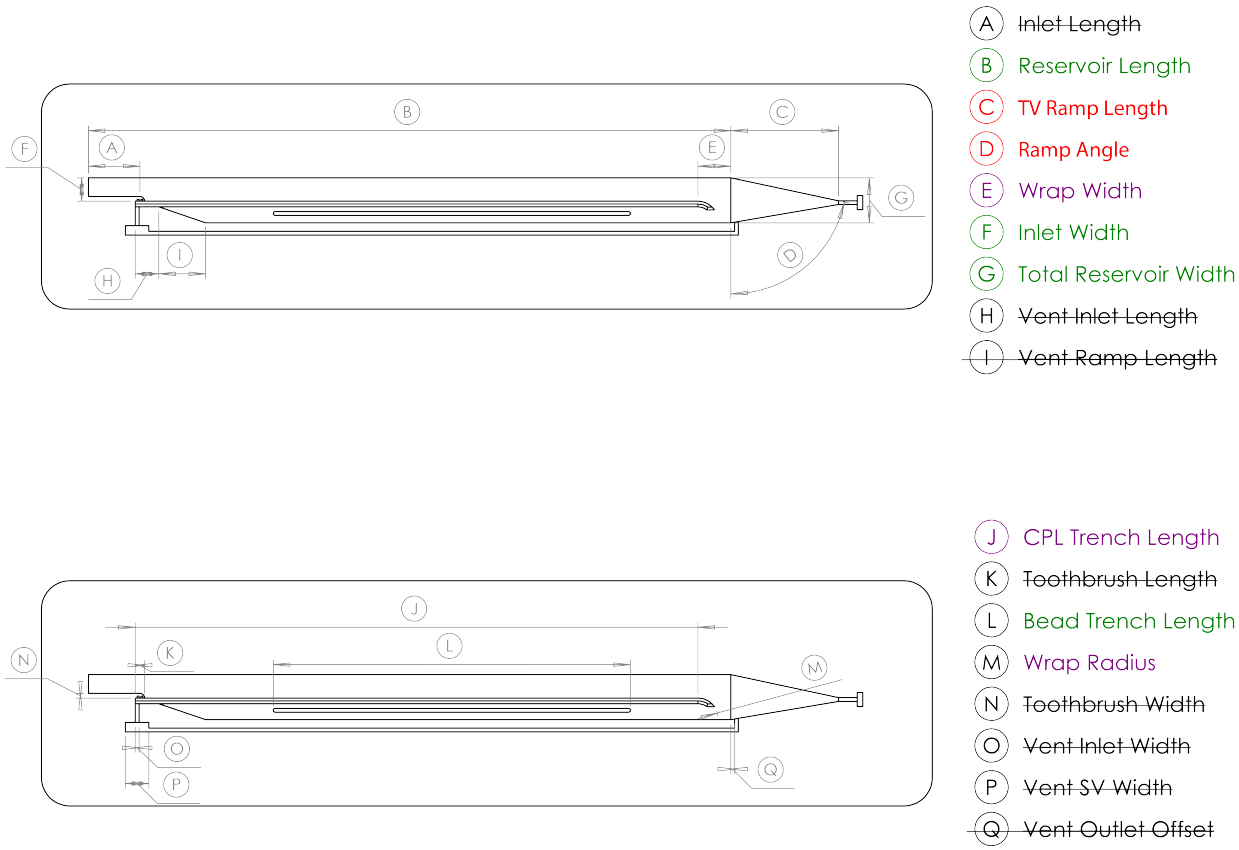

Figure A.7: SolidWorks schematic of the self-coalescence module (SCM) geometry used to guide chip characterization. Key geometric parameters include trench depth and width, wrap radius, stop valve placement, and vent channel alignment. Labeled features correspond to fixed design values (green), optimizable parameters (purple), and critical-to-optimize regions (red).

A.4.2 Characterization Chip 2: Ramp Stops and Curl Geometry

Introducing a step down (Δh) from the reservoir to the outlet and varying curl geometries (radius and extension) aimed to support wrapping and coalescence. However, most designs failed due to premature wetting of vent walls, highlighting the need for more controlled fluid interfaces.

	CPL Trench Depth	CPL Trench Width	Step Down Δh
Characterization Chip 2: Varying Reservoir to Outlet Step Down	1200 μm	200 μm	Δ400 μm
	1200 μm	200 μm	Δ500 μm
	1200 μm	200 μm	Δ600 μm
	1200 μm	200 μm	Δ700 μm

Table A.4: Step height variations between reservoir and outlet in Characterization Chip 2.

	CPL Trench Depth	CPL Trench Width	Curl Radius / Angle / Extension
Characterization Chip 2: Varying Curl Geometry	1200 μm	200 μm	1500 μm / 45° / +0 μm
	1200 μm	200 μm	2100 μm / 45° / +500 μm
	1200 μm	200 μm	1500 μm / 60° / +500 μm
	1200 μm	200 μm	1500 μm / 60° / +1000 μm

Table A.5: Curl geometry variations tested in Characterization Chip 2.

A.4.3 Characterization Chip 3: SCM Redesign 1 (Self-Wetting & Venting Modules)

Explored more complex geometries, including a self-wetting variant and modules with dedicated venting channels. All designs failed due to wetting at the trench inlet or vent, suggesting that passive venting geometries can introduce instability.

A.4.4 Characterization Chip 4: SCM Redesign 2 (Corrugation Configurations)

Focused on venting modules with enhanced stop valves and two "corrugation" inlet shapes—one flush with the trench wall, one inset by 0.1 mm. Only one trial partially succeeded (outside of captured video), emphasizing that stop valve masking and inlet shape can modestly help but were insufficient alone.

A.4.5 Characterization Chip 5: Curl Optimization

Modified the wrap geometry to increase curl aggressiveness and redesigned the inlet angle. All iterations failed, largely due to fluid pre-wetting the vent wall or failing to reach the wrap, indicating excessive wrapping resistance.

A.4.6 Characterization Chip 6: Ramp Stop Redesign ("Salmon Belly" Design)

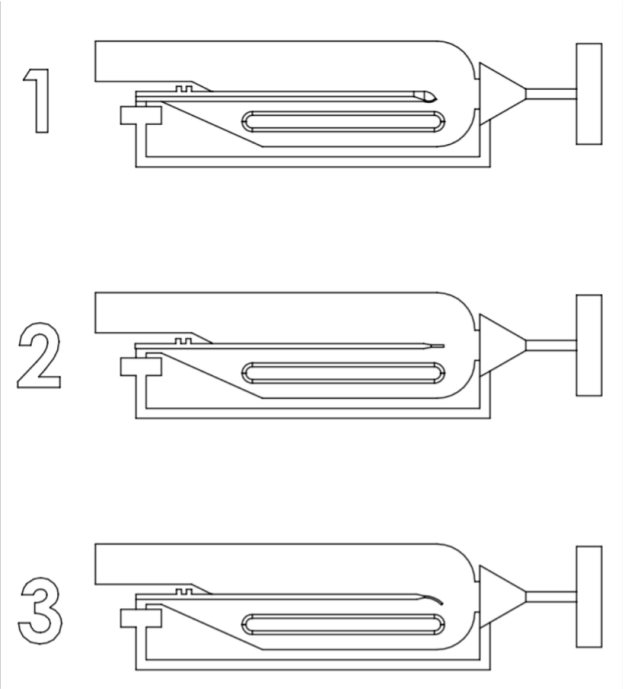

Figure A.8: Design variations to promote fluid wrapping and self-coalescence in SCMs. The "salmon belly" ramp geometry aimed to provide a convex contact interface, while curl modifications tested changes in radius, angle, and extension length. Despite improvements in inlet shaping, most designs failed due to pre-wetting of trench walls or incomplete wrap initiation.

Aimed to promote coalescence by creating a curved ramp surface for the fluid to meet. Failures stemmed from tape defects and fluid leaking under the tape from oversized reservoirs, reinforcing that the reservoir scale must match circuit constraints.

A.4.7 Characterization Chip 7: Miniaturized SCMs

Shrunk reservoir height and trench dimensions (100–400 μm deep, 100–400 μm wide) to better align with RBV requirements. Several conditions succeeded—especially narrower, shallower trenches—demonstrating the benefits of reduced resistance and faster unzipping.

	CPL Trench Depth	CPL Trench Width	CPL Trench Chamfer
Characterization Chip 7: Varying CPL Trench Depth	100 μm	400 μm	0 μm
	200 μm	400 μm	0 μm
	300 μm	400 μm	0 μm
	400 μm	400 μm	0 μm
Characterization Chip 7: Varying CPL Trench Width	400 μm	300 μm	0 μm
	400 μm	200 μm	0 μm
	400 μm	150 μm	0 μm
	400 μm	100 μm	0 μm

Table A.6: Trench depth and width variations tested in Characterization Chip 7. This miniaturized SCM series targeted improved performance with reduced scale.

A.4.8 Beads V7/V8: Circuit-Level Testing

Integrated the best-performing SCM into full circuits and tested with and without the SCM present. Beads V8 added particulate flow. These tests verified functionality under real loading conditions, showing SCM robustness when scaling was properly managed.

A.4.9 Hydrophilic Resin Trials

Tested location-specific hydrophilic surfaces to guide flow. Despite added mixing steps, results were inconsistent and often led to bursting flows, suggesting that local surface treatment may introduce more variability than control.

A.4.10 Conclusion

Across the series of characterization chips, we identified critical design principles for reliable SCM performance. Shallow trench depths (≤ 400 μm) and narrow trench widths (≤ 300 μm) consistently improved wrapping and unzipping behavior by reducing capillary resistance and minimizing pre-wetting of vent walls. Curl geometry had limited impact unless paired with aggressive inlet shaping and tight stop valve control. Attempts to introduce local surface treatment or self-wetting designs were ultimately less robust than purely geometric solutions. The final SCM design used in the full circuit leverages these insights—employing a compact trench profile, constrained wrap width, and fixed stop valve alignment—to ensure repeatable coalescence and integration within a multilayer capillaric workflow.

A.5 Failure Mode Analysis

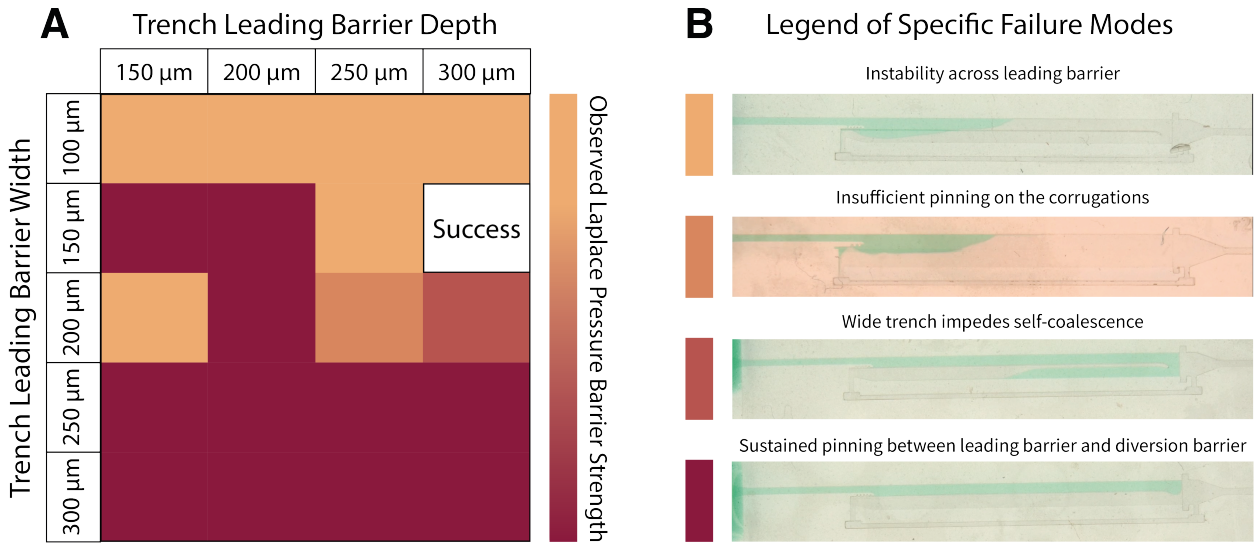

Figure A.9: Failure modes in miniaturized SCMs reveal the role of Laplace barriers. (A) Heatmap summarizing self-coalescence outcomes across trench depth and width combinations. Each square is colored by failure severity, from minor instability to total arrest, with one successful geometry outlined in white. (B) Representative images from failure conditions, organized from weakest to strongest Laplace barriers: (1) instability across the leading barrier, (2) insufficient pinning on trench corrugations, (3) failure to coalesce across wide trenches, and (4) sustained pinning between leading and diversion barriers. These outcomes guided refinement of trench geometry for robust SCM performance.

A.5.1 Successful coalescence

The sole successful geometry (300 μm trench depth $\times$ 150 μm width) enabled fast and reliable self-coalescence. The fluid front wrapped cleanly around the trench, rapidly unzipped the opposing plug, and exited without vent fouling or flow stagnation. This geometry appears to balance pinning and propulsion, establishing the minimum Laplace barrier needed to guide wrapping without resisting it. This is the final trench dimension presented in SCMs in the main body of the paper

A.5.2 Instability across leading barrier

In the shallowest trench geometries, the fluid front often paused at the trench, indicating the presence of a momentary pressure barrier, but failed to maintain stable contact.

Rather than wrapping or coalescing, the fluid advanced into the reservoir as if no capillary pinning line were present. This behavior suggests that the Laplace pressure at the trench edge was too weak to anchor the meniscus, resulting in premature breakthrough and failed coalescence.

A.5.3 Insufficient pinning on the corrugations

Some geometries enabled partial filling along the trench but, due to leakage at the back wall, failed to generate a self-sustaining coalescence event. The fluid front made contact with the trench but was able to traverse the pressure barrier by creeping along the rear surface, indicating that surface energy and geometry were insufficient to pin the flow. Without effective anchoring to contain the meniscus, the fluid bypassed the intended path and short-circuited the vent.

A.5.4 Wide trench impedes self-coalescence

Geometries with wide trenches often allowed fluid to enter the reservoirh but prevented it from wrapping tightly enough to self-wet the laplace pressure barrier, initiating self-coalescence. The wide trench made it energetically unfavorable for the fluid to bridge the coalescence gap. These conditions illustrate how wide trenches blunt the driving pressure for unzipping.

A.5.5 Sustained pinning between leading barrier and diversion barrier

In the deepest trench geometries, the fluid front pinned along the length of the trench and remained pinned for extended periods without initiating wrapping. Rather than failing due to instability, the meniscus was stably anchored between geometric barriers but could not overcome the Laplace pressure threshold required for self-coalescence. This high-barrier failure mode represents a stable but non-functional state.

A.5.6 Conclusion

Together, these failure modes illustrate the delicate balance of capillary forces required for successful SCM operation. Too little resistance results in unstable or misdirected flow, while too much creates energetic barriers that stall coalescence entirely. The successful geometry emerged not from maximizing or minimizing pinning, but from tuning trench

dimensions to sustain controlled wrapping and self-wetting. This failure analysis validated trench geometry as a primary determinant of SCM reliability and directly informed the final design used in the main study.

A.6 Preliminary Integration of RESTRICT with SCM-Based Microfluidics

The work described here represents preliminary integration of the RESTRICT assay with 3D-printed self-coalescence modules (SCMs). These experiments lay the groundwork for a fully self-contained diagnostic chip and will be completed by a future student following the conclusion of my PhD.

A.6.1 Demonstration of an Enzyme Inhibition Assay Using 3D-Printed SCMs

The REverSe TRanscrIptase Chain Termination (RESTRICT) assay is a clinically validated method for monitoring HIV antiretroviral drug levels, including tenofovir diphosphate (TFV-DP)[1]. Designed for speed, low cost, and ease of use, RESTRICT measures reverse transcriptase activity in the presence of drug metabolites by synthesizing DNA from nucleic acid templates and quantifying output with an intercalating fluorescent dye. Importantly, the master mix components, nucleic acids, dNTPs, and enzymes, are readily dryable on microchip surfaces, making RESTRICT highly compatible with surface-based microfluidic integration.

To minimize user intervention and reduce reliance on external lab equipment, we implemented RESTRICT on a 3D-printed capillaric microfluidic chip with resuspension of reagents via 3D-printed SCMs. This platform enables automation of the assay's critical timed steps, including the addition of intercalating dye for fluorescence-based readout. RESTRICT has already been validated for on-chip incubation and detection[2], and here we introduce precise spotting and drying of nucleic acids and synthesis reagents directly onto the SCM surface using methods validated in Figure 5. By incorporating these dry reagents into a self-powered chip, we aim to streamline assay execution for point-of-need HIV drug monitoring.

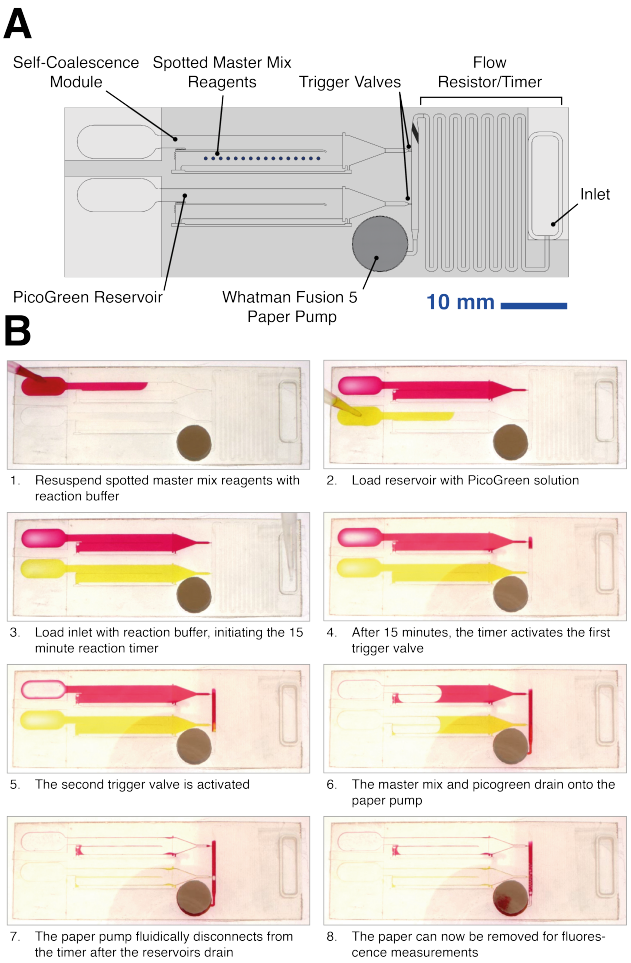

Figure A.10: Fluidic demonstration of RESTRICT assay integration with a 3D-printed self-coalescence module (SCM)

References

1. Sullivan, B. P. *et al.* Validation of the REverSe TRanscrIptase Chain Termination assay for measuring tenofovir diphosphate in dried blood spots from a clinical pharmacokinetic trial. *Journal of Antimicrobial Chemotherapy,* dkaf049. ISSN: 0305-7453, 1460-2091 (Feb. 25, 2025).
2. Lin, C., Craig, C., Leong, K., Chang, M. & Olanrewaju, A. *TOWARDS AUTONOMOUS MEASUREMENT OF ANTIRETROVIRAL DRUGS WITH 3D-PRINTED MICROFLUIDICS* en. in *2024 MicroTAS Book of Abstracts* (Chemical and Biological Microsystems Society, Montréal, QC, CANADA, Oct. 2024).